REPORT DOCUMENTATION PAGE

Form Approved
OMB No. 0704-0188

1. AGENCY USE ONLY (Leave blank)	2. REPORT DATE	3. REPORT TYPE AND DATES COVERED
	1996	Performance

4. TITLE AND SUBTITLE
The Turbulence Structure of Trailing Vortice Wakes

5. FUNDING NUMBERS
N00014-94-1-0744

6. AUTHOR(S)
Gordon J. Follin and William J. Devenport

7. PERFORMING ORGANIZATION NAME(S) AND ADDRESS(ES)
Virginia Polytechnic Institute and State University
Aerospace and Ocean Engineering
215 Randolph Hall
Blacksburg, VA 24061-0203

8. PERFORMING ORGANIZATION REPORT NUMBER
VPI-AOE-235

9. SPONSORING / MONITORING AGENCY NAME(S) AND ADDRESS(ES)
Office of Naval Research
800 N. Quincy St
Arlington, VA 22217

10. SPONSORING / MONITORING AGENCY REPORT NUMBER

11. SUPPLEMENTARY NOTES

12a. DISTRIBUTION / AVAILABILITY STATEMENT
Unclassified

12b. DISTRIBUTION CODE

13. ABSTRACT *(Maximum 200 words)*

The present investigation is a two-part study of the mean flow and turbulence structure of isolated vortices and counter-rotating vortex pairs. In the first part, the turbulence structure of an isolated vortex was studied using three-component velocity measurements. Vortices were generated using two symmetrical airfoils. Measurements were made in cross-sectional grids and profiles over a range of Reynolds numbers and downstream distances. Contours of axial normal stress were high-pass filtered to remove the contributions of wandering to the velocity fluctuations. This process reveals a vortex core which is laminar and is surrounded by a region of high turbulence. Core velocity profiles reveal that maximum tangential velocity increases with Reynolds number and decreases with distance downstream. Core radius increases with distance downstream and decreases with Reynolds number.

In the second part, flow visualizations of the wake behind a delta wing model were made for a range of Reynolds numbers and lift coefficients. These visualizations reveal the near-instantaneous turbulence structure of the wing wake which is dominated by a vortex pair and a connecting "braid" wake. The braid spacing decreases with increasing Reynolds number and is independent of lift coefficient. The extent of the braid downstream of the wing increases with lift coefficient and decreases with increasing Reynolds number. The large turbulence scales in the wing wake were found to increase in discrete jumps indicating some sort of reorganization of turbulence such as pairing. This reorganization of turbulence was found to occur more quickly as Reynolds number is increased.

14. SUBJECT TERMS
Trailing Vortices, wakes, turbulence

15. NUMBER OF PAGES

16. PRICE CODE

17. SECURITY CLASSIFICATION OF REPORT	18. SECURITY CLASSIFICATION OF THIS PAGE	19. SECURITY CLASSIFICATION OF ABSTRACT	20. LIMITATION OF ABSTRACT
Unclassified	Unclassified	Unclassified	

DISCLAIMER NOTICE

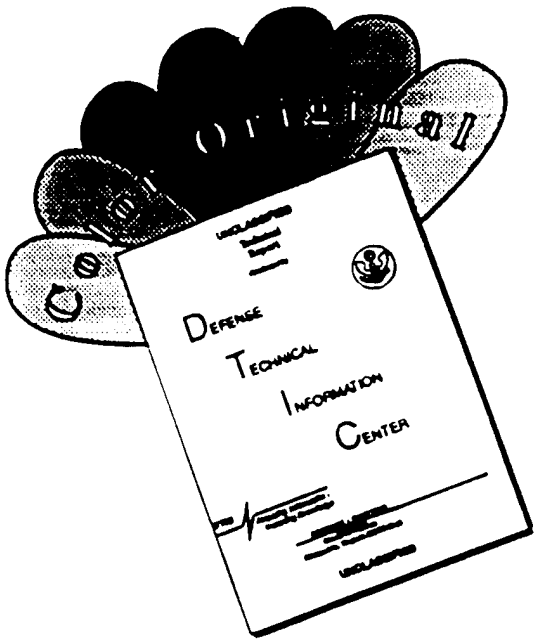

THIS DOCUMENT IS BEST QUALITY AVAILABLE. THE COPY FURNISHED TO DTIC CONTAINED A SIGNIFICANT NUMBER OF COLOR PAGES WHICH DO NOT REPRODUCE LEGIBLY ON BLACK AND WHITE MICROFICHE.

THE TURBULENCE STRUCTURE OF TRAILING VORTEX WAKES

by

Gordon J. Follin

William J. Devenport, Chairman

Department of Aerospace and Ocean Engineering

The present investigation is a two-part study of the mean flow and turbulence structure of isolated vortices and counter-rotating vortex pairs. In the first part, the turbulence structure of an isolated vortex was studied using three-component velocity measurements. Vortices were generated using two symmetrical airfoils. Measurements were made in cross-sectional grids and profiles over a range of Reynolds numbers and downstream distances. Contours of axial normal stress were high-pass filtered to remove the contributions of wandering to the velocity fluctuations. This process reveals a vortex core which is laminar and is surrounded by a region of high turbulence. Core velocity profiles reveal that maximum tangential velocity increases with Reynolds number and decreases with distance downstream. Core radius increases with distance downstream and decreases with Reynolds number.

In the second part, flow visualizations of the wake behind a delta wing model were made for a range of Reynolds numbers and lift coefficients. These visualizations reveal the near-instantaneous turbulence structure of the wing wake which is dominated by a vortex pair and a connecting "braid" wake. The braid spacing decreases with increasing

Reynolds number and is independent of lift coefficient. The extent of the braid downstream of the wing increases with lift coefficient and decreases with increasing Reynolds number. The large turbulence scales in the wing wake were found to increase in discrete jumps indicating some sort of reorganization of turbulence such as pairing. This reorganization of turbulence was found to occur more quickly as Reynolds number is increased.

Acknowledgments

First and foremost I would like to thank my parents for their love and support. They taught me many lessons of life, but in particular, that through dedication and hard work anything is possible. Without them none of this would have ever been. I would also like to thank my new wife, Michelle, for her many hours of waiting around as I needed "just fifteen more minutes". Also, without her I would still be cutting and pasting the many photographs presented here.

Special thanks are in order to my principal advisor, Dr. William J. Devenport. He has been an ideal mentor; giving me a sense of direction when I felt I had none but at the same time allowing me to be independent in my research pursuits. His door was always open to me and I appreciate his many hours of help.

I would also like to thank the many people who helped me perform the research presented in the current study. First of all, thanks to my good friend Ken Wittmer for his endless patience in helping me repair and calibrate the fragile hot-wire system as well as for his help in much of the data acquisition. Thanks to Mike Rife who also helped take many of the hot-wire measurements and first taught me their significance. Many thanks to those who helped bring my ideas to reality: Bruce Stanger, Greg Dudding, and Kent Morris. Thanks to Semere Bereketab and Kurt Elkins for their many hours of cheap labor. Their efforts were truly above and beyond the call of duty. The assistance of Christine

Vogel, Mark Engel, and Joe Miranda in acquiring the data is also gratefully acknowledged.

Special thanks are also extended to Greg Miller and Charles Williamson at Cornell University for their help in developing much of the flow visualization test apparatus as well as for the idea of free flying delta wing models. It was their beautiful pictures which first inspired me to undertake the flow visualization study.

I would also like to thank the Office of Naval Research, in particular Dr. L. Patrick Purtell, for their support under AASERT award number N00014-94-1-0744.

Table of Contents

List of Tables

List of Figures

List of Symbols

A_i, B_i, n	empirical constants in King's Law
a, b, c, d, h	geometrical parameters used in the bridle angle determination
c	wing chord
C_D	drag coefficient
C_L	lift coefficient
C_P	pressure coefficient
d	radial scale of the axial profile
D	drag force
D_m	delta wing drag
D_w	drag acting on support wire
E_i	hot-wire voltages
E_c	temperature corrected hot-wire voltage
f	high-pass filtering frequency
k	turbulence kinetic energy
L	lift force
L_m	delta wing lift
L_w	lift acting on support wire
L_1, L_2	lengths of the front and rear support wires forming the bridle
Q	magnitude of the velocity vector, $= \sqrt{U + V^2 + W^2}$

r, θ	polar coordinate system
r_l	measured core radius
Re_c	Reynolds number based on wing chord
T_{act}	actual tension in support wire
T_c	correction temperature
T_m	measured temperature
T_{meas}	measured wire tension
u', v', w'	fluctuating velocity components in the x, y, and z directions
U, V, W	mean velocity components in the x, y, and z directions
U_c	velocity out of wire plane
U_D	centerline axial velocity
U_{eff}	effective wire cooling velocity
$U_{est}, V_{est}, W_{est}$	estimated mean velocities
U_n	velocity normal to wire
U_{ref}	free-stream velocity
U_t	velocity tangential to wire
V_r	radial velocity
V_θ	tangential velocity
$V_{\theta l}$	measured peak tangential velocity
$V_{\theta max}$	maximum tangential velocity
x, y, z	Cartesian coordinate system

α	angle of attack, bridle angle
Δ_y, Δ_z	measurement volume dimensions in the y- and z-directions
γ	overheat ratio, typically 1.7
Γ	circulation
λ_b	delta wing braid wake spacing
λ_t	scale of largest turbulence structures in delta wing wake
θ	support wire angle relative to the vertical
θ_1, θ_2, θ_3, θ_4	wire angles
σ_y, σ_z	wandering amplitudes in the y- and z-directions

Chapter 1 - Introduction

The present investigation is a two-part study of the mean flow and turbulence structure of both isolated vortices and counter-rotating vortex pairs. This chapter presents a brief survey of what is presently known about such vortices thus placing the present work in context.

1.1 - Isolated Vortices

Wing-tip vortices have been the topic of much research over the past sixty years, including the work of Betz (1933) which laid the theoretical groundwork for future investigations of vortex behavior. These flows came to prominence as congestion at commercial airports increased and empirical models predicting their behavior were required for the safety of airline passengers. In spite of their importance, tip vortices are still poorly understood. In particular, most of the underlying turbulence structure and its variation with flow parameters remains a mystery. Before one can model the behavior of trailing vortices or hope to control this behavior, more work must be done to gain understanding of their underlying structure.

Whenever an experimental investigation into the structure of trailing vortices is undertaken, one must deal with two primary problems: vortex wandering and probe interference. Vortex wandering, or meander, is characterized as a slow, coherent motion of the vortex core which appears unavoidable in wind tunnel generated flows and acts to obscure important flow details. In particular, wandering produces fixed probe measurements which underestimate the magnitude of the vortex tangential velocity and overestimate the radius of the vortex core and the magnitude of the velocity fluctuations. Several previous researchers (Corsiglia *et al.*, 1973, Baker *et al.*, 1974, and Green and Acosta, 1991) have noticed the effects of wandering in their measurements. Corsiglia *et al.* (1973) determined from power spectra of vortex motion that there is no dominant characteristic frequency and therefore hypothesized that wandering is a result of wind tunnel turbulence. Baker *et al.* (1974) later concurred with these results and found that wandering is also due to mutual vortex pair instability far downstream of the wing. However, no one except for Baker *et al.* (1974) has attempted to perform a theoretical analysis of wandering effects. A more complete discussion of wandering will be presented in Chapter 2.

Several experimental approaches have been used to eliminate wandering effects but each has been met with limited success. Hoffmann and Joubert (1962) and Phillips and Graham (1984) used a split wing configuration to generate a tip vortex. They found that this method produces a more stable vortex than that generated by a single wing and that the position of this vortex in the tunnel is very steady and nearly independent of velocity,

angle of attack, or distance downstream. However, a split wing vortex is formed from two co-rotating vortices and has a turbulence structure that is quite different than a single tip vortex (Zsoldos and Devenport, 1992). Rapid-scanning laser Doppler anemometry (LDA) measurements made by Orloff (1974) have been effective in eliminating the effects of wandering by scanning the measurement volume along a profile through the core quickly enough so that the vortex does not move significantly during the measurement profile. However, such measurements are limited to near-instantaneous velocity profiles and time-averaged turbulence measurements are not possible. Also, sufficient seeding of the vortex core is difficult for these scanning LDA systems and poor sampling rates in the vortex core result. Green and Acosta (1991) and Shekarriz *et al.* (1993) have made global instantaneous velocity measurements using particle image velocimetry (PIV) which are inherently immune to wandering. However, this method is best suited to instantaneous velocity measurements and it is difficult to determine the mean flow characteristics from these types of measurements. McCormick *et al.* (1968), Mertaugh *et al.* (1977) and Panton *et al.* (1980) measured the vortices generated by full-scale aircraft in free-flight. While this eliminates any artificial wind tunnel effects, other instrumentation difficulties arise such as the difficulty in determining the location of measurement (i.e. the location of the following measurement aircraft relative to the vortex) and difficulty in keeping parameters such as angle of attack and free-stream velocity constant (level flight). Another solution, implemented by Corsiglia *et al.* (1973) used a rotating arm traversing

mechanism which allowed them to present results using a near-instantaneous traverse instead of fixed-probe time-averaged results.

Probe interference effects have been investigated by Baker *et al.* (1974) who determined from flow visualizations that trailing vortices may be sensitive to disturbances by even very small probes and the introduction of such a probe into a vortex core causes either a displacement of the vortex around the probe or a "bursting" of the vortex core on the probe tip. In contrast, Mason and Marchman (1973) found that a yaw probe has a negligible effect on the vortex as long as the probe is held parallel to the vortex core.

The formation of wing-tip vortices has been well documented in the flow visualizations of Francis and Katz (1988), Katz and Bueno Galdo (1989), and Engel (1995) and in the measurements of McCormick *et al.* (1968), Singh and Uberoi (1976), Mertaugh *et al.* (1977), Francis and Kennedy (1979), Shekarriz *et al.* (1993), and Chow *et al.* (1994). Francis and Katz (1988) performed flow visualizations of a tip vortex produced by a rectangular tipped NACA-66 hydrofoil. They observed that the vorticity generated in the wing boundary layer rolls up into multiple vortex structures including a primary vortex, counter-rotating vortices, shear layer eddies, and several secondary co-rotating vortices. The primary vortex was found to rise and move towards the wing root as it progresses downstream of the wing. This movement was found to increase with angle of attack and decrease with increasing free-stream velocity. The primary vortex was found to increase in size as it progresses downstream and increasing angle of attack was found to magnify this effect. The secondary structures observed include the counter-

rotating vortices, secondary vortices, and shear layer eddies. The counter-rotating vortices were first observed near the mid-chord and then wrap around the primary vortex as it progresses along the chord. At low angles of attack, these vortices appear to be larger than the primary vortex but as angle of attack is increased, their relative strength decreases. The secondary vortices were also first observed at the mid-chord. These vortices rotate in the same direction as the primary vortex and are formed by tip separation. These vortices progress downstream along the side of the wing and then roll over onto the top surface of the wing where they wrap around the primary vortex. Shear layer eddies were found to form at the trailing edge and become entrained in the main vortex further downstream. All of these vortex structures roll-up into a distinct tip vortex within a chordlength downstream of the trailing edge of the wing and form the "core" of the trailing vortex.

Katz and Bueno Galdo (1989) also made flow visualizations of the tip vortex produced by a rectangular tipped NACA-66 hydrofoil. Their observations confirmed the existence of the multiple vortex structures seen by Francis and Katz (1988). They found that the relative strength and importance of these structures is dependent on angle of attack, distance downstream, free-stream velocity, and surface roughness. Large vortex structures were observed on the side of the wing which move to the wing's suction side. The location at which this takes place was found to move upstream with increasing surface roughness. However, surface roughness has little effect on the vortex size and location.

Engel (1995) made flow visualizations of a blunt tipped NACA 0012 wing using helium-filled soap bubbles. He observed two vortices in his tip flow studies: a primary vortex which forms just downstream of the wing leading edge on the suction side of the airfoil and a weaker secondary vortex which forms on the blunt wing tip. The primary vortex was observed to lift away from the wing surface as it progresses down the chord with the magnitude of this displacement being dependent on angle of attack. The primary vortex was also observed to move inboard towards the wing root as it moves downstream. This movement was found to be highly dependent on chord Reynolds number. The primary and secondary vortices were observed to co-rotate in a helical pattern after leaving the wing tip.

Shekarriz *et al.* (1993) made particle displacement velocimetry (PDV) measurements in the near field of a low aspect ratio wing. They found the primary vortex to move inboard and down as it progresses downstream with the inboard movement being the most pronounced. They also noted the presence of secondary vortices which rotate in the same direction as the primary vortex. These vortices were found to dominate the circulation and tangential velocity profiles in the near field. However, as Reynolds number and angle of attack were increased, the effects of these secondary vortices was reduced.

Away from the wing tip, the vorticity generated in the wing's boundary layer becomes part of the wing wake which forms a vortex sheet at the trailing edge of the wing. This sheet is unstable and within several chordlengths downstream of the trailing edge rolls up around the core produced at the wing tip to form the trailing vortex. The

downstream distance required for vortex roll-up to be complete has been investigated by McCormick *et al.* (1968), Bilanin and Donaldson (1975), and others and is a function of wing geometry. Spreiter and Sacks (1951) and Mason and Marchman (1973) found that a trailing vortex will roll-up much more quickly for a low aspect ratio wing and for wings with wing loading concentrated near the wing tips.

A short distance downstream of the trailing edge, the trailing vortex consists of two discernible regions: the vortex core and the surrounding region. Measurements of the tangential velocity distribution by McCormick *et al.* (1968), Chigier and Corsiglia (1972), Mason and Marchman (1973), Orloff (1974), and Green and Acosta (1991), show that the tangential velocity in the core is similar to a solid-body rotation where the tangential velocity, V_θ, increases linearly with radius, r, from zero at the core center (r=0) to a maximum at the core edge. Outside of the core, the mean tangential velocity varies approximately inversely proportional to radial distance as is the case for a potential vortex. Inspection of the tangential velocity distribution by Green and Acosta (1991) shows that the vortex core becomes axisymmetric within a few chordlengths of the trailing edge. McCormick *et al.* (1968) find that the value of the maximum tangential velocity increases with angle of attack, wing aspect ratio (up to aspect ratios of 4 and then becomes independent), and taper ratio but the overall shape of the tangential velocity profile is unaltered. Measurements by Chigier and Corsiglia (1972) verify this increase in tangential velocity with increasing angle of attack for their rectangular wing. The vortex model of Bilanin and Donaldson (1975) predicts tangential velocity variations with angle of attack

that compare favorably to those measured in experiment. Mason and Marchman (1973) found that moving the wing loading towards the wing tip also increases the magnitude of the maximum tangential velocity.

Axial flow in the vortex has also been measured by Chigier and Corsiglia (1972), Lezius (1974), Orloff (1974), Green and Acosta (1991), Shekarriz *et al.* (1993), and others and is highly dependent upon flow conditions and wing geometry. High rates of rotation present in the vortex shortly after roll-up produce low pressures in the vortex core creating an axial velocity surplus. Orloff (1974) found that for large angles of attack, a velocity excess may persist downstream for large distances while for smaller angles a velocity deficit appears almost immediately downstream of the trailing edge. This is due to the physical relationships between induced drag, parasite drag, and head loss given by Batchelor (1964). Singh and Uberoi (1976) indicate that wing lift to drag ratio, L/D, is also important for determining axial flow characteristics. They found that for $L/D<20$, an axial defect was present while for $L/D=60$, and axial surplus was found.

The circulation distribution of the vortex has been examined through the work of Hoffmann and Joubert (1962), McCormick *et al.* (1968), Lezius (1974), Donaldson and Bilanin (1975), Phillips (1981), and Phillips and Graham (1984). Inside of the vortex core where the shear stresses are very small, the circulation, Γ, is proportional to the radial distance squared, r^2. Outside of this region, the circulation distribution is much more constant and is proportional to log r. These two regions are smoothly joined together by a

buffer region (Hoffmann and Joubert, 1962). Lezius (1974) and McCormick *et al.* (1968) found that the value of the core circulation remains constant with distance downstream.

The evolution of the axial and tangential velocity distributions and the turbulence structure of the trailing vortex has been documented by numerous fixed probe studies but very few have attempted to eliminate the effects of wandering thus undermining physical interpretation of their results. The most useful of the fixed-probe studies are the split wing measurements of Donsanjh *et al.* (1962), Phillips and Graham (1984), and Bandyopadhyay *et al.* (1991) and the low Reynolds number conventional wing measurements of Singh and Uberoi (1976). Donsanjh *et al.* (1962) made measurements of axial and tangential velocity for a laminar vortex which agree well with the laminar theory of Lamb (1932). Phillips and Graham (1984) found the development of the axial and tangential velocity fields to be coupled such that a decrease in axial velocity deficit produces a decrease in tangential velocity. Measurements by Bandyopadhyay *et al.* (1991) indicate that the turbulence structure is determined by Rossby number and not the vortex Reynolds number. From flow visualizations, they conclude that the vortex core exchanges momentum with the outer flow. At quasi-periodic intervals, the core receives a lump of turbulent fluid from the outer region where it is re-laminarized by the centrifugal motion of the core. These split wing results are of limited value however due to the aforementioned turbulence structure differences between split wing vortices and tip vortices (Zsoldos and Devenport, 1992). The low Reynolds number laminar vortex measurements are also of limited value due to the presence of a large de-stabilizing axial velocity deficit which is not

present in a turbulent tip vortex. Therefore, the majority of useful information concerning the streamwise evolution of the axial and tangential velocity profiles and turbulence structure comes from free-flight measurements (McCormick *et al.,* 1968, Iverson, 1976, Mertaugh *et al.,* 1977, and Panton *et al.*, 1980), rapid-scanning LDA measurements (Orloff, 1974, and Ciffone and Orloff, 1975), and PIV measurements (Green and Acosta, 1991, and Shekarriz *et al.,* 1993).

These studies reveal that the core, which is formed from the separated turbulent boundary layer of the wing, is initially a highly turbulent region of the vortex (McCormick *et al.*, 1968). The axial velocity is very unsteady and this unsteadiness increases as the vortex centerline is approached reaching levels as high as 20% of the free stream velocity. The tangential velocity distribution is also highly unsteady reaching levels as high as 15% of the free stream velocity in the vortex core (Green and Acosta, 1991). Increasing angle of attack acts to increase this unsteadiness. High levels of turbulence in the vortex core would lead to high values of turbulence momentum and mass exchange which would quickly destroy the vortex. This does not occur. Instead, the vortex must somehow confine the turbulence to the small core region and damp out the turbulence there (Chigier and Corsiglia, 1972). This idea agrees with the work of Bandyopadhyay *et al.* (1991) discussed previously. According to Rayleigh's criterion, solid body rotation such as that found in the vortex core is highly stable so that any turbulence should rapidly decay. The idea of laminar flow in the vortex core agrees well with the measurements of Corsiglia *et al.* (1973) and Phillips and Graham (1984), the full-scale visualizations of Huffaker *et al.*

(1970), and recent numerical simulations by Ragab and Sreedhar (1995) but accurate measurements of the turbulence structure in the vortex which have been corrected for wandering are required to develop a clear picture of the true turbulent structure of the trailing vortex.

As the vortex moves downstream, the core grows in size as the tangential velocity decays such that the product of core radius and maximum tangential velocity is constant (McCormick et al., 1968). Batchelor (1964), Bilanin and Donaldson (1975), Phillips and Graham (1984), and Shekarriz *et al.* (1993) determined that the variation of core size, axial, and tangential velocity profiles are coupled and not independent of each other. The effect of the decay of the tangential velocity is to increase the core diameter and to reduce the peak tangential velocity which in turn increases the pressure in the vortex core and consequently reduces the axial velocity deficit there. Measurements by McCormick *et al.* (1968), Singh and Uberoi (1976), and Green and Acosta (1991) reveal that tangential velocities show a quick expansion of the vortex over the first five chordlengths downstream of the wing but then change more slowly over the next 80 chords showing a decay with downstream distance, x, proportional to $\frac{1}{\sqrt{x}}$. The axial velocity deficit also decreases with downstream distance.

The measurements of Chigier and Corsiglia (1972) and Donsanjh *et al.* (1962) as well as the flow visualizations of Francis and Katz (1988) and Shekarriz *et al.* (1993) show that the vortex core moves in the crossflow plane as it progresses downstream. This

movement is in accordance with that predicted by Betz's (1933) theories of vortex motion. The core was found to move inboard with downstream distance due to non-uniform span load distributions. The core also moves above the wing with increasing distance downstream. The magnitude of the core movement is amplified with increasing angle of attack and decreasing free stream velocity. The spanwise movement was found to be greater than the upward movement.

The effect of Reynolds number on the streamwise variation of the mean axial and tangential velocity profiles and more importantly, on the turbulence structure, far from the wing has not yet been adequately determined. The primary reason that this type of information has been slow to develop is due to the difficulty in making reliable measurements of trailing vortices far downstream because of wandering effects. However, some results obtained through flow visualizations and full-scale, PIV, or rapid-scanning LDA testing are worth noting. In the near field, Francis and Katz (1988) and Green and Acosta (1991) found that Reynolds number effects are negligible on the axial and tangential velocity fields at low Reynolds numbers (for $x/c<2$) but do affect the location of the vortex core in the crossflow plane. This is contrary to the idea that Reynolds number effects are due to boundary layer transition on the wing. Shekarriz *et al.* (1993) found that increasing the Reynolds number makes the core appear more axisymmetric and secondary vortices are less evident. For downstream locations greater than $x/c=2$ but still in the near wake, the flow becomes highly Reynolds number dependent.

Studies by McCormick *et al.* (1968), Lezius (1974), and Mayer and Powell (1992) find that there exist large differences between the results of scale model tests and free-flight tests. Panton *et al.* (1980) report that the magnitude of the tangential velocity was 2.5 times higher than for model experiments. Vortex dissipation rates are also much slower in free-flight than for model tests. The magnitude of vorticity in the vortex system for model tests was found to be only 33% of that for free-flight. Also, at corresponding downstream locations, the vortex sheet behind a full-scale aircraft appears to be more completely rolled up producing a smaller vortex core. The circulation distribution of the vortex was found to be roughly exponential at model Reynolds numbers but changes to a logarithmic form at full-scale.

There has been very little work to date on the effects of Reynolds number in the far field with the possible exception of Ciffone and Orloff (1975), who note that several hundred spans downstream of the wing the value of maximum tangential velocity is independent of Reynolds number, and the vortex decay correlation of Iverson (1976).

In order to obtain a better perspective on how Reynolds number effects trailing vortex flow structure, and thus how well model tests duplicate the flow in actual free flight, measurements need to be made in the far field over a wide range of Reynolds numbers that have been corrected for wandering effects.

1.2 - Vortex Pairs

The wake behind a lifting vehicle is dominated by a pair of counter-rotating streamwise vortices. Such vortices are subject to two primary types of inviscid

instabilities. The most well-known is long-wave instability first described by Crow (1970). He found that trailing vortices undergo a symmetric near-sinusoidal instability with a wavelength of about 8 spans in planes inclined at about 45° to the horizontal. The amplitude of this instability grows to a point where the vortex pair joins at intervals to form vortex rings. Flow visualizations and observations by Scorer and Davenport (1970), Chevalier (1973), Sarpkaya (1992), and Liu (1992) verify the existence of Crow instabilities in real flows. Chevalier (1973) and Liu (1992) also found that vortex bursting prevents the formation of vortex rings if significant atmospheric turbulence was present.

The second type of inviscid instability is short-wave instability, first discussed by Crow and later by Widnall *et al.* (1974) and others. Widnall predicts this bending-mode instability to occur on both vortex rings and pairs. Flow visualizations by Maxworthy (1972, 1974, 1976) show short-wave instability on vortex rings at moderate Reynolds numbers. Here it causes the vortex ring to disperse into a "turbulent blob". He also observed that for sufficiently high Reynolds numbers (Re>1,000), a new vortex ring forms from this apparently disorganized velocity field. This new ring is larger and convects itself more slowly than the original vortex ring. Flow visualizations on vortex pairs by Locke *et al.* ((1993) and Thomas and Auerbach (1994) also show the presence of short-wave instability but at wavelengths much longer than that predicted by Widnall *et al.* (1974). Thomas and Auerbach (1994) also found that both short- and long-wave instability can exist on a vortex pair at the same time.

There have been surprisingly few observations of turbulence structure in vortex pair wakes. Two recent studies which have shed some light on this are Miller and Williamson (1995) and Devenport *et al.* (1996a). Devenport *et al.* (1996a) investigated the time-averaged turbulence structure of the vortex pair using detailed three-component hot-wire velocity measurements at two streamwise locations. They found that the turbulence structure around the vortex cores to be quite different at the two locations. At the upstream location, the cores are laminar but are embedded in turbulence formed by the roll-up and merger of the two wing wakes. Parts of this turbulence are heavily stretched by the mean motion of the vortices. This stretching intensifies large-scale turbulent structures aligned with the stretching direction. Further downstream the flow field is very different. The wake spirals disappear and are replaced by a more homogenous turbulent structure. True turbulence levels in the vortex are much greater indicating a transition to turbulence. They concluded that the interaction between a pair of counter-rotating vortices stimulates a turbulent decay which is absent in isolated vortices. This type of two-stage decay offers a possible explanation of the "plateau" and "decay" regions seen in the mean velocity measurements of Ciffone (1974), Ciffone and Orloff (1975), and Iverson (1976).

Miller and Williamson (1995) investigated the downstream wake of a delta wing (Re_c=10,000) using flow visualizations and velocity spectrum measurements to reveal the instantaneous turbulence structure of the vortex pair. These visualizations reveal the development of the primary vortex pair and spanwise turbulent structures connecting the

primary pair, which they call the "braid" wake. These highly regular structures, consisting of spanwise eddies spaced at even intervals of about 0.12 chords (c), were seen to dominate the near field of the wake. From velocity spectra at various points in the wake they found that there is a link between the turbulence scales in the "braid" wake and the primary vortices. They find that as the wake evolves, the scale of the turbulence structures it contains increases in discrete jumps. This could be a result of pairing. Further behind the wing they observe significant growth in the vertical extent of the wake. They propose that this is due to the diffusion of turbulence out of the Kelvin oval. Streamwise instabilities with a wavelength of about 4 or 5 initial vortex spacings were observed in the evolving wake, significantly less than that predicted by Crow (1970). At great distances (650 initial vortex spacings) behind the wing they observed vortex loops which then evolve into vortex rings. Between these rings they noticed interconnecting strands of dye which they hypothesize to be highly stretched limbs of the vortex loops as they evolve into vortex rings.

1.3 - Objectives

This work is a two-part study into the mean flow and turbulence structure of wing-tip vortices. The first part is a wind-tunnel investigation into the mean flow and time-averaged turbulence structure of a tip vortex shed by a symmetrical, rectangular wing using three-component hot-wire velocity measurements. This investigation forms part of a larger study by Devenport *et al.* (1996b) which presents detailed velocity measurements of the vortex core and surrounding wing wake.

The objectives of the wind tunnel investigation are:

1) To measure the mean velocity field and velocity fluctuations in the mid- and far-field of a single wing-tip vortex.

2) To correct these measurements for the effects of wandering to reveal the true underlying mean flow and time-averaged turbulence structure in the vortex core.

3) To examine the influences of wing geometry, Reynolds number, and downstream distance on this mean flow and turbulence structure.

4) To examine the mean flow and turbulence structure in the near two-dimensional wing wake far from the vortex core.

5) To determine if vortex wandering amplitudes are dependent on downstream distance or Reynolds number.

The second part of the present study consists of flow visualizations of the turbulent wake shed by a delta wing.

The objectives of the towing tank investigation are:

1) To develop a flow visualization test apparatus.

2) To determine if this apparatus is practical for visualizing delta wing wakes.

3) To visualize the wake shed by a delta wing to better understand the near-instantaneous turbulence structure of the wake.

4) To determine how this turbulence structure varies with Reynolds number and wing lift coefficient.

5) To reveal any mechanisms contributing to the decay of the wake as it evolves downstream.

Chapter 2 - Velocity Measurement Apparatus and Techniques

2.1 - Wind Tunnel

Experiments were performed in the Virginia Tech Stability Wind Tunnel (Figure 2.1). This facility is a continuous, closed jet, single return, subsonic wind tunnel with a contraction ratio of 9:1. The rectangular test section is 7.33m long and 1.83 x 1.83m in cross-section. The tunnel is powered by a 600 hp DC motor which allows for a maximum tunnel airspeed of 67m/s. The tunnel has seven turbulence screens located in the settling chamber, straightening vanes at all four turns, and vortex generators at the beginning of the diffuser which result in an overall flow quality in the bare test section that is nearly uniform with turbulence levels less than 0.10% and less than 2° flow angularity at test speeds (Choi and Simpson, 1987). Due to boundary layer growth, there exists a slight favorable streamwise pressure gradient $dC_p/dx = -0.003/m$.

2.2 - Vortex Generators (Wings)

Two wing types were used to generate vortices in this experiment. The first is a blunt-tip, aluminum, rectangular planform, NACA 0012 half-wing with a chord of

0.2032m. The second wing is similar to the first but is a NACA 0016 half-wing with a chord of 0.6096m. The wings' boundary layers were tripped using a single layer of 0.5mm diameter glass beads glued in a random pattern in accordance with previous experiments by Devenport *et al.* (1995). The average density of the beads was 200 beads/cm^2. For the NACA 0012 wing, these beads were placed between the 20% and 40% chord locations. The trip on the NACA 0016 wing was the same absolute size corresponding to between the 20% and 26.7% chord locations.

The wings were mounted vertically from the center of the upper wall at the upstream end of the test section with 0.879m and 1.219m protruding into the flow for the NACA 0012 and NACA 0016 wings respectively (Figure 2.2). The NACA 0012 wing was mounted using a turnstile (Figure 2.3) attached to the center of the upper wall of the test section which allowed the wing to be rotated about its quarter-chord for variation of wing angle of attack. A 101.6mm wide aluminum removable wing tip with 48 static pressure ports was used to set the wing at zero degrees angle of attack. This was accomplished by equalizing the pressure distributions on both sides of the wing. The pressure taps and wind tunnel pitot tube were connected to a scanivalve system and pressures were measured using a SETRA model 239 pressure transducer interfaced to an IBM AT computer through a Data Translation D2801-A A/D converter. A scribe mark was then placed on the turnstile corresponding to zero degrees angle of attack. Dial calipers were used to make additional scribe marks relative to the zero degree mark

corresponding to various angles of attack. The turnstile was then clamped into place to prevent unwanted rotation of the wing once the flow was turned on.

The NACA 0016 wing was mounted using the apparatus illustrated in Figure 2.4. This device mounts directly to the test section supports and allows the wing to be pivoted about its quarter-chord to vary the angle of attack. The wing is held in place within this structure by 8 threaded support screws and a horizontal beam support (Figure 2.4). The wing has 21 static pressure ports (one at the stagnation point and 10 on each surface) located around the wing 41mm from the wing tip which are used to set the wing to zero degrees angle of attack. This was accomplished in the same manner as for the NACA 0012 wing. Once the wing was set at zero degrees, the offset angle that the side support (Figure 2.4) made with the wind tunnel test section support was determined using dial calipers at two locations along the side support. The desired angle of attack was set by pivoting the support until the angle between the side support and the tunnel test section support was equal to the desired angle plus the offset angle. C-clamps were used to secure the wing support to the test section support.

2.3 - Traversing Mechanism

A two-dimensional, computer controlled, traversing gear mounted in the wind tunnel allowed the hot-wire probe to be positioned at any point in the cross-flow plane of the tip vortex (Figure 2.2). This traversing gear was set at a desired streamwise location and secured to the test section by adjusting the eight threaded feet. Movement within the cross-flow plane was controlled by three Compumotor RM series stepper motors, two for

the vertical axis and one for the horizontal. These motors were controlled by an IBM compatible computer which sent position locations through an RS-232 port to a SD drive system. This traversing system is accurate to within 0.50mm.

The probe was held parallel to the free-stream direction using a probe holder (Figure 2.2) which positioned the tip of the probe 0.559m upstream of the traversing gear. The length of the probe holder was determined as a compromise between two constraints: a long probe holder reduces the effects of the traversing gear on the measured flow upstream but can result in unacceptable vibration of the probe. In other words, the length of the probe holder was made as long as possible without introducing any noticeable vibration when viewed through a cathetometer.

2.4 - Hot-Wire Techniques

A sub-miniature 4-sensor hot-wire probe consisting of two orthogonal X-wire arrays (Auspex Corp. AVOP-4-100) was used for making velocity measurements in the vortices (Figure 2.5). Its 5μ tungsten wire sensors are 0.84mm in length with nominal wire angles of 45° relative to the free-stream creating a measurement volume of $0.50mm^3$. This type of probe was selected based on a study by Devenport *et al.* (1995) which showed it to be superior to triple and X-array probes for trailing vortex measurements.

An investigation into probe interference effects for this type of hot-wire probe was conducted by Devenport *et al.* (1995) . They performed flow visualizations over a range of conditions which clearly illustrate that probe interference effects are small. In addition, they performed wave speed calculations which confirmed that even the fastest waves are

swept downstream at 40% of the tunnel free stream velocity. A potential flow model of the probe was also used to evaluate probe interference and it was found that the probe would decelerate the flow a mere 0.4% in velocity at the measurement point.

Each hot-wire sensor was independently operated using a Dantec 56C17 bridge and a 56C01 constant temperature anemometer. The bridges were balanced and the frequency response was set flat out to 30kHz using the square-wave test. The anemometer outputs were passed through four x10 buck-and-gain differential amplifiers which were built in-house using Burr-Brown integrated circuits. These amplifiers were used to subtract an offset voltage from each of the anemometer outputs and then multiply the result by 10. The amplified anemometer signals were sampled by an IBM PC compatible computer using an Analogic 12-bit HSDAS-12 A/D converter. This A/D converter can simultaneously sample four channels at a maximum rate of 100kHz. Outputs from the tunnel pitot-static probe and the tunnel thermocouple were also sampled using two additional channels of the A/D converter. The computer made use of an 18-8 Laboratories PL2500 array processor to hasten the conversion of hot-wire voltage signals to velocity components.

The rest of this chapter describes how the final velocity estimates were determined from the measured hot-wire voltages. This was done using a method in which the unlinearized hot-wire voltages were calibrated to yield the effective velocities experienced by each wire. These effective velocities were used to determine first estimates of the velocity components and corrections to these first estimates were then performed to

compensate for flow angles relative to the probe axis, velocity gradient errors, and wandering effects. Section 2.4.1 describes how the wire effective velocities were determined from the wire voltages and corrected for temperature drift. Section 2.4.2 presents the equations used to obtain first estimates of the velocity components from the wire effective velocities. Section 2.4.3 details the procedure used to correct for the flow angle relative to the probe axis. Section 2.4.4 presents the procedure used to determine if velocity gradient errors were significant in the present measurements and outlines a feasible correction scheme. Finally, section 2.4.5 describes the procedure used to correct the mean velocity measurements for the effects of vortex wandering.

2.4.1 - Velocity Calibration

A velocity calibration was performed at a common location in the wind tunnel free-stream before and after each set of measurements was taken. This calibration was used to relate the wire voltages to their effective velocities using King's Law which states:

$$E_i^2 = A_i + B_i U_{eff_i}^n \qquad (2.1)$$

where E_i is a wire voltage, U_{effi} is that wire's effective velocity, n=0.45, and A_i and B_i are undetermined constants. A pitot-static probe was used to determine the wire cooling velocities for a given set of effective wire angles and local flow direction at the calibration location. This local flow direction was determined using a 7-hole yaw probe. The values of the constants A and B were determined from a least squares fit of the measured wire voltages to the determined effective wire velocities using 10 to 15 measurements over a

range of free-stream velocities. This procedure resulted in a wire voltage-to-velocity calibration accurate to within 1%.

Due to ambient temperature changes, it was not uncommon for the wind tunnel flow temperature to drift several degrees during a measurement. An increase in flow temperature will reduce the voltage required to maintain a constant wire temperature and introduces errors into the velocity measurements. A correction scheme based on the method developed by Bearman (1970) is used to correct all hot-wire data presented here. This method corrects the unlinearized voltages based on the measured voltages and temperatures and the temperature that one wishes to correct to. This correction is given by:

$$E_c = E_m \sqrt{\frac{\gamma - 1}{\gamma - T_m/T_c}} \qquad (2.2)$$

where γ is the overheat ratio (typically 1.7), T is the flow temperature, and E is the unlinearized voltage. The subscripts m and c stand for measured and corrected respectively.

2.4.2 - First Estimates of Velocities

To obtain a first estimate of the velocity components from the hot-wire probe we consider the probe illustrated in Figure 2.5. U, V, and W are the velocity components in the x, y, and z coordinate directions respectively. Using the method of Jorgenson (1971), the approximate relations for the four effective velocities inferred from the probe outputs are given by:

$$U_{eff1}^2 = U_{n1}^2 + k_1^2 U_{t1}^2 + h_1^2 U_{c1}^2 \qquad (2.3)$$

$$U_{eff2}^2 = U_{n2}^2 + k_2^2 U_{t2}^2 + h_2^2 U_{c2}^2 \qquad (2.4)$$

$$U_{eff3}^2 = U_{n3}^2 + k_3^2 U_{t3}^2 + h_3^2 U_{c3}^2 \qquad (2.5)$$

$$U_{eff4}^2 = U_{n4}^2 + k_4^2 U_{t4}^2 + h_4^2 U_{c4}^2 \qquad (2.6)$$

where wires 1 and 3 are in the *UV* plane , wires 2 and 4 are in the *UW* plane, and U_{ni}, U_{ti}, and U_{ci} refer to the normal, tangential, and out-of-plane velocities respectively as seen by the *i*th wire. *k* and *h* are the pitch and yaw factors respectively. Substituting for the normal, tangential, and out-of-plane velocity components for each wire gives:

$$U_{eff1}^2 = (U_1 \sin\theta_1 + V_1 \cos\theta_1)^2 + k_1^2 (V_1 \sin\theta_1 - U_1 \cos\theta_1)^2 + h_1^2 W_1^2 \qquad (2.7)$$

$$U_{eff2}^2 = (U_2 \sin\theta_2 + W_2 \cos\theta_2)^2 + k_2^2 (W_2 \sin\theta_2 - U_2 \cos\theta_2)^2 + h_2^2 V_2^2 \qquad (2.8)$$

$$U_{eff3}^2 = (U_3 \sin\theta_3 - V_3 \cos\theta_3)^2 + k_3^2 (V_3 \sin\theta_3 + U_3 \cos\theta_3)^2 + h_3^2 W_3^2 \qquad (2.9)$$

$$U_{eff4}^2 = (U_4 \sin\theta_4 - W_4 \cos\theta_4)^2 + k_4^2 (W_4 \sin\theta_4 + U_4 \cos\theta_4)^2 + h_4^2 V_4^2 \qquad (2.10)$$

where U_i, V_i, W_i are the mean velocity components acting on the *i*th wire. The pitch and yaw factors, *k* and *h*, were assumed to be 0.0 and 1.0 respectively for each of the for wires. The effective wire angles were estimated for each wire by making velocity measurements over a range of pitch and yaw angles in a uniform flow of known direction. The effective wire angles were determined to be θ_1=53.7°, θ_2=51.6°, θ_3=47.9°, and θ_4=47.5°. By splitting the velocity components into their mean and fluctuating terms, ignoring all terms higher than second order, and assuming that the *V* (for Equations 2.7 and 2.9) and *W* (for equations 2.8 and 2.10) velocities are small relative to the *U* velocity, we obtain the following relationships for the effective wire velocities:

$$U_{eff1}=U_{est}\sin\theta_1+V_{est}\cos\theta_1 \qquad (2.11)$$

$$U_{eff2}=U_{est}\sin\theta_2+W_{est}\cos\theta_2 \qquad (2.12)$$

$$U_{eff3}=U_{est}\sin\theta_3-V_{est}\cos\theta_3 \qquad (2.13)$$

$$U_{eff4}=U_{est}\sin\theta_4-W_{est}\cos\theta_4 \qquad (2.14)$$

Manipulating Equations (2.11-2.14) yields the following expressions for the estimated velocity components:

$$V_{est}=\frac{U_{eff3}\sin\theta_1-U_{eff1}\sin\theta_3}{-\cos\theta_1\sin\theta_3-\cos\theta_3\sin\theta_1} \qquad (2.15)$$

$$W_{est}=\frac{U_{eff4}\sin\theta_2-U_{eff2}\sin\theta_4}{-\cos\theta_4\sin\theta_2-\cos\theta_2\sin\theta_4} \qquad (2.16)$$

$$U_{est}=\frac{1}{2}\left[\frac{U_{eff1}\cos\theta_3+U_{eff3}\cos\theta_1}{\sin\theta_1\cos\theta_3+\sin\theta_3\cos\theta_1}+\frac{U_{eff2}\cos\theta_4+U_{eff4}\cos\theta_2}{\sin\theta_2\cos\theta_4+\sin\theta_4\cos\theta_2}\right] \qquad (2.17)$$

Note that the U velocity component is estimated by taking the average of its values from the two pairs of sensors. As will be shown, this tends to minimize the gradient errors. Equations (2.15-2.17) are the relationships used to obtain first estimates of the velocity components from the hot-wire probe and now corrections may be performed to further improve these estimates.

2.4.3 - Full Angle Calibration

A quad hot-wire probe is extremely sensitive to the angle the flow makes with the probe axis. Even moderate probe angles will result in velocity component estimates that vary significantly from their actual values. To correct for this effect, a method similar to

that presented by Mathioudakis and Breugelmans (1985) was used see (Wittmer *et al.*, 1996, for more details). In this method, the probe was placed in a uniform flow of known velocity and direction and rotated through a range of pitch and yaw angles. A total of 361 combinations of pitch and yaw angles ranging from +45° to -45° were used. At each angle combination, the velocity components determined from the hot-wire probe were compared to the actual velocity components determined analytically from the pitch and yaw angles. From this comparison a look-up table was created for the errors in the V, W, and Q velocities (where $Q = \sqrt{U^2 + V^2 + W^2}$) normalized on Q itself. With increasing flow angles, the velocity estimates determined from the hot-wire probe increased to a maximum value and then decreased again. All measurements made beyond this maximum value were ignored in this correction so that they would not be confused with measurements at lower pitch and yaw angles resulting in an "acceptance cone". By doing so we are limiting the measurement range of the hot-wire probe to points only within this "acceptance cone". However, it was found that this range was sufficiently large to include all possible angle combinations found in a wing tip vortex. The repeatability of this procedure was found to be very good for a given probe but was a strong function of prong geometry. Therefore, an angle calibration must be performed for each hot-wire probe used. This calibration was found to be relatively independent of the calibrating jet speed and therefore, one angle calibration could be performed for measurements over a range of Reynolds number.

2.4.4 - Velocity Gradient Error Analysis

Hot-wire probes can be made with very small measurement volumes. However, any finite measurement volume size restricts us from making a true point measurement of velocity. This complicates the interpretation of any hot-wire velocity measurements because the measured flow velocities U, V, and W are not constant across the measurement volume. These velocities vary not only from sensor to sensor, but also along the length of a single sensor. For an actual probe of finite size in a flow region characterized by large velocity gradients, the flow velocities may vary significantly across the probe's measurement volume and induce error into the velocity measurements .

The concept of errors being introduced into mean velocity measurements due to the velocity gradients at the point of measurement is not new. Vukoslavcevic and Wallace (1981) investigated the effects of cross-stream velocity and velocity gradients on streamwise vorticity measurements made using a miniature four-sensor hot-wire probe in a turbulent boundary layer. They determined that streamwise vorticity can be accurately measured with this type of probe in flows where the velocity gradients $\frac{\partial u}{\partial y}$ and $\frac{\partial u}{\partial z}$ can be neglected with respect to the cross-flow velocity gradients, $\frac{\partial v}{\partial z}$, and $\frac{\partial w}{\partial y}$. However, they found that for practical boundary layer flows this is rarely the case. For example, they found errors as large as 30% in instantaneous streamwise vorticity measurements and as much as 80% in the instantaneous cross-stream velocity components, V and W. For all measured flow variables they found that reducing the wire spacing reduced these errors.

Cutler and Bradshaw (1991) have also investigated the effects of velocity gradients on measurements of mean velocity and Reynolds stress using a two-sensor X-wire type hot-wire probe. They derived simple analytic expressions for the errors in measured mean velocities and Reynolds stresses assuming nominal wire angles of 45°. They found to a first-order approximation that the errors in the mean velocity components are merely functions of wire separation distance and local mean velocity gradients while the errors in the Reynolds stresses are functions of the instantaneous velocity gradients and can not be determined from available measurements. From measurements of a vortex/boundary layer interaction they computed the gradient errors in the mean velocity components. They found these errors to be most significant near the vortex center but were always less than 3% of the free stream.

To determine if these types of errors were significant in the present wing-tip vortex flows, a full analysis similar to that of Vukoslavcevic and Wallace (1981) and Cutler and Bradshaw (1991) was performed. This analysis assumes that the approximate relations used to obtain first estimates of the velocity components (U, V, and W) from the four effective velocities output by the sensors (U_{eff1}, U_{eff2}, U_{eff3}, and U_{eff4}) are sufficient to extract the velocity gradient errors, i.e. the direct angle calibration is not considered in this analysis.

Consider the probe illustrated in Figure 2.5 with U, V, and W being the velocity components in the x, y, and z coordinate directions respectively. Recall from section 2.4.2 the following relationships:

$$V_{est} = \frac{U_{eff3}\sin\theta_1 - U_{eff1}\sin\theta_3}{-\cos\theta_1\sin\theta_3 - \cos\theta_3\sin\theta_1} \qquad (2.15)$$

$$W_{est} = \frac{U_{eff4}\sin\theta_2 - U_{eff2}\sin\theta_4}{-\cos\theta_4\sin\theta_2 - \cos\theta_2\sin\theta_4} \qquad (2.16)$$

$$U_{est} = \frac{1}{2}\left[\frac{U_{eff1}\cos\theta_3 + U_{eff3}\cos\theta_1}{\sin\theta_1\cos\theta_3 + \sin\theta_3\cos\theta_1} + \frac{U_{eff2}\cos\theta_4 + U_{eff4}\cos\theta_2}{\sin\theta_2\cos\theta_4 + \sin\theta_4\cos\theta_2}\right] \qquad (2.17)$$

Note that the U velocity component is estimated by taking the average of its values from the two pairs of sensors. Positive streamwise vorticity will increase the effective velocity seen by wires 1 and 3 and decrease the effective velocity seen by wires 2 and 4. Therefore, we average the two U_{est} to reduce the errors introduced in the mean U velocity by streamwise vorticity.

Equations (2.15-2.17) are the relationships used to obtain first estimates of the instantaneous velocity components from the hot-wire probe. However, these equations assume that the velocity components are constant across the measurement volume (e.g. $U_1=U_2=U_3=U_4$). We can better approximate these velocities using a first order Taylor series expansion of the velocity field about a point located at the center of the measurement volume:

$$U_1 = U - \Delta_z\frac{\partial u}{\partial z} \qquad V_1 = V - \Delta_z\frac{\partial v}{\partial z} \qquad W_1 = W - \Delta_z\frac{\partial w}{\partial z} \qquad (2.18)$$

$$U_3 = U + \Delta_z\frac{\partial u}{\partial z} \qquad V_3 = V + \Delta_z\frac{\partial v}{\partial z} \qquad W_3 = W + \Delta_z\frac{\partial w}{\partial z} \qquad (2.19)$$

$$U_2 = U - \Delta_y\frac{\partial u}{\partial y} \qquad V_2 = V - \Delta_y\frac{\partial v}{\partial y} \qquad W_2 = W - \Delta_y\frac{\partial w}{\partial y} \qquad (2.20)$$

$$U_4 = U + \Delta_y \frac{\partial u}{\partial y} \qquad V_4 = V + \Delta_y \frac{\partial v}{\partial y} \qquad W_4 = W + \Delta_y \frac{\partial w}{\partial y} \qquad (2.21)$$

where U, V, and W are the mean velocities across the measurement volume and Δ_y and Δ_z are the measurement volume dimensions in the y- and z-directions respectively. By using this approximation we are implicitly assuming a linear variation of the velocity and that each wire responds to the velocity at its center. Substituting equations (2.18-2.21) into equations (2.7-2.10) we can show that:

$$U_{eff1}{}^2 = \left[\left(U - \Delta_z \frac{\partial u}{\partial z}\right)\sin\theta_1 + \left(V - \Delta_z \frac{\partial v}{\partial z}\right)\cos\theta_1\right]^2 + \left(W - \Delta_z \frac{\partial w}{\partial z}\right)^2 \qquad (2.22)$$

$$U_{eff2}{}^2 = \left[\left(U - \Delta_y \frac{\partial u}{\partial y}\right)\sin\theta_2 + \left(W - \Delta_y \frac{\partial w}{\partial y}\right)\cos\theta_2\right]^2 + \left(V - \Delta_y \frac{\partial v}{\partial y}\right)^2 \qquad (2.23)$$

$$U_{eff3}{}^2 = \left[\left(U + \Delta_z \frac{\partial u}{\partial z}\right)\sin\theta_3 - \left(V + \Delta_z \frac{\partial v}{\partial z}\right)\cos\theta_3\right]^2 + \left(W + \Delta_z \frac{\partial w}{\partial z}\right)^2 \qquad (2.24)$$

$$U_{eff4}{}^2 = \left[\left(U + \Delta_y \frac{\partial u}{\partial y}\right)\sin\theta_4 - \left(W + \Delta_y \frac{\partial w}{\partial y}\right)\cos\theta_4\right]^2 + \left(V + \Delta_y \frac{\partial v}{\partial y}\right)^2 \qquad (2.25)$$

Proceeding as was done for equations (2.11-2.14) by splitting the velocity components into their mean and fluctuating terms, ignoring all terms higher than second order, and assuming that the V and W velocities are small relative to U, we obtain new expressions for the effective velocities:

$$U_{eff1} = \left[\left(U - \Delta_z \frac{\partial u}{\partial z}\right)\sin\theta_1 + \left(V - \Delta_z \frac{\partial v}{\partial z}\right)\cos\theta_1\right] \qquad (2.26)$$

$$U_{eff\,2} = \left[\left(U - \Delta_y \frac{\partial u}{\partial y}\right)\sin\theta_2 + \left(W - \Delta_y \frac{\partial w}{\partial y}\right)\cos\theta_2\right] \qquad (2.27)$$

$$U_{eff\,3} = \left[\left(U + \Delta_z \frac{\partial u}{\partial z}\right)\sin\theta_3 - \left(V + \Delta_z \frac{\partial v}{\partial z}\right)\cos\theta_3\right] \qquad (2.28)$$

$$U_{eff\,4} = \left[\left(U + \Delta_y \frac{\partial u}{\partial y}\right)\sin\theta_4 - \left(W + \Delta_y \frac{\partial w}{\partial y}\right)\cos\theta_4\right] \qquad (2.29)$$

Equations (2.26-2.29) represent improved estimates of the effective velocities for each wire. Subtracting equations (2.11-2.14) from equations (2.26-2.29) and substituting the result into equations (2.15-2.17), we obtain expressions for the errors in the measured mean velocity components:

$$V - V_{est} = \frac{\Delta_z \frac{\partial u}{\partial z}\left(\cos(\theta_1 - \theta_3) - \cos(\theta_1 + \theta_3)\right) + \Delta_z \frac{\partial v}{\partial z}\left(\sin(\theta_3 - \theta_1)\right)}{\sin(\theta_1 + \theta_3)} \qquad (2.30)$$

$$W - W_{est} = \frac{\Delta_y \frac{\partial u}{\partial y}\left(\cos(\theta_2 - \theta_4) - \cos(\theta_2 + \theta_4)\right) + \Delta_y \frac{\partial w}{\partial y}\left(\sin(\theta_4 - \theta_2)\right)}{\sin(\theta_2 + \theta_4)} \qquad (2.31)$$

$$U - U_{est} = \frac{1}{2}\left[\frac{-\Delta_z \frac{\partial v}{\partial z}\left(\cos(\theta_1 - \theta_3) + \cos(\theta_1 + \theta_3)\right) + \Delta_z \frac{\partial u}{\partial z}\left(\sin(\theta_3 - \theta_1)\right)}{-\sin(\theta_1 + \theta_3)}\right]$$

$$+\frac{1}{2}\left[\frac{-\Delta_y \frac{\partial w}{\partial y}\left(\cos(\theta_2 - \theta_4) + \cos(\theta_2 + \theta_4)\right) + \Delta_y \frac{\partial u}{\partial y}\left(\sin(\theta_4 - \theta_2)\right)}{-\sin(\theta_2 + \theta_4)}\right] \qquad (2.32)$$

To perform the corrections, equations (2.30-2.32) are added to the corresponding mean velocities obtained from the hot-wire probe.

Now that a method for correcting the hot-wire mean velocity measurements has been developed, we must determine when these correction factors are significant. For the special case of an ideal probe where $\theta_1=\theta_2=\theta_3=\theta_4=45°$ and $\Delta_y=\Delta_z=\Delta$, these error expressions reduce to:

$$U - U_{est} = \frac{1}{2}\Delta\left[\frac{\partial v}{\partial z} + \frac{\partial w}{\partial y}\right] \qquad (2.33)$$

$$V - V_{est} = \Delta\frac{\partial u}{\partial z} \qquad (2.34)$$

$$W - W_{est} = \Delta\frac{\partial u}{\partial y} \qquad (2.35)$$

Equations (2.33-2.35) illustrate the basic relationship between the mean velocity errors and the local mean velocity gradients. These equations are similar in form to those derived by Cutler and Bradshaw (1991), the differences being a result of differing wire configuration. For a given probe geometry, the velocity gradient errors will be greatest in regions of large velocity gradients. It is also important to note that the error in the mean axial velocity, U, is proportional to the streamwise strain rate.

Example 1: Mean velocity gradient errors in the measurement of a q-vortex

Consider a Batchelor q-vortex with a tangential velocity given by:

$$V_\theta = V_{\theta 1}\left(1 + \frac{0.5}{\alpha}\right)\frac{r_1}{r}\left[1 - \exp\left(-\alpha\frac{r^2}{r_1^2}\right)\right] \qquad (2.36)$$

and an axial velocity given by:

$$U = U_D \exp\left(-\alpha \frac{r^2}{d^2}\right) + U_\infty \quad (2.37)$$

where $r^2=y^2+z^2$, $\alpha=1.25643$, and $V_{\theta 1}$, r_1, U_D, and d are respectively the measured peak tangential velocity, core radius, centerline axial velocity, and radial scale of the axial profile. Re-writing these expressions in Cartesian coordinates (Figure 2.6) we obtain for the cross-flow velocities:

$$V = -\frac{r_1 V_{\theta 1} z}{y^2+z^2}\left(1+\frac{0.5}{\alpha}\right)\left[1-\exp\left(\frac{-\alpha\left(y^2+z^2\right)}{r_1^2}\right)\right] \quad (2.38)$$

$$W = \frac{r_1 V_{\theta 1} y}{y^2+z^2}\left(1+\frac{0.5}{\alpha}\right)\left[1-\exp\left(\frac{-\alpha\left(y^2+z^2\right)}{r_1^2}\right)\right] \quad (2.39)$$

To determine the velocity gradient errors for a q-vortex we can analytically compute the required velocity gradients from the U, V, and W velocity equations. Taking the required derivatives and substituting the velocity gradients back into equations (2.33-2.35) and by assuming that all measurements are made along the z-axis ($\theta=0$), we can determine the velocity gradient errors present in mean velocity measurements as would be made by an ideal hot-wire probe in a q-vortex. This yields:

$$U - U_{est} = \frac{1}{2} r_1 V_{\theta 1} \Delta\left(1+\frac{0.5}{\alpha}\right)\left[\frac{2\alpha}{r_1^2}\exp\left(\frac{-\alpha r^2}{r_1^2}\right)+\frac{1}{r^2}\left(\exp\left(\frac{-\alpha r^2}{r_1^2}\right)-1\right)\right.$$

$$\left.+\frac{1}{r^2}\left(\exp\left(\frac{-\alpha r}{r_1^2}\right)-1\right)\right] \quad (2.40)$$

$$V - V_{est} = \frac{2\alpha r U_D \Delta}{d^2} \exp\left(\frac{-\alpha r^2}{d^2}\right) \qquad (2.41)$$

$$W - W_{est} = 0 \qquad (2.42)$$

Figure 2.7 shows equations (2.40-2.42) plotted for any set of q-vortex parameters r_1, $V_{\theta 1}$, d, and U_D, and any hot-wire probe dimension, Δ.

Example 2: Mean velocity gradient errors in actual trailing vortex measurements

Figures 2.7, 2.8, and 2.9 show the errors in mean velocity measurements U, V, and W computed both for and ideal probe ($\theta_1=\theta_2=\theta_3=\theta_4=45°$, $\Delta_y=\Delta_z$) and for our actual probe ($\theta_1=53.7°$, $\theta_2=51.6°$, $\theta_3=47.9°$, $\theta_4=47.5°$, $\Delta_y=0.0003$m, $\Delta_z=0.000295$m). Errors are presented for both a hypothetical q-vortex velocity field (Figures 2.7 and 2.8) as well as a velocity field measured in an actual tip vortex (Figure 2.9) as part of our experimental program. The q-vortex results were obtained assuming that $V_{\theta 1}=-4.877U_D$ and $d=4.92r_1$ based upon the comparison of a typical measured vortex to the q-vortex model (Figure 2.10). The q-vortex model overestimates the slopes present in the tangential velocity profile for a small region just outside the core edge and the actual vortex has a minimum just outside the core edge that the q-vortex model can not predict. The tip vortex velocity field measured in Figure 2.9 was generated by a NACA 0012 half-wing at 5° angle of attack (α). Measurements were made for a Reynolds number of 1,000,000 in the y-z plane along a z-profile a distance 10 chordlengths downstream of the generating wing.

For an ideal probe in a q-vortex (Figure 2.7), the errors are presented as a function of probe size to core radius (Δ/r_1) and are scaled on the tangential and axial velocity

parameters for the axial velocity errors and the tangential velocity errors respectively. For this case it is unnecessary to choose the ratios d/r_1 and $U_D/V_{\theta 1}$ with the errors presented in this way. Note that the errors in the W velocity component are not shown because they are identically zero for all radial distances. This is a direct result of the assumption that the axial velocity profile is a function of radial distance alone (i.e. contours of axial velocity in the y-z plane are concentric circles centered at the origin) which results in the fact that $\frac{\partial u}{\partial y}$ is zero.

For the actual probe (Figure 2.8), results for d/r_1=4.92 and $V_{\theta 1}/U_D$=-4.877 are presented. In all cases examined (probe size to core radius ratios form 0.01 to 0.05), the errors appear reassuringly small. For the ideal probe (Figure 2.7) the error in axial velocity increases from near zero at the core center to a maximum value just outside the core edge and then decays to 25% of its maximum value about 3.5 core radii out from the vortex center. The error in the tangential velocity (V in this case) has a similar shape reaching its maximum value at a radial distance slightly larger than one-half of d and decays to 25% of its maximum value at about 1.5d. For the actual probe (Figure 2.8), the errors in the axial velocity, U, have a similar shape but the magnitude of these errors is reduced slightly. For the errors in the cross-flow velocities, V and W, the shape of errors are drastically different due to the effects of the $\frac{\partial v}{\partial z}$ and $\frac{\partial w}{\partial y}$ velocity gradients which were neglected for the ideal probe. Now, the maximum value of these errors occurs at the core center and quickly decays back to zero (with an oscillation in the V velocity errors).

For the real vortex (Figure 2.9), the errors, normalized on the q-vortex parameters, are presented as a function of radial distance scaled on r_l (for U) or d (for V and W) for a single probe size to core size ratio (Δ/r_l=0.025). For the U, the maximum error is about half of that found for the q-vortex case. The maximum V velocity error is about 50% larger than for the q-vortex but the oscillation is much more pronounced. Finally, the maximum value of the W velocity error is about the same as for the q-vortex but the error does not decay back to zero as quickly.

In conclusion, the velocity gradient errors presented for an ideal probe in a q-vortex equations (Equations 2.31-2.33) can only adequately predict the gradient errors for a non-ideal probe in a real vortex if the ratio of r_l/d is near unity and if all of the actual wire angles are near their nominal values of 45°. In general this is not the case and one must calculate the velocity gradient errors using the exact equations presented in Equations (2.28-2.30) for the actual measured vortex. However, for the measurements at hand, the errors in the mean velocities due to velocity gradients are negligible and corrections are not necessary.

2.4.5 - Wandering Effects

When measuring wind-tunnel generated vortices with a fixed probe one encounters a problem known as vortex wandering. Wandering is characterized as a low frequency random motion of the vortex core which may be due to mutual instability (in the case of vortex pairs) or as a result of free-stream unsteadiness. Regardless of its source, the most significant effect of vortex wandering is to obscure important details of the flow by

smoothing out mean velocity profiles and increasing the magnitude of the velocity fluctuations. However, because its frequency of motion is so much smaller than the frequencies associated with turbulence, its influence on vortex development is probably negligible.

In order to present accurate mean velocity measurements, one must be able to estimate the effects of wandering on these measurements. Without these estimates, the unknown errors complicate physical interpretation and can render fixed probe measurements useless. Baker *et al.* (1974) were the first to attempt to quantify the effects of wandering and correct mean velocity measurements for these effects. They approximated a trailing vortex using the laminar vortex model of Saffman and determined a probability density function for the vortex center position as a function of the turbulence viscosity, κ. They could then quantify the effects of wandering and correct mean velocity measurements. However, their corrected measured results were not in good agreement with the theory due to uncertainties associated with the selection of theoretical constants. Corsiglia *et al.* (1973) also investigated wandering effects but found that the wandering amplitude in their measurements was several times larger than the vortex core diameter and therefore the effects of wandering could not be corrected. Little else was done to investigate the effects of wandering until Devenport *et al.* (1995) developed a method for correcting mean velocity profiles for the effects of wandering and to estimate the wandering amplitudes and its effects on Reynolds stress fields. This method will be briefly summarized here.

When vortex measurements are made using a fixed probe, the measurements are in terms of a fixed reference frame but because of wandering, the position of a tip vortex generated in a wind tunnel is time dependent and moves relative to this fixed frame. We would like to be able to present the measurements relative to a reference frame that moves with the wandering. In order to do this we must assume that the wandering is independent of any turbulent motion and that the velocities associated with wandering are negligible when compared to the velocities generated by the vortex. Consider the situation illustrated in Figure 2.11. The origin of the coordinate system is defined as the time-averaged location of the vortex center. The instantaneous location of the vortex center is defined as (y_v,z_v) and the location of the probe is defined *as* (y_p,z_p). The position (y,z) is the location of the instantaneous vortex center relative to the position of the probe. $U,V,$ and W are the Cartesian components of velocity generated by the vortex and sensed by the probe. Due to wandering motions, the position of the instantaneous vortex center relative to the origin (time-averaged location of the vortex center) changes with time. This position over a long period of time is represented using a probability density function:

$$p = p(y_v, z_v) \qquad (2.43)$$

So, given the probability density function we know that the probe will measure velocities over a long period of time as given by:

$$U_m(y_p, z_p) = \int_{-\infty}^{\infty}\int_{-\infty}^{\infty} p(y_v, z_v) U(y_p - y_v, z_p - z_v)\, dy_v\, dz_v \qquad (2.44)$$

A comparable expression can be derived for any quantity that is linearly related to the Cartesian velocity components including the three velocity components themselves, the Reynolds stresses, and the streamwise vorticity.

We want to reverse the smoothing process due to wandering and determine the true mean velocity field in terms of the measured field and then compute the contributions of wandering to the Reynolds stresses. One method for solving this problem is to convolve the wandering probability density function with the appropriate measured velocities, numerically calculate the 2-D Fourier transform of this convolution, and then numerically solve for the inverse Fourier transform to get the corrected values of the appropriate mean velocities. However, this procedure is impractical due to the uncertainties inherent in numerical Fourier transforms and therefore an analytic solution is preferred.

In order to estimate the effects of wandering without using numerical techniques we must first make some simplifying assumptions. The first of these is that the flow near the core center is assumed to be axisymmetric and that the true axial velocity and vorticity fields may be expressed as a series of the form:

$$f(y,z)=\sum_{i=1}^{n} A_i \exp\left(\frac{-(y^2+z^2)}{a_i^2}\right) \qquad (2.45)$$

where A_i and a_i are constant coefficients. Taking Equation 2.45 as the axial vorticity results in the following true tangential velocity field:

$$V_\theta(y,z) = \sum_{i=1}^{n} \frac{B_i}{r}\left[1-\exp\left(\frac{-(y^2+z^2)}{a_i^2}\right)\right] \qquad (2.46)$$

where $B_i=A_i a_i^2/2$.

The second simplifying assumption is that the probability density function for the vortex center can be adequately approximated by a general correlated Gaussian (which allows for anisotropic wandering) of the form:

$$p(y_v,z_v) = \frac{1}{2\pi\sigma_y\sigma_z\sqrt{1-e^2}}\exp\left(\frac{-1}{2(1-e^2)}\left(\frac{z_v^2}{\sigma_z^2}+\frac{y_v^2}{\sigma_y^2}-\frac{2y_v z_v}{\sigma_y\sigma_z}\right)\right) \qquad (2.47)$$

where σ_y and σ_z are the wandering amplitudes in the y and z coordinate directions respectively and e is the correlation. Using this p.d.f. (Equation 2.47) and the appropriate axial velocity or vorticity distribution (Equation 2.45) and performing the necessary integration as required by Equation 2.44, we see that the measured quantity f_m is given by:

$$f_m(y_p,z_p) = \sum_{i=1}^{n} \frac{A_i a_i^2}{\sqrt{E_i}}\exp\left(\frac{-1}{E_i}\left(y_p^2(2\sigma_z^2+a_i^2)+z_p^2(2\sigma_y^2+a_i^2)-4y_p z_p e\sigma_y\sigma_z\right)\right) \qquad (2.48)$$

where $E_i=(2\sigma_y^2+a_i^2)(2\sigma_z^2+a_i^2)-4e^2\sigma_y^2\sigma_z^2$. By considering data along a y=0 profile (a z-profile through the core center) we can simplify this equation to:

$$f_m(y_p,z_p) = \sum C_i \exp(-z_p^2/c_i^2) \qquad (2.49)$$

We can solve for the series coefficients C_i and c_i by comparison to the measured data. These coefficients are related to the actual series coefficients A_i and a_i by the relationships:

$$a_i^2 = \frac{1}{2}c_i^2-\sigma_y^2-\sigma_z^2+\frac{1}{2}\sqrt{(2\sigma_y^2+2\sigma_z^2-c_i^2)^2-16\sigma_y^2\sigma_z^2(1-e^2)+8\sigma_y^2 c_i^2} \qquad (2.50)$$

$$A_i = C_i\sqrt{E_i} \,/\, a_i^2 \qquad (2.51)$$

Using these relationships, the true corrected axial velocity can then be determined from these measured velocities given the values of σ_y, σ_z, and e.

The tangential velocity is related to the axial vorticity such that the measured tangential velocity can be approximated by the series:

$$V_{\theta m}(0,z_p) = \sum_{i=1}^{n} \frac{D_i}{z_p}\left(1-\exp\left(\frac{-z_p^2}{c_i^2}\right)\right) \qquad (2.52)$$

where $D_i=C_ic_i^2/2$. The coefficients D_i and c_i are determined by comparison to the measured tangential velocity profile as they were for the axial velocity profile. The coefficients of the true tangential velocity field B_i and a_i are related to the coefficients of the measured profile D_i and c_i using Equation 2.50 and the following relationship:

$$B_i = D_i(2\sigma_y^2 + a_i^2) \,/\, \sqrt{E_i} \qquad (2.53)$$

Using these relationships, the true corrected tangential velocity profile can be determined from the measured tangential velocity profile given the values of σ_y, σ_z, and e.

To get the values for σ_y, σ_z and e for the vortex, initial values are estimated by assuming that $\overline{V_{\theta m}'^2}$ at the core center is due solely to wandering. We then estimate σ_y and σ_z by dividing $\sqrt{\overline{V_{\theta m}'^2}}$ by the measured $\frac{\partial V_\theta}{\partial r}$. Using the curve fit parameters to the measured velocity profiles, U_m and $V_{\theta m}$, and these first estimates of the wandering amplitudes, the estimated true velocity field for the vortex is calculated using Equations 2.50 and 2.53. The apparent stresses $\overline{v'^2}$, $\overline{w'^2}$, and $\overline{v'w'}$ are computed at the core center

using the estimated true velocity field and the wandering amplitudes. These values are compared to the measured stresses and new values of σ_y, σ_z and e are determined. This process is repeated until the computed stresses match the measured stresses. This method has been applied to the core velocity profile measurements presented in the next section.

Chapter 3-Velocity Measurement Results

3.1-Introduction

The velocity measurements presented in this thesis are composed of two parts (Table 1). The first part of this investigation is a component of a larger study by Devenport *et al.* (1996b). In this study, they investigate the mean flow and turbulence structure of a wing-tip vortex and the surrounding spiral wake using three-component velocity measurements. The objective of the first part of the present work is to perform detailed velocity measurements within the vortex core to determine its turbulence structure. To meet this objective, grids of three-component time series velocity measurements were made 10 and 30 chordlengths downstream of a NACA 0012 wing at 5° angle of attack with an aspect ratio of 8.66 at a Reynolds number based on chord ($Re_c=U_{ref}c/\nu$) of 530,000. The results of this part of the investigation are presented in Section 3.2.

The objective of the second part of the present work is to determine the effects of wing geometry, Reynolds number, and downstream distance on the mean flow and time-

averaged turbulence structure of a vortex. This was done by performing three-component velocity measurements behind a NACA 0016 wing with an aspect ratio of 4.0 at 5° angle of attack for various Reynolds numbers and downstream locations. Velocity profiles were measured through the vortex core as well as in the near two-dimensional wing wake for Reynolds numbers ranging from 530,000 up to 1,600,000 and streamwise measurement locations 5 to 10 chordlengths downstream of the wing. A grid of velocity measurements was also taken ten chordlengths downstream of the wing at Re_c=1,825,000 to allow the overall flow structure for this case to be compared to the flow structure of the vortex generated by the NACA 0012 wing. The results of these measurements are presented in Section 3.3.

The Cartesian and cylindrical coordinate systems illustrated in Figure 3.1 will be used to present all measurements. The x-axis is aligned with the wind tunnel free-stream velocity vector, the y-axis measures along the span of the wing from the wing tip, and the z-axis completes the right-hand set. Unless otherwise noted, all y-, z-, and r-coordinates presented are relative to the vortex center and all x-coordinates are measured relative to the leading edge of the generating wing. The velocity components U, V, and W are defined in the x-, y-, and z-coordinate directions respectively. Distances are normalized on the wing chord, c, and velocities are normalized on the wind tunnel free-stream, U_{ref}. Uncertainties in the mean velocity components are presented in Table 2 normalized on the wing chord.

3.2 - Measurements of a NACA 0012 Vortex

3.2.1 - Grid Measurements at x/c=10, Re_c=530,000

The grid of velocity measurements at this location was actually made up of two grids: a 12x15 (y by z) coarse grid and a 17x16 fine grid centered about the vortex core. Figure 3.2 illustrates the measurement locations making up the grid. From these measurements, contour plots of various normalized flow quantities can be produced. Figures 3.3-3.6 show the overall form of the vortex using contours of axial velocity, U/U_{ref}, cross-flow velocity magnitude, $\sqrt{V^2+W^2}/U_{ref}$, axial normal stress, $\overline{u'^2}/U_{ref}^2$, and turbulence kinetic energy, k/U_{ref}^2 (not yet corrected for wandering effects). These plots reveal a concentrated vortex core surrounded by a spiral wake. From Figure 3.3 we see that axial velocity in the vortex decreases from free-stream values at the vortex edge to about 85% of the free-stream in the vortex core. Progressing along the centerline of the wake spiral away from the vortex core, the axial velocity gradually increases to about 98% of the free-stream in the horizontal portion of the wing wake. Contours of cross-flow velocity magnitude (Figure 3.4) appear as a series of roughly circular curves increasing from near zero at the vortex center to a maximum at the edge of the vortex core and then fall back to zero at the edge of the vortex. It is important to note that for an ideal vortex these contours would appear as concentric circles. The presence of the wake spiral and the likelihood that the coordinate system is not exactly aligned with the vortex core result in measured contours that are not concentric circles. Contours of axial normal stress (Figure 3.5) increase in magnitude across the wake spiral from near zero at the edge

of the wake to a maximum along the wake centerline. The highest values of axial normal stress occur where the wake first curves and begins to spiral around the vortex core. This maximum decreases along the wake centerline towards the vortex core. The edge of the vortex core is shown as a dark circle in Figures 3.5 and 3.6. Axial normal stress levels appear to peak in the vortex core, however, this is a result of vortex wandering which increases the levels of $\overline{u'^2}/U_{ref}^2$, particularly near the core center where axial velocity gradients are greatest. Contours of turbulence kinetic energy (Figure 3.6) demonstrate a turbulence structure that is very similar to that identified in Figure 3.5. Turbulence levels increase across the wake spiral to a maximum at its centerline. The magnitude of the turbulence along the centerline is greatest where the wake first bends and spirals around the vortex core and decreases as the vortex core is approached. Turbulence levels in the vortex core appear to be extremely high but, as was the case before, this apparent maximum in turbulence is the result of vortex wandering.

3.2.2 - Grid Measurements at x/c=30, Re_c=530,000

The measurement grid at this location was made up of a 17x14 coarse grid and a 17x17 fine grid centered about the vortex core. Figure 3.7 shows the measurement locations making up the grid. Contours of axial velocity, U/U_{ref}, cross-flow velocity magnitude, $\sqrt{V^2+W^2}/U_{ref}$, axial normal stress, $\overline{u'^2}/U_{ref}^2$, and turbulence kinetic energy, k/U_{ref}^2, are shown in Figures 3.8-3.11. These plots show a similar structure to that measured at *x/c=10* (Figures 3.3-3.6) but upon close examination, significant differences

may be noted. The core axial velocity deficit noted at x/c=10 still exists but is much less pronounced at a value of 90% of the free-stream. The axial velocity contours outside of the vortex core appear more irregular in general due uncertainty in the mean velocity measurements (about 1.5% of U_{ref}). Contours of cross-flow velocity magnitude (Figure 3.9) are less circular and are reduced in magnitude compared to those found at x/c=10. Contours of axial normal stress and turbulence kinetic energy (Figures 3.10 and 3.11) reveal that the vortex has grown in size and that turbulence levels outside of the vortex core have decreased. Once again, the dark circle in these figures is the approximate core edge. Turbulence levels inside the vortex core appear to be about the same as those at x/c=10 but are not reliable due to vortex wandering. Contours of turbulence kinetic energy (Figure 3.11) show a similar type of decay. Turbulence levels have decreased outside of the vortex core but remain nearly constant inside the core where turbulence levels are significantly affected by wandering.

3.2.3 - Digital Filtering

In order to determine the true turbulence structure within the vortex core, the contributions of low-frequency wandering to the turbulence stresses must be separated from the true turbulence. This was done by high-pass filtering the grid measurements. A square filter was employed to remove all contributions to the measured axial normal stress by any motions whose frequency is less than a cut-off frequency. This process can not distinguish the source of these fluctuations so contributions from large scale turbulence as well as vortex wandering are removed. Therefore, the absolute values of the filtered

contours have limited meaning. However, the relative values of the contours for a given case can lend some insight into the turbulence structure of the vortex core. High frequency noise levels present in the measurements at 30 chordlengths made digital filtering impractical so only the data at x/c=10 is presented.

Contours of axial normal stress high-pass filtered at non-dimensional cut-off frequencies of $fc/U_{ref} = 3$ and $fc/U_{ref} = 40$ are shown in Figure 3.12 a) and b). The color bar at the bottom of this figure indicates increasing turbulence levels from left to right. Filtering at $fc/U_{ref} = 3$ (corresponding to a streamwise length scale about equal to the width of the wing wake) eliminates the majority of the low-frequency velocity fluctuations associated with wandering as well as the lowest frequency turbulence. At this cut-off frequency, we see that the large spike of turbulence present in the unfiltered data at the vortex core has been reduced in both magnitude and radius but is still present. This spike indicates that the vortex core is either truly turbulent or that velocity fluctuations are produced by other inactive core motions. To resolve this issue, the data was high-pass filtered at $fc/U_{ref} = 40$ (corresponding to a streamwise length scale about equal to the core radius) which eliminates all but the smallest scale turbulence structures (Figure 3.12c). The turbulence spike present in the vortex core of the unfiltered and $fc/U_{ref} = 3$ data has been eliminated and turbulence levels in the vortex core appear much lower than those surrounding the core. If the vortex core was truly turbulent there would be an energy cascade producing small scale turbulence which would appear on this plot. Instead, the turbulence levels appear to be about equal to those found in the free-stream implying that

the vortex core is in fact laminar and is surrounded by a region of high turbulence. The appearance of high turbulence levels in the vortex core is therefore due to inactive core motions as the laminar core is buffeted about by the surrounding turbulent region. This result is consistent with the spectral scaling results of Devenport *et al.* (1996b).

3.3 - Measurements of a NACA 0016 Vortex

3.3.1 - Grid Measurements at x/c=10, Re_c=1,825,000

To allow for comparison of the overall flow structure of the vortex shed by a NACA 0016 wing to the flow structure presented previously for the NACA 0012 wing, a grid of velocity measurements was made ten chordlengths downstream of the NACA 0016 wing at a Reynolds number of 1,825,000. The measurement grid used for this case is shown in Figure 3.13. Note that for this case only a coarse grid was used and therefore, the details of the flow structure near the vortex core are not reliable. Figures 3.14-3.17 show contours of axial velocity, U/U_{ref}, cross-flow velocity magnitude, $\sqrt{V^2+W^2}/U_{ref}$, axial normal stress, $\overline{u'^2}/U_{ref}^2$, and turbulence kinetic energy, k/U_{ref}^2, for this case. These figures reveal a flow structure similar to that observed for the NACA 0012 vortex at x/c=10 (Figures 3.3-3.6). However, two distinct differences can be seen. The axial velocity contours appear more irregular in this case due to measurement uncertainty and the core axial velocity has increased to 96% of the free-stream. Contours of turbulence kinetic energy show the vortex to be about the same non-dimensional size as the NACA 0012 case but the levels of turbulence have decreased significantly. The vortex also

appears to be not as tightly "rolled-up". The reduction in turbulence levels is most likely a result of differences in the size of the transition strip (relative to the wing chord) in the two cases. The NACA 0012 wing has a larger non-dimensional trip and therefore produces a more turbulent vortex. The appearance of a more tightly rolled-up vortex for the NACA 0012 case is probably due to differences in aspect ratio.

3.3.2 - Core Profile Measurements

To investigate the effects of Reynolds number and downstream distance on the mean flow of a vortex, measurements were made 5 to 10 chordlengths downstream of a NACA 0016 wing for Reynolds numbers from 530,000 to 1,600,000.

As mentioned previously, fixed probe velocity measurements are subject to the effects of vortex wandering (see Section 2.4.5). Therefore, before interpretation of the vortex core profile measurements can be made, the data must be corrected for wandering effects (this procedure will be referred to as "unwandering"). This is performed using the method of Devenport *et al.* (1995) and discussed in Section 2.4.5. This procedure reveals the true unwandered mean velocity field and the apparent stress field imposed by wandering.

The measured axial and tangential velocity profiles and the corresponding curve fits required for the unwandering procedure are shown for each case in Figures 3.18-3.19. The axial velocity curve fits (Figure 3.18) appear to fit the measured data quite well, in spite of some scatter in the data due to asymmetry of the profile. These profiles show that at x/c=10, two local minima exist in the axial velocity profile. The first of these is centered

at the vortex core center and the secondary deficit is centered outside the core edge. At other locations further upstream, only the secondary deficit exists. The tangential velocity curve fits (Figure 3.19) also fit the data reasonably well, particularly outside of the core region. These profiles show tangential velocity, V_θ, to increase from zero at the vortex core center to a maximum at the core edge and then decay asymptotically back to zero far away from the vortex center. Due to a limited number of measurement points in the core region in each case, the curve fits were less accurate inside the core for the Re_c=1,000,000, x/c=10 (b) and the Re_c=1,600,000, x/c=7.5 (d) cases. This will be discussed in more detail later.

The corrected for wandering curve fits produced by the unwandering procedure are also shown for all cases in Figures 3.18-3.19. For some of the axial velocity profiles (Figures 3.18a, b, and c), the unwandering procedure increased the velocity deficit at the vortex core and reduced the secondary velocity deficit. For cases d) and e) where a local maximum in axial velocity at the vortex core was observed, the unwandering procedure reduced the velocity deficit at the vortex core and increased the secondary deficit. For all cases, the basic shape of the profiles was unchanged. The tangential velocity profiles (Figure 3.19) were also affected by the unwandering procedure. In each case, the corrected profiles display higher peak tangential velocities and smaller core radii than the curve fit results. The corrected results also show an inflection in the tangential velocity profiles for several cases. A close examination of the curve fits reveals these inflections to be present before the unwandering procedure was implemented and therefore are not a

result of the unwandering process. The unwandering procedure merely magnifies these inflections making them more obvious.

A comparison of these profiles to those presented by Devenport *et al.* (1996b) at x/c=10, Re_c=530,000, is shown in Figure 3.20. The tangential velocity comparison reveals that the vortex core radius measured in the present study is about half of that found by Devenport *et al.* (1996b). Tangential velocities measured here are greater at all radial locations than their data indicating that the total circulation is larger for the NACA 0016 wing.. The maximum tangential velocity is also about 40% higher than they measured. Comparison of the axial velocity profiles reveals that the core axial velocity deficit is about 45% less than they measured. Also, the shape of the axial velocity profiles is very different. In their data, only a single velocity deficit at the vortex core was found while in the present measurements a secondary deficit was found just outside the vortex core.

The differences between the present data and the data presented by Devenport *et al.* (1996b) could have several causes. Blockage effects are likely to be significant for this wing and would act to increase the apparent wing angle of attack. This effect could account for some of the increase in maximum tangential velocity. Differences in boundary layer trip could also contribute to differences in the axial and tangential velocity profiles. Figures 3.21 and 3.22 show axial and tangential velocity distributions for various trip sizes. Figure 3.21 illustrates that increasing the size of the trip decreases the axial velocity at all radial distances. For the case of no trip, a secondary velocity deficit was found which is very similar to that found in the present data. Figure 3.22 shows that decreasing

trip size produces greater tangential velocities and increases the total circulation on the wing. Another possible source of these differences in mean velocity profiles is that the tip flow is actually different for the two wings. Engel (1995) showed that the mean velocity profiles downstream of the wing are highly dependent on the vortex formation at the wing tip. Decreasing aspect ratio was found to increase the relative strength of the secondary vortex structures relative to the primary vortex which could explain the appearance of the secondary axial velocity deficit. Differences in wing section could also effect the tip flow. Flow visualizations of the tip flow of the NACA 0016 wing are needed to compare to the NACA 0012 visualizations of Engel (1995). This comparison would help determine the source of these differences in mean velocity profiles.

Due to the unpredicted reduction in core size stated previously, the number of measurement points within the core were about half of the expected number. As a result, uncertainties in core profiles of axial and tangential velocity were increased. As will be discussed later, the curve fits of these profiles created problems in the unwandered data.

The r.m.s. wandering amplitudes, σ_y and σ_z, and the correlation coefficient, e, determined from the unwandering procedure are listed in Table 3. The wandering amplitudes are also shown in Figures 3.23 and 3.24 as a function of Reynolds number, Re, and downstream distance, x/c. These figures indicate wandering amplitudes to be relatively independent of streamwise distance but do display an increase with Reynolds number. A comparison of the wandering amplitudes measured in this experiment to those presented by Devenport *et al.* (1996b) (Table 3) show similar non-dimensional wandering

amplitudes at a common case of Re_c=530,000, x/c=10, particularly for σ_z. This similarity in wandering amplitudes implies that the vortex wandering amplitudes scale on the wing chord. Wandering amplitudes are significantly higher in the present experiment for a given downstream location than those reported by Devenport *et al.* (1995). This is most likely the Reynolds number effect observed previously since the data presented here correspond to a Reynolds number three times that of Devenport *et al.* (1995) for a given location downstream.

3.3.2.1 - Streamwise Evolution

The corrected axial , U, and tangential velocity, V_θ, profiles for streamwise locations 5 to 10 chordlengths downstream of the generating wing at a constant Reynolds number of 1,600,000 are shown in Figures 3.25 and 3.26. Figure 3.25 shows the shape of the axial velocity profile to be dependent on streamwise location. At x/c=5, the axial velocity is nearly equal to the free-stream at the vortex center. Proceeding away from the core, the axial velocity reaches a minimum at about r/c=0.03 and then increases back to near free-stream levels far away from the core. Further downstream at x/c=7.5, the same shape exists but the axial velocity has been reduced at the core center and increased at the secondary deficit at r/c=0.03. At x/c=10, the shape of the curve has changed and two minima exist in the profile: a new one at the vortex center and the one noted previously near r/c=0.03. At this station, the axial velocity has been reduced even further at the core center and has been increased at the secondary deficit.

The streamwise evolution of the tangential velocity profiles (Figure 3.26) is difficult to determine. A comparison of the curves for x/c=5 and x/c=10 indicate that maximum tangential velocity decreases and core radius increases as the vortex evolves downstream (Figures 3.27 and 3.28). However, the curve corresponding to x/c=7.5 does not follow this trend. At this location, the maximum tangential velocity appears less and the core radius appears larger than at x/c=10. This is possibly the result of uncertainty in the curve fit used in the unwandering procedure. A close inspection of Figure 3.19d reveals that the curve fit underestimates the measured peak tangential velocity and overestimates the core radius. These differences are magnified by the unwandering procedure and could be responsible for the curious shape of the tangential velocity profile at x/c=7.5. Attempts to improve the curve fit for this case were unsuccessful due to the presence of one odd point within the vortex core in the measured profile. Because of this point, more measurements are required within the vortex core to confirm the profile shape at x/c=7.5. This profile is therefore ignored and only the results at x/c=5 and x/c=10 are considered.

3.3.2.2 - Reynolds Number Effects

The corrected axial and tangential velocity profiles measured ten chordlengths downstream of the generating wing for Reynolds numbers of 530,000 to 1,600,000 are presented in Figures 3.29 and 3.30. Both axial and tangential velocity profiles show a dependence on Reynolds number. Two minima are observed in the axial velocity profile for every Reynolds number. Increasing Reynolds number reduces the magnitude of the

core velocity deficit and increases the magnitude of the secondary velocity deficit. This behavior is opposite to that found for increasing distance downstream. Also, the location of the secondary deficit appears to move towards the vortex core as Reynolds number is increased.

Increasing Reynolds number also produces an increase in maximum tangential velocity and a decrease in core radius (Figures 3.31 and 3.32). These trends are opposite to the effects of increasing distance downstream.

3.3.3 - Wake Profile Measurements

3.3.3.1 - Variations With Streamwise Distance

Axial velocity and axial normal stress profiles at y/c=0.5 were measured 5 to 10 chordlengths downstream of the generating wing at *Rec*=1,600,000 and are presented in Figures 3.33 and 3.34. Axial velocity profiles in the wing wake exhibit a U-shape which varies from free-stream levels at the edge of the wake to a minimum (a deficit) at the wake center. The magnitude of the axial velocity deficit in the horizontal portion of the wing wake is reduced as it evolves downstream. Axial normal stress levels also appear to diminish with streamwise distance.

3.3.3.2 - Reynolds Number Variations

Axial velocity and axial normal stress profiles for Reynolds numbers of 530,000 to 1,600,000 ten chordlengths downstream of the generating wing are presented in Figures 3.35 and 3.36. In these figures, the profiles appear to lie on top of each other. This

indicates that Reynolds number has no distinct effect on either of these two flow quantities.

Chapter 4 - Flow Visualization Apparatus and Techniques

4.1 - Towing Tank Basin

Flow visualizations were performed in the Virginia Tech Towing Basin (Figure 4.1). This facility is a rectangular channel made from reinforced concrete and painted with a waterproof enamel paint. The 29.87m long channel is 1.83m wide and has a maximum water depth of 1.22m. The first 1.22m and the last 7.32m of the channel are used for breaking the carriage leaving a useable test length of 21.33m. There is an observation pit located at the center of the test region and the walls and floor of the channel in this area are painted flat black to improve the flow visualizations. Wave absorbers located at either end of the channel are used to reduce turbulence levels in the tank.

4.2 - Towing Tank Carriage

The carriage and rails were designed and built by Kemp and Remes in Germany. Each rail is set on 52 supports and is accurate to within 0.1mm in height and 0.2mm in alignment. The carriage (Figure 4.1) is driven by a 400V DC motor through a gear reduction box. The carriage can maintain a maximum run speed of 1.8m/s with the gear

box set at the position used in this test. The speed of the carriage is controlled electronically using a feedback control from the motor armature voltage. This control can operate the carriage at a nearly uniform speed and allows for a maximum carriage acceleration of $0.7m/s^2$. The carriage is braked automatically at both ends using a magnetic clutch type brake which brakes the DC motor directly.

Figure 4.2 shows the voltage-to-velocity calibration used to set the carriage speed when the motor is set in position II (0-1500 rpm) as it was for this test. This calibration was determined by timing the carriage between two points along the rail for a range of voltage settings. The velocity of the carriage is then given by simply dividing the length the carriage traveled by the amount of time required to travel that distance. Performing a least squares regression on the resulting data points gave the relationship: Velocity (in ft/s) = 0.0304485*Voltage Setting - 0.22923. From Figure 4.2 we see that this linear relationship between the voltage setting and the carriage velocity models the measured data quite well.

4.3 - Delta Wing Models

Three 75° delta wing models were used for the flow visualizations. The first of these is the dye injection model illustrated in Figure 4.3a. This model is a 1.7% thick aluminum plate with a chord of 0.254m. Two 5mm diameter mounting holes were drilled into the model surface to allow for the model to be supported from the pressure side using a support strut. 1.6mm diameter copper tubing was inlaid into the upper surface of the model just behind the leading edge and epoxy is used to hold the tubing in place and fill in

the gaps around the tubing. The leading edge of this model is rounded with a 3.175mm radius of curvature. Testing of several dye hole configurations revealed that the vortex pair visualizations were best when the dye was injected along the leading edge near the rear of the model and along the trailing edge. Based upon these tests, nine 0.79mm diameter holes were drilled into copper tubing in 25.4mm intervals as shown in Figure 4.3a to allow for injection of fluorescent dye into the flow.

The other two delta wing models used are geometrically similar 1.7% thick flat plates with chordlengths of 0.15m and 0.30m (Figure 4.3b). Each model was machined from aluminum and has a triangular steel plate inserted into its front section to move the model center of gravity to the 60% chord location. Small holes were drilled through each model to allow for the model to be supported from above by fine wires.

These models were towed through the tank using two different support configurations: a strut-supported configuration and a wire-supported configuration. The details of these two support configurations is described in the next two sections.

4.3.1 - Strut-Supported Configuration

The strut-supported configuration is shown in Figure 4.4. A circular aluminum mounting pole 0.064m in diameter and 1.02m long is fastened into the mounting strut holder of the carriage. One end of this pole is attached to a square base plate which is used to secure an airfoil shaped mounting strut to the aluminum mounting pole. This airfoil shaped strut is 0.737m long and tapers from a 0.076m chord at the base plate to a 0.025m chord where it connects to the dye injection model. With the model supported in

this manner, a test depth of 0.61m is achieved. The model angle of attack is varied by placing spacers under the front edge of the wing support.

Fluorescent dye was used to visualize the delta wing wake. The dye injection apparatus (Figure 4.5) was used in conjunction with the dye injection model to introduce the dye into the flow. This apparatus consists of three cylindrical Plexiglas canisters mounted at the rear of the carriage. Gravity provides the force to inject dye into the flow. A stopcock at the bottom of each of these canisters can be opened to allow a variable quantity of dye to flow through 1.59mm diameter plastic tubing down along the wing support strut and into the copper tubing inlaid into the dye injection model. From there, the dye is slowly released into the surrounding fluid through the holes in the copper tubing.

4.3.2 - Wire-Supported Configuration

The wire-supported configuration is illustrated in Figure 4.6. A circular aluminum mounting pole 0.064m in diameter was used to support a force measurement apparatus (see below). The models were suspended from the force measurement apparatus using 0.127mm and 0.254mm diameter alumel wire for the 0.15m and 0.30m chord wings respectively. Two different support wire configurations were tested. The first support configuration tested was a two point attachment. According to Newman (1974), a two point attachment can be used if the two attachment points are along the model line of symmetry with the forward attachment point at 33% chord and the rear attachment point at the trailing edge. This configuration worked well in some cases but the models were

difficult to control due to a lack of roll stability. To remedy this situation, a three point attachment configuration was used which kept the forward attachment point at the 33% chord location while the rear attachment was replaced with two attachments at the trailing edge just inboard of each of the wing tips. This type of attachment configuration proved very successful and was used in all wire-supported flow visualizations presented.

The support wires formed a bridle which was created by tying two additional support wires to the main support wire. The knot formed by these three wires was approximately 1 chordlength above the model surface. Each of these support wires was pushed through an attachment point and fastened to the bottom side of the model with 3M transparent tape. The length of the two rear support wires were set equal to each other to produce a zero roll angle in flight. The proportion of the lengths of the rear support wires (L_2) relative to the front support wire (L_1) could be varied to produce any bridle angle, α (See Figure 4.7) using the relationships:

$$L_1^2 = h^2 + (h\tan(\alpha+\theta) + d - a)^2 \qquad (4.1)$$

$$L_2^2 = h^2 + (c - d - h\tan(\alpha+\theta))^2 + \left(\frac{b}{2}\right)^2 \qquad (4.2)$$

where c is the wing chord, b is the wing span, and a, d, and h are defined in Figure 4.7. It is important to note that the bridle angle, α, is not the wing angle of attack. This is due to the fact that as the wing begins to fly, the drag on the wing will cause the wing to rotate back to some non-zero wire angle, θ. Therefore, the angle of attack of the wing in flight

can not be prescribed as it will be determined through moment equilibrium about the bridle point for a given flight condition.

To visualize the delta wing wakes in this configuration, the models were painted with a mixture of Liquitek acrylic paint thickener and fluorescent dye. The paint thickener gave the mixture the consistency of oil paint which allowed the dye to be applied to the model with a paint brush. The proportions of paint thickener to dye could be varied depending on test conditions. For low speed tests much less dye was required than for the high speed tests.

4.4 - Force Measurement

The free-body diagram in Figure 4.8 illustrates the system of forces acting on the wing. We see that if we desire to know the aerodynamic forces acting on the wing, namely lift and drag, then we need to measure the tension in the support wire, T_{act}, and the angle that the support wire makes with the vertical, θ. We also need to estimate the lift and drag forces on the support wire and subtract those from the measured forces to get the true lift and drag on the wing.

The force measurement apparatus developed to do this is illustrated in Figure 4.6. This apparatus consists of an L-shaped bracket, a load cell, and protractor. The L-shaped bracket is made of aluminum and bolts directly to a 0.064m diameter aluminum mounting pole. The protractor, fastened to the vertical side of the L-shaped bracket, allows the angle of the support wire relative to the gravity vector to be measured. The load cell,

mounted to the horizontal side of the L-shaped bracket is used to measure the tension in the support wire.

The load cell used for this purpose is an Interface, Inc. SM-10 super-mini load cell. This load cell features a maximum load capacity of 10 lbs. with an output resolution of 3.361mV/V. The output voltage of this device was amplified using a Gould bridge amplifier. This output was zeroed and then calibrated within 0.0003 lbs. using a known weight. Because the tension in the support wire is not always aligned with the sensitive axis of the load cell, it was necessary to perform an angle calibration. This was done by applying a known weight to the load cell and rotating the load cell axis through a series of angles. The results of this procedure are illustrated in Figure 4.9 for both clockwise and counter-clockwise rotations of the load cell. One would expect that the load cell will only measure the component of the wire tension parallel to the cell's sensitive axis and thus obeys the law:

$$T_{meas} = T_{act} \cos\theta \qquad (4.3)$$

However, from Figure 4.9a it appears that the load cell does not respond in this way. This is due to the fact that in this calibration procedure the load cell itself is rotated while the weight is aligned with the gravity vector. Therefore, the load cell also measures a weight component of the active end of the load cell itself in addition to the wire tension. To correct for this, the unloaded load cell was pitched through a range angles and the resulting forces were noted. A curve fit was determined for this weight contribution (Figure 4.9b) and was subtracted from the calibration results. These corrected calibration

results are shown in Figure 4.9c and compare within 1% for our range of angles to the model of Equation 4.3.

4.4.1 - Force Calculations

From Figure 4.8 we see that the equations of motion for the system are:

$$T_{act}\cos\theta = L_m + L_w + W \qquad (4.4)$$

$$T_{act}\sin\theta = D_m + D_w \qquad (4.5)$$

where L and D are lift and drag respectively and the subscript 'm' refers to the aerodynamic forces on the wing itself and the subscript 'w' refers to the lift and drag contributions of the wire.

In order to estimate the lift and drag contributions from the wire, tests were performed using two different wire lengths, 0.305m and 0.610m. Changing the wire length did not appear to significantly influence the angle of attack of the wing allowing the lift and drag contributions of the wire to be estimated. Figure 4.10 shows the lift and drag on the wire as a function of model Reynolds number for the two wire diameters used in this test. In most cases, the wire contribution to the wing lift was negligible relative to the model lift.

4.5 - Free-flight Configuration

Delta wing wake flows are known to be highly sensitive to support interference. Demonstrating the absence of interference from the very thin towing wires was thus an

important pre-requisite of the present study. This was done by repeating a few tests with the models in free-flight.

It was determined that a delta wing model will undergo stable flight if the center of gravity (c.g.) of the model is located between the 45% and 62% chord locations. The further back the wing c.g. is located within these limits, the further the range of the model will be. If the c.g. is located forward of the 45% chord location, the wing will dive swiftly to the tank bottom. If the c.g. is located aft of the 62% chord location, the wing will undergo periodic stall characterized by a wave-like flight pattern. In order to fix the wing c.g. location, a triangular metal plate was inserted into the forward tip of the wing (Figure 4.3b). To maximize model range while avoiding periodic wing stall, the c.g. of the models was placed at 60% chord which allowed for a glide angle of about 18.5°.

Preliminary tests showed that in order to produce a repeatable flight pattern which crosses through the light sheet, a repeatable model launching mechanism is required. To achieve this end, the model launcher developed by Miller and Williamson (1995) and illustrated in Figure 4.11 was used. This launcher is made up of a steel platform with four aluminum legs. The rear legs were used to support the trailing edge of the model via two pinpoint supports at the wing tips. The front two legs have holes drilled into them to support a 1.75cm diameter stainless steel tube. This tube has a notch cut into it to support the leading edge of the wing. Each leg of the model launcher is attached to the base plate using threaded rods to allow for vertical adjustment of the leg. This allows the model to be launched from any initial angle of attack, yaw angle, or roll angle. To launch the

model, the stainless steel tube was rotated thereby dropping the front tip of the model. The model would then glide smoothly off of the rear pin supports and enter a repeatable and stable flight. To estimate the free-flight velocity, a stopwatch was used to time the length of the flight and a tape measure was using to measure the model range. The free-flight lift-to-drag ratio, *L/D*, was determined from the range.

4.6 - Fluorescent Dye

Fluorescent dyes were used to visualize the delta wing wakes. Two types of fluorescent dye were in this experiment: rhodamine dye which fluoresces at a wavelength of 556nm (red) and is visible to 1 part per million and fluorescein dye which fluoresces at a wavelength of 494nm (yellow/green) and is also visible to 1 part per million. From preliminary testing of the two dyes it was determined that the fluorescein dye illuminates much more brightly and is therefore more suited to flow visualizations.

4.7 - Dye Illumination and Photography

The fluorescent dye was illuminated using a laser beam generated using a Spectra Physics 5W argon-ion laser. The beam produced by this laser traveled 89mm and was then focused using a 50mm focal length bi-convex lens. It then traveled 12.7mm and was expanded using a 76.2mm focal length half-cylindrical lens to create an oval-shaped laser light beam (Figure 4.12). This light beam was deflected into the water and down the length of the tank using common rear-silvered mirrors. All beam turns were made to be

90° to preserve the shape of the light sheet. In the test section, the light sheet was expanded to approximately 0.3048m wide by 0.4572m high.

Two Nikon N6006 cameras were used to take pictures of the model through the glass windows in the observation pit (Figure 4.13). A 0.4574m x 0.6096m mirror was placed on the bottom of the towing tank near the observation pit to allow pictures to be taken of the bottom view of the model. The second camera was used to take direct side view pictures of the flowfield. The total line of sight distance from each camera was set constant for each camera so that the length scales on the bottom and side view photographs would be the same.

A Beckman Industrial Model FG2A function and a Hewlett Packard 5326A timer/counter were used to log the time delay between successive photographs. Mirrors were used to reflect the display of the frequency counter into the bottom left corner of the bottom view camera (Figure 4.13).

Pictures were taken using Fuji HG 1600 color film at shutter speeds of 1/60 to 1/15 seconds at f/1.8.

Chapter 5 - Flow Visualization Results

5.1 - Introduction

Flow visualizations of the wake of a 75° delta wing were made over a range of Reynolds numbers ($Re_c=U_{ref}c/\nu$) and wing lift coefficients (C_L) at various locations behind the wing (Table 4). Two orthogonal views of the model were photographed simultaneously to reveal the three-dimensional structure of the wake. The planform view of the delta wing model was photographed through the bottom observation window using the bottom view mirror (Figure 4.13). The side view of the model was photographed directly through the middle observation window (Figure 4.13). Note that these pictures are not truly instantaneous "snapshots" of the flow but are very short time averages due to the exposure times of the film (never greater than 1/15 seconds).

The Cartesian coordinate system (x,y,z) shown in Figure 5.1 will be used in describing all of the flow visualization results. The origin of the coordinate system is fixed at the midspan of the trailing edge of the model. The x-axis is aligned with the tank centerline and points opposite the velocity vector of the delta wing model so that pictures

downstream of the wing will be at a positive x-coordinate. The y-axis points downwards to the tank floor in the direction of lift, and the z-axis completes the right hand set.

The remainder of this chapter describes both qualitative and quantitative aspects of this delta wing vortex flow. Section 5.2 describes the results of a support interference study which validate the flow visualizations. The aerodynamic characteristics of the delta wing models used in this test are presented in Section 5.3. Section 5.4 describes the flow visualizations and is broken up into three parts. Flow visualizations made for a baseline case are presented in Section 5.4.1. Variations in the flow structure due to Reynolds number and wing lift coefficient effects are presented in Sections 5.4.2 and 5.4.3.

5.2 - Support Interference Study

Figures 5.2 and 5.3 show the wake for the first few chordlengths downstream of the free-flight and supported models, respectively. For both the free-flight (Figure 5.2) and wire-supported (Figure 5.3a) tests, the chord Reynolds number is 140,560 and the lift-to-drag ratio is 2.95 corresponding to a C_L of about 0.09. For the strut-supported test (Figure 5.3b) the chord Reynolds number is 44,200 and the angle of attack is at 5°. Miller and Williamson (1995) found that the feature of the wake most sensitive to support interference is the braid wake. A comparison of Figures 5.2 and 5.3a reveals a similar flow structure exists for the free-flight and wire-supported tests. The free-flight model produces a braid wake which extends about 0.33 chords behind the wing with a braid spacing of about 0.05 chords. The wire-supported model produces a braid wake of essentially identical characteristics considering the uncertainty associated with setting the

test conditions equal for the two cases. Further evidence for lack of support interference effects for the wire-supported configuration comes from a comparison of the shape of the braid wake produced by each model. For both tests, the braids form the same V-shape structure. From these comparisons, we conclude that support interference effects are negligible for the wire-supported configuration used in this experiment.

Comparison of the strut-supported configuration photographs (Figure 5.3b) to the free-flight photographs reveals very different wake structures. For the strut-supported case, the braid wake is non-existent and the only identifiable structure at the model trailing edge is the vortex pair. From these visualizations, strut interference effects appear to drastically change the flow structure and therefore this type of model support configuration is not feasible.

Figure 5.3c shows the free-flight flow visualizations made by Miller and Williamson (1995) for their 75° delta wing at 10° angle of attack and for a Reynolds number of 10,000. Figure 5.3d shows a duplication of their results using the wire-supported configuration discussed above. A comparison of these two sets of photgraphs shows that the wakes are in fact similar. Both tests reveal a highly regular braid wake as well as a vortex pair. The braid wake spacing in each case is about 0.11 chordlengths. The free-flight model braid wake does appear to stay regular for a longer distance downstream than the towed model wake. This is possibly due to differences in free-stream turbulence levels in the towing tanks. The side views reveal that the towed model is actually at a slightly higher angle of attack than the free-flight model which would

produce a larger vortex Reynolds number. This also could explain why the wake is more regular for the free-flight test. A close inspection of the braid wake near the trailing edge reveals that the braid wake shed by the towed model has a small notch cut out of it at the wake center that is absent in the free-flight photographs. This indicates that there is some small hint of wire interference but does not change the major structures in the flow.

5.3 -Wing Aerodynamic Characteristics

As a precursor to the main flow visualizations, it was necessary to document the lift coefficient generated by the delta wings as a function of bridle angle (α) and Reynolds number. Using these measurements it was then possible to choose the appropriate bridle angles to vary lift coefficient while holding Reynolds number constant and vary Reynolds number while holding lift coefficient constant. Figure 5.4 shows this relationship. The dotted lines in Figure 5.4 represent the two test vectors examined in the present work. The intersection of these test vectors (Re=151,800 and C_L=0.30) is termed the baseline case.

5.4 - Flow Visualizations

5.4.1 - Baseline Case

Figures 5.5a and 5.6a show the bottom and side views of the delta wing wake for the baseline case just aft of the of the wing up to about 1 chordlength downstream. In the bottom view, the wing can be seen as a blue triangle with green dye trailing behind it. In this picture, and in all flow visualizations that follow, the wing is moving from right to left

and the wing is lifting up out of the paper (the suction side of the wing is viewed). The wing appears blue due to the laser light reflecting from it. The two bright streaks extending down the wing chord exist as a result of the machining of the wing and are not flow structures. The tape used to secure the support wires to the wing can be seen as three white rectangles on the wing surface. An orange number just ahead of the wing apex is an inadvertent reflection of the counter/timer display described previously. The trailing edge of the wing appears blurred due to the exposure time of the photograph.

Green dye can be seen starting at the trailing edge and extending to the right edge of the photograph. At the trailing edge, this dye reveals two main features. The first is a series of spanwise U-shaped lines of dye which appear periodically behind the wing. These lines of dye make up what will from here on be referred to as the "braid wake" with each individual line being referred to as a "braid". First-hand observations of this flow reveal that the braids are not irrotational. Spanwise vorticity generated in the upper and lower boundary layers of the wing is shed alternately into the wing wake from the top and bottom wing surfaces and therefore consecutive braids have opposite signs of rotation. However, since dye was only painted on the pressure side of the wing, only half of the braid wake is illuminated. The other half of the braid wake is not visible in most of the pictures.

The second feature visible at the trailing edge is a pair of streamwise structures which appear near the wing tips. These structures are the counter-rotating vortex pair which one would expect to see in this region and can be clearly identified as such from

first-hand observations. These structures are formed when separated shear layers at the leading edges of the wing roll up.

The braid wake and the counter-rotating vortex pair are not independent structures. For the isolated vortex velocity measurements presented in Chapter 3, the wing wake was observed to spiral around the vortex core. For the delta wing wake, the braid wake is stretched as it spirals around the counter-rotating vortex pair.

From Figure 5.5a, we see that the individual braids in the braid wake are spaced about 0.058 chordlengths apart and can be discerned for about 0.5 chordlengths behind the wing. However, it is very difficult to determine the exact extent of the braid wake as the braid wake does not disappear uniformly: the center of the braids are the first to become unrecognizable while the ends can be identified much further downstream. The vortex pair is at first very difficult to identify due to the quantity of dye between them. However, about 1 chordlength behind the wing most of this dye has disappeared making the vortex pair much easier to see. The edges of the vortex pair billow periodically revealing a dominant wavelength of the large-scale turbulence within them. Near the trailing edge this wavelength is observed to be the same as that for the braid wake, about 0.058 chordlengths. At the far right of the picture (about 1 chordlength behind the wing), this dominant wavelength has increased to about 0.12 chordlengths, about double that at the trailing edge.

Figure 5.6a is the corresponding side view of Figure 5.5a. In this figure, the wing can be seen in the center of the picture with a trail of green dye streaming from it revealing

the wing wake. From this picture, the angle of attack of the wing is measured to be about 12°. The wires used to support the wing can also be seen attached to the top surface of the wing and appear blurred due to the exposure time of the photograph. Dye can be seen below the wing beginning at the apex and continuing back along the chord in a wedge shape at an angle of 5° to the chordline. This is the shear layer rolling up to form the vortex pair. At the trailing edge, bright spots of dye appear at the top of the wake which are slanted with respect to the horizontal by about 45°. These spots are actually the edges of the braid wake seen in Figure 5.5a (first-hand observations reveal this more clearly). A closer look at the edges of the braid wake reveals that a few of them have small filaments of dye extending down to the vortex pair. These filaments are the sides of the braid wake as it spirals around the vortex pair. Just behind the trailing edge, the bottom of the wake expands downward to an angle of about 10° to the wing. At the right end of the picture, a thin dark region can be seen in the wake just below the braid wake edges and above the vortex pair. This is probably due to stretching of the vertical extent of the wake resulting in a gap between the braid wake and the vortex pair.

Figures 5.5c (bottom view) and 5.6c (side view) reveal the wing wake 2.6 to 5.4 chordlengths behind the wing. From the bottom view we see the vortex pair with little dye between them. At the left edge of the photo, the vortices are spaced about 1/3 of the span apart. However, at the right edge of the photo, the vortices have grown together and their inner edges are now almost touching. A closer look at the vortex pair reveals that they appear to be made up of a series of structures that are at a 45° angle to the vortex

centerline. These structures appear to be spaced about 0.12 chordlengths apart, consistent with dominant wavelength in the pair noted before. By looking at the region between the vortex pair, one can see that the these structures on each vortex are in phase at in this picture. From the side view, we see that the thin dark region noted previously extends throughout the wake. The structure above and below this dark region appear to be very different. Above this region, there appears to be very little dominant structure suggesting that the remains of the braid wake above the vortex pair is breaking down into finer turbulence scales. Below this region, the wake appears to be made up of finger-like structures which extend the width of the wake. These structures have a wavelength of about 0.12 chordlengths. At the bottom of the wake, there appear to be smaller scale structures as well. These structures protruding from the bottom of the wake form what will be referred to as the "curtain".

The next set of pictures (Figures 5.5d and 5.6d) show the region of the wake from 11.7 chordlengths to 14.5 chordlengths behind the wing. In these pictures, the wake has grown so large that it has begun to extend outside of the light beam. In the bottom view, we see the vortex pair separated by a very thin dark region. Within each vortex the same scale structures (0.12 chordlengths) noticed in the previous set of pictures can be seen. However, these structures in each vortex now appear to be out of phase and no longer appear to be at 45° to the vortex centerline. The region between the vortex pair takes on a sinusoidal shape as the structures in each vortex alternately jut out between the pair. The outer edges of the vortex pair reveal not only the 0.12 chordlength wavelength structures

but a new 0.5 chordlength wavelength structure. Note also three dark patches present in the upper vortex. The side view reveals extremely fine scale structures at the top of the wake. At the bottom of the wake, the "curtain" referred to earlier has continued to grow and now much larger scale structures can be seen. The wavelength of these structures is on the order of 0.18 chordlengths.

Figures 5.5e and 5.6e show the wake from 17.5 to 20.3 chordlengths behind the wing. The left half of Figure 5.5e (bottom view) reveals the alternating interaction of the vortex pair which was noted in the previous set. However, the right half of this picture shows that this alternating structure has ceased and now V-shaped structures can be seen which extend all the way across the wake. These structures may be the result of a merging of similar structures on each side of the wake. At this point the vortex pair can no longer be distinguished in the bottom view. The three dark patches in the wake which were noticed in the previous set can been more clearly seen here and have grown in size. Bright spots of dye can also be seen scattered about in the wake indicating some sort of vertically aligned flow structure. The side view shows a structure similar to that noted previously. The top of the wake appears very smooth with very little irregularity. Below this is the "curtain" which has a large range of turbulence scales within it. In addition to the structure of the curtain, there is now a much larger scale waviness of the outer edge of the curtain. About 5 peaks of this waviness can be seen indicating a wavelength of about 0.67 chordlengths. Within each peak of this structure there are many smaller scale structures which can not be measured. An interesting feature of this picture is that now

one of the vortex cores can be seen for the first time. This core is at the top of the picture and is indicated by a dull green structure extending horizontally across the picture. The "curtain" appears to be dangling down from this vortex core suspended by periodic strands of dye. The other vortex core is not visible as it is most likely hidden behind the one that is visible.

Figures 5.5f and 5.6f are the last two pictures for this case. This pictures show the wake from 20.8 to 23.6 chordlengths behind the wing. The bottom view shows that paths of turbulence now appear across the entire wake and much of the wake is outside of the light beam. The three dark spots noticed before can still be seen and have grown even larger. The bright spots noticed before are still visible and now appear to be connected by curved structures. At this point, a very broad range of turbulence scales are present and no one wavelength appears dominant. The side view shows that the vertical extent of the wake has grown tremendously and the vortex cores noted in the previous pictures has risen out of the picture view. The curtain however, is still visible and strands of dye can be seen extending up to the top of the picture presumably connecting the curtain to the vortex core. This curtain now appears less dense than in previous photos and seems to be made up of many distinct dye filaments.

At this point it is necessary to clarify a possibly confusing point concerning the flow visualizations. From the previous pictures, we observed that the vortex pair could be readily identified in the first four bottom view photographs. However, in the next few pictures the vortex pair could no longer be identified from the bottom view possibly

implying that the vortex pair had decayed. This is obviously not the case because at one point the vortex pair can be identified from the side view while the bottom view reveals no identifiable structure. It is important to remember that in the bottom view, the vortices are convected away from the camera. Initially, the vortex pair is below the braid wake and can therefore be easily identified from the bottom view. As the vortex pair rises in the tank, it eventually rises above the braid wake and is therefore hidden behind the braid wake in the bottom view. What is then seen in the bottom view is the fluid left behind by the vortex pair. A similar type of structure has been seen by Maxworthy (1972) in his vortex ring experiments. He found that a cross-section of a vortex ring forms a Kelvin oval (Figure 5.7). Vorticity can diffuse out of this oval into the outer irrotational fluid and collect at the bottom of the Kelvin oval. This type of phenomena offers a feasible explanation of the "curtain" observed in the flow visualizations.

5.4.2 - Reynolds Number Effects

To determine the effects of Reynolds number, flow visualizations were made at eight different Reynolds numbers (from Re=24,890 to Re=370,455) at the same lift coefficient (C_L=0.30) as the baseline case. Figures 5.8-5.22 show the bottom and side view photographs taken for each case. They are arranged by ascending Reynolds number with the bottom view photographs preceding the side views. Since these photographs show similar trends in turbulence structure, presenting comparisons of two of these cases to the baseline case is adequate to determine Reynolds number effects on the wake

structure. The two cases selected bracket the baseline case at Reynolds numbers of 24,890 and 285,400.

Figures 5.8 and 5.9 are the photographs taken of the wake produced by a delta wing at C_L=0.30 and Re=24,890. In general, these figures reveal a flow structure which is very similar to that found for the baseline case. However, a close inspection of these figures reveals that there are some important differences. The most obvious difference between these two cases is the appearance of the braid wake. For this case, the braids are seen to be spaced further apart (about 0.098 chordlengths) and the braid wake extends further behind the wing (to about 3 chordlengths). The orientation of these braids has changed and they are now are inclined to the vortex centerline by about 65°. The side views also show that the braid extends much further back. Dye filaments extending from the top to the bottom of the wake appear throughout.

The turbulence structure has changed throughout the flow. At all locations behind the wing, there are fewer turbulence scales present and those that exist are larger than for the baseline case. Near the trailing edge, the only identifiable feature of the wake between the vortex pair is the braid wake. The "curtain" structure is present in this case but contains only the larger turbulence scales. The waviness noted in the "curtain" for the baseline case is also found here but has a much longer wavelength (about 3.5 chordlengths). In Figure 5.9 we can see both the vortex core and the "curtain" hanging below it. The instabilities in the "curtain" are much smaller than those found in the vortex core.

The scale of the turbulence structures in the wake appears to increase in discrete jumps as it did for the baseline flow. Near the trailing edge, the dominant scale of the turbulent structure in the vortex pair is about 0.098 chordlengths, the same as the braid wake. This dominant wavelength continues for about 4 chordlengths behind the wing at which point the dominant turbulence scale increases to about 0.27 chordlengths. About 28 chordlengths downstream the dominant wavelength again increases to about 0.45 chordlengths.

The vortex pair does not grow together as quickly as for the baseline flow. In this case, it takes about 20 chordlengths downstream while for the baseline case it was only 12 chordlengths. For a given location behind the wing, the lobes on the sides of the vortex pair are much bigger than the baseline case and contain bright filaments of dye. These filaments appear to form some kind of ring structure and may be a remnant of the braid wake.

Figures 5.20 and 5.21 are photographs of the flow visualizations made for Re=285,400 and C_L=0.30. For this case we see that the braid wake is spaced closer together (0.056 chordlengths) and does not extend as far downstream (0.33 chordlengths) as it did for the baseline case. The range of turbulence scales is much greater and the largest structures in the wake are smaller than in the other cases making it hard to measure the dominant wavelengths in the wake. However, we can still see some dominant structure. At the trailing edge, the wavelength of turbulence is about the same as the braid spacing (0.056 chordlengths). About 2 chordlengths behind the wing this wavelength has

increased to about 0.093 chordlengths and by about 8 chordlengths downstream this wavelength has increased to about 0.16 chordlengths. The "curtain" seen in Figure 5.22 can be seen to be made up of large finger-like structures with a wavelength of about 0.4 chordlengths. Within these finger-like structures there are many smaller scale structures which can not be identified.

To quantify the observation that the scale of the dominant turbulence structures (λ_t) in the wing wake appears to increase in discrete jumps, these structures were measured with a ruler as a function of downstream distance, x/c, for the three Reynolds numbers cases discussed previously. The results of these measurements are presented in Figure 5.23. This plot reveals that the scale of the dominant turbulence structures does actually increase in discrete jumps. Furthermore, this plot shows that the downstream distance required for these jumps to occur and the spacing between successive jumps is reduced as Reynolds number is increased. The fact that the turbulence scales increase in discrete jumps indicates that the smaller structures are combining to form larger ones through some sort of reorganization of turbulence. Figure 5.23 shows that these jumps are usually less than a factor of two indicating that this reorganization may be in the form of pairing of successive counter-rotating braids or alternating co-rotating braids. More work needs to be done to clarify the exact mechanism of turbulence reorganization found in the braid wake.

To more clearly illustrate the effects of Reynolds number on the braid wake, a plot of braid spacing, λ_b, as a function of Reynolds number was created (Figure 5.24) from all

flow visualizations. This plot indicates that braid spacing does indeed decrease with increasing Reynolds number up to some limiting value (approximately Re=150,000) and then becomes fairly constant.

5.4.3 - Lift Coefficient Effects

To determine the effects of lift coefficient on the delta wing wake, flow visualizations were made for five different wing lift coefficients (from C_L=0.01 to C_L=0.34) at the same Reynolds number (Re=151,800) as the baseline case. Figures 5.25-5.34 show the bottom and side view photographs taken for each case. They are arranged by ascending lift coefficient with the bottom view photographs preceding the side views. As was the case for the Reynolds number effects photographs, these photographs show similar trends in turbulence structure and therefore presenting comparisons of two of these cases to the baseline case is adequate to determine effects of lift coefficient on the wake structure. The two cases selected bracket the baseline case at lift coefficients of 0.15 and 0.34.

Figures 5.29 and 5.30 show the flow visualizations made for the C_L=0.15 case. Figure 5.29 shows that a braid wake forms at the trailing edge with a braid spacing of 0.058 chords and persists about 0.33 chords downstream. This is the same braid spacing observed in the baseline case but the braid wake disappears more quickly in this case. The wake appears more disorganized in this case and the turbulence structure associated with the vortex pair appears to be thinner and less clear than in the baseline case. A large amount of disorganized turbulence appears between the vortex pair which was not present

in the baseline flow. The inner edges of the vortex pair appear to begin to interact about 20 chordlengths downstream of the wing which is further than the 12 chordlenths found for the baseline case. The side view reveals that the vertical extent of the wake for a given location behind the wing is significantly smaller for this case than for the baseline. The "curtain" observed in the baseline case also appears here but is smaller and much less distinct.

Figures 5.33 and 5.34 show the flow visualizations for the C_L=0.34 case. In these photos a braid wake can be seen to be forming at the wing trailing edge with a braid spacing of 0.58 chords and is visible to about 0.583 chords behind the wing. This is the same braid spacing as seen in the baseline case but the braid extends back further here. The inner edges of the vortex pair appear to begin interacting at about 7 chords behind the wing as compared to about 12 chords for the baseline case. The turbulence structure of the wake appears less clear in all photos than it did in the baseline case. This may be due to an accumulation of dye in the tank from previous runs or may be due to more disorganized structure present in this case. The side views reveal very little change from the baseline case except that the vertical extent of the wake does appear to grow slightly faster for this case. The vortex pair can be seen to rise above the braid wake within 10 chords behind the wing whereas it was not visible until about 15 chords back for the baseline case. Therefore, the vortices appear to rise more quickly for this case. This is because increasing lift coefficient increases the vortex strength and therefore increases the convection velocity of the vortex pair.

To more clearly illustrate the effects of lift coefficient on braid spacing, a plot of braid spacing as a function of lift coefficient was created (Figure 5.35) from all flow visualizations. This plot indicates that braid spacing is fairly constant for all lift coefficients considered in this test and supports the results of the two cases presented above.

Chapter 6 - Conclusions

The turbulence structure and mean flow of an isolated vortex has been studied through three-component time-series velocity measurements. Vortices were generated using two different symmetrical airfoils at 5° angle of attack. Measurements were made in both cross-sectional grids and profiles over a range of Reynolds numbers and downstream distances. From these measurements, the following conclusions may be drawn:

1) Turbulence levels increase across the wake spiral to a maximum at the wake centerline. The magnitude of the turbulence is greatest where the wake first bends and begins to spiral about the vortex core.

2) Digital filtering of turbulence measurements indicates that vortex cores are laminar and are surrounded by an annulus of turbulence. Velocity fluctuations in the vortex core are the result of vortex wandering and inactive core motions as the laminar core is buffeted about by the surrounding turbulence.

3) The NACA 0016 wing produces a vortex which is less turbulent and is not as tightly rolled up as the NACA 0012 wing tip vortex. This is due to differences in aspect ratio and boundary layer trip.

4) The core radius for the NACA 0016 vortex is about half as large as that for the NACA 0012 vortex.

5) The maximum tangential velocity for the NACA 0016 vortex is 40% higher than that for the NACA 0012 vortex.

6) The axial velocity profile of the NACA 0016 vortex has a secondary deficit which is not present in the NACA 0012 vortex.

7) Vortex wandering amplitudes are independent of downstream distance but increase with Reynolds number.

8) Vortex wandering amplitudes scale on the wing chord.

9) Axial velocity deficit in the vortex core increases with distance downstream. A secondary deficit located just outside the vortex core edge decreases with distance downstream.

10) Axial velocity deficit in the vortex core decreases with increasing Reynolds number while the secondary deficit increases with Reynolds number. The radial location of this secondary deficit moves towards the core center as Reynolds number is increased.

11) Maximum tangential velocity decreases with increasing downstream distance and increases with Reynolds number.

12) Core radius appears to increase with downstream distance and decrease with increasing Reynolds number.

13) Wake velocity profiles show no dependence on Reynolds number.

14) Axial velocity deficit and axial normal stress magnitudes in the near 2-D wake decrease as the vortex evolves downstream.

Flow visualizations of the wake of a 75° delta wing model were made for a range of Reynolds numbers and lift coefficients. These visualizations reveal the near-instantaneous turbulence structure of the vortex pair and the connecting braid wake. The evolution of this turbulence structure could be determined from successive photographs. From these visualizations, the follow conclusions may be drawn:

1) Strut interference effects on the delta wing wake are negligible for the wire-supported configuration used in this test.

2) The strut-supported configuration tested significantly alters the turbulent structure of the wing wake and is therefore not a feasible test configuration.

3) The wing wake is dominated by a counter-rotating vortex pair and a connecting braid wake. The braid is stretched as it spirals around the vortex core.

4) The vortex pair is initially below the braid wake but rises with time and eventually moves above the braid wake leaving a wake (the "curtain") of turbulence behind.

5) Increasing Reynolds number decreases the braid wake spacing up to $Re \approx 150{,}000$. Beyond this limiting value Reynolds number has little effect on the braid wake spacing.

6) Increasing Reynolds number reduces the extent of the braid wake behind the wing.

7) The large-scale turbulent structures are largest for the lowest Reynolds numbers.

8) The wavelength of the dominant turbulent structures in the wing wake increase in discrete jumps. This is perhaps a result of smaller structures combining to form larger ones through some sort of reorganization of turbulence.

9) As Reynolds number is increased, the downstream location of these jumps moves towards the trailing edge. The downstream distance between successive jumps is also decreased as Reynolds number is increased.

10) The braid wake spacing is independent of lift coefficient.

11) The chordwise extent of the braid increases with C_L.

12) The vertical extent of the wake increases with C_L. This is probably due to an increase in the convection velocity of the vortex pair with increasing C_L.

13) The amount of turbulent fluid entrained in the vortex pair appears to increase with C_L.

14) The distance behind the wing at which point the turbulence structure from each vortex begins to interact is reduced for increasing C_L.

References

Baker, G. R., Barker, S. J., Bofah, K. K., and Saffman, P. G., 1974, "Laser anemometer measurements of trailing vortices in water", *Journal of Fluid Mechanics*, vol. 65, part 2, pp.325-336.

Barker, S. J., and Crow, S. C., "The motion of two-dimensional vortex pairs in ground effect," *Journal of Fluid Mechanics*, vol. 82, part 4, 1977, pp. 659-671.

Bandyopadhyay, P. R., Stead, D. J., and Ash, R. L., 1991, "The organized nature of a turbulent trailing vortex", *AIAA Journal*, vol. 29, no. 10, pp. 1627-1633.

Batchelor, G. K., 1964, "Axial flow in trailing line vortices," *Journal of Fluid Mechanics*, vol. 20, pp. 645-658.

Bearman, P. W., 1971, "Corrections for the effect of ambient temperature drift on hot-wire measurements in incompressible flow," *DISA Information*, vol. 11, pp. 25-30.

Betz, A. "Behavior of vortex systems," *National Advisory Committee for Aeronautics*, Technical Memo, no. 713, pp. 237-255.

Bilanin, A. J., Donaldson, C. duP., 1975, "Estimation of velocities and roll-up in aircraft vortex wakes," *Journal of Aircraft*, vol. 12, July 1975, pp.578-585.

Chevalier, H., 1973, "Flight test studies of the formation and dissipation of trailing vortices," *Journal of Aircraft*, vol. 10, no. 1, pp. 14-18.

Chigier, N. A., and Corsiglia, V. R., 1972, "Wind tunnel studies of wing wake turbulence," *AIAA Paper 72-41*.

Choi, K., and Simpson, R. L., 1987, "Some mean-velocity, turbulence and unsteadiness characteristics of the VPI&SU Stability Wind Tunnel", *Rep. VPI-AOE-161*, VPI&SU, Blacksburg, VA.

Chow, J. S., Zilliac, G. G., and Bradshaw, P., 1994, "Turbulence measurements in the near-field of a wingtip vortex," *ASME Forum on Turbulence in Complex Flows*, Chicago, IL, Nov. 6-11.

Ciffone D L, 1974, "Correlation for estimating vortex rotational velocity downstream dependence", *Journal of Aircraft*, vol. 11, no. 11, pp. 716-717.

Ciffone, D L and Orloff, K L, 1975, "Far-field wake-vortex characteristics of wings", *Journal of Aircraft*, vol. 12, no. 5, pp. 464-470.

Corsiglia, V R, Schwind, R G, and Chigier, N A, 1973, "Rapid scanning, three-dimensional hot-wire anemometer surveys of wing-tip vortices", *Journal of Aircraft*, vol. 10, no. 12, pp. 752-757.

Crow, S.C., 1970, "Stability theory for a pair of trailing vortices," *AIAA Journal*, vol. 8, no. 12, pp. 2172-2179.

Cutler, A. D., and Bradshaw, P., 1991, "A crossed hot-wire technique for complex turbulent flows," *Experiments in Fluids*, vol. 12, pp. 17-22.

Devenport, W. J., Rife, M. C., Liapis, S. I., and Follin, G. J., 1995, "Turbulence structure and scaling in trailing vortices," *AIAA 95-0588.*

Devenport, W. J., Zsoldos, J. S., and Vogel, C. M., 1996a, "The structure and development of a counter-rotating wing-tip vortex pair," *Journal of Fluid Mechanics*, In Press.

Devenport, W. J., Rife, M. C., Liapis, S. I., and Follin, G. J., 1996b, "The structure and development of a wing-tip vortex," *Journal of Fluid Dynamics*, vol. 312, pp. 67-106.

Donaldson, C. duP., and Bilanin, A. J., 1975, "Vortex wakes of conventional aircraft," *AGARD AG-204.*

Donaldson, C. duP., Snedeker, R. S., and Sullivan, R. D., 1974, "Calculat6ion of aircraft wake velocity profiles and comparison with experimental measurements," *Journal of Aircraft*, Vol. 11, No. 9, pp. 547-555.

Dosanjh, D. S., Gasparek, E. P., and Eskinazi, S., 1962, "Decay of a Viscous Trailing Vortex," *The Aeronautical Quarterly*, pp. 167-188.

Eliason, B. G., Gartshore, I. S., Parkinson, G. V., 1975"Wind tunnel investigation of crow instability," *Journal of Aircraft*, vol. 12, no. 12, pp. 985-988.

Engel, M. E., 1995, "A wind tunnel investigation of a wing-tip trailing vortex," MS Thesis, AOE Dept., VPI&SU, Blacksburg, VA.

Francis, T. B., Katz, J., 1988, "Observations on the development of a tip vortex on a rectangular hydrofoil," *Journal of Fluids Engineering*, vol. 110, pp. 208-215.

Francis, M. S., Kennedy, D. A., 1979, "Formation of a trailing vortex," *Journal of Aircraft*, vol. 16, no. 3, pp. 148-154.

Green, S. I., and Acosta, A. J., 1991, "Unsteady flow in trailing vortices," *Journal of Fluid Mechanics*, vol. 227, pp. 107-133.

Hoffmann, E. R., and Joubert, P. N., 1962, "Turbulent line vortices," *Journal of Fluid Mechanics*, pp. 395-411.

Huffaker, R. M., Jelalian, A. V., and Thomson, J. A. L., "Laser-doppler system for detection of aircraft trailing vortices," *Proceedings of the IEEE*, vol. 58, no. 3, 1970.

Iverson, J. D., 1976, "Correlation of turbulent trailing vortex decay data," *Journal of Aircraft*, vol. 13, no. 5, pp.338-342.

Jorgenson, F. E., 1971, "Directional sensitivity of wire and fiber-film probes," *DISA Information*, vol. 11, pp. 6-10.

Katz, J., Bueno Galdo, J., 1989, "Effect of roughness on rollup of tip vortices on a rectangular hydrofoil," *Journal of Aircraft*, vol. 26, no. 3, pp. 247-253.

Lamb, H., 1932, "Hydrodynamics," 6th edition, Dover, pp. 223-230.

Lezius, D. K., 1974, "Water tank study of the decay of trailing vortices," *AIAA Journal*, vol. 12, no. 8, pp. 1065-1071.

Liu, H. T., 1992, "Effects of ambient turbulence on the decay of a trailing vortex wake," *Journal of Aircraft*, vol. 29, no. 2, pp. 255-263.

Locke, C., Hirsa, A., and Rubin, M. D., 1993, "Short-wave instability in a laminar vortex pair," *FED-Vol. 157, Unsteady Flows*, pp. 73-81.

Mathioudakis, K., and Breugelmans, F. A. E., 1985, "Use of triple hot wires to measure unsteady flows with large direction changes," *Journal of Physics, E: Sci. Instrum.*, vol. 18, pp. 414-419.

Mayer, E. W., Powell, K. G., 1992, "Similarity solutions for viscous vortex cores," *Journal of Fluid Mechanics*, vol. 238, pp. 487-507.

Mason, W. H., Marchman, J. F., 1973, "Far-tield structure of aircraft wake turbulence," *Journal of Aircraft*, vol. 10, no. 2, pp.86-92.

Maxworthy, T., 1976, "Some experimental studies of vortex rings," *Journal of Fluid Mechanics*, vol. 81, part 3, pp. 465-496.

Maxworthy, T., 1972, "The structure and stability of vortex rings," *Journal of Fluid Mechanics*, vol. 51, part 1, pp. 15-32.

Maxworthy, T., 1974, "Turbulent vortex rings," *Journal of Fluid Mechanics*, vol. 64, part 2, pp. 227-239.

McCormick, B. W., Tangler, J. L., and Sherrieb, H. E., 1968, "Structure of trailing vortices," *Journal of Aircraft*, vol. 5, no. 3, pp. 260-1071.

Mertaugh, L. J., Damania, R. B., and Paillet, F. L., 1977, "An investigation of the near-field wake behind a full-scale test aircraft," *Journal of Aircraft*, vol. 14, no. 9, pp. 894-902.

Miller, G. D., and Williamson, C. H. K., 1995, "Turbulent structures in the trailing vortex wake of a delta wing," *AGARD Hydrodynamics Conf.*, part 3, pp. 7-12.

Orloff, K. L., 1974, "Trailing vortex wind-tunnel diagnostics with a laser velocimeter," *Journal of Aircraft*, vol. 11, no. 8, pp. 477-482.

Panton, R. L., Oberkampf, W. L., and Soskic, N., 1980, "Flight measurements of a wing tip vortex," *Journal of Aircraft*, vol. 17, no. 4, pp. 250-259.

Phillips, W. R. C., 1981, "The turbulent trailing vortex during roll-up," *Journal of Fluid Mechanics*, vol. 105, pp. 451-467.

Phillips, W. R. C., and Graham, J. A. H., 1984, "Reynolds-stress measurements in a turbulent trailing vortex," *Journal of Fluid Mechanics*, Vol. 147, pp. 353-371.

Pope, A., and Harper, J. J., 1966, "Low speed wind tunnel testing," John Wiley & Sons, New York, pp. 300-315.

Ragab, S. A., and Sreedhar, M., 1995, "Numerical simulation of vortices with axial velocity deficits," *Physics of Fluids*, No. 7, 549-558.

Rossow, V. J., 1973, "On the inviscid rolled-up structure of lift-generated vortices", *Journal of Aircraft*, Vol. 10, No. 11, pp. 647-650.

Sarpkaya, T., 1992, "Three-dimensional interactions of vortices with a free surface," *AIAA 92-0059*, 30th Aerospace Sciences Meeting & Exhibit.

Scorer, R. S., and Davenport, L. J., 1970, "Contrails and aircraft downwash," *Journal of Fluid Mechanics*, vol. 43, part 3, pp. 451-464.

Shekarriz, A., Fu, T. C., Katz, J., and Huang, T. T., 1993, "Near-field behavior of a tip vortex," *AIAA Journal*, vol. 31, no. 1, pp. 112-118.

Singh, P. I., and Uberoi, M. S., 1976, "Experiments on vortex stability", *Physics of Fluids*, vol. 19, no. 12, pp. 1858-1863.

Spreiter, J. R., Sacks, A. H., 1951, "The rolling up of the trailing vortex sheet and its effect on the downwash behind wings," *Journal of the Aeronautical Sciences*, pp. 21-32.

Thomas, P. J., and Auerbach, D., 1994, "The observation of the simultaneous development of a long- and short-wave instability mode on a vortex pair," *Journal of Fluid Mechanics*, vol. 265, pp. 289-302.

Vukoslavcevic P., and Wallace, J. M., 1981, "Influence of velocity gradients on measurements of velocity and streamwise vorticity with hot-wire X-array probes", *Rev. Sci. Instrum.*, vol. 52, no. 6, June, pp.869-879.

Widnall, S. E., Bliss, D. B., and Tsai, C. Y., 1974, "The instability of short waves on a vortex ring," *Journal of Fluid Mech.*, vol. 66, part 1, pp. 35-47.

Wittmer, K. S., Devenport, W. J., and Follin, G. J., 1996, A four-sensor hot-wire probe system for three-component velocity measurements," *AOE Report*, VPI&SU, Blacksburg, VA.

Zsoldos, J. S., and Devenport, W. J., 1992, "An experimental investigation of interacting trailing vortex pairs," *Proceedings from 19th Symposium on Naval Hydrodynamics*, Seoul, South Korea, August.

Tables

Table 1: Test conditions for the velocity measurements

Wing	α (°)	x/c	Re_c	Measurement type
NACA 0012	5	10	530,000	Grid
NACA 0012	5	30	530,000	Grid
NACA0016	5	10	1,825,000	Grid
NACA0016	5	5	1,600,000	Core and wake profiles
NACA0016	5	7.5	1,600,000	Core and wake profiles
NACA0016	5	10	1,600,000	Core and wake profiles
NACA0016	5	10	1,000,000	Core and wake profiles
NACA0016	5	10	530,000	Core and wake profiles

Table 2: Uncertainties in the measured velocities normalized on U_{ref}

	Uncertainty	
Quantity	Spiral Wake	Core
U, V, W	0.015	0.015
ω_x	0.034	-
$\overline{u'^2}$	$3.1\text{x}10^{-6}$	$1.4\text{x}10^{-5}$
$\overline{v'^2}$	$9.5\text{x}10^{-6}$	$1.5\text{x}10^{-5}$
$\overline{w'^2}$	$9.9\text{x}10^{-6}$	$2.0\text{x}10^{-5}$
$\overline{u'v'}$	$4.3\text{x}10^{-6}$	$1.4\text{x}10^{-5}$
$\overline{u'w'}$	$4.5\text{x}10^{-6}$	$2.3\text{x}10^{-5}$
$\overline{v'w'}$	$2.9\text{x}10^{-6}$	$8.5\text{x}10^{-6}$

Table 3: Wandering amplitudes

x/c	Re_c	σ_y/c	σ_z/c	e
5	1,600,000	0.008	0.007	0.232
7.5	1,600,000	0.007	0.007	0.212
10	1,600,000	0.009	0.008	0.198
10	1,000,000	0.008	0.008	0.429
10	530,000	0.005	0.005	0.387
10[†]	530,000	0.007	0.005	-
5[†]	530,000	0.004	0.004	-

[†]from Devenport *et al.* (1996b)

Table 4: Test conditions for the flow visualizations

Case	Re_c	C_L
1	24,890	0.3
2	49,200	0.3
3	60,150	0.3
4	88,100	0.3
5	125,800	0.3
6	151,800	0.3
7	200,400	0.3
8	285,400	0.3
9	370,500	0.3
10	151,800	0.01
11	151,800	0.08
12	151,800	0.15
13	151,800	0.22
14	151,800	0.34

Figures

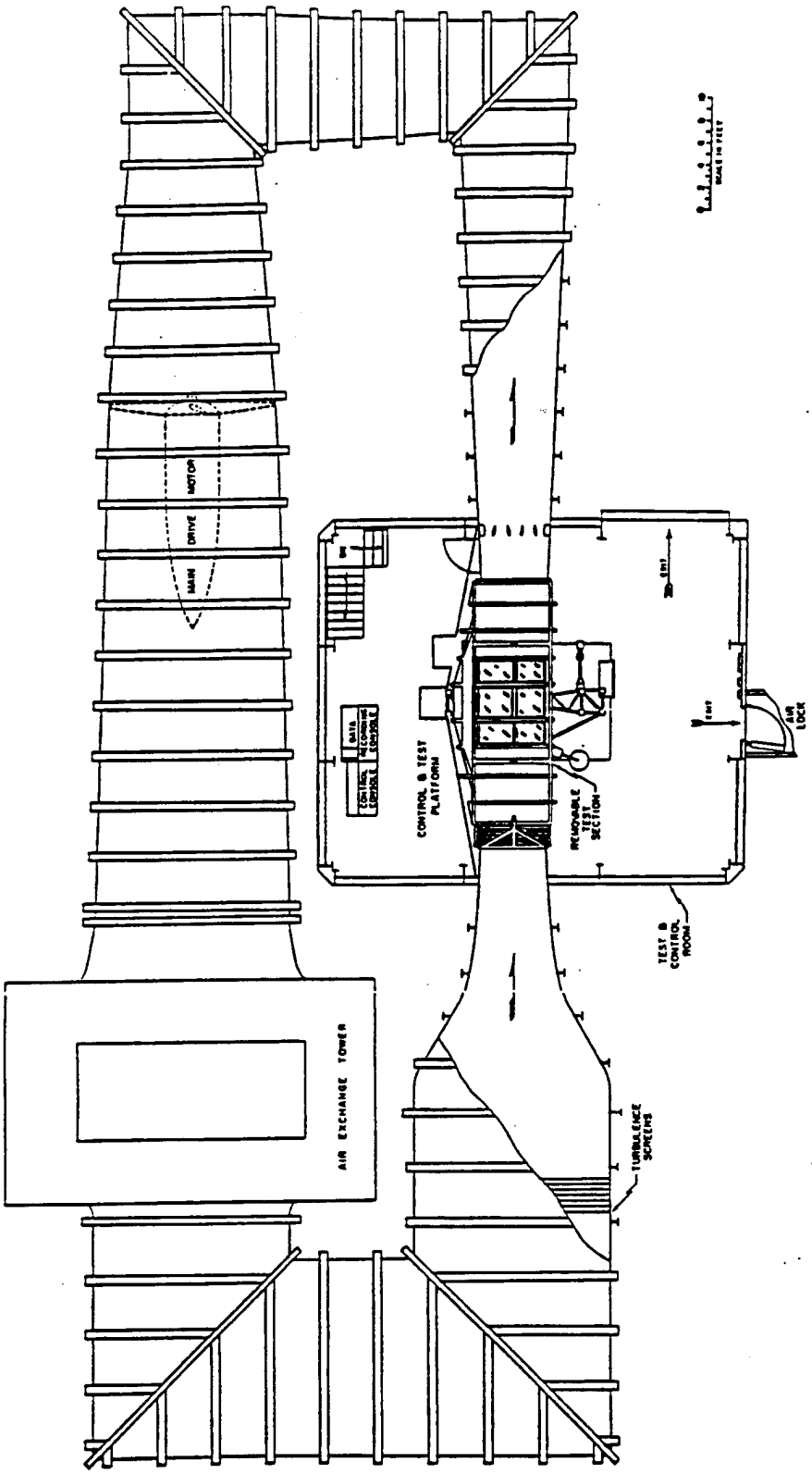

Figure 2.1 - The Virginia Tech Stability Wind Tunnel

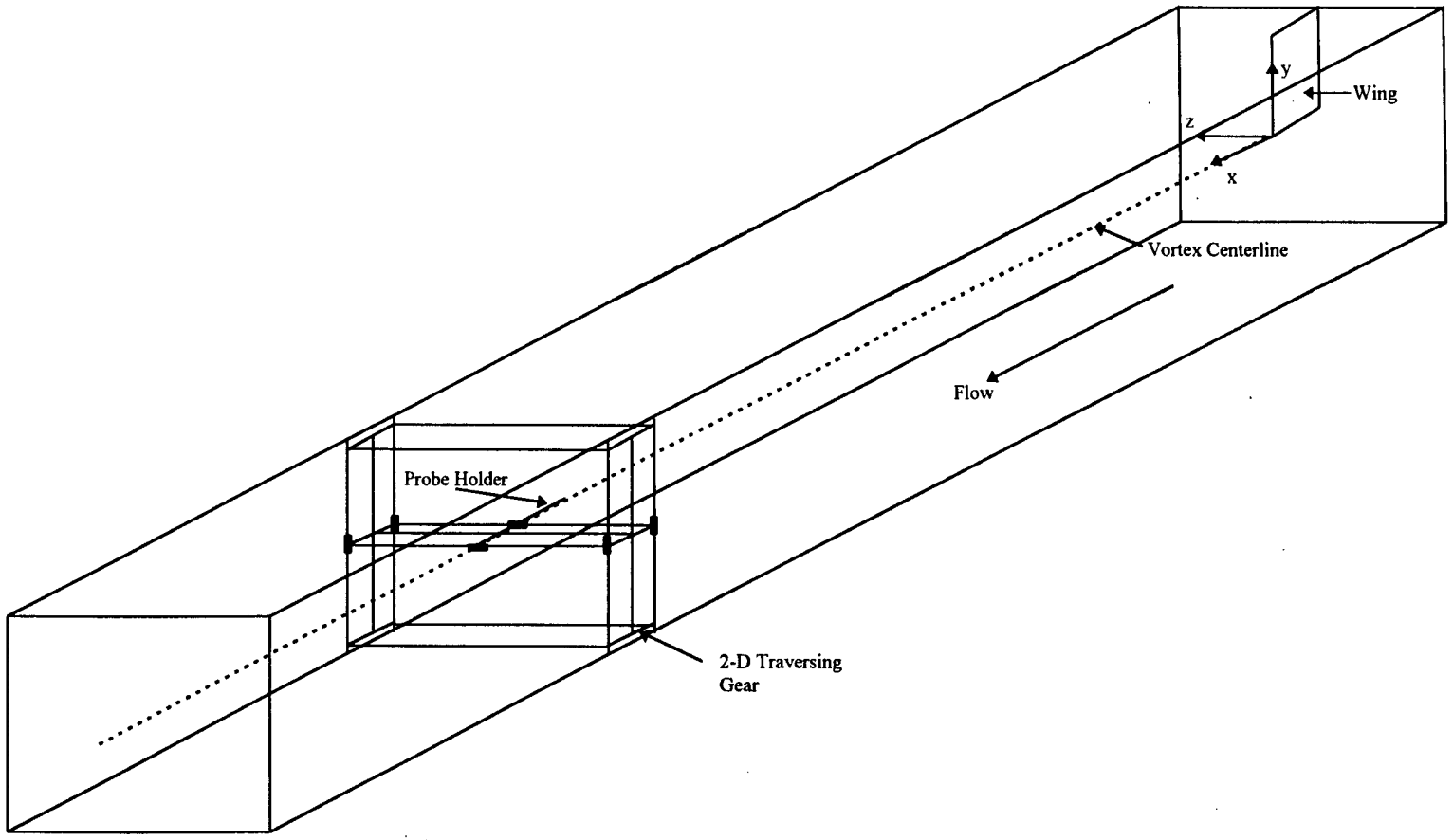

Figure 2.2 - Test section of the stability wind tunnel showing vortex generator and traverse

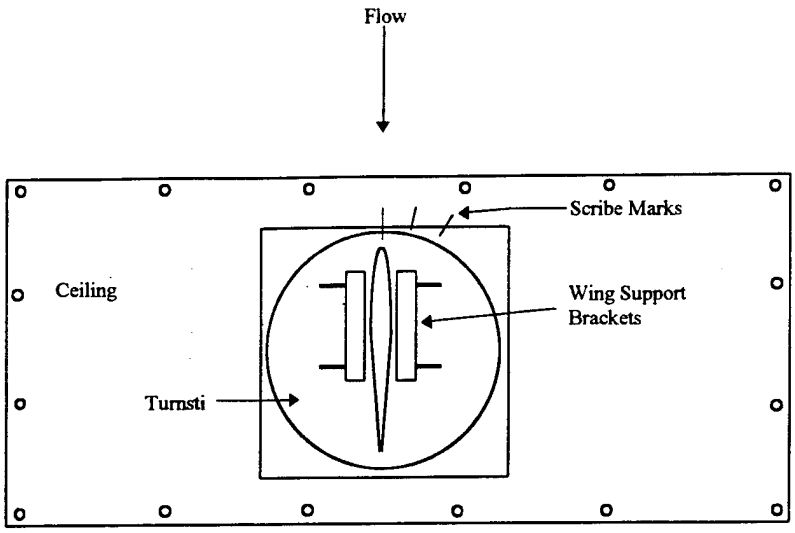

Figure 2.3 - NACA 0012 turnstile ceiling panel (top view)

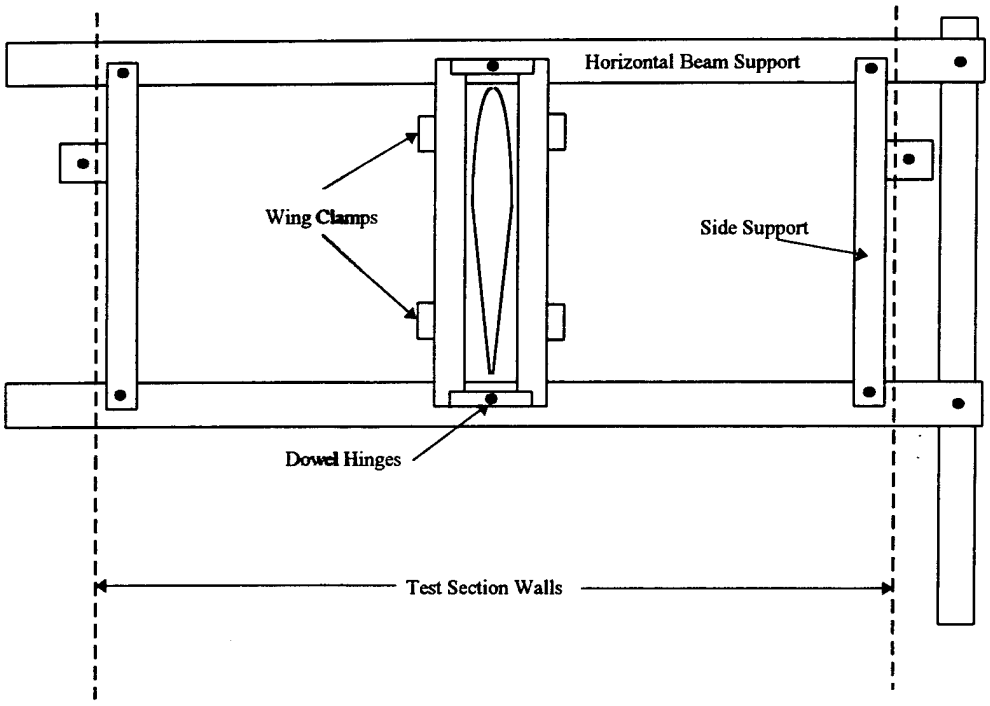

Figure 2.4 - NACA 0016 wing mount

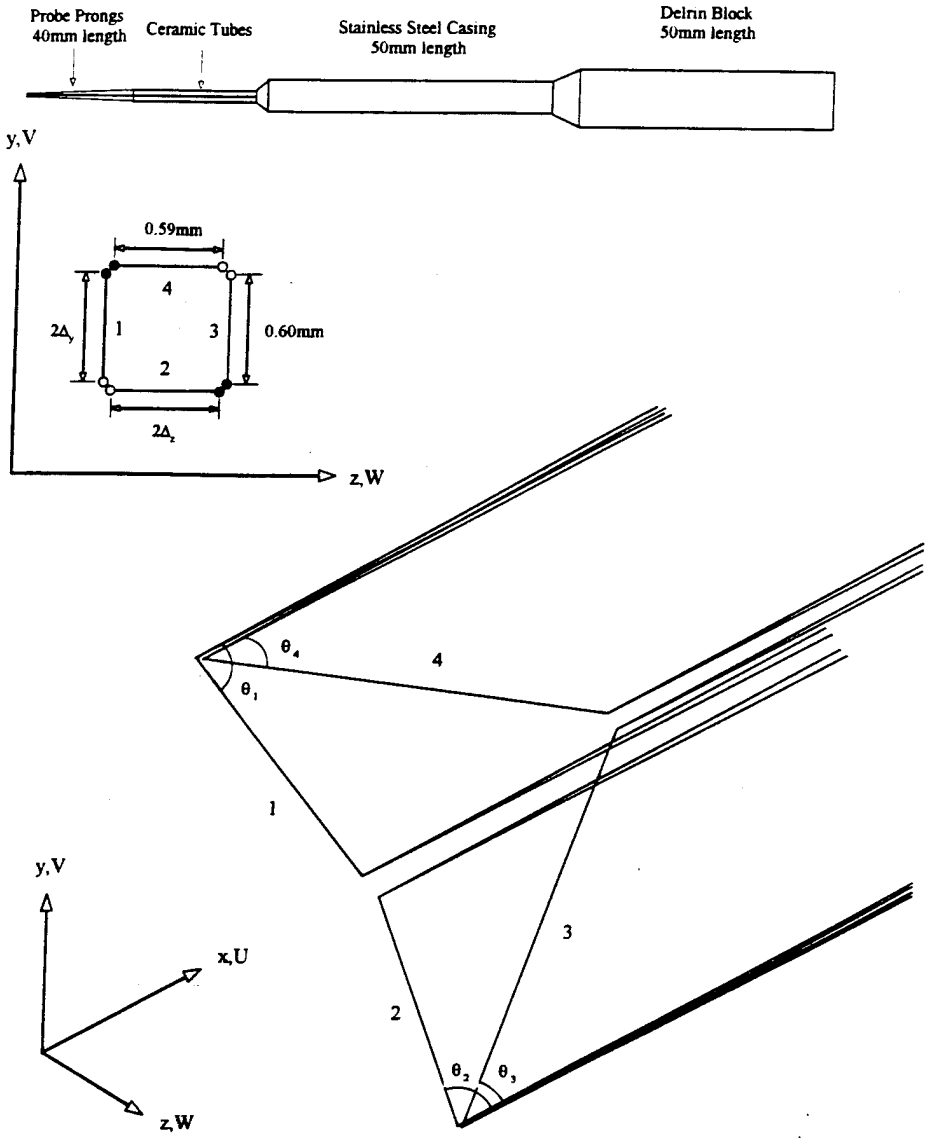

Figure 2.5 - Four sensor sub-miniature hot-wire probe

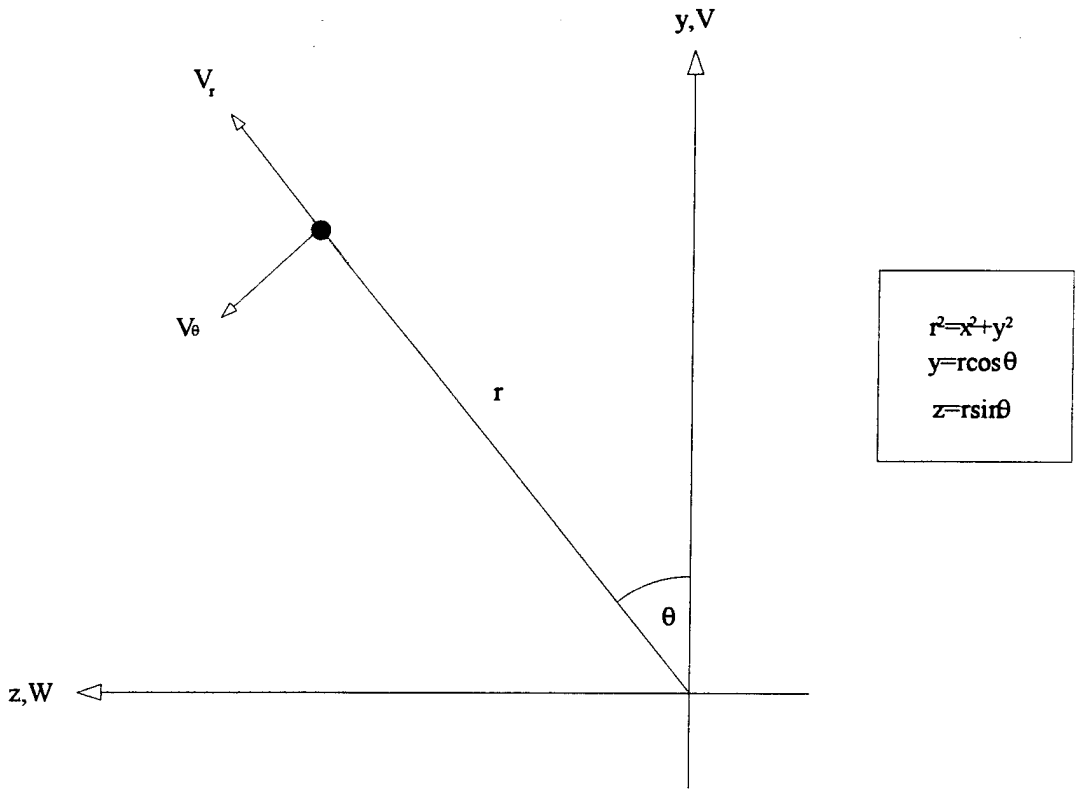

Figure 2.6 - Cartesian coordinate system used in the velocity gradient error analysis

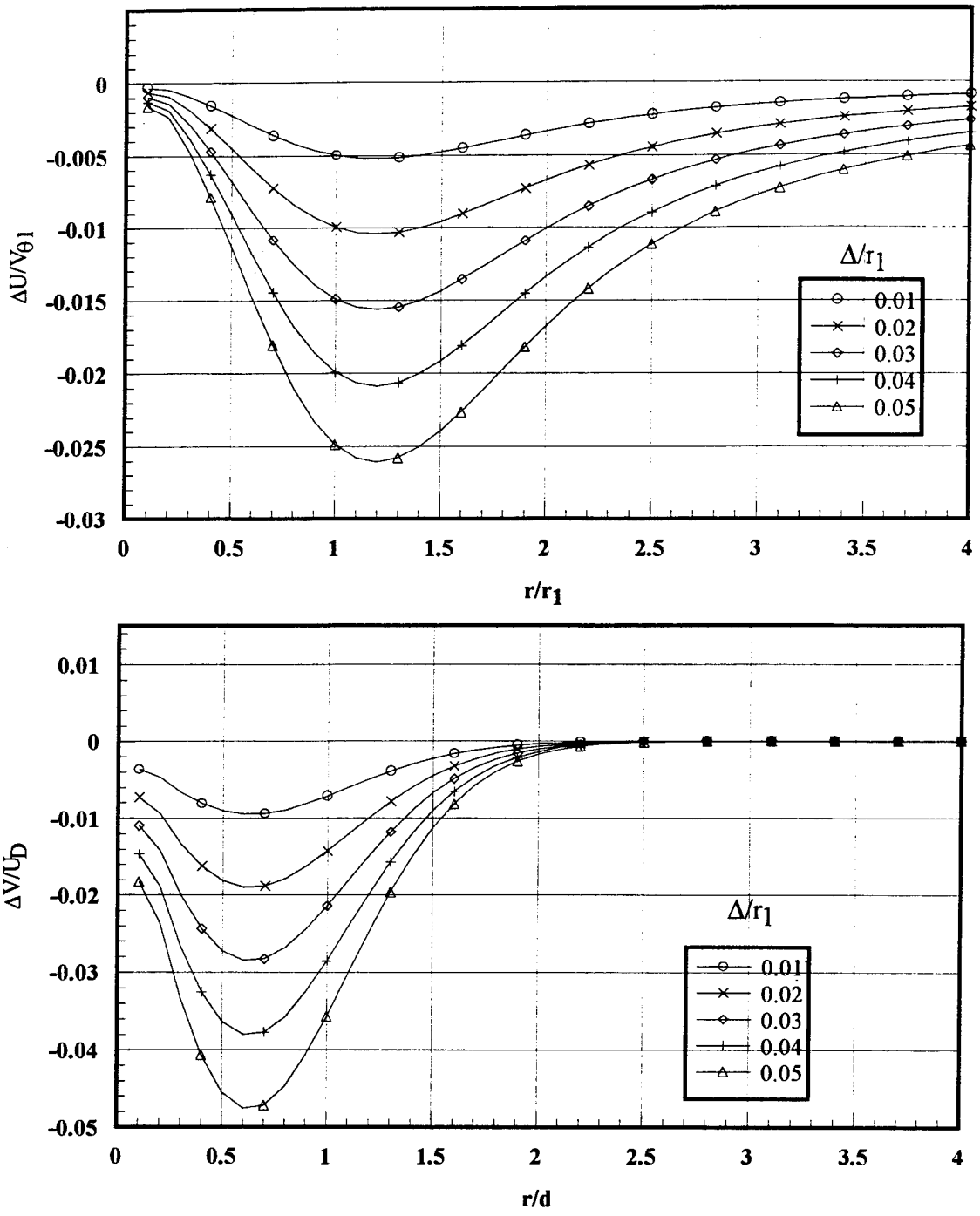

Figure 2.7 - Mean velocity corrections for an ideal probe in a q-vortex

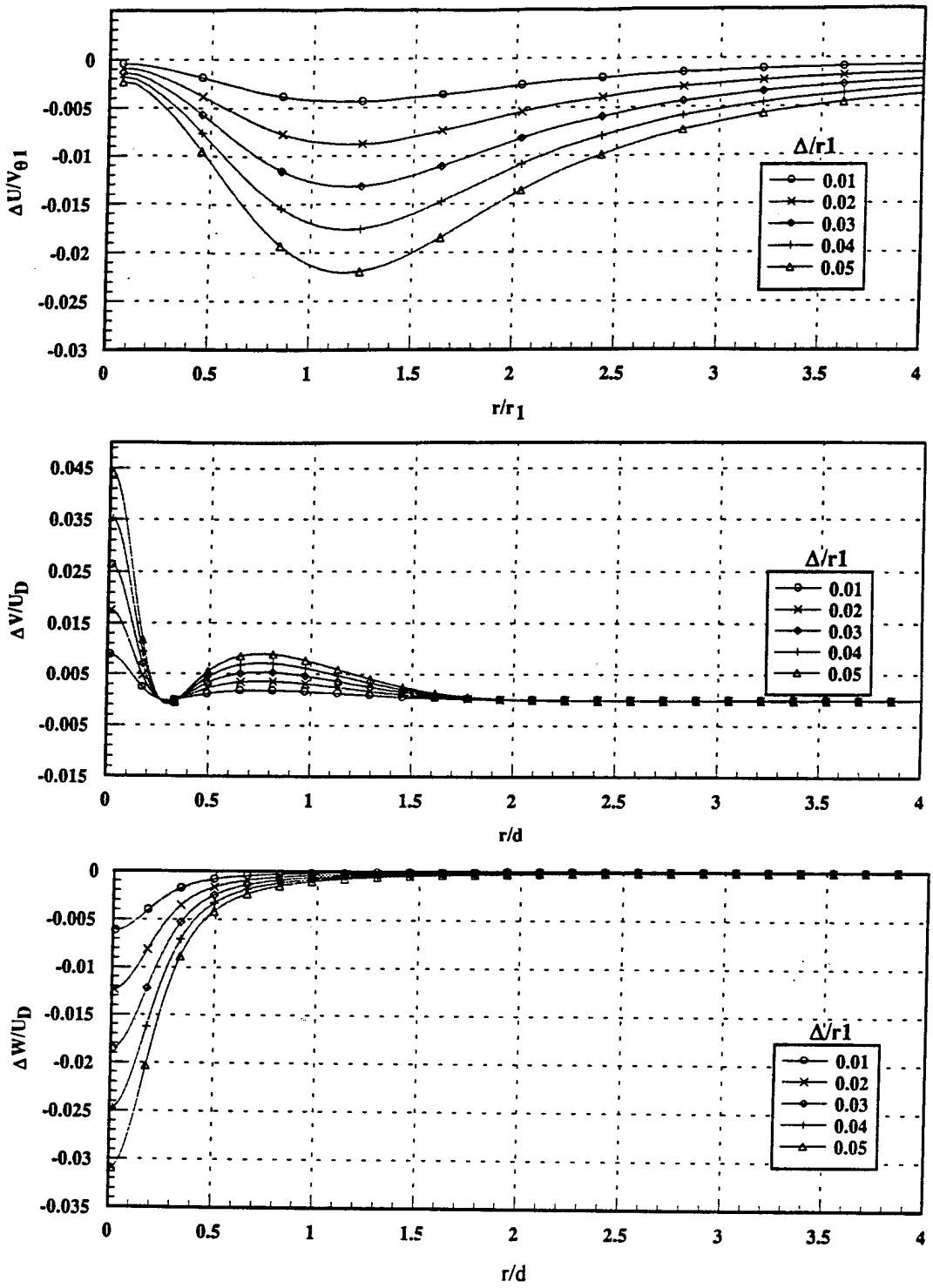

Figure 2.8 - Mean velocity corrections for a real probe in a q-vortex

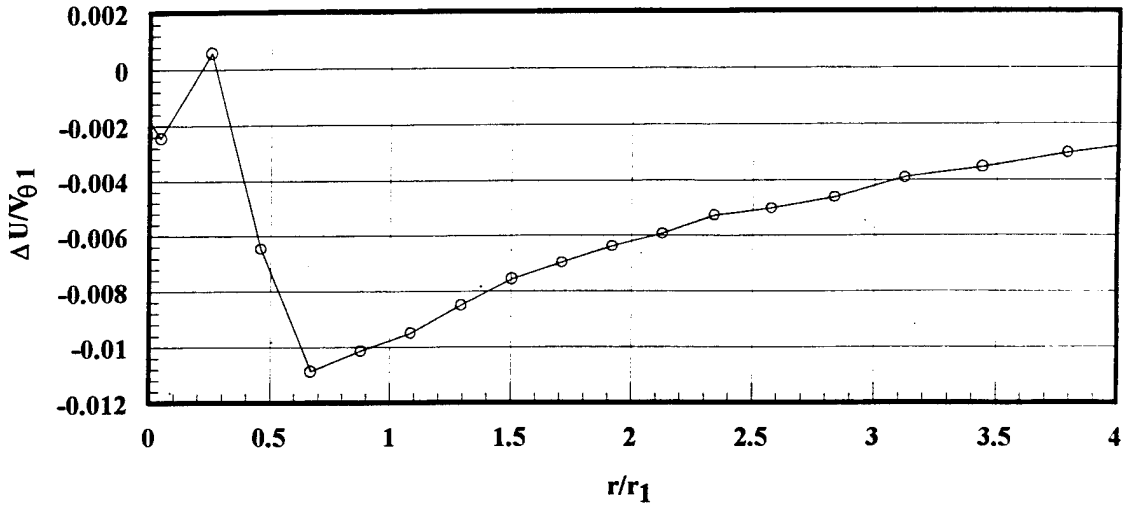

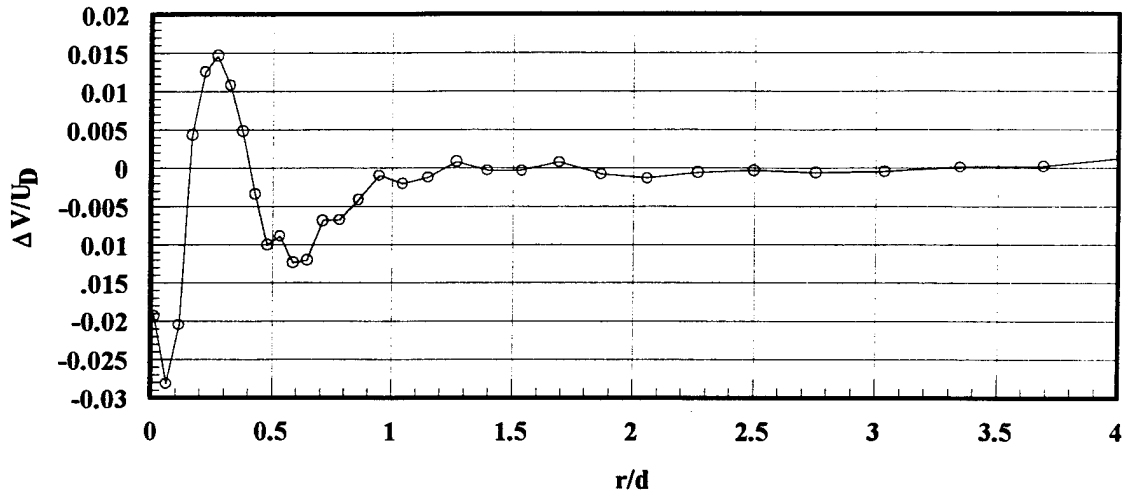

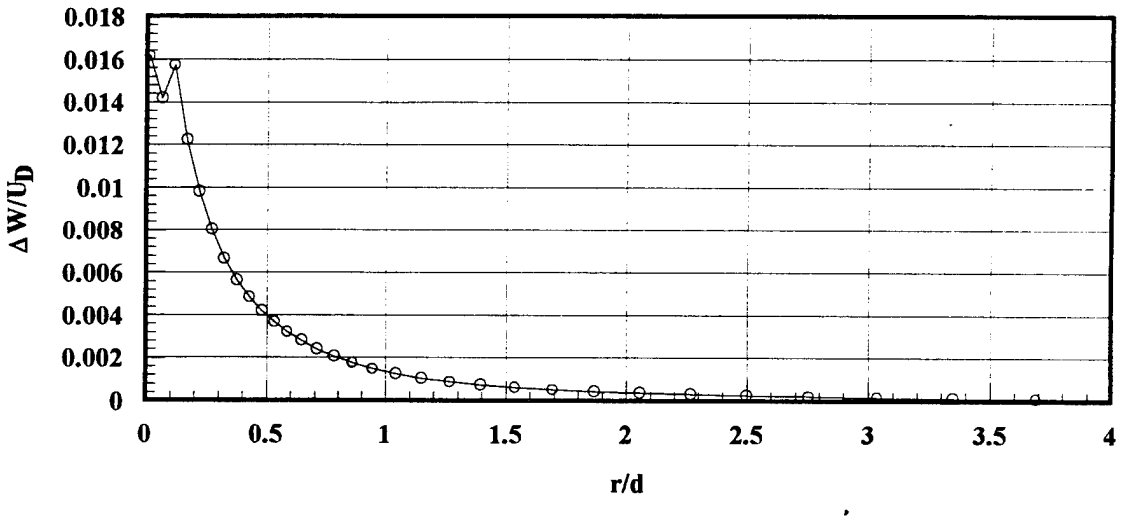

Figure 2.9 - Mean velocity corrections for a real probe in a measured vortex

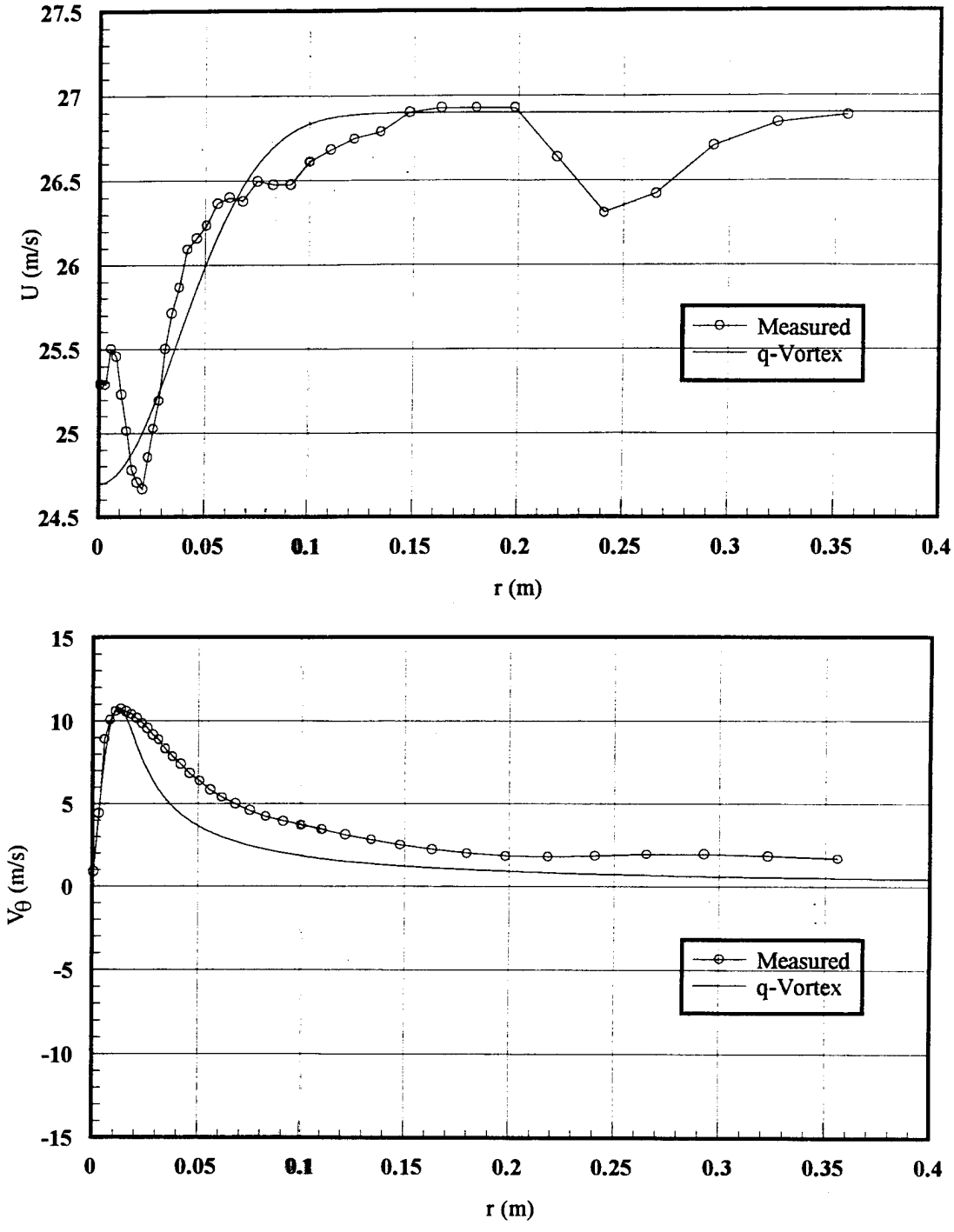

Figure 2.10 - Comparison of a measured vortex to the q-vortex model

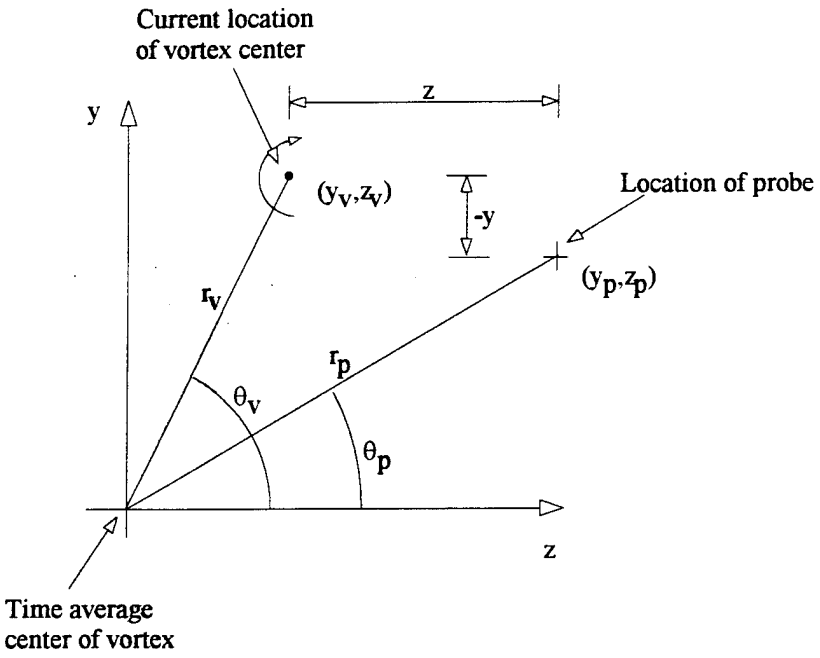

Figure 2.11 - Wandering correction procedure coordinate system and terminology

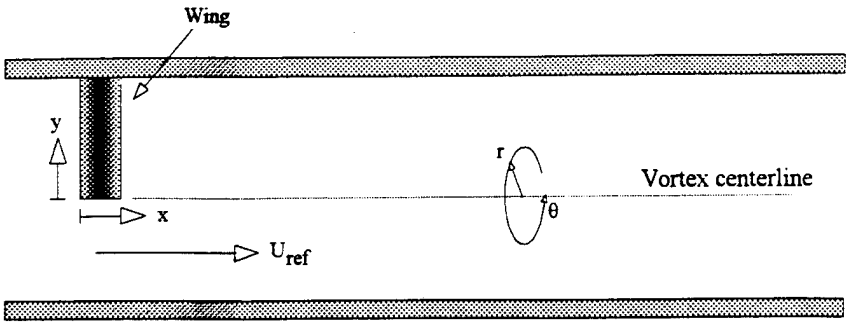

Figure 3.1 - Vortex coordinate system

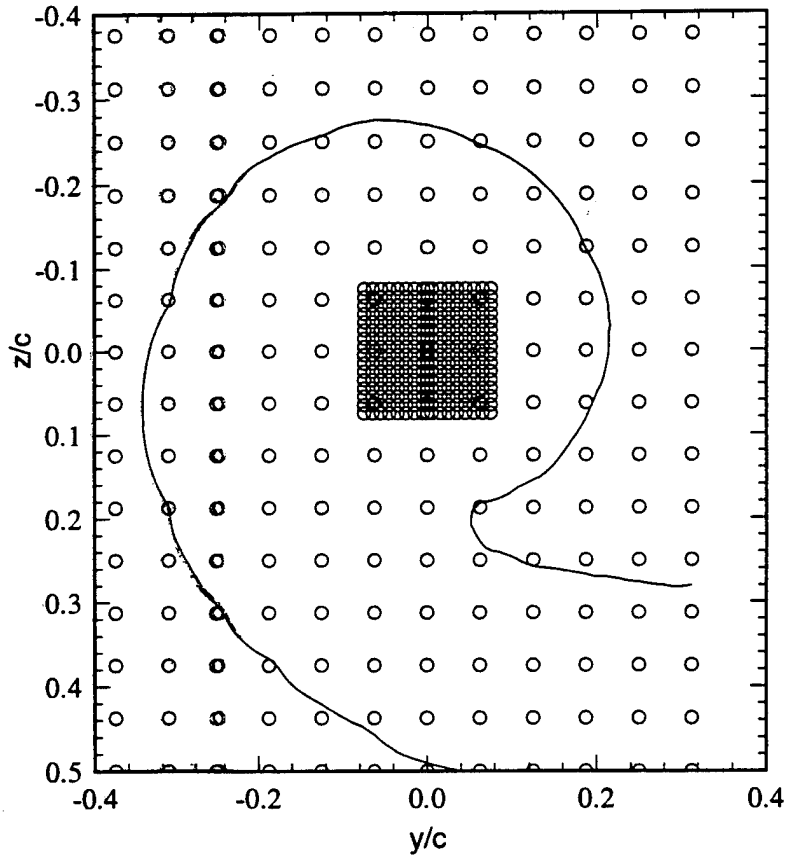

Figure 3.2 - Measurement grid for NACA 0012 wing, x/c=10, Re=530,000

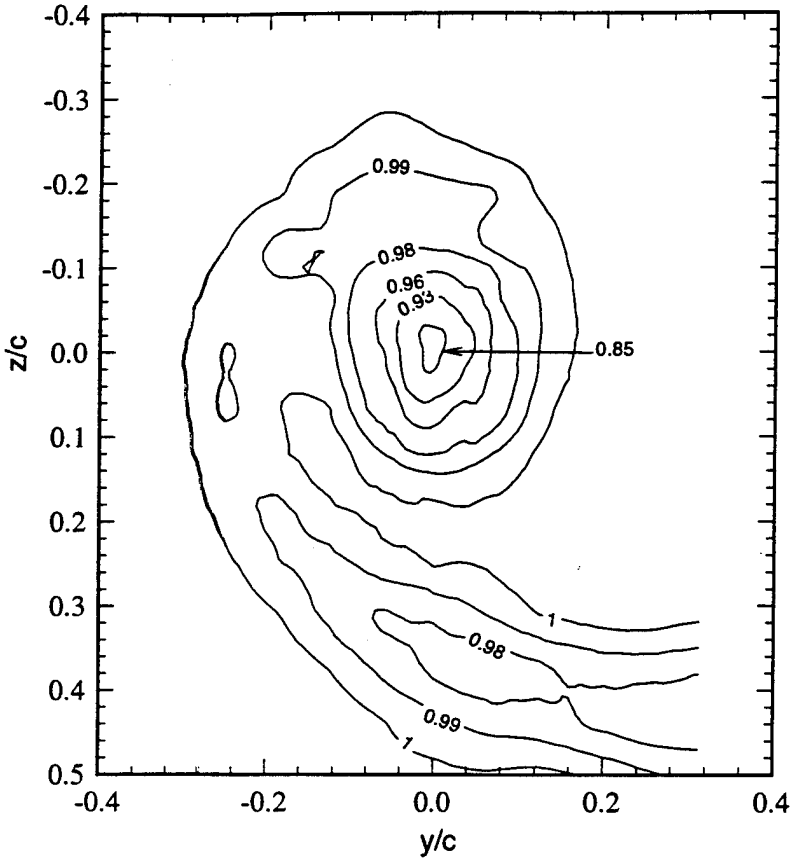

Figure 3.3 - Contours of axial velocity, NACA 0012, x/c=10, Re=530,000

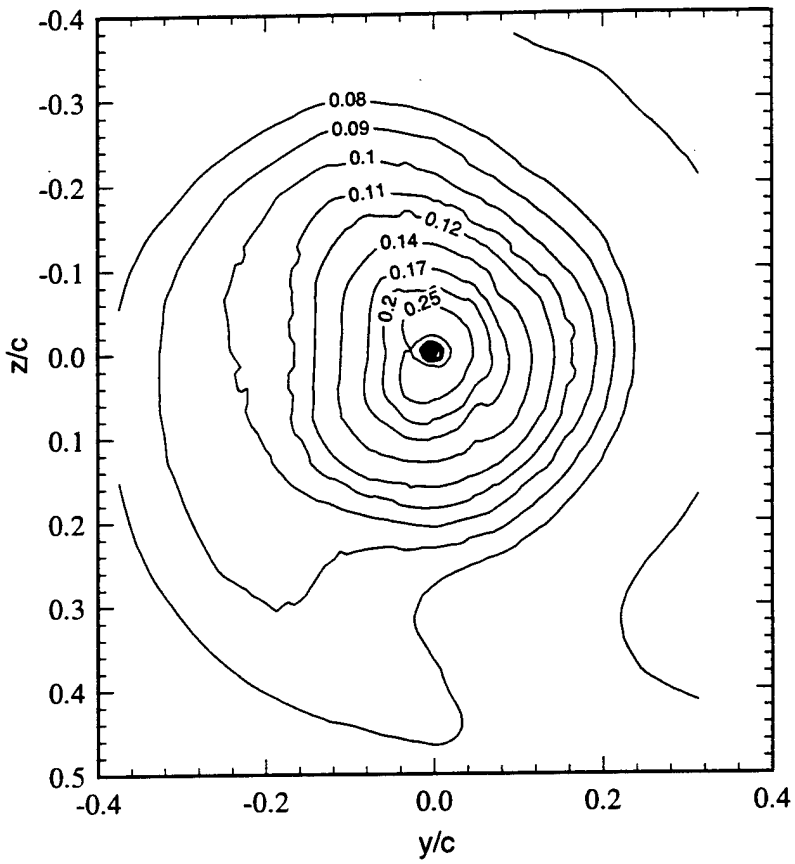

Figure 3.4 - Contours of tangential velocity, NACA 0012, x/c=10, Re=530,000

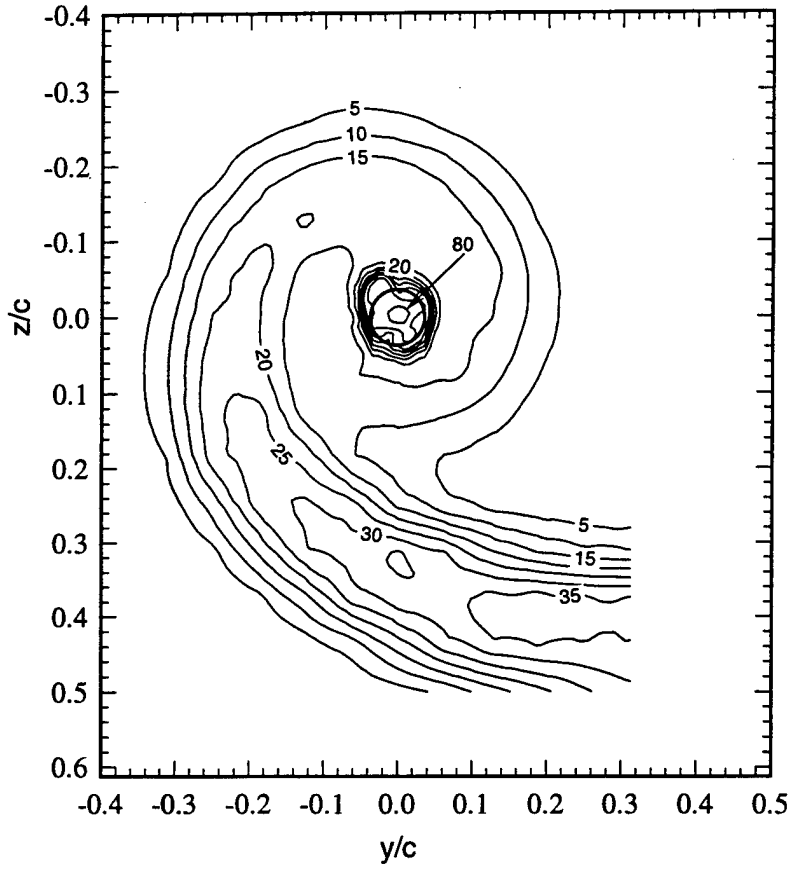

Figure 3.5 - Contours of axial normal stress, NACA 0012, x/c=10, Re=530,000. Levels multiplied by 10^5.

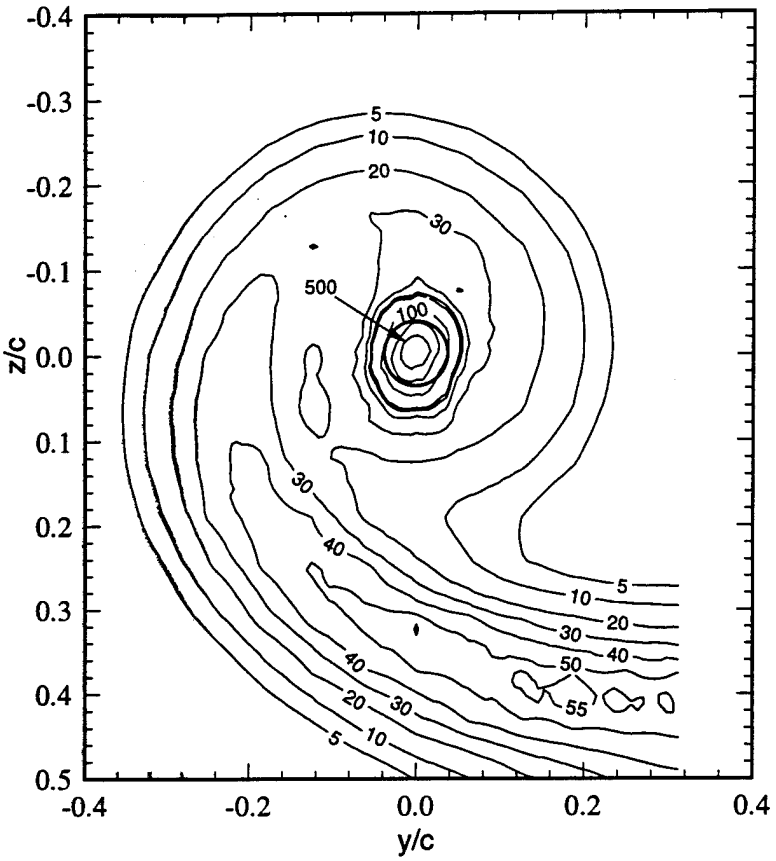

Figure 3.6 - Contours of turbulence kinetic energy, NACA 0012, x/c=10, Re=530,000. Levels multiplied by 10^5.

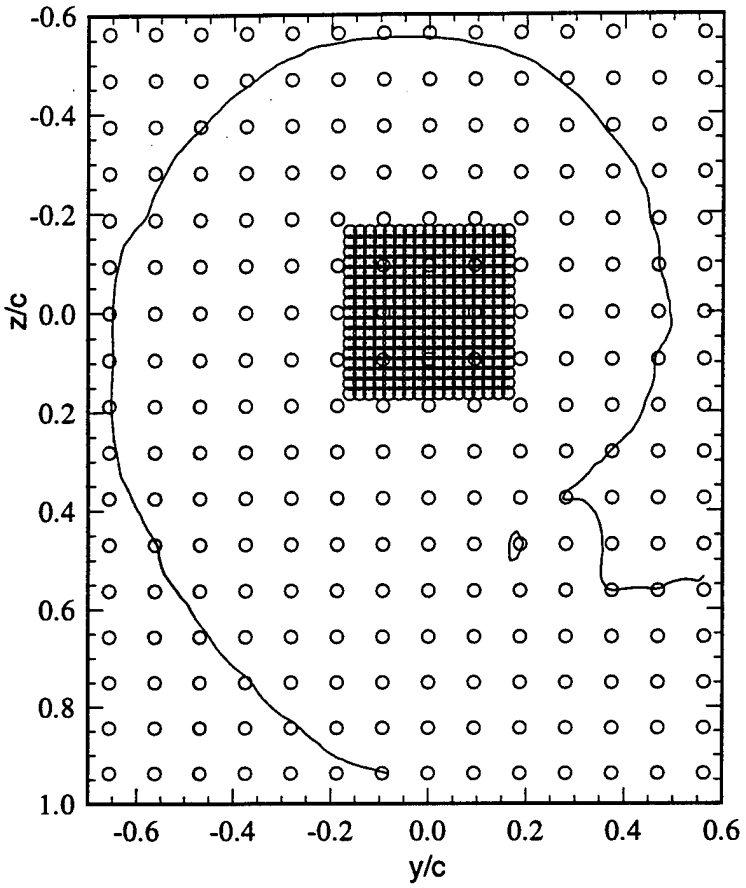

Figure 3.7 - Measurement grid for NACA 0012 wing, x/c=30, Re=530,000.

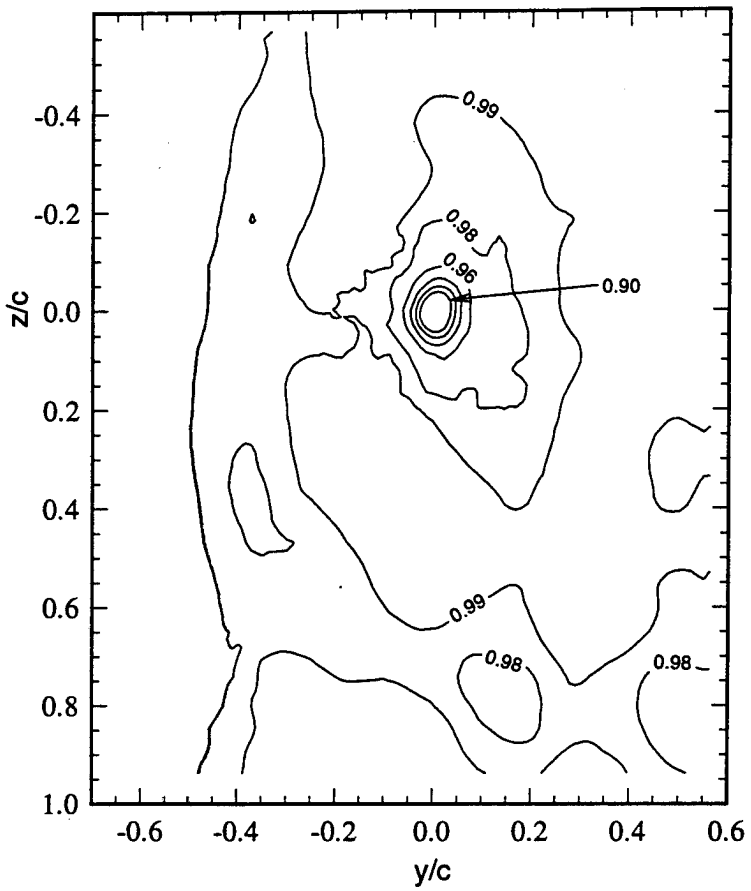

Figure 3.8 - Contours of axial velocity, NACA 0012, x/c=30, Re=530,000.

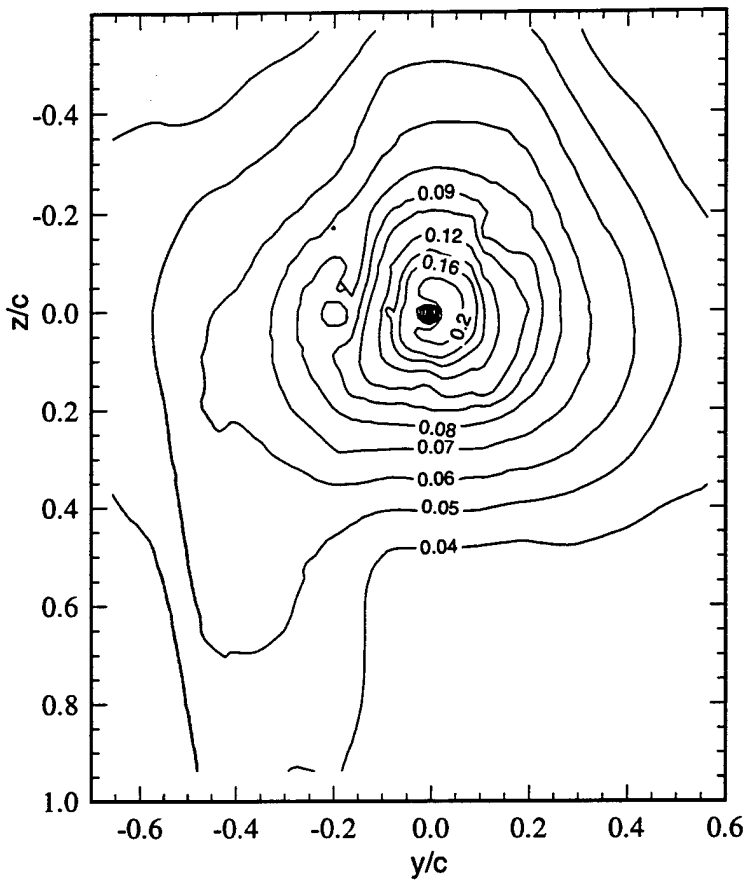

Figure 3.9 - Contours of tangential velocity, NACA 0012, x/c=30, Re=530,000.

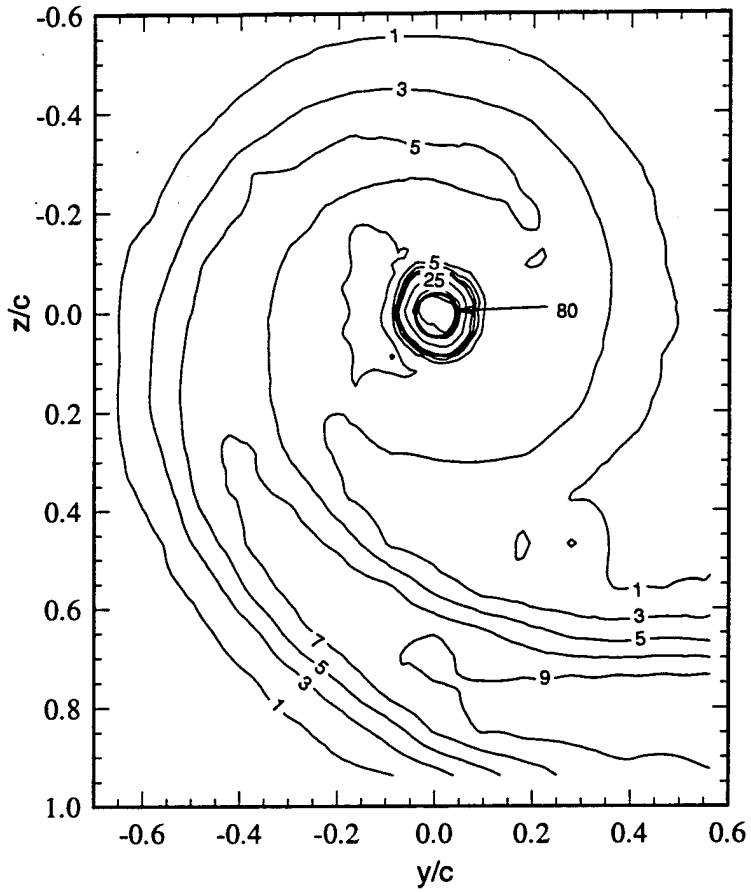

Figure 3.10 - Contours of axial normal stress, NACA 0012, x/c=30, Re=530,000. Levels multiplied by 10^5.

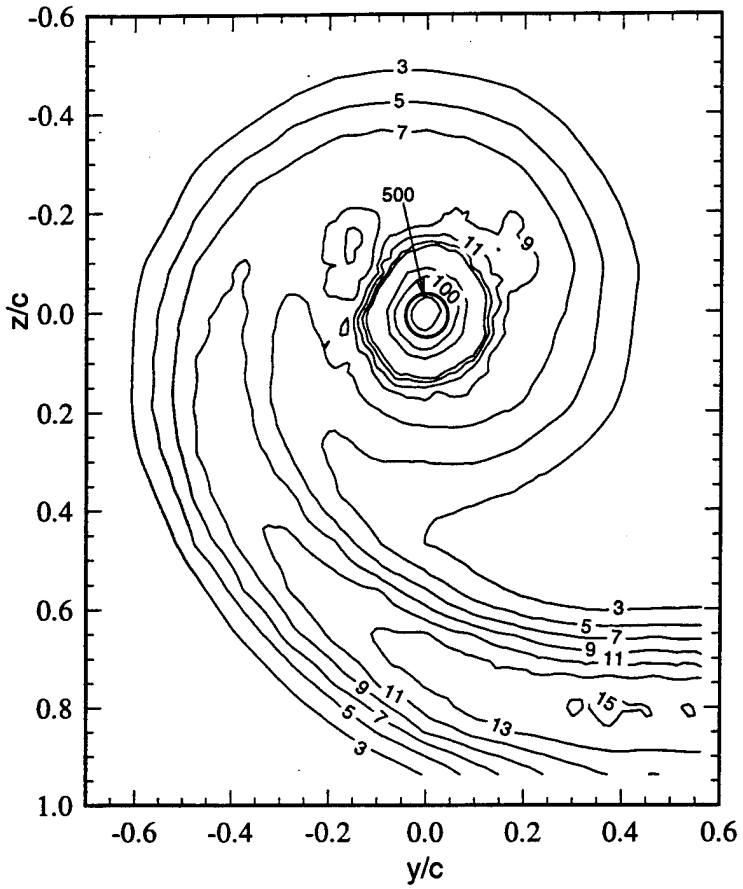

Figure 3.11 - Contours of turbulence kinetic energy, NACA 0012, x/c=30, Re=530,000. Levels multiplied by 10^5.

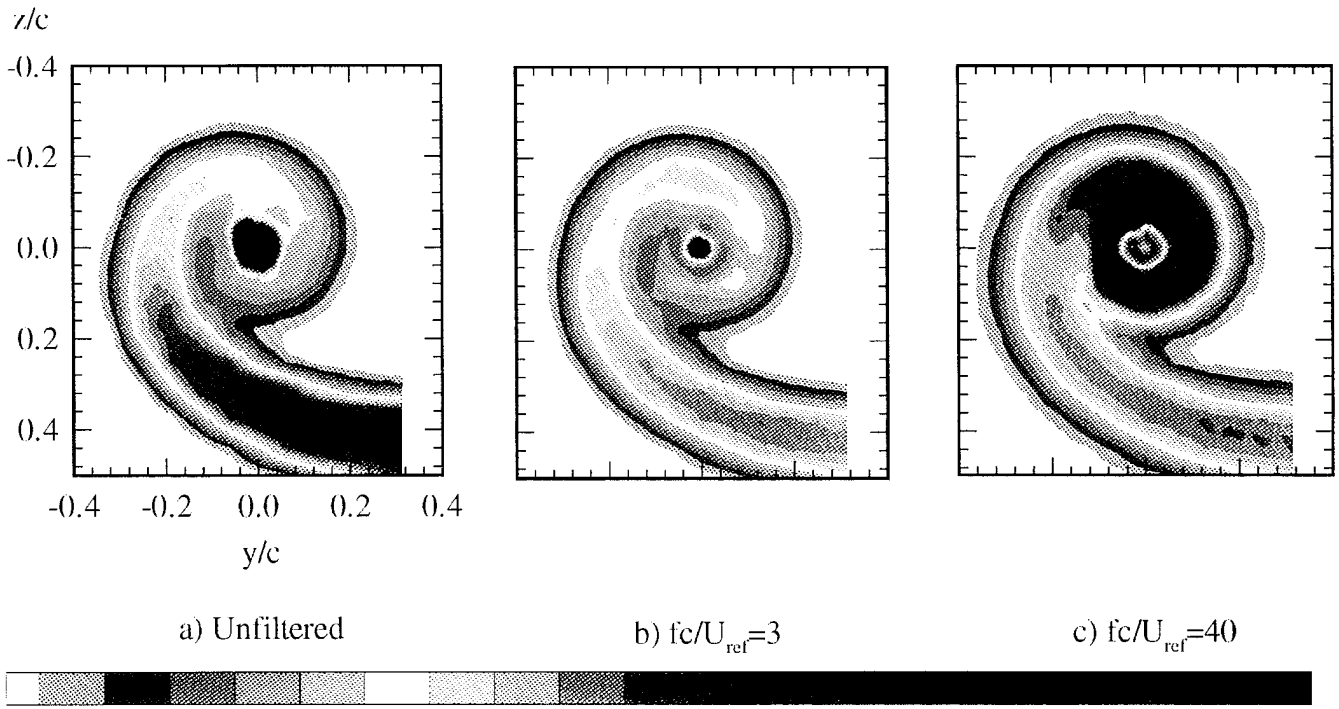

Figure 3.12 - Comparison of high-pass filtered axial normal stress contours, NACA 0012, x/c=10, Re=530,000.

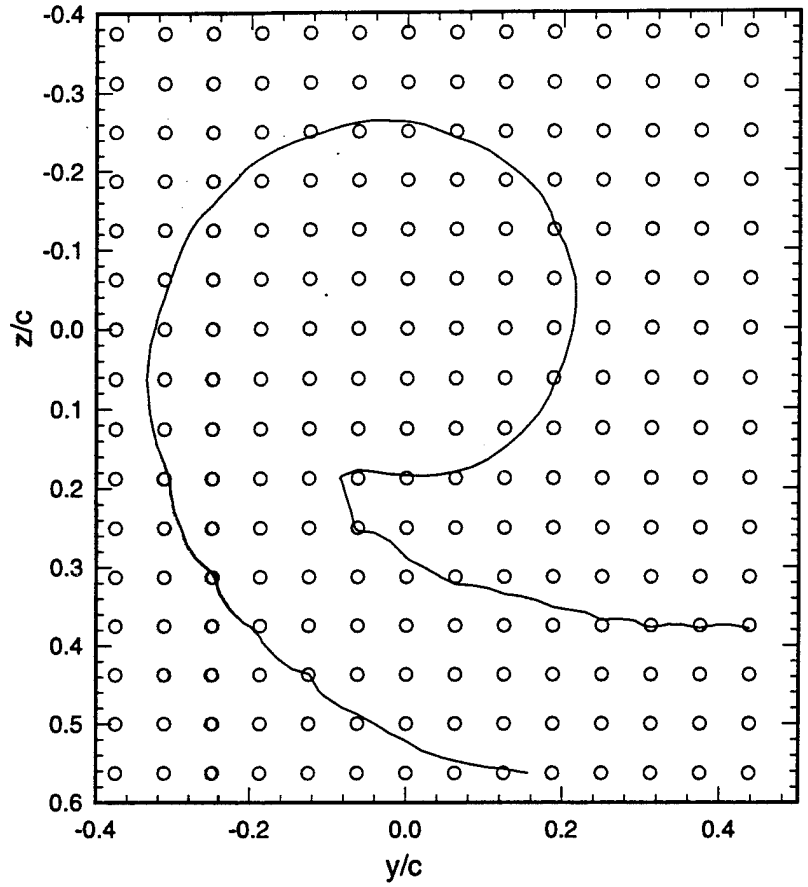

Figure 3.13 - Measurement grid for NACA 0016 wing, x/c=10, Re=1,825,000.

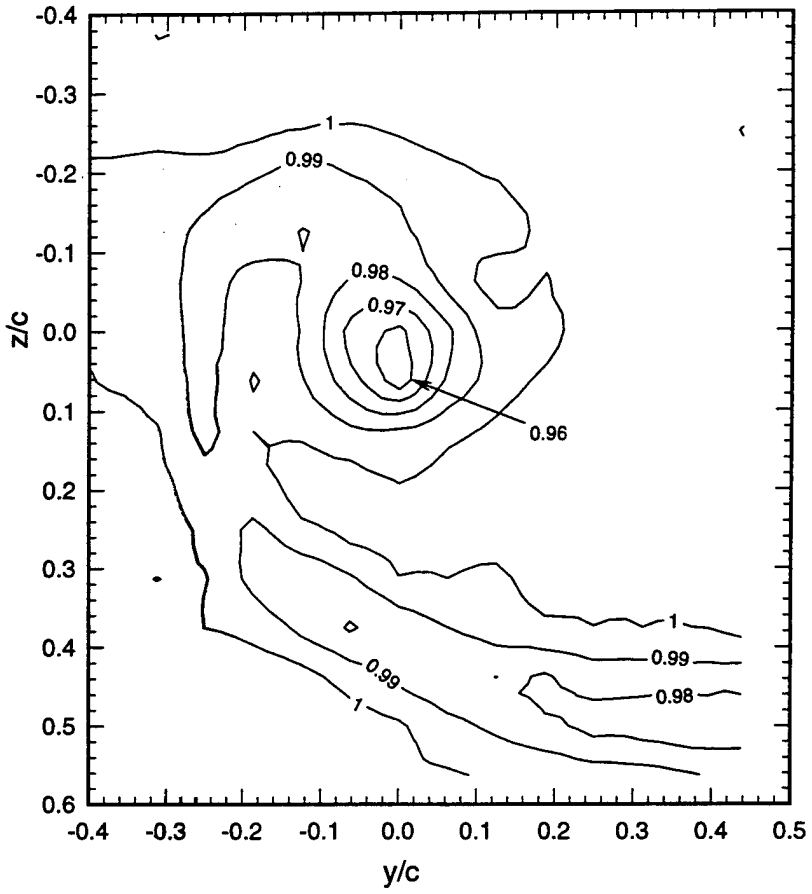

Figure 3.14 - Contours of axial velocity, NACA 0016 wing, x/c=10, Re=1,825,000.

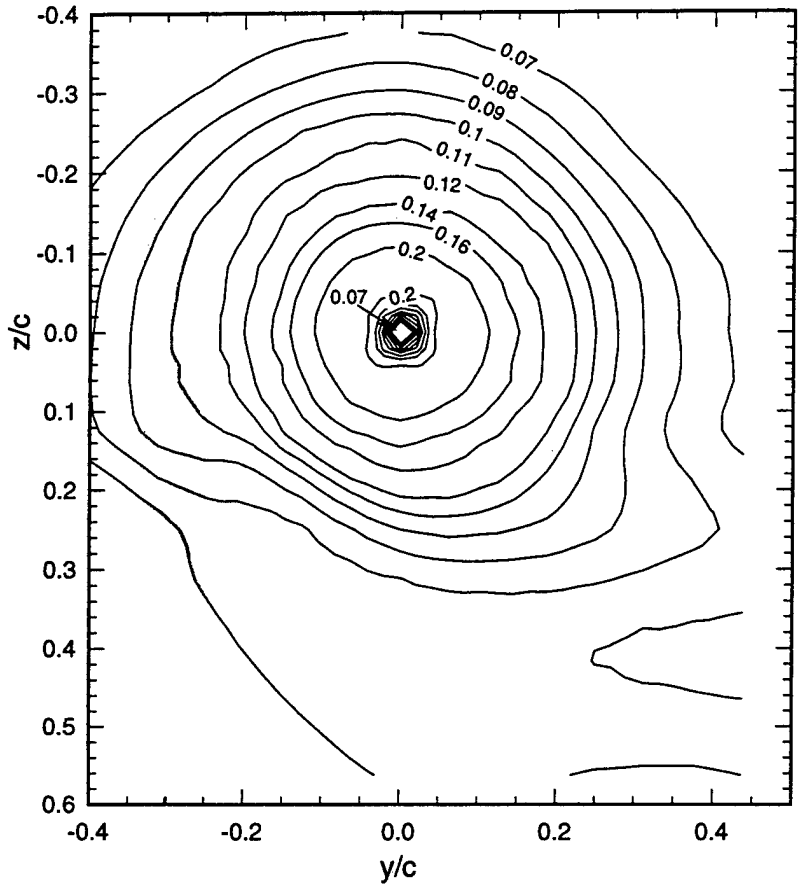

Figure 3.15 - Contours of cross-stream velocity magnitude, NACA 0016 wing, x/c=10, Re=1,825,000.

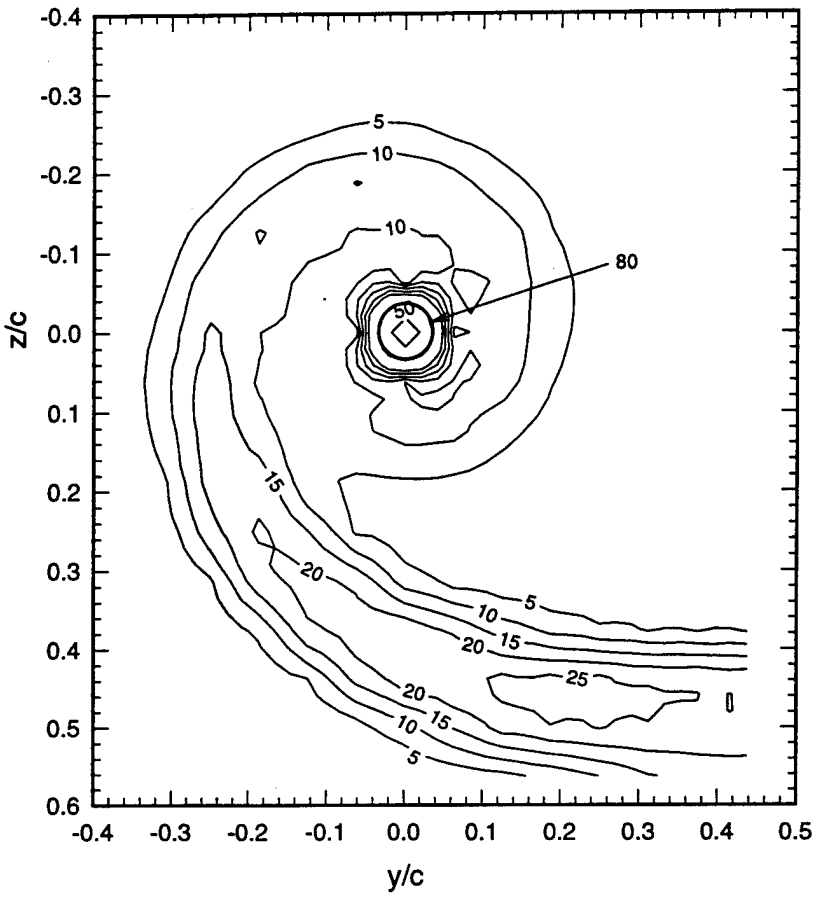

Figure 3.16 - Contours of axial normal stress, NACA 0016, x/c=10, Re=1,825,000. Levels multiplied by 10^5.

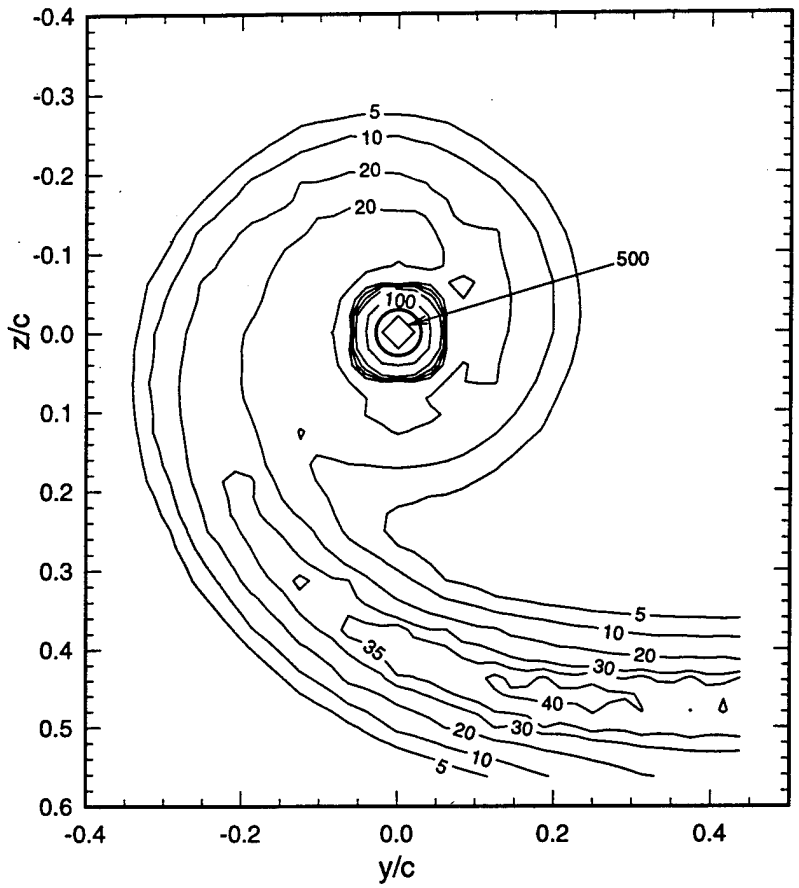

Figure 3.17 - Contours of turbulence kinetic energy, NACA 0016, x/c=10, Re=1,825,000. Levels multiplied by 10^5.

a) Re=530,000
α= 5°, x/c=10

b) Re=1,000,000
α= 5°, x/c=10

c) Re=1,600,000
α= 5°, x/c=10

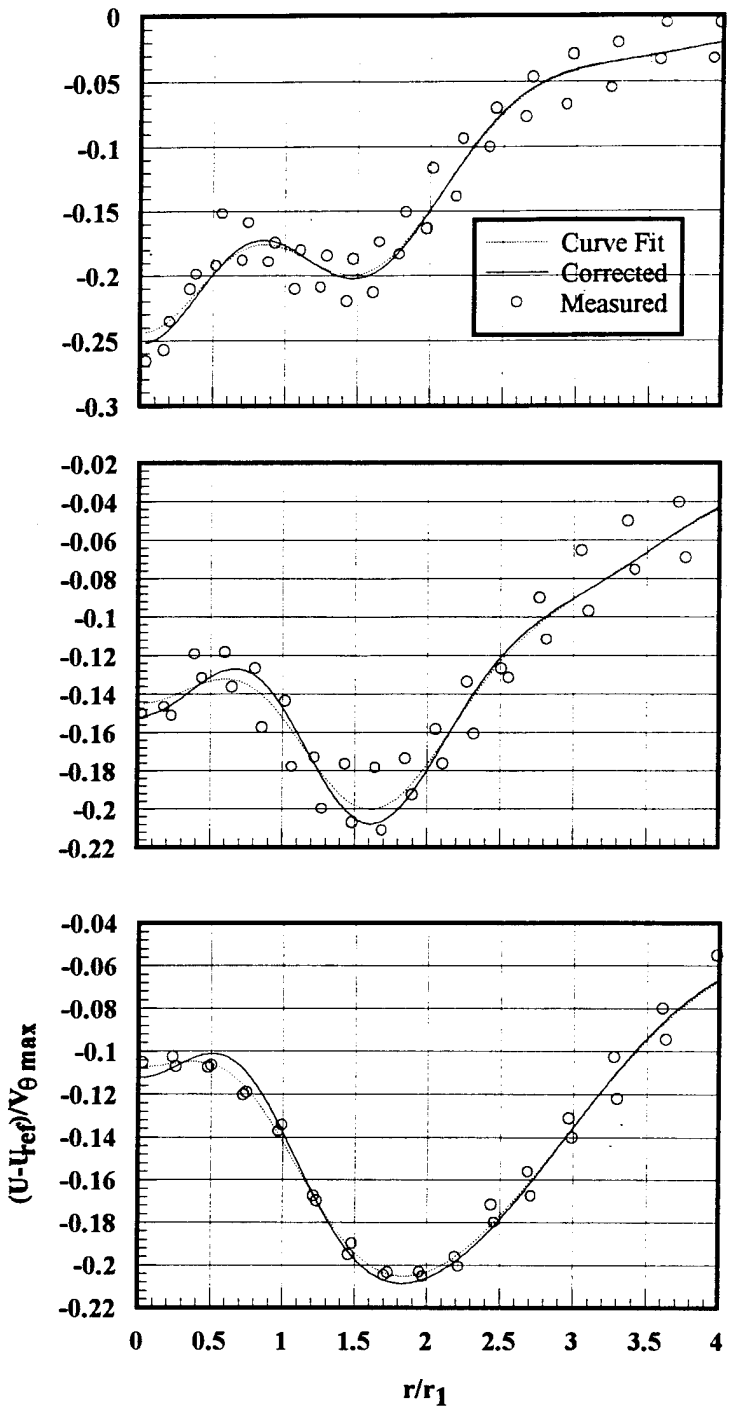

Figure 3.18 - Measured, curve fit, and corrected for wandering axial velocity profiles

d) Re=1,600,000
α=5°, x/c=7.5

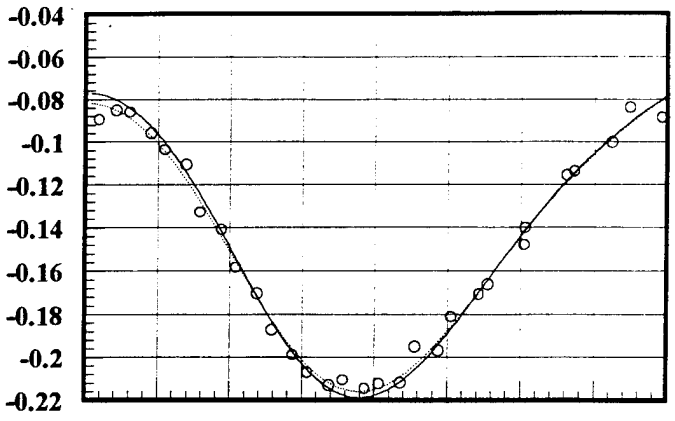

e) Re=1,600,000
α=5°, x/c=5

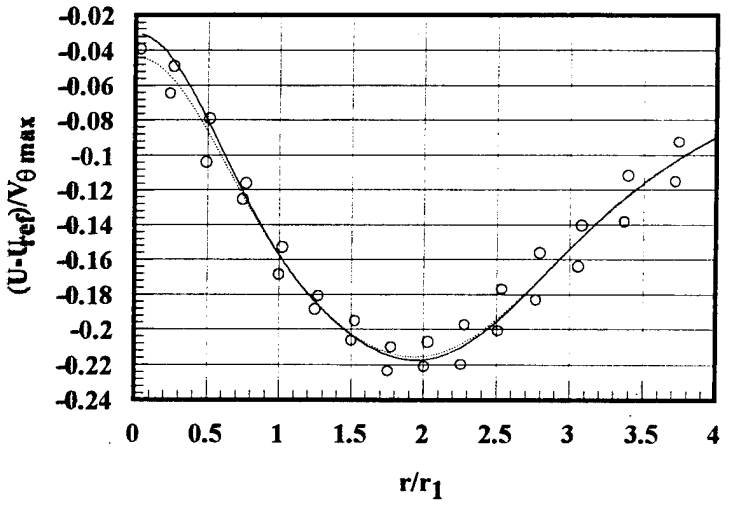

Figure 3.18 (cont'd) - Measured, curve fit, and corrected for wandering axial velocity profiles

a) Re=530,000
α=5°, x/c=10

b) Re=1,000,000
α=5°, x/c=10

c) Re=1,600,000
α=5°, x/c=10

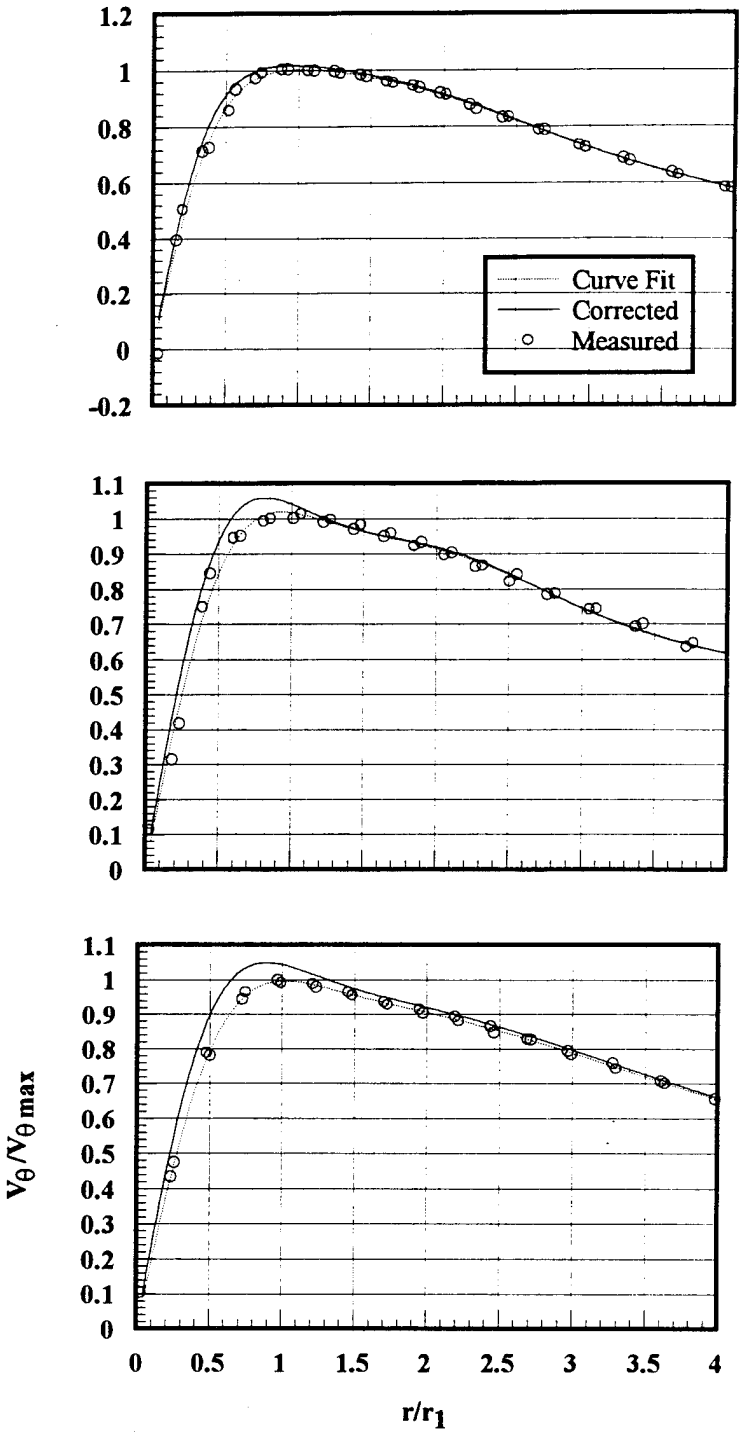

Figure 3.19 - Measured, curve fit, and corrected for wandering tangential velocity profiles

d) Re=1,600,000
α=5°, x/c=7.5

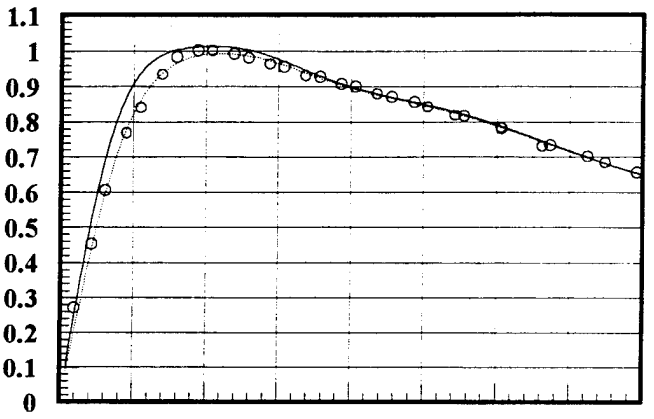

e) Re=1,600,000
α=5°, x/c=5

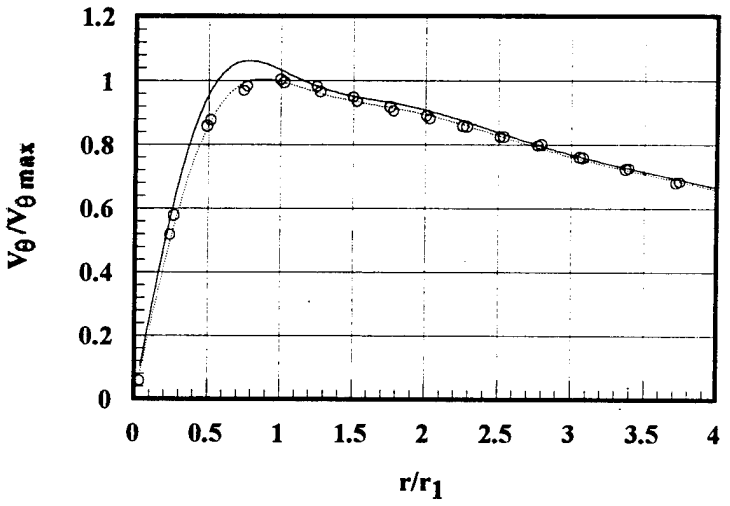

Figure 3.19 (cont'd) - Measured, curve fit, and corrected for wandering tangential velocity profiles

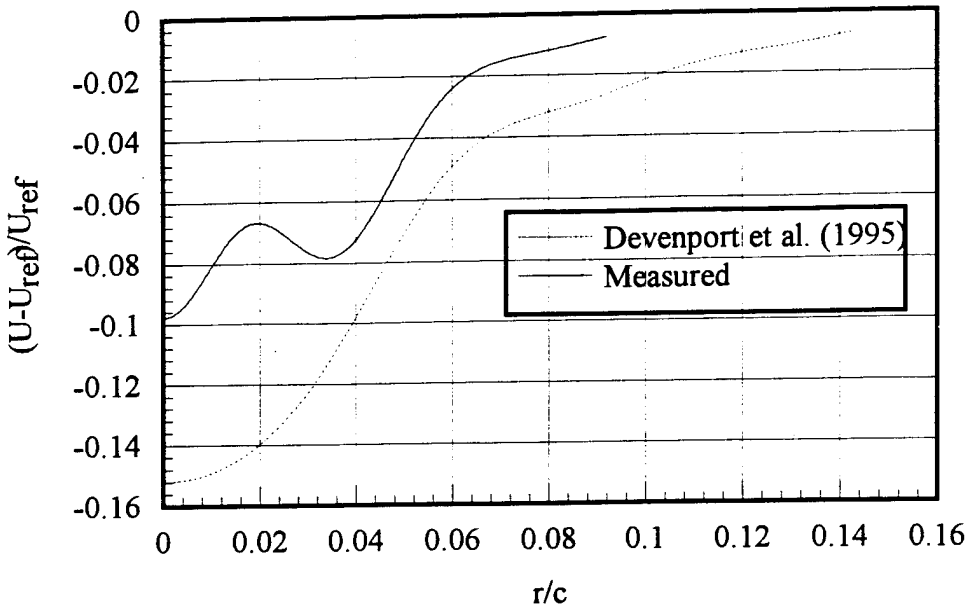

a) axial velocity deficit

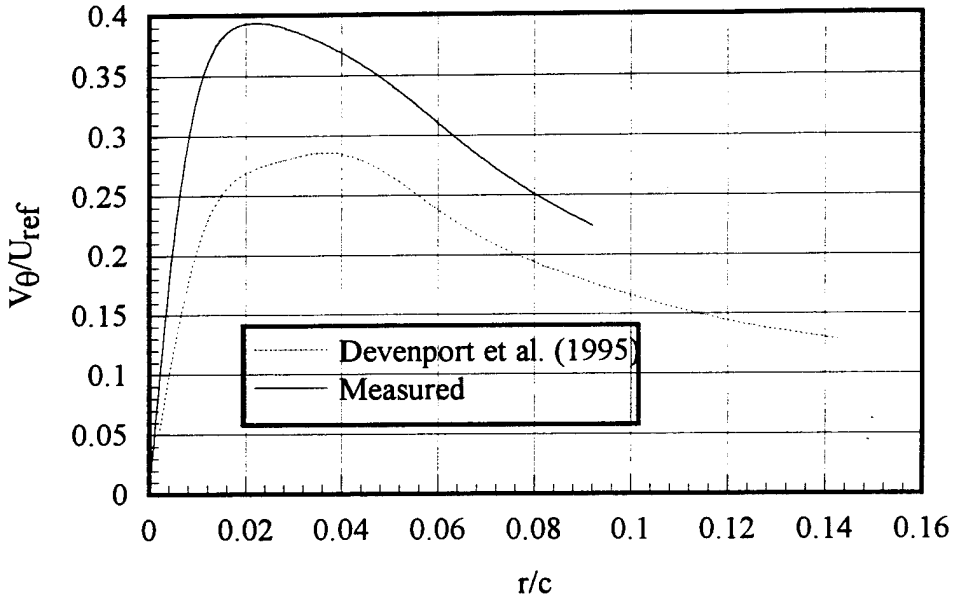

b) tangential velocity

Figure 3.20 - Comparison of axial and tangential velocity profiles measured in the present experiment to those presented by Devenport et al. (1995).

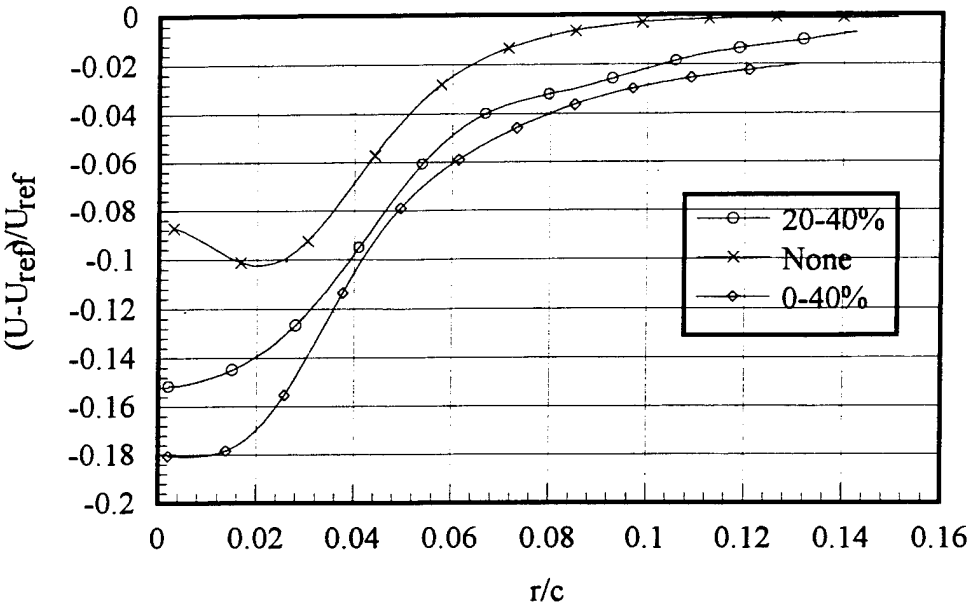

Figure 3.21 - Axial velocity distributions for various trip strips

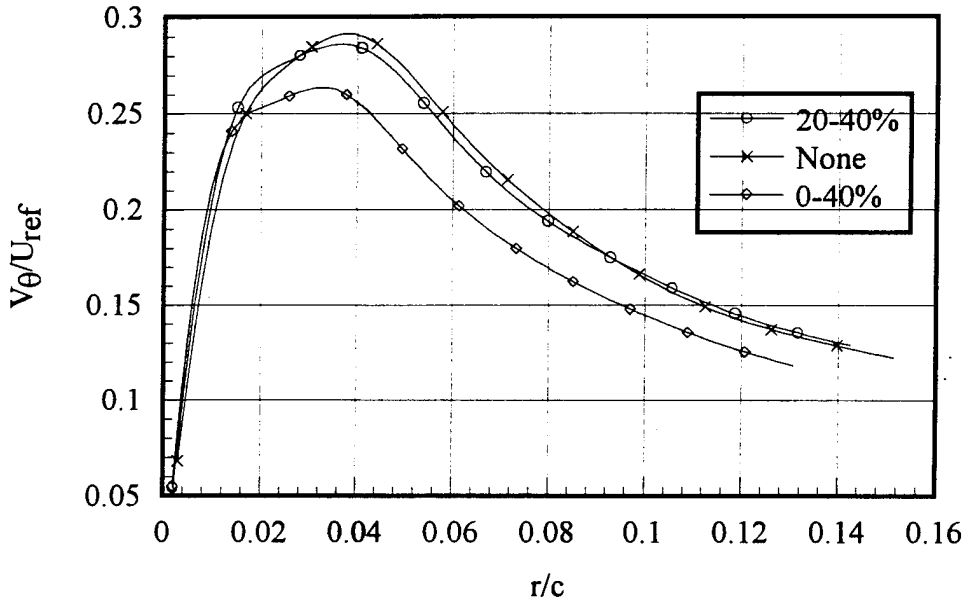

Figure 3.22 - Tangential velocity distributions for various trip strips

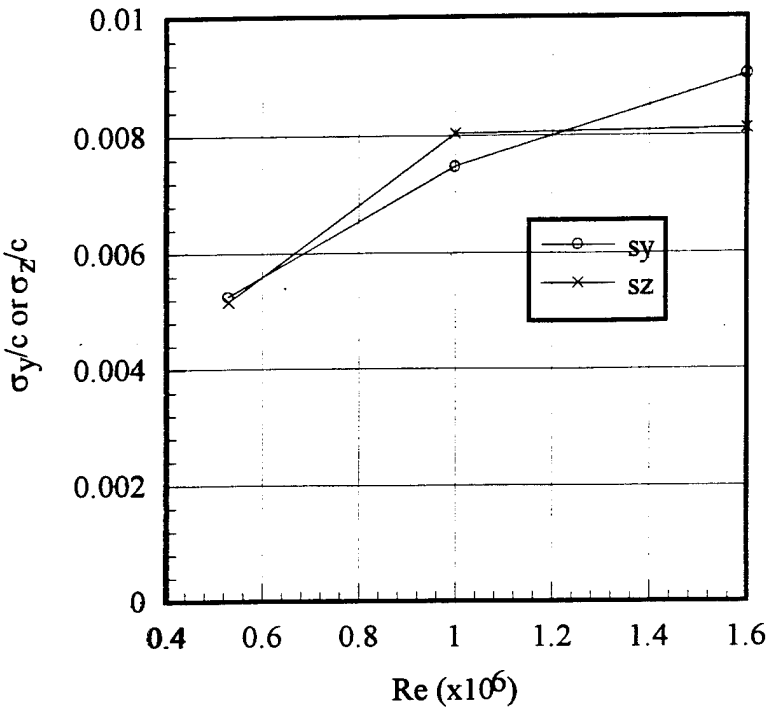

Figure 3.23 - Wandering amplitude as a function of Reynolds number

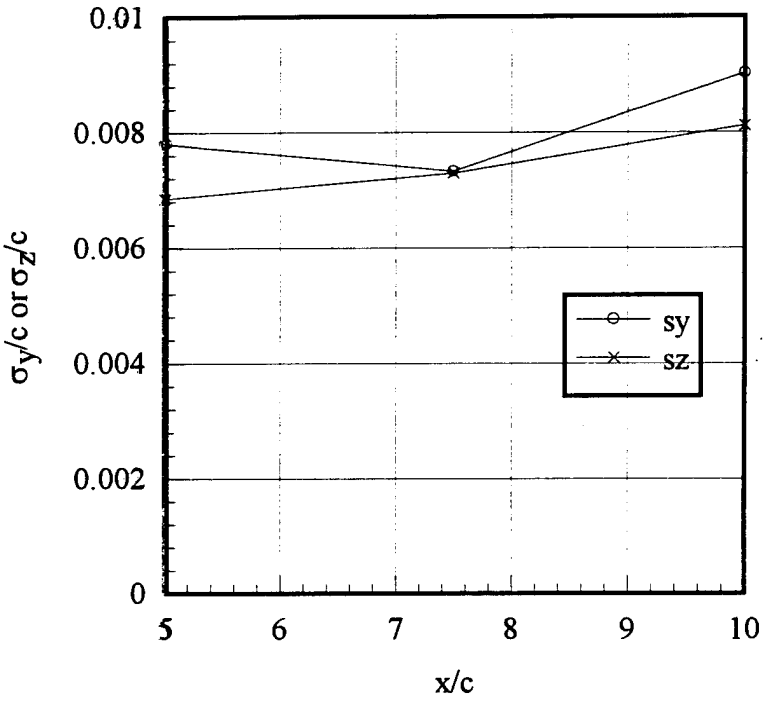

Figure 3.24 - Wandering amplitude as a function of distance downstream

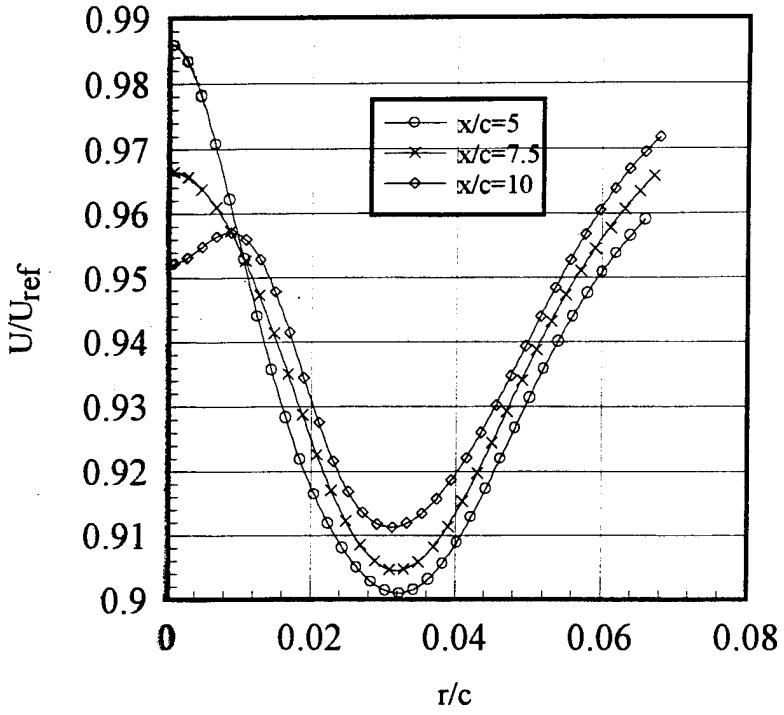

Figure 3.25 - Axial velocity profiles as a function of distance downstream

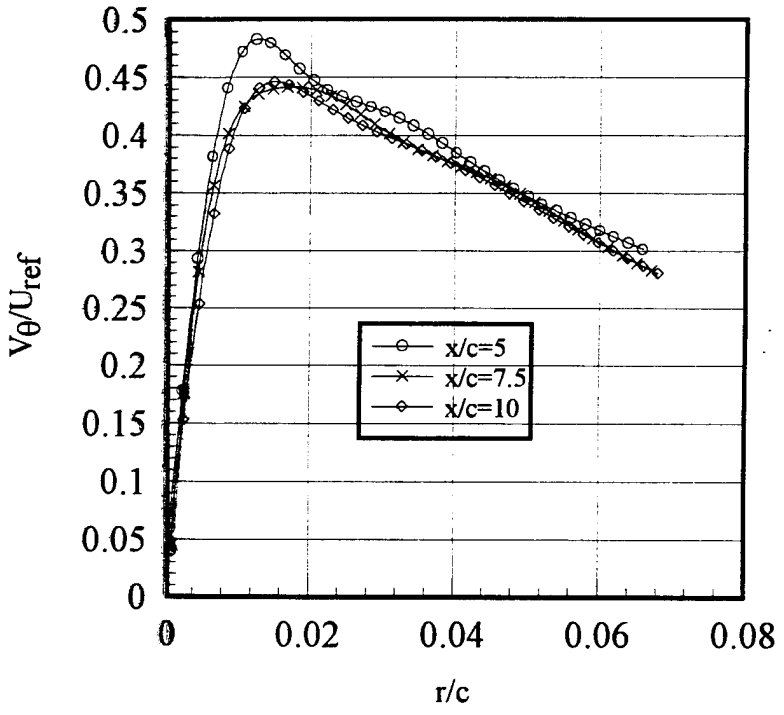

Figure 3.26 - Tangential velocity profiles as a function of distance downstream

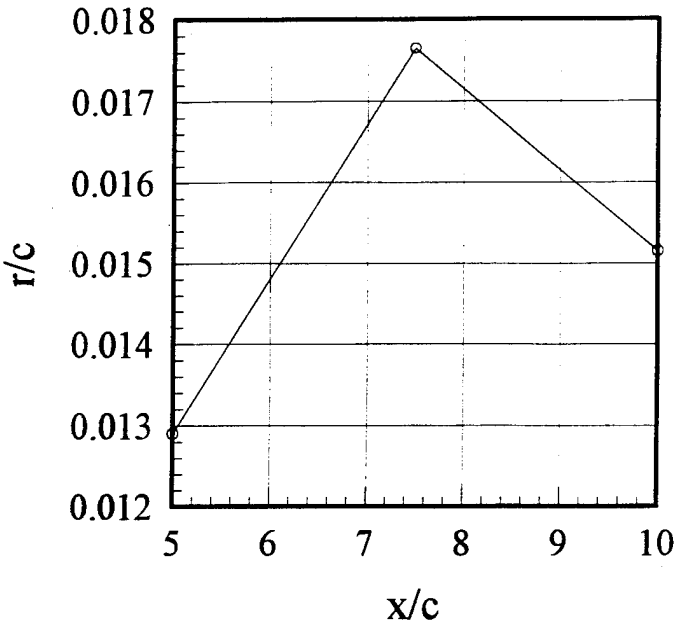

Figure 3.27 - Vortex core radius as a function of distance downstream

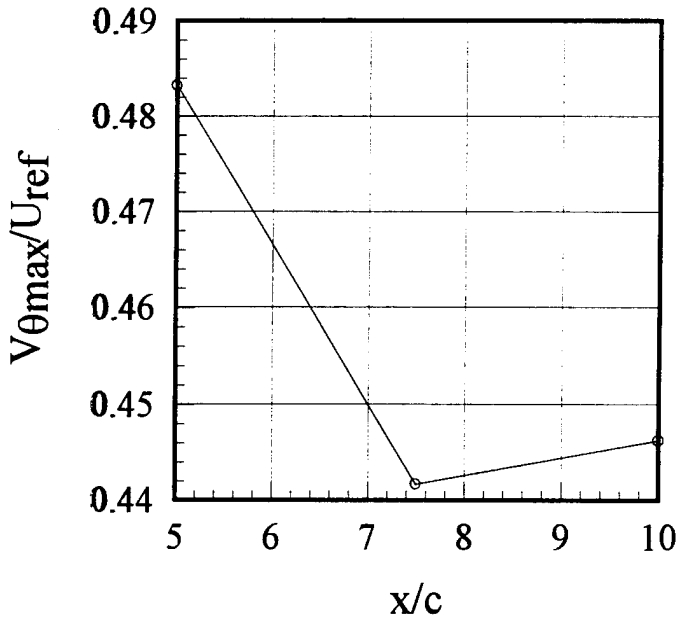

Figure 3.28 - Vortex maximum tangential velocity as a function of distance downstream

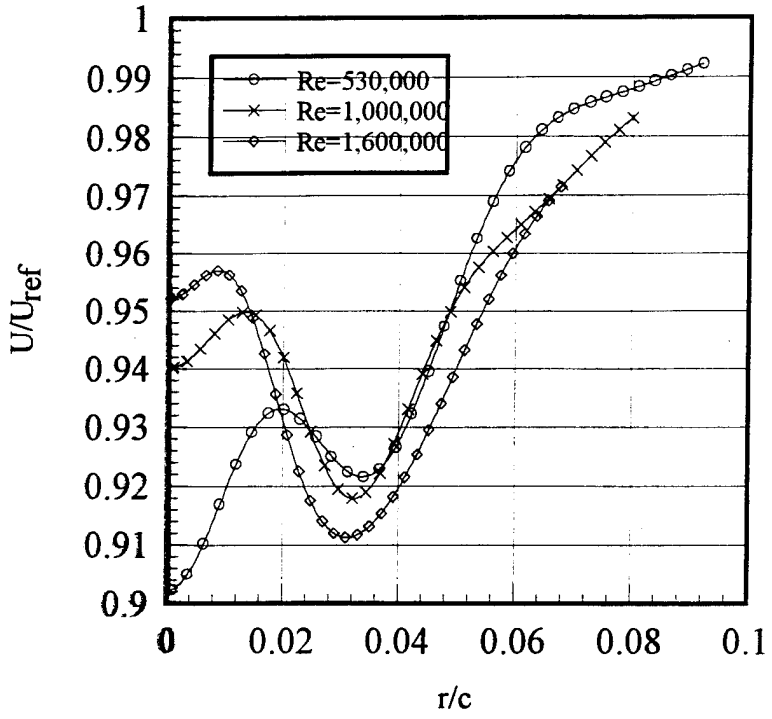

Figure 3.29 - Axial velocity profiles as a function of Reynolds number

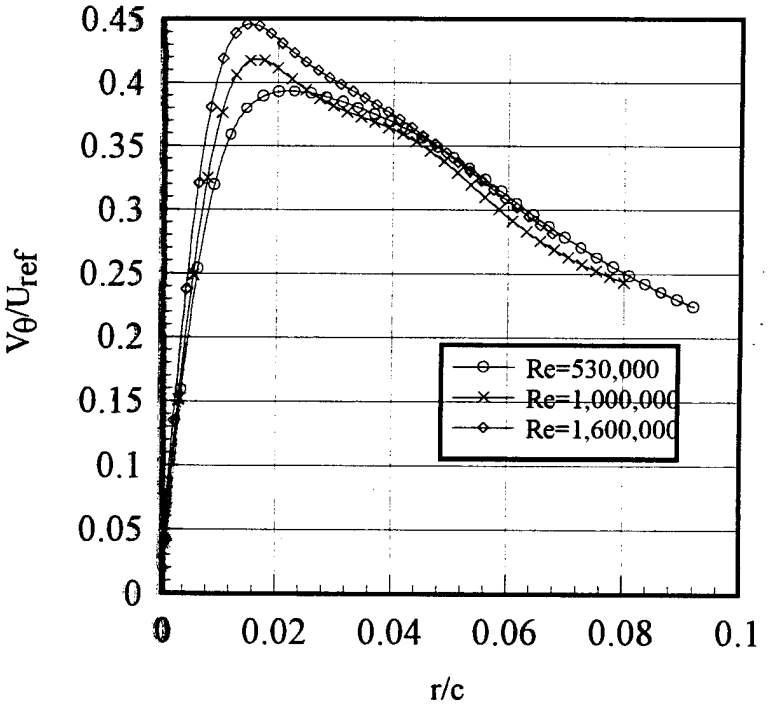

Figure 3.30 - Tangential velocity profiles as a function of Reynolds number

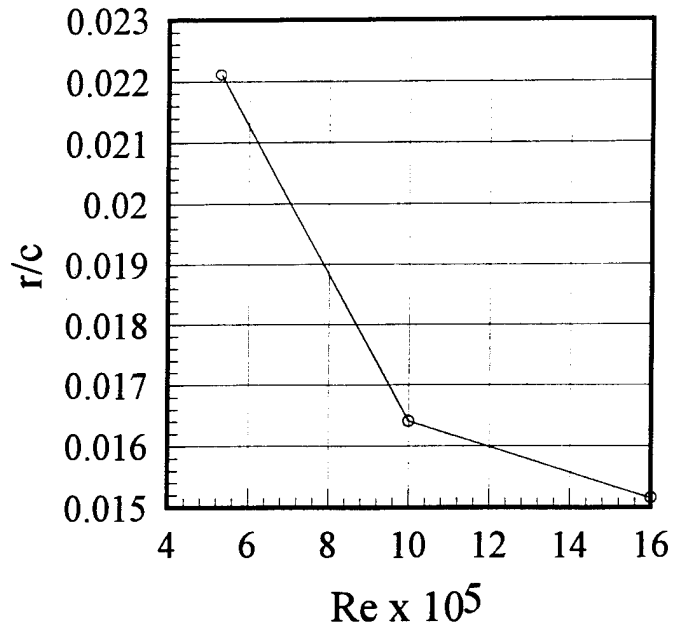

Figure 3.31 - Vortex core radius as a function of Reynolds number

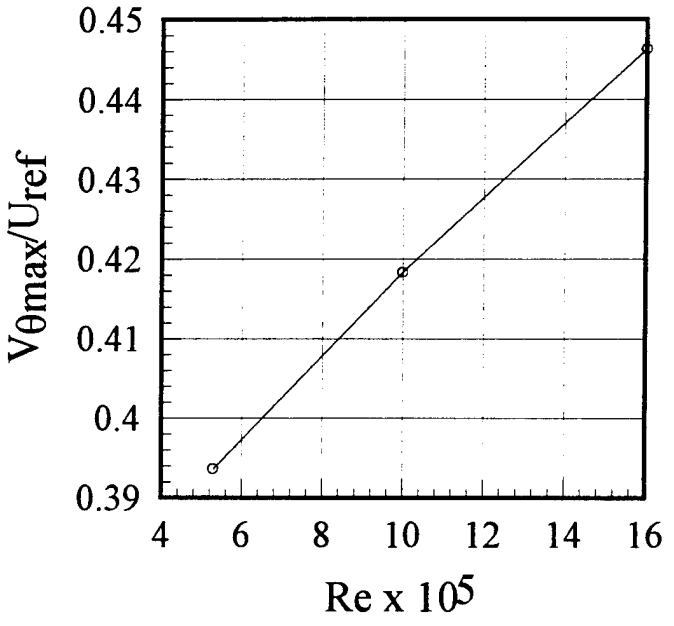

Figure 3.32 - Vortex maximum tangential velocity as a function of Reynolds number

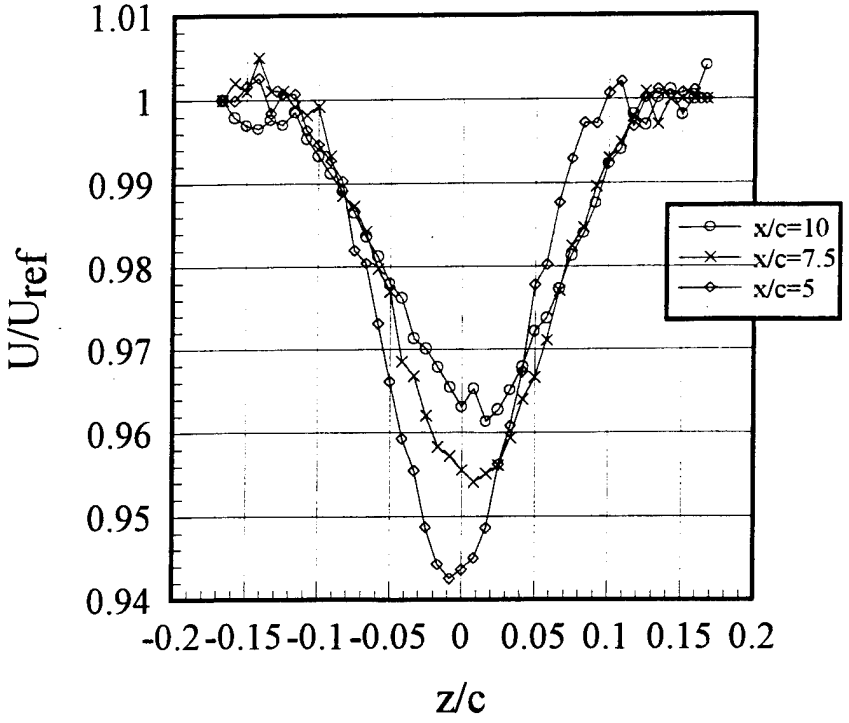

Figure 3.33 - Wake axial velocity profiles as a function of distance downstream

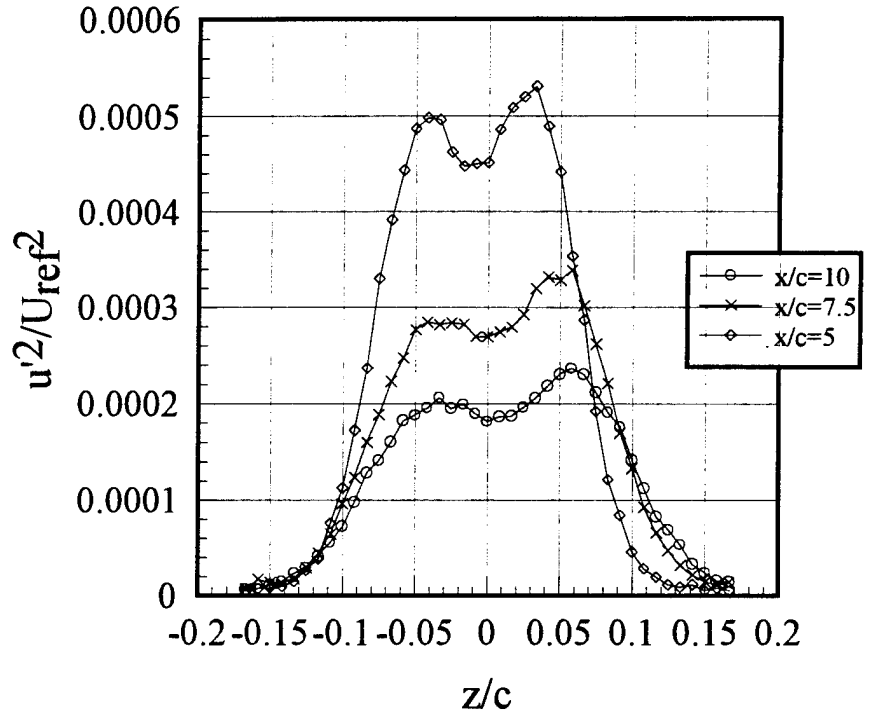

Figure 3.34 - Wake axial normal stress profiles as a function of distance downstream

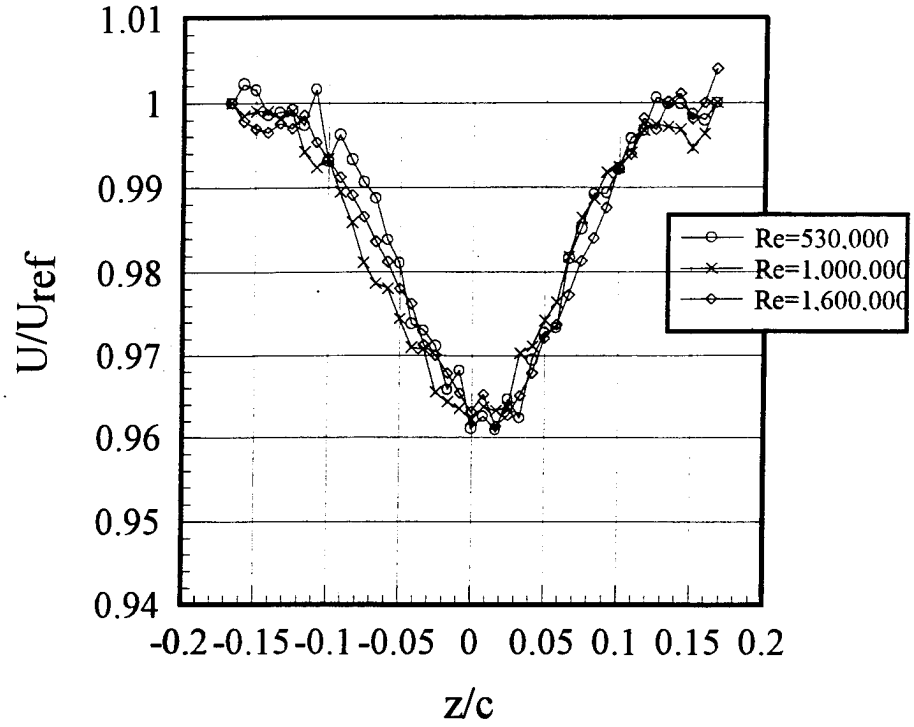

Figure 3.35 - Wake axial velocity profiles as a function of Reynolds number

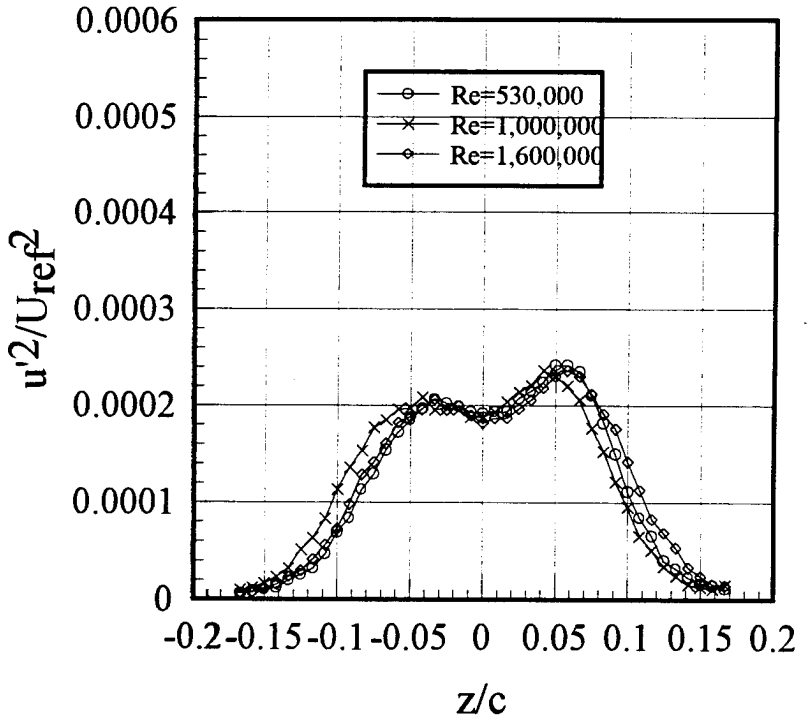

Figure 3.36 - Wake axial normal stress profiles as a function of Reynolds number

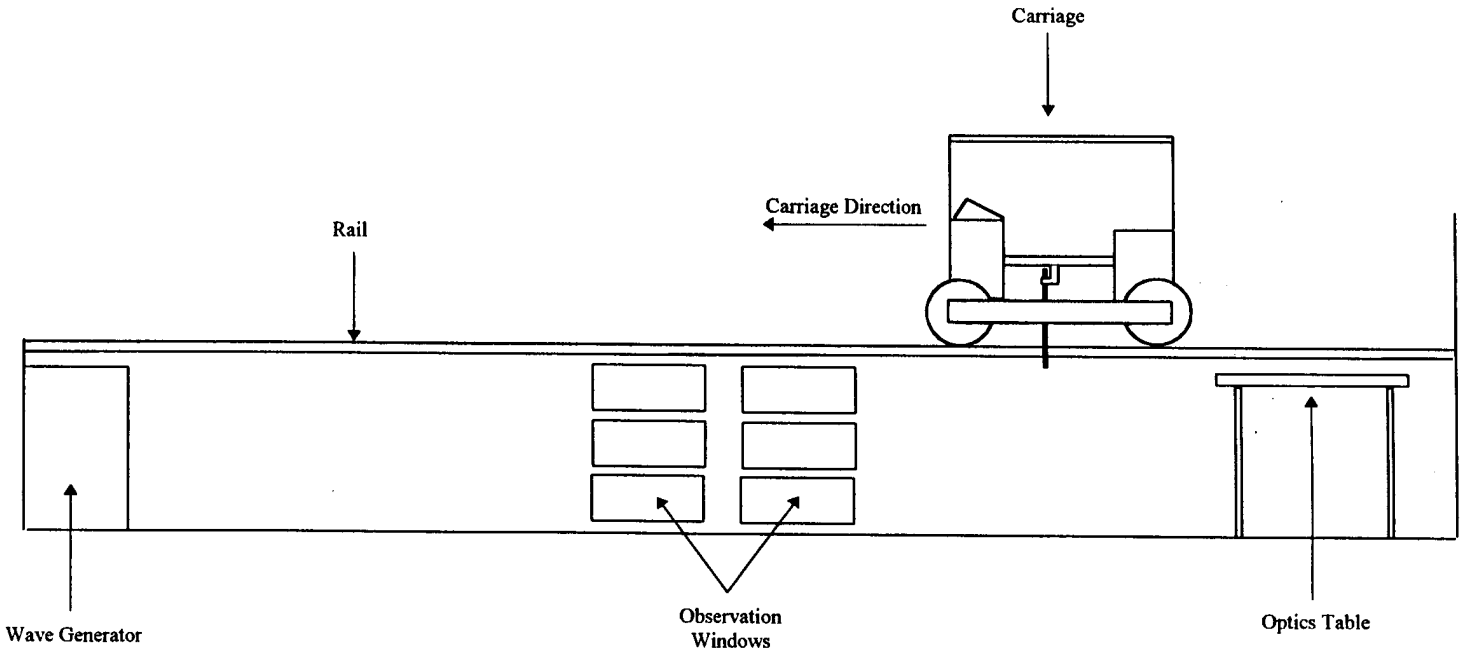

Figure 4.1 - The Virginia Tech Towing Tank Basin

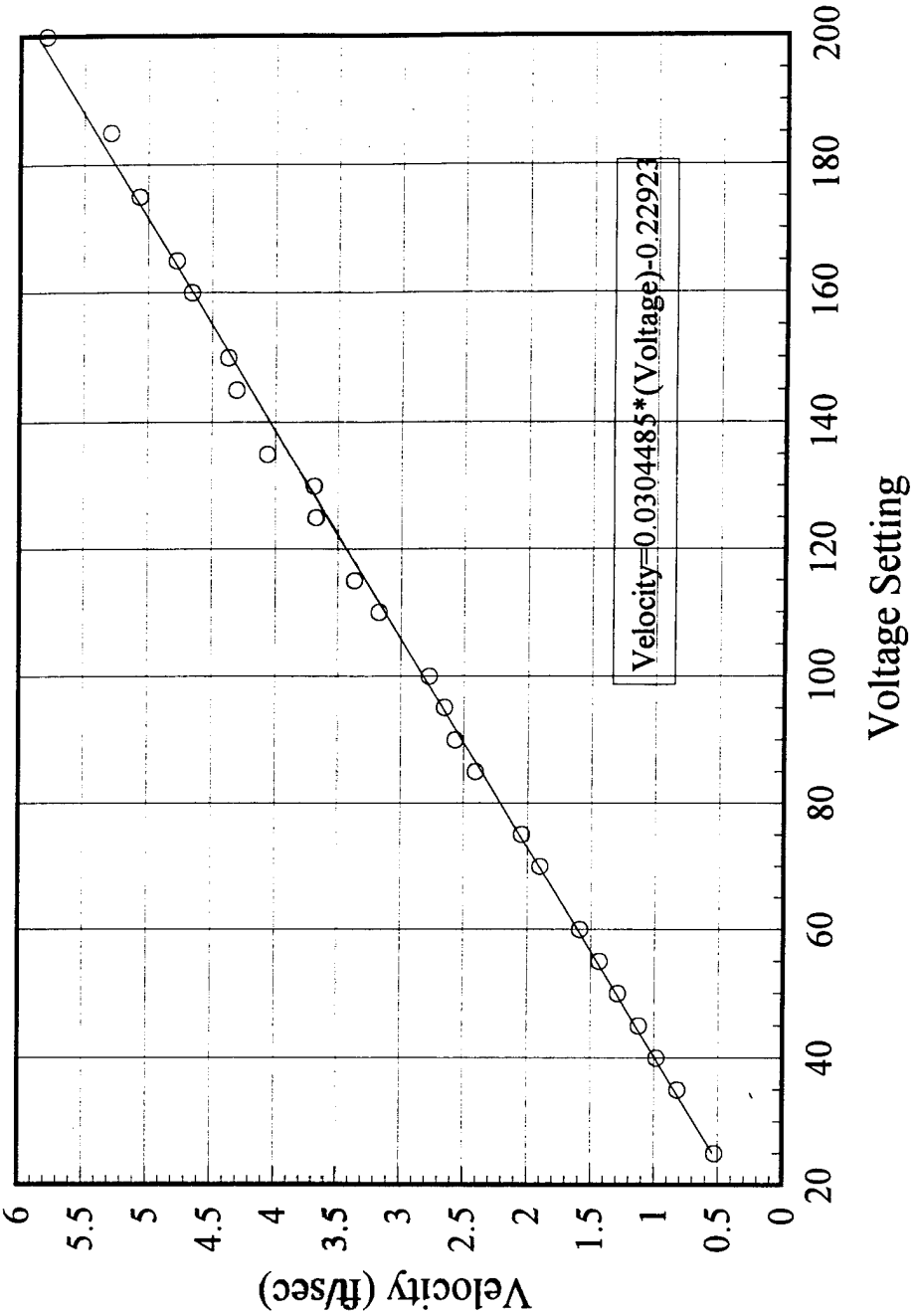

Figure 4.2 - Carriage voltage-to-velocity calibration

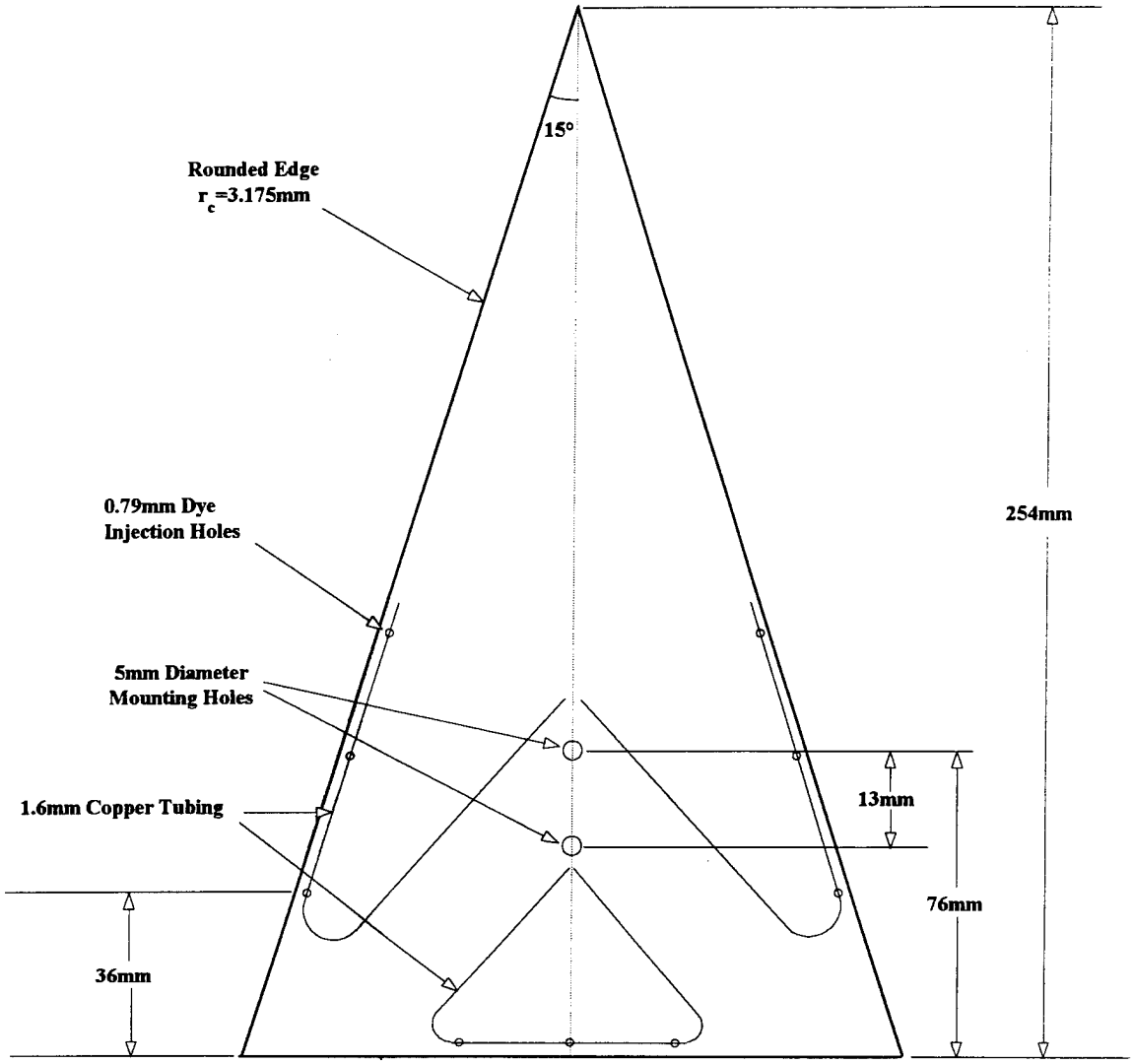

Figure 4.3a - Dye injection model

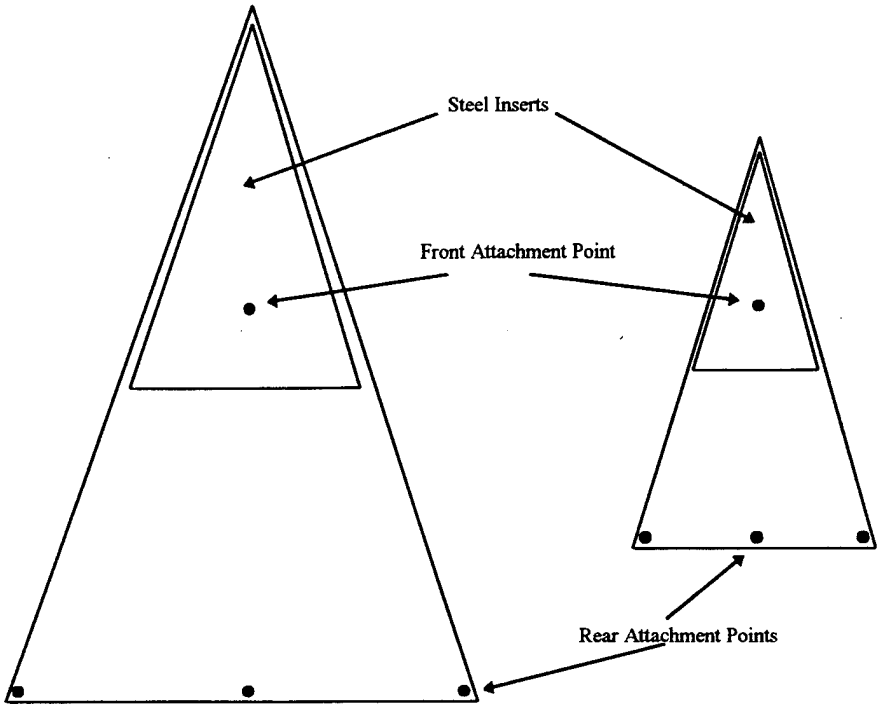

Figure 4.3b - Free-flight and wire-supported configuration models

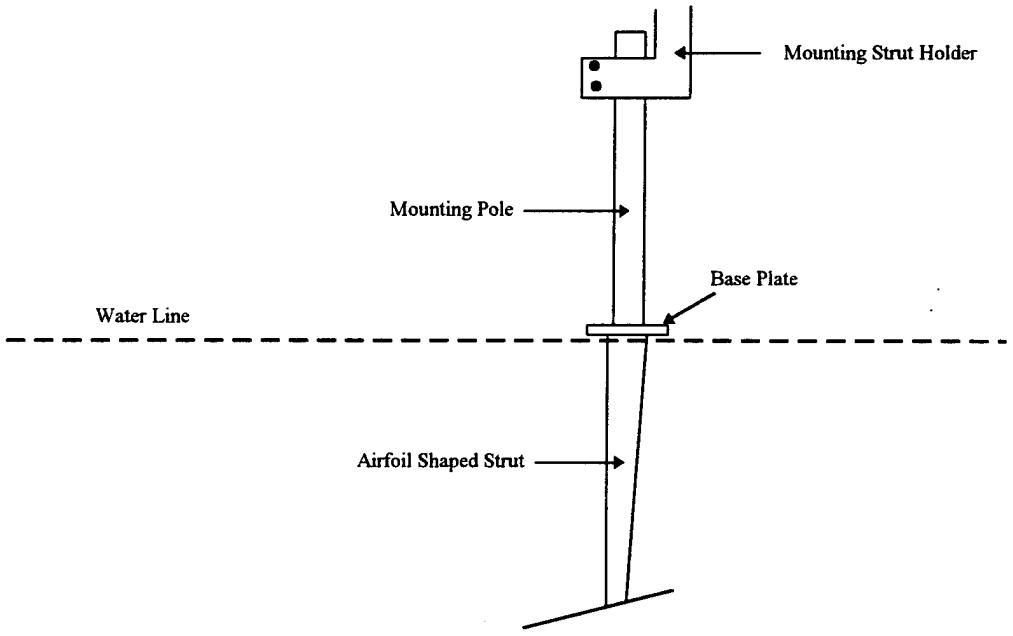

Figure 4.4 - Strut-supported configuration

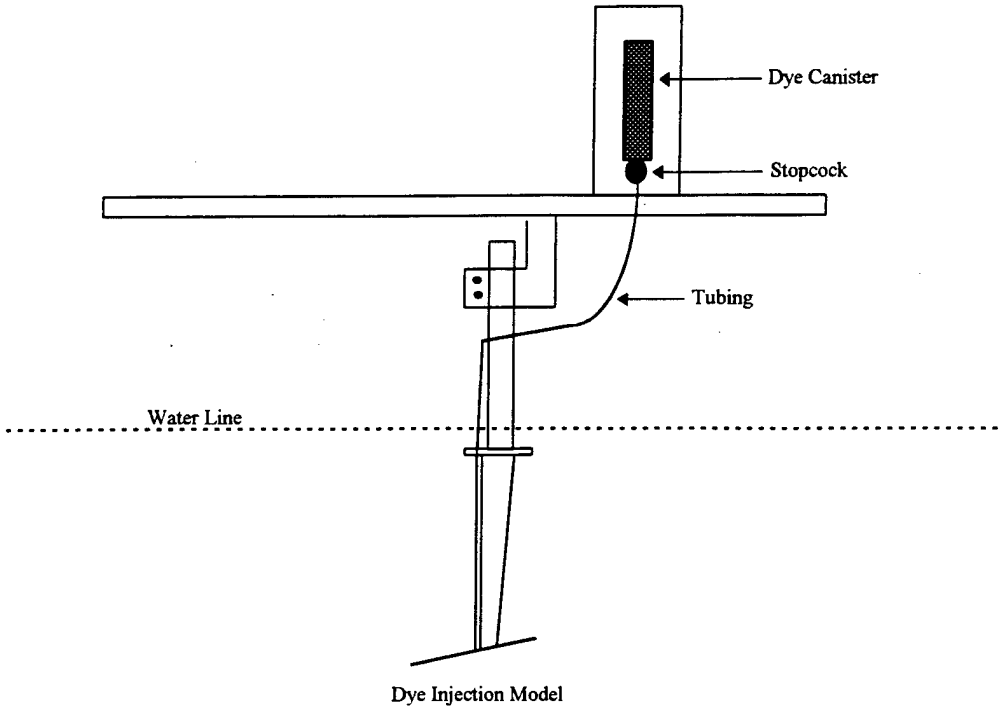

Figure 4.5 - Dye injection apparatus

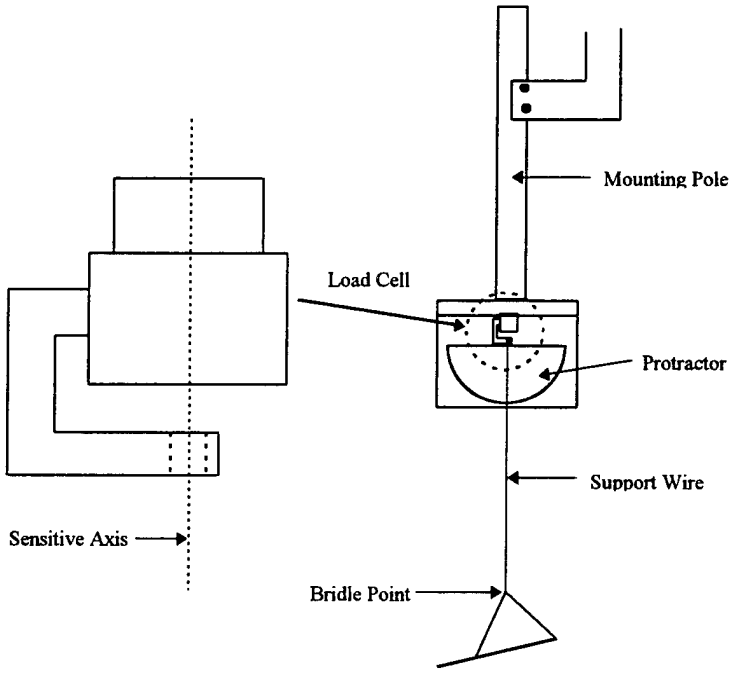

Figure 4.6 - Wire-supported configuration

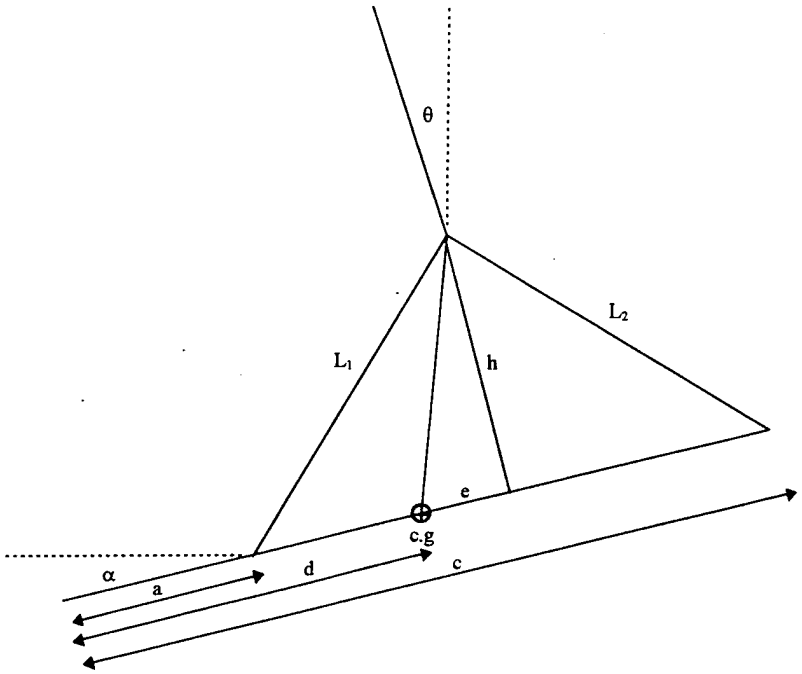

Figure 4.7 - Kite and bridle schematic

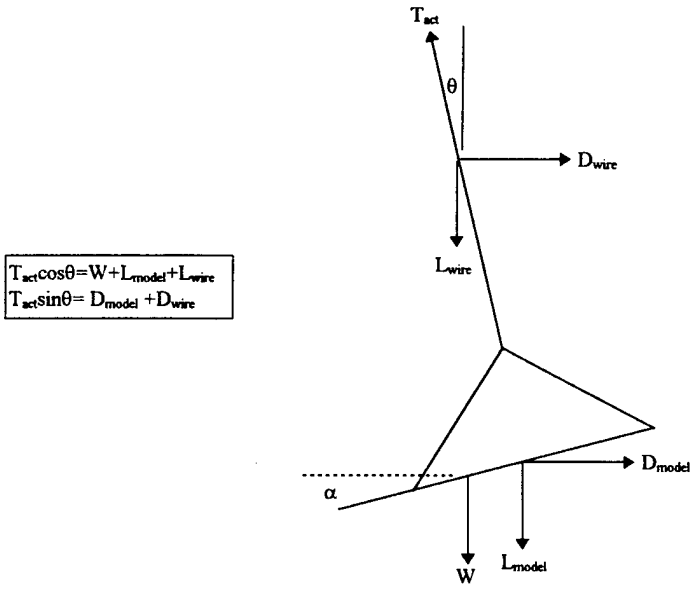

$T_{act}\cos\theta = W + L_{model} + L_{wire}$

$T_{act}\sin\theta = D_{model} + D_{wire}$

Figure 4.8 - Free-body diagram of the wire-supported configuration

a)

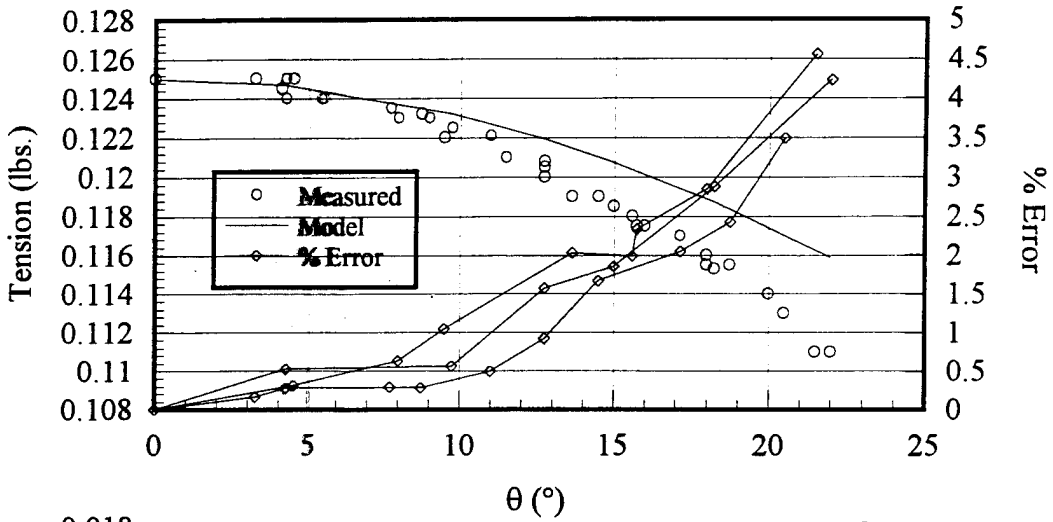

b)

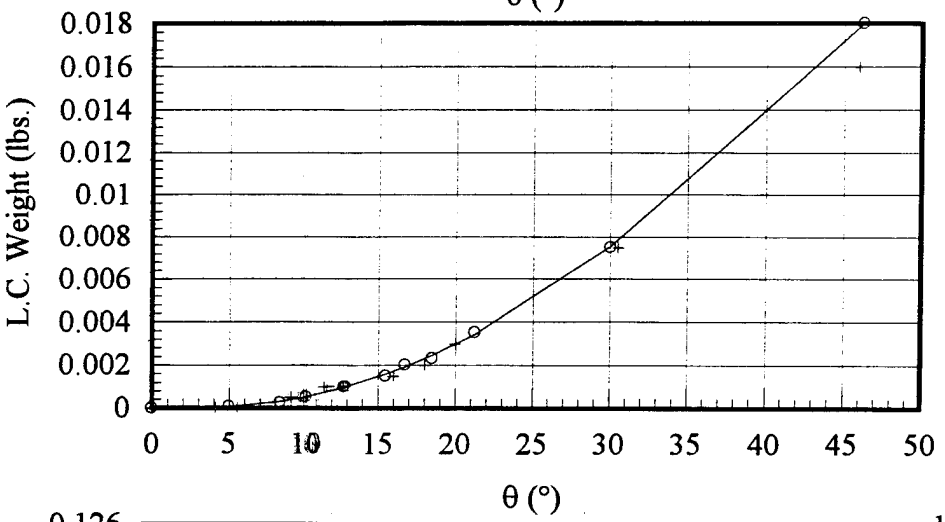

c)

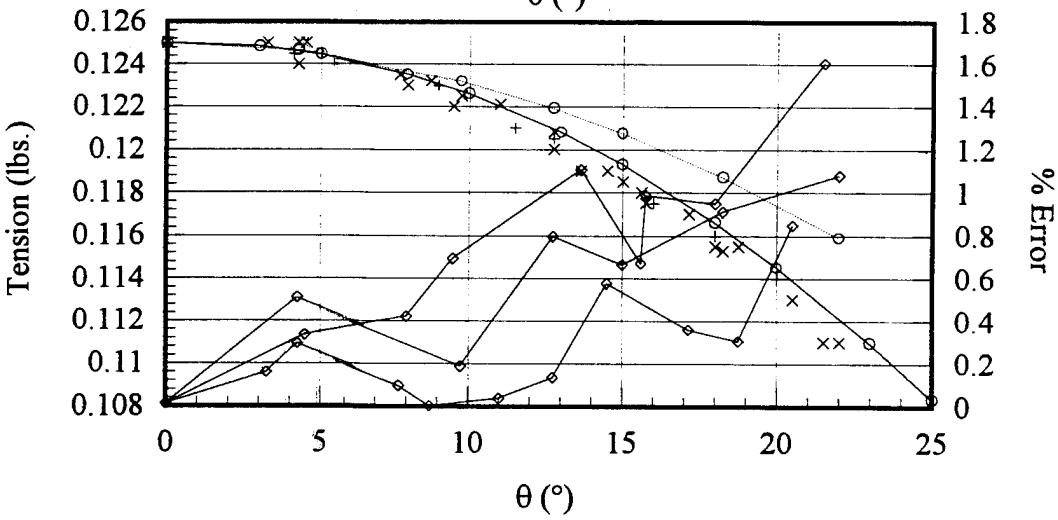

Figure 4.9 - Load cell calibration

a)

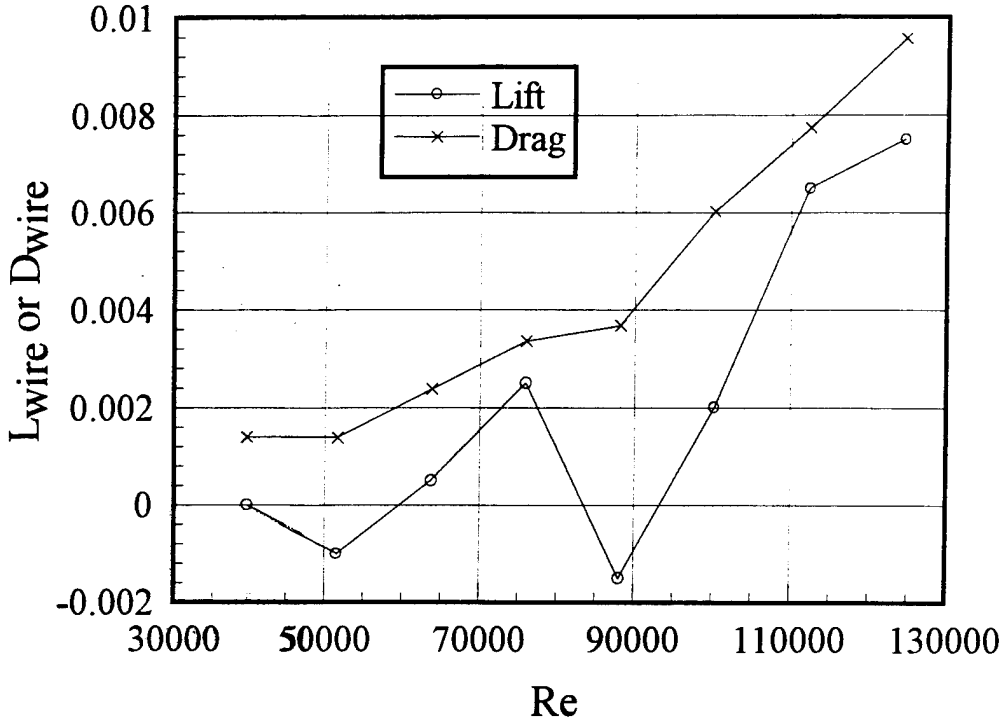

b)

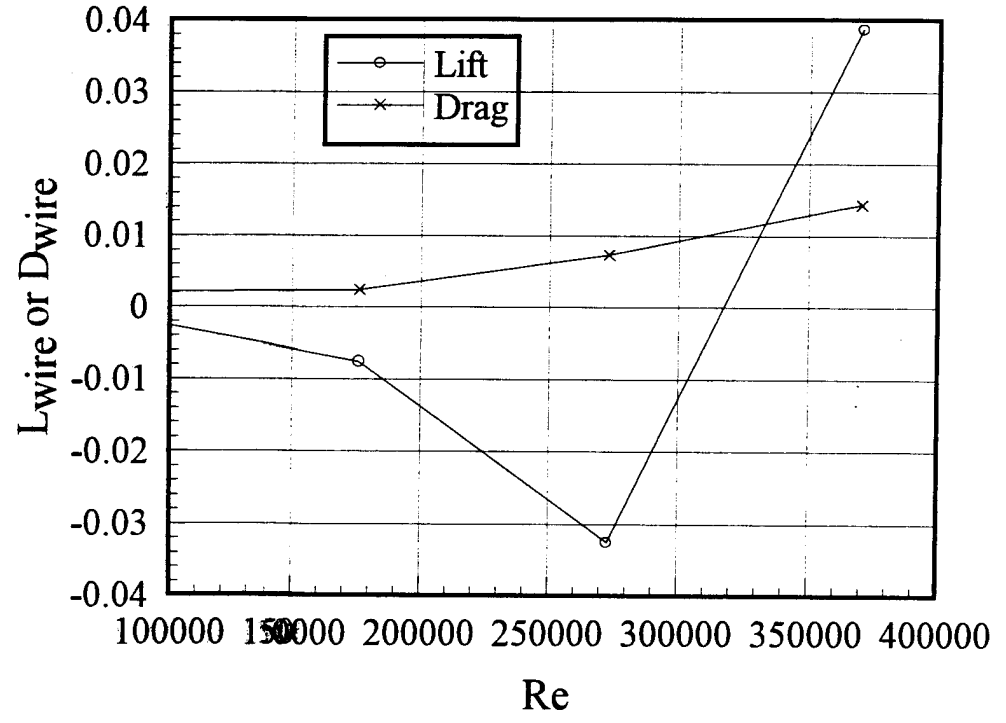

Figure 4.10 - Lift and drag on the support wire for a) d=0.127mm and b) 0.254mm

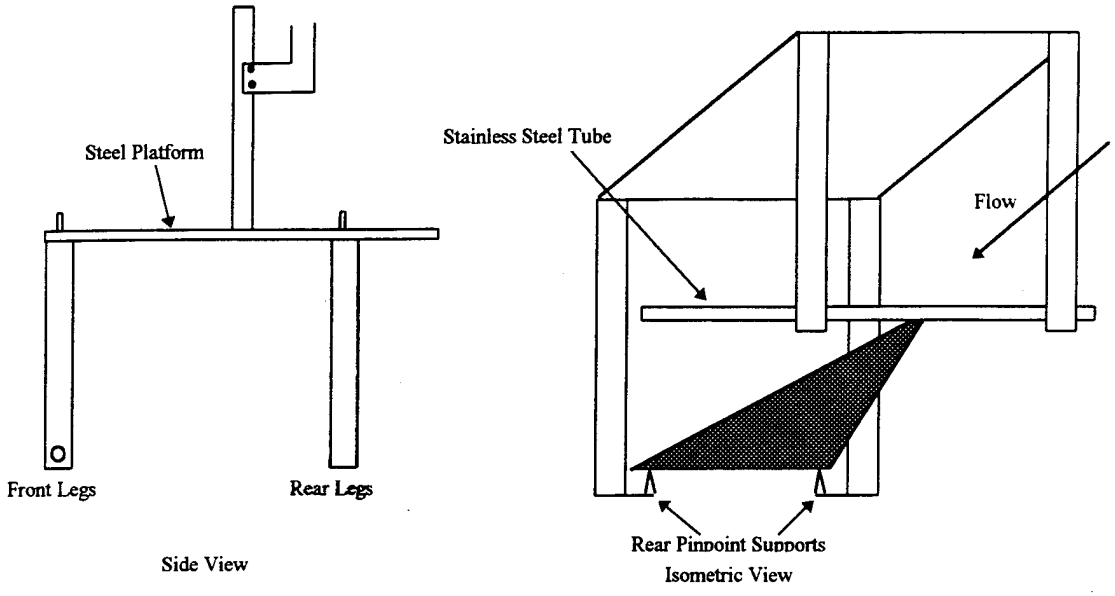

Figure 4.11 - Free-flight model launcher

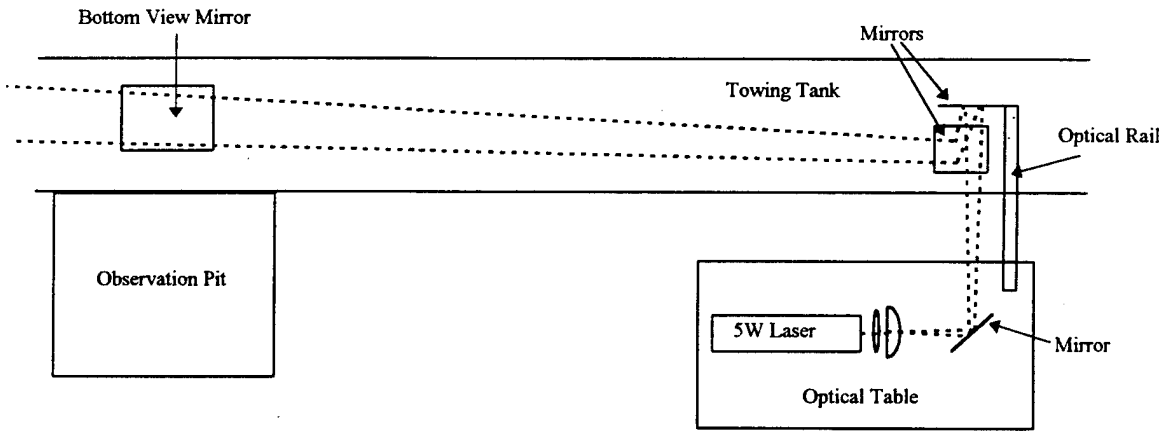

Figure 4.12 - Laser light sheet diagram

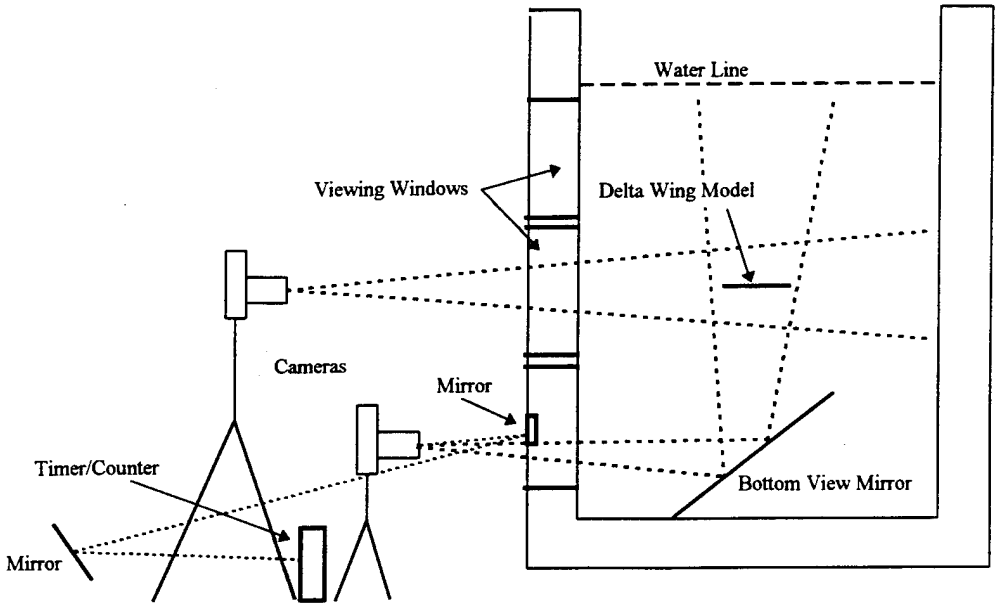

Figure 4.13 - Photographic set-up

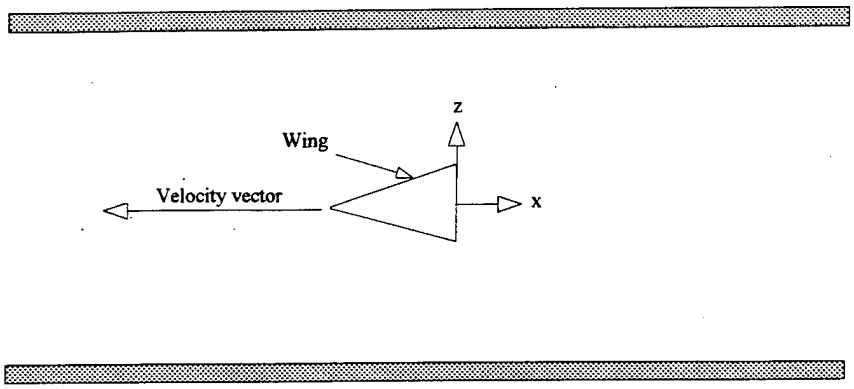

Figure 5.1 - flow visualization coordinate system

Figure 5.2 - Free-flight test, Re=140,560, L/D=2.95.

x/c=0-1.0

x/c=0.4-3.2

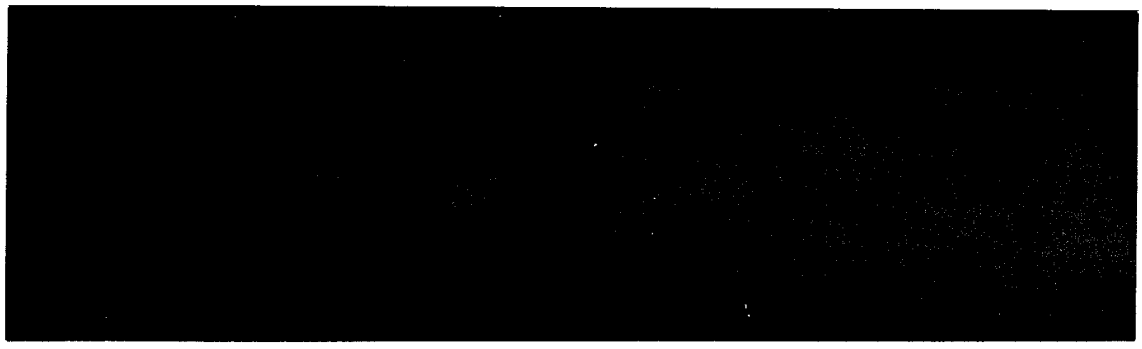

Figure 5.3a - Wire-supported towed test, Re=140,560, L/D=2.95 (C_L=0.09).

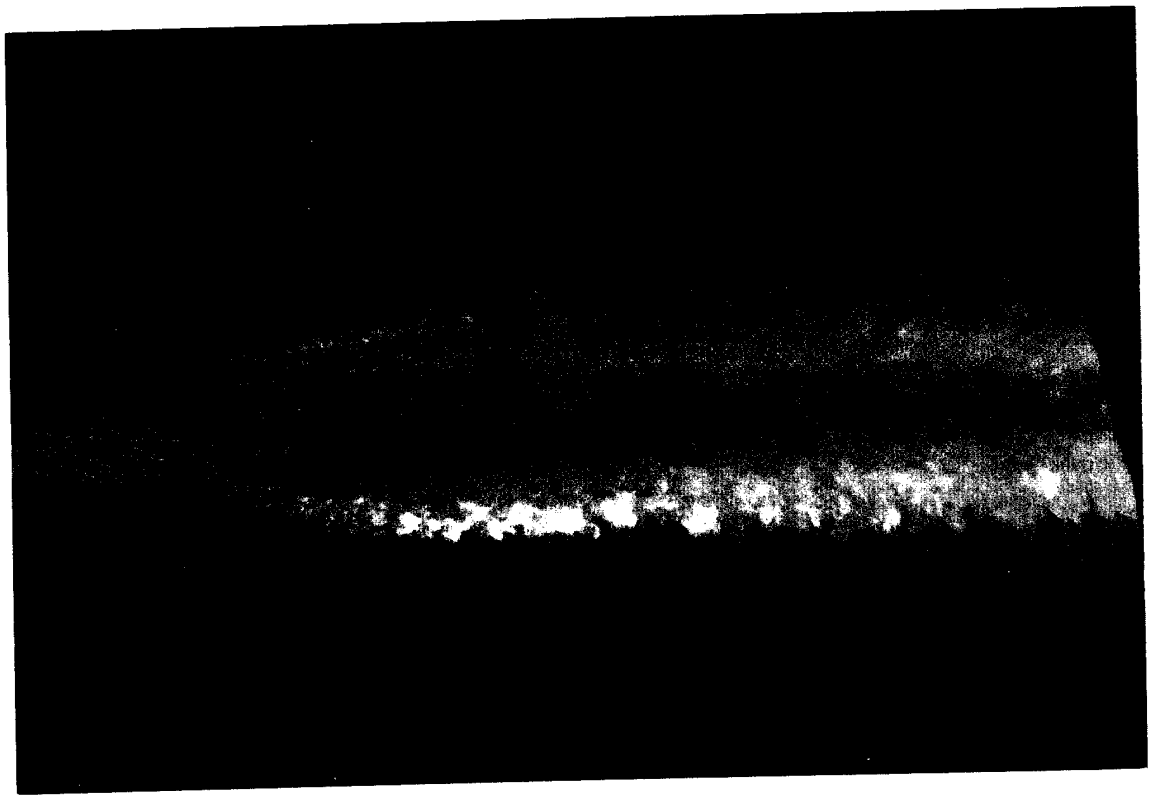

Figure 5.3b - Strut-supported towed test, Re=44,200, α=5°.

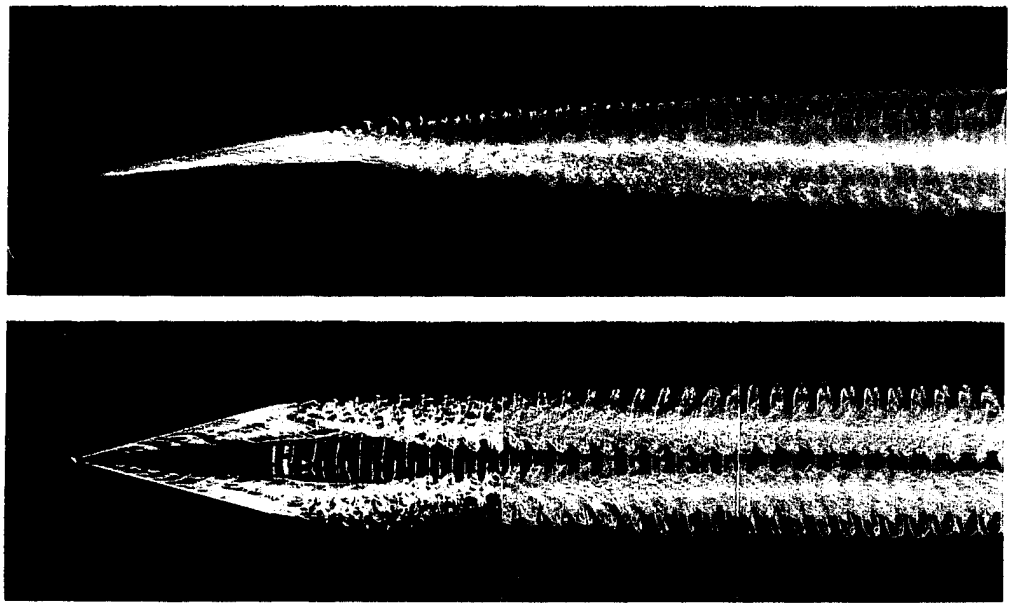

Figure 5.3c - Flow visualizations of Miller and Williamson (1995), Re=10,000, α=10°.

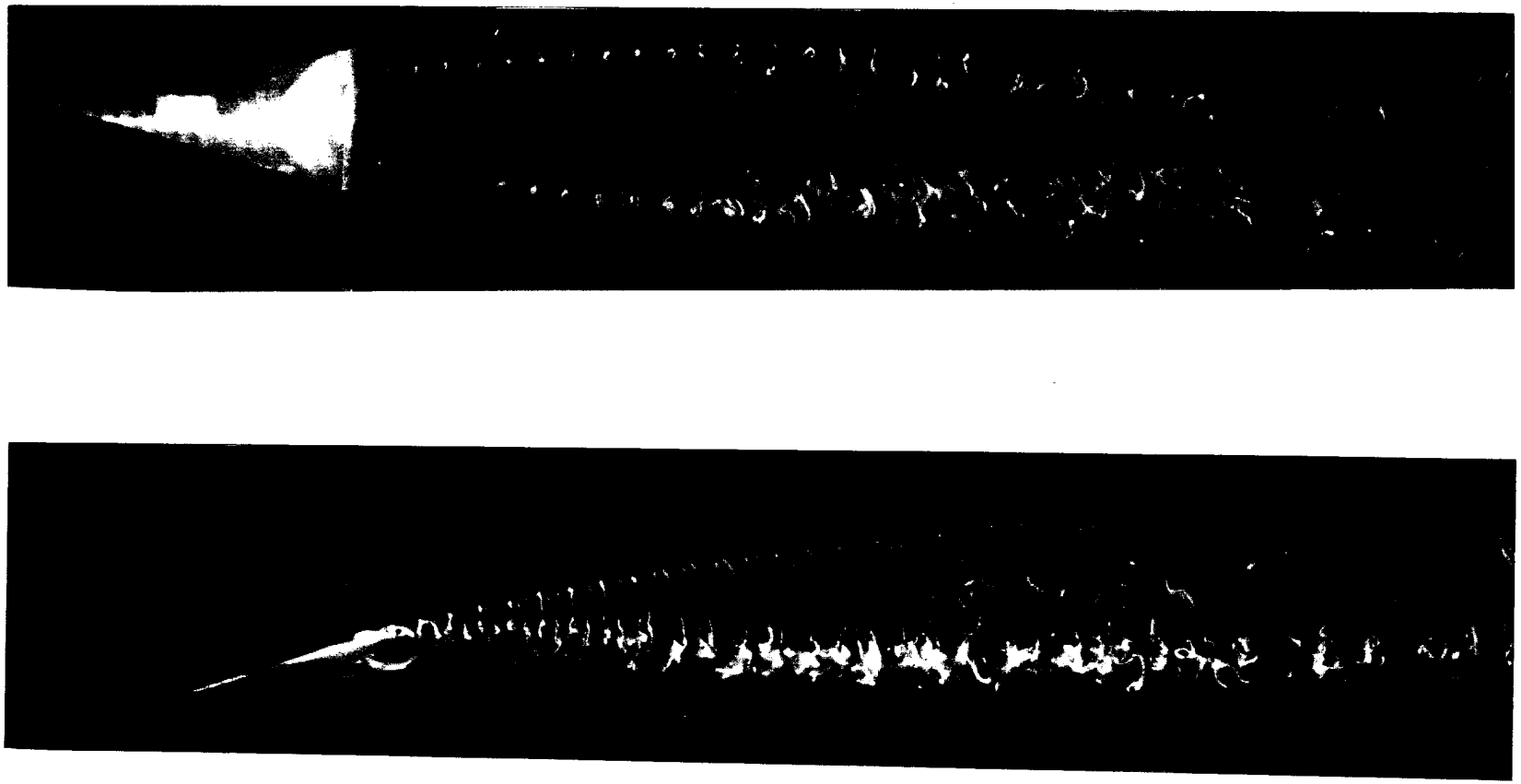

Figure 5.3d - Duplicaton of the flow visualizations of Miller and Williamson using the wire-supported configuration, Re=10,000, α=10°.

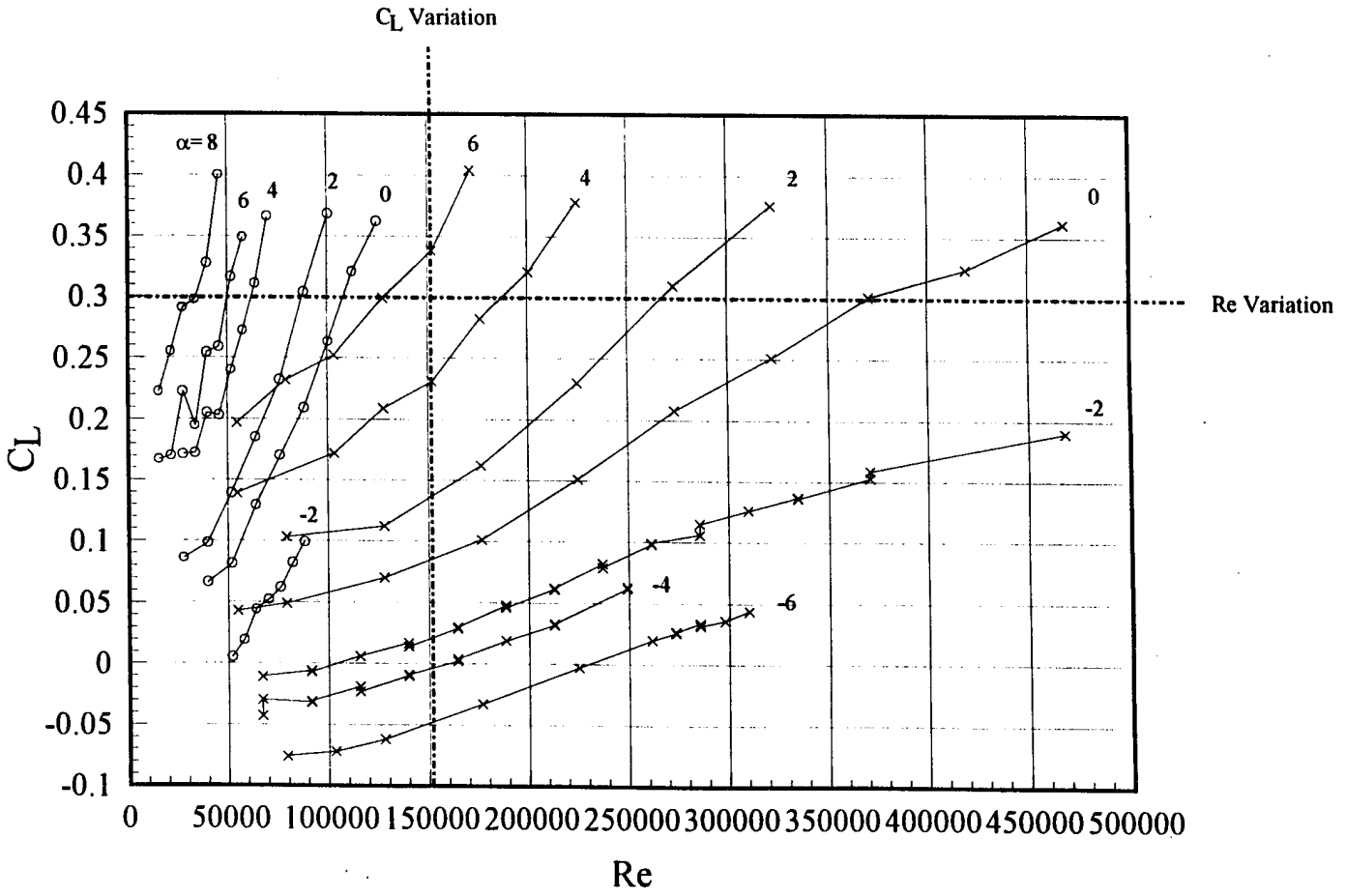

Figure 5.4 - Wing lift coefficient as a function of bridle angle, α, and wing Reynolds number, Re.

a) x/c: 0-1.1

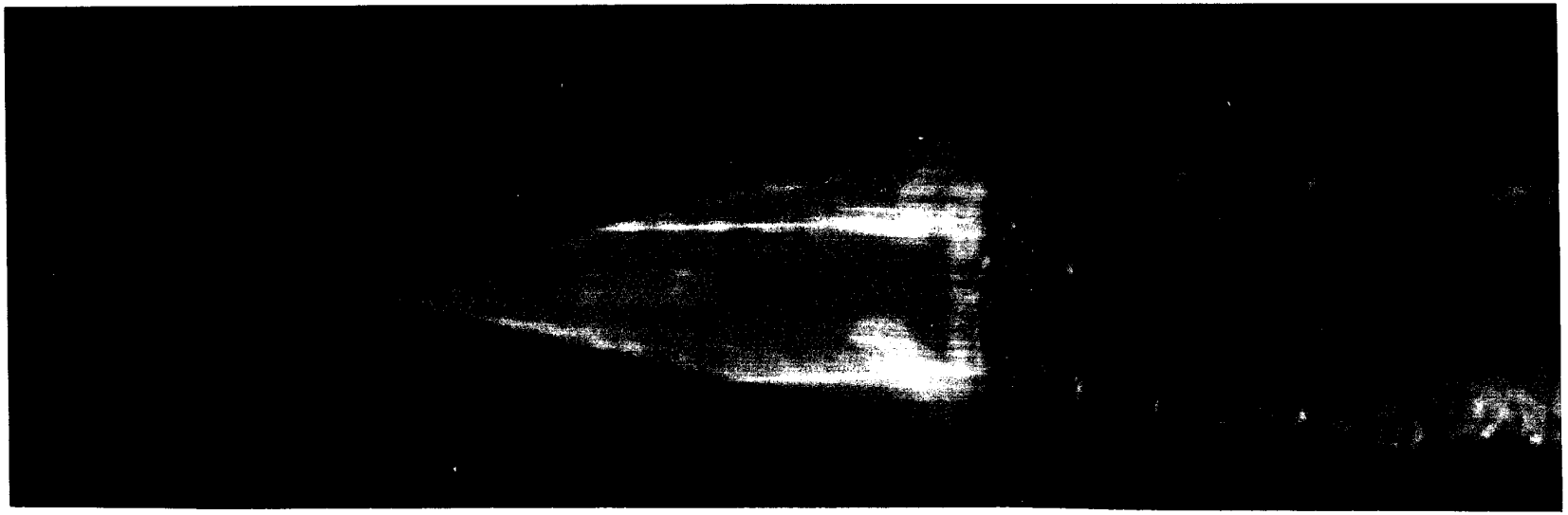

b) x/c: 1.4-4.2

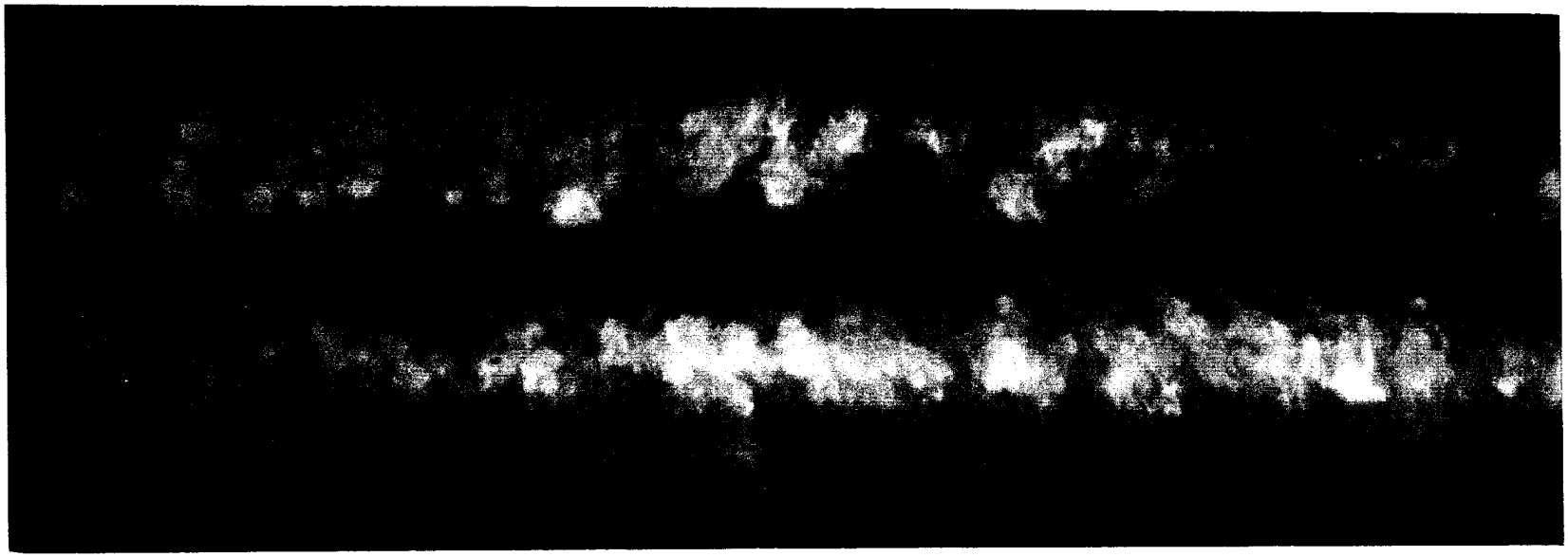

Figure 5.5 - Bottom view flow visualizations for baseline case, Re=151,800, C_L=0.3

c) x/c: 2.6-5.4

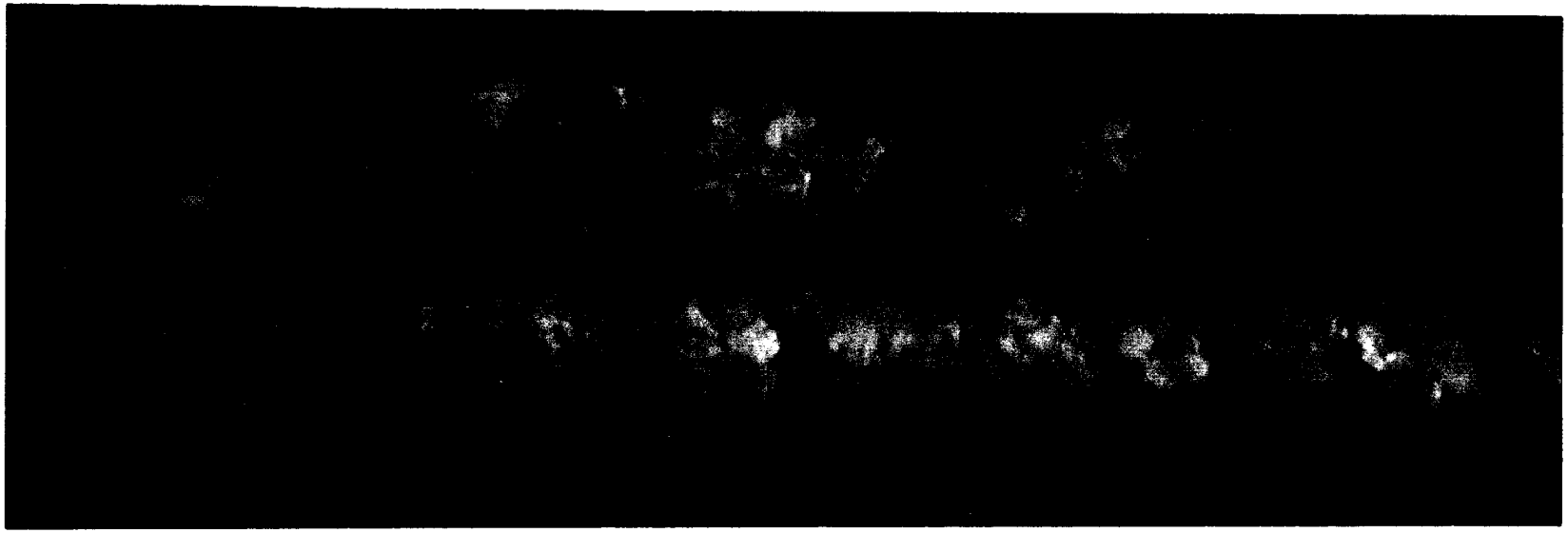

d) x/c: 11.7-14.5

Figure 5.5 - Bottom view flow visualizations for baseline case, Re=151,800, C_L=0.3

e) x/c: 17.5-20.3

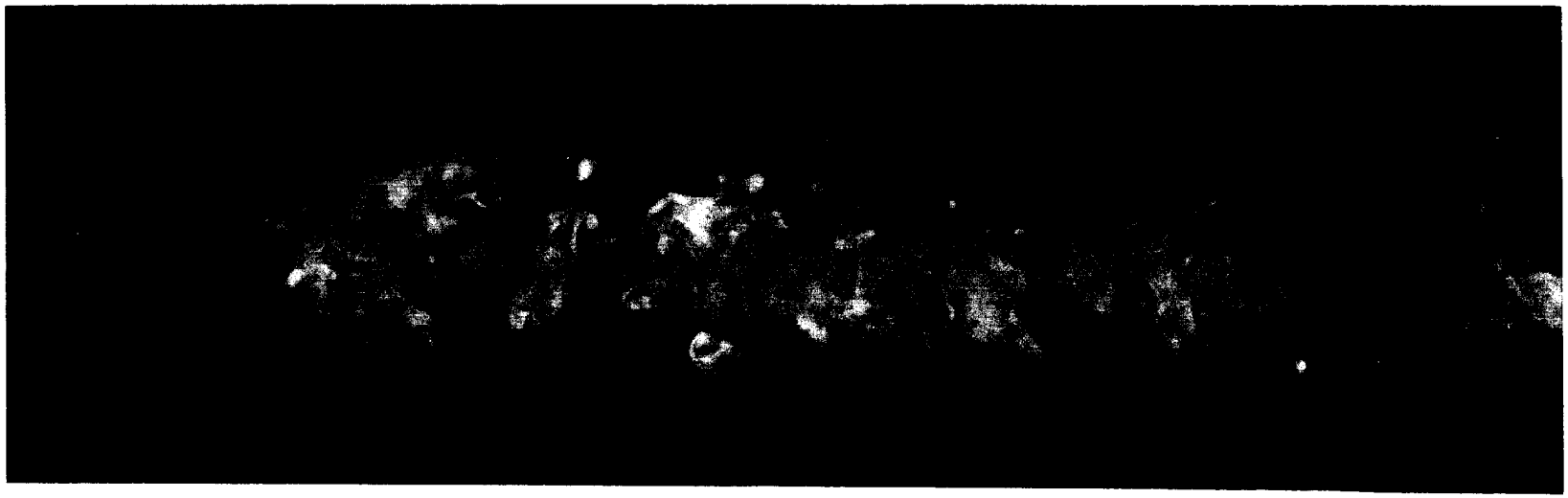

f) x/c: 20.8-23.6

Figure 5.5 - Bottom view flow visualizations for baseline case, Re=151,800, C_L=0.3

a) x/c: 0-1.1

b) x/c: 1.4-4.2

Figure 5.6 - Side view flow visualizations for baseline case, Re=151,800, C_L=0.3

c) x/c: 2.6-5.4

d) x/c: 11.7-14.5

Figure 5.6 - Side view flow visualizations for baseline case, Re=151,800, C_L=0.3

e) x/c: 17.5-20.3

f) x/c: 20.8-23.6

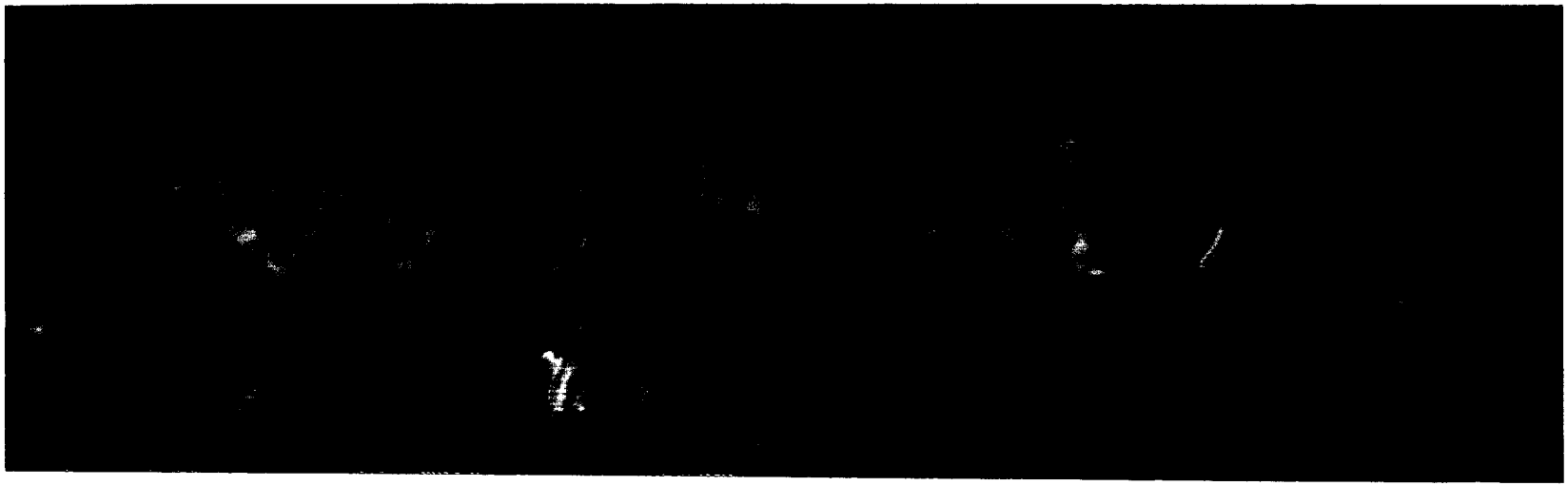

Figure 5.6 - Side view flow visualizations for baseline case, Re=151,800, C_L=0.3

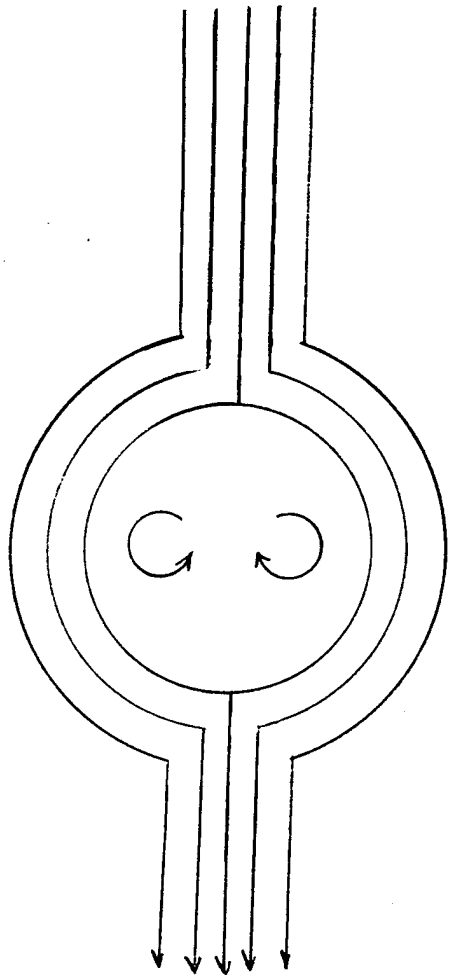

Figure 5.7 - Kelvin Oval

a) x/c: 0-1.3

b) x/c: 0.04-5.5

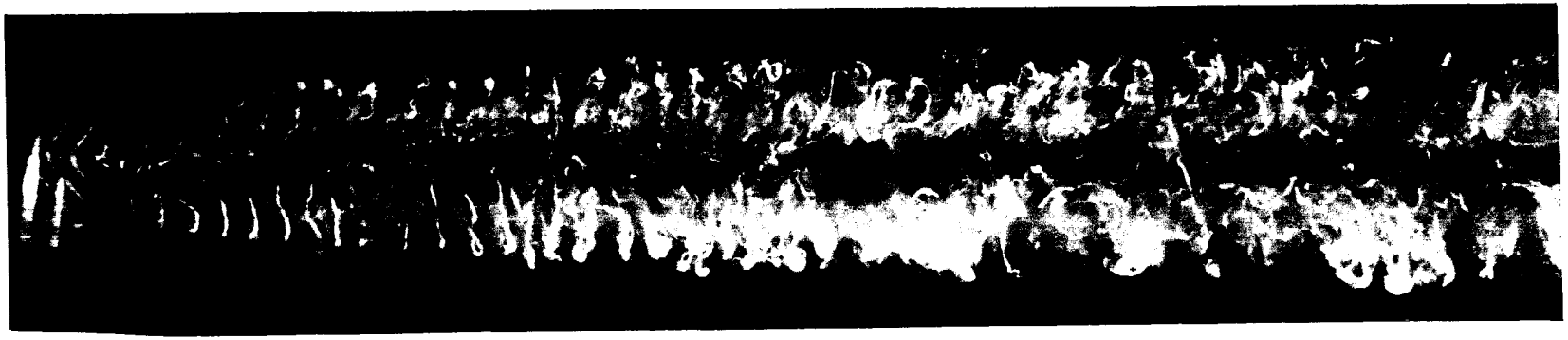

c) x/c: 6.3-11.7

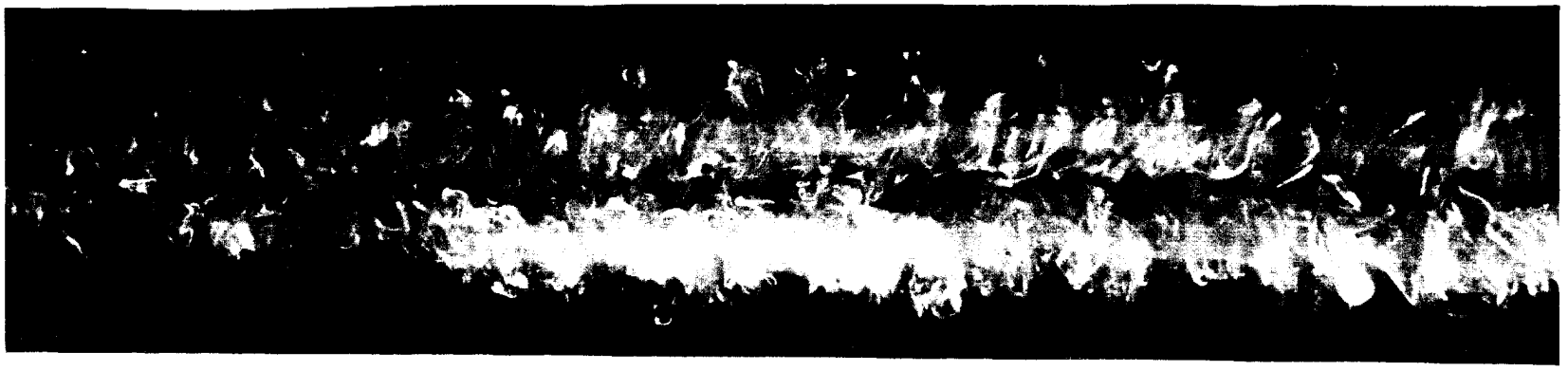

Figure 5.8 - Bottom view flow visualizations, Re=24,890, C_L=0.3

d) x/c: 13.7-19.2

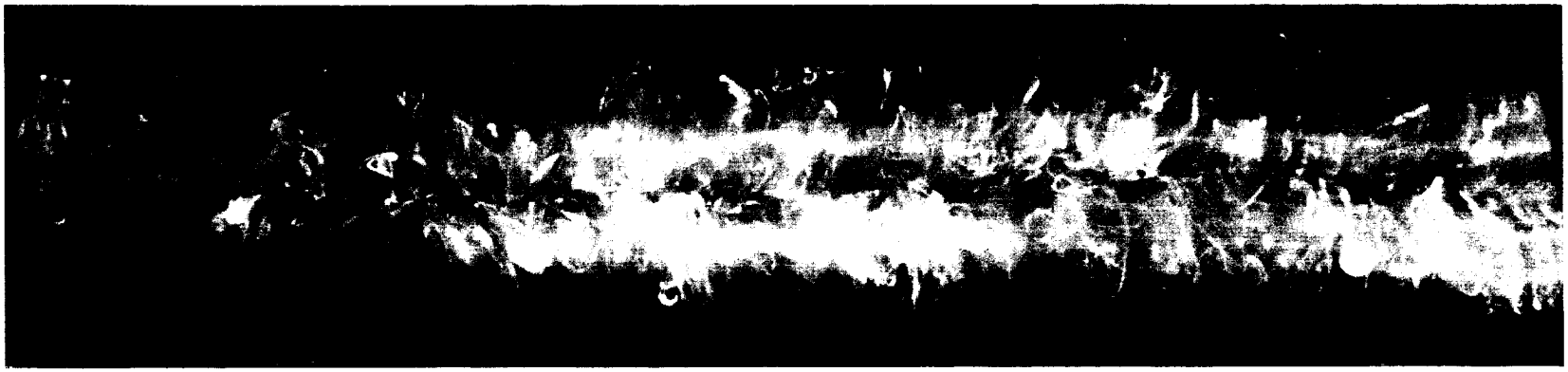

e) x/c: 26.3-31.7

Figure 5.8 - Bottom view flow visualizations, Re=24,890, C_L=0.3

f) x/c: 31.0-36.5

g) x/c: 35.3-40.8

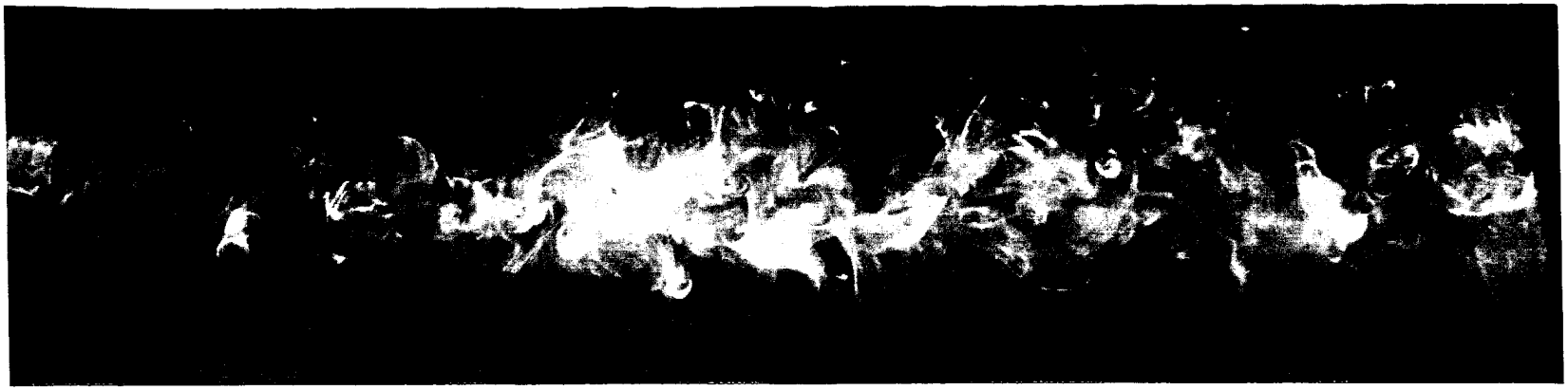

Figure 5.8 - Bottom view flow visualizations, Re=24,890, C_L=0.3

a) x/c: 0-1.3

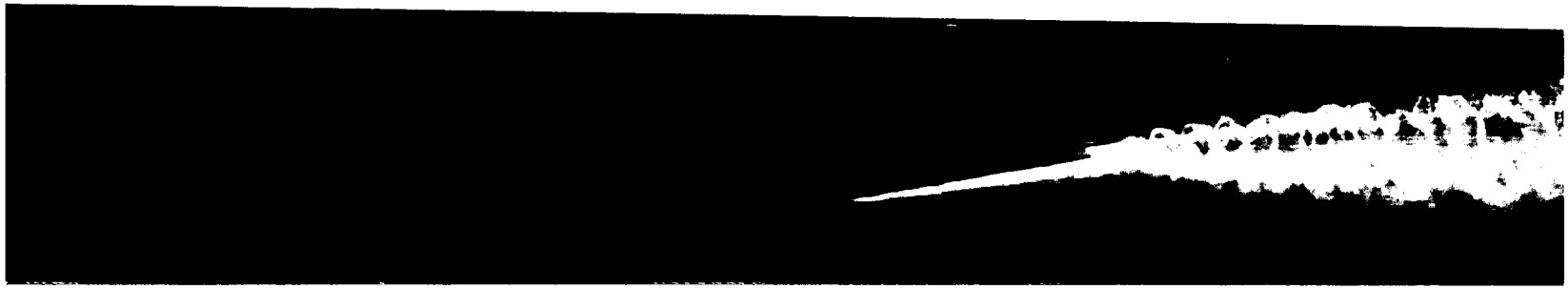

b) x/c: 0.04-5.5

c) x/c: 6.3-11.7

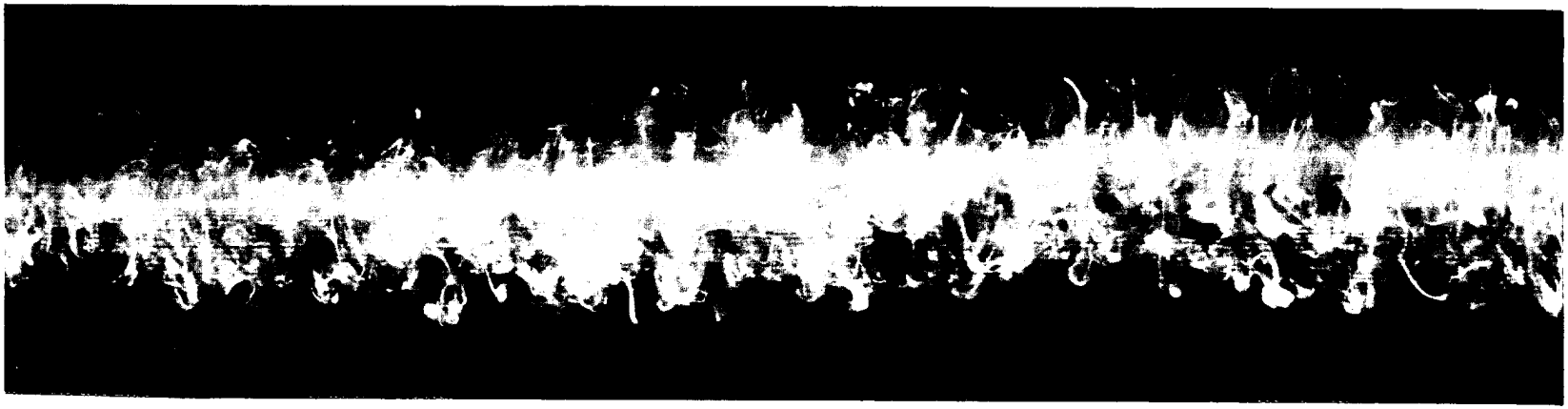

Figure 5.9 - Side view flow visualizations, Re=24,890, C_L=0.3

d) x/c: 13.7-19.2

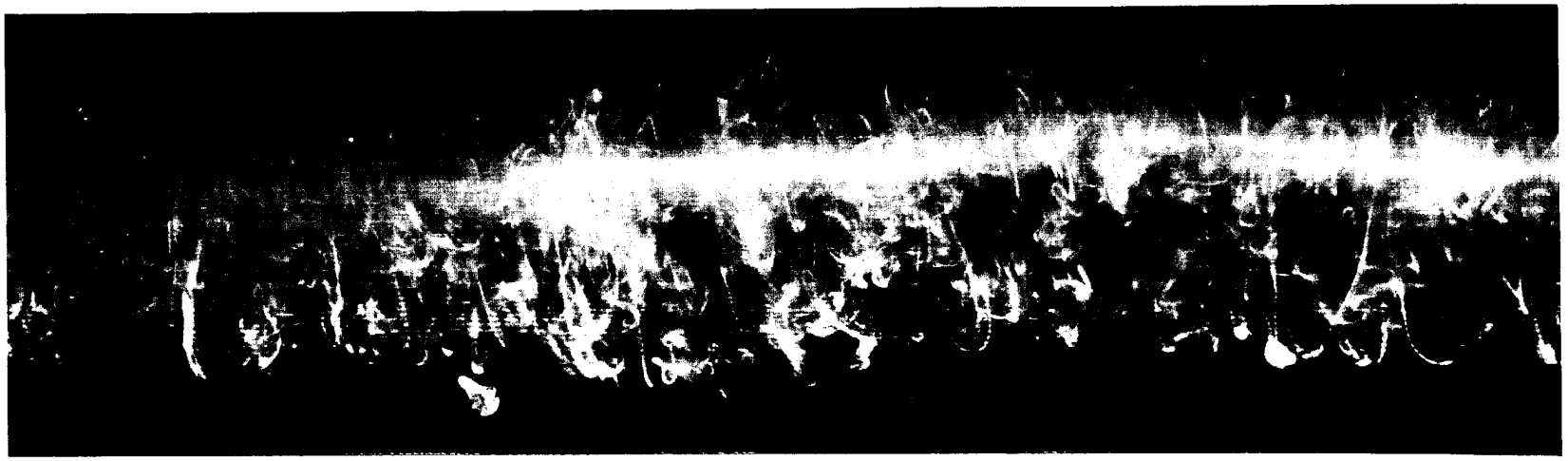

e) x/c: 26.3-31.7

Figure 5.9 - Side view flow visualizations, Re=24,890, C_L=0.3

f) x/c: 31.0-36.5

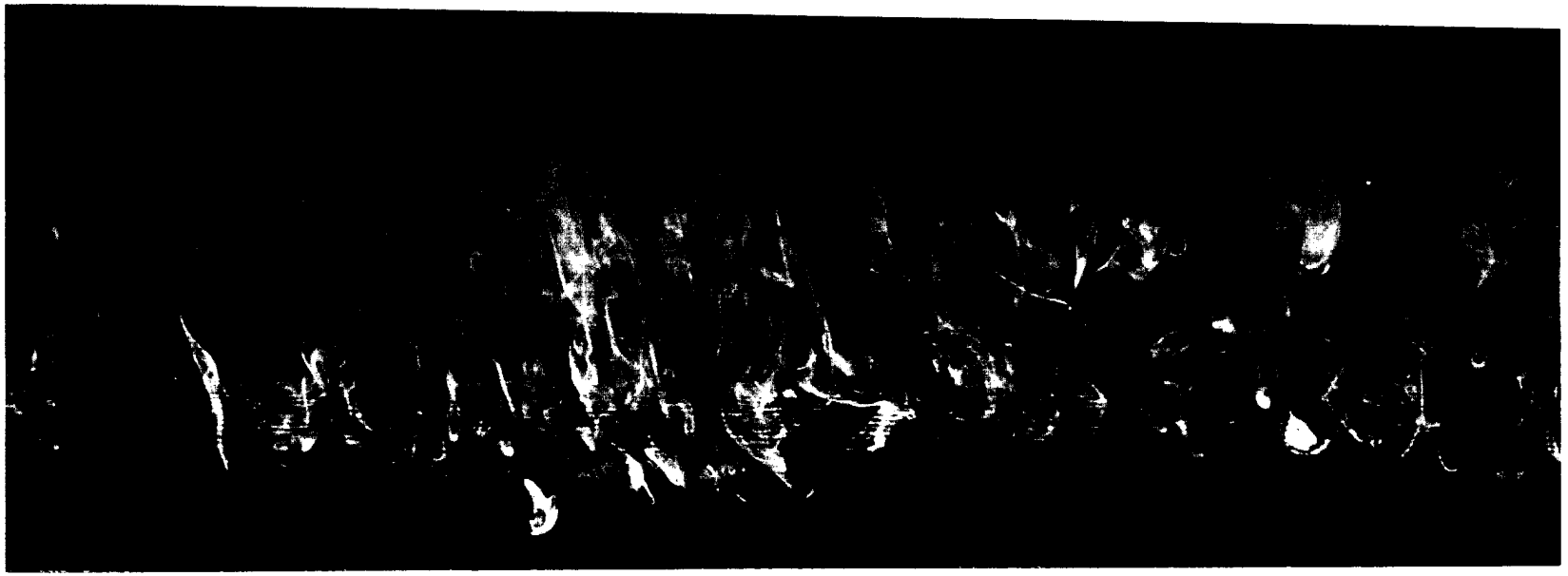

g) x/c: 35.3-40.8

Figure 5.9 - Side view flow visualizations, Re=24,890, C_L=0.3

a) x/c: 0-3.1

b) x/c: 5.4-10.6

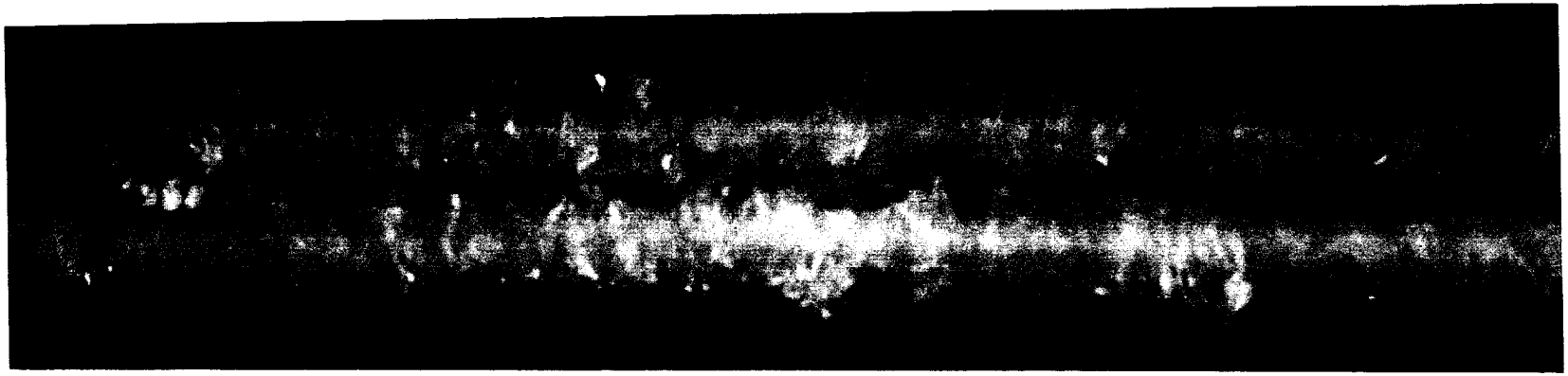

c) x/c: 6.9-12.1

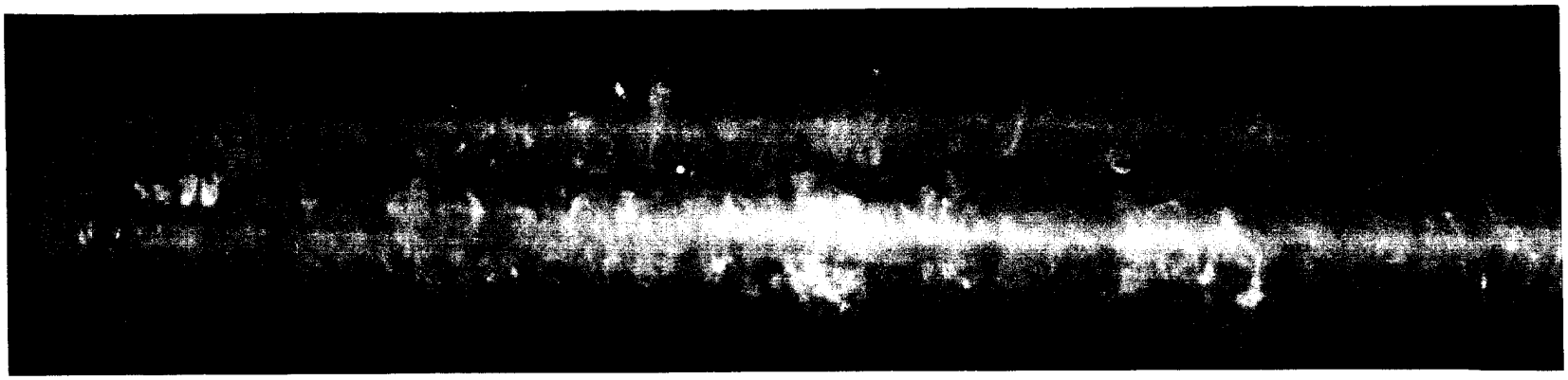

Figure 5.10 - Bottom view flow visualizations, Re=49,200, C_L=0.3

d) x/c: 18.5-23.7

e) x/c: 27.4-32.6

f) x/c: 32.6-38.1

Figure 5.10 - Bottom view flow visualizations, Re=49,200, C_L=0.3

a) x/c: 0-3.1

b) x/c: 5.4-10.6

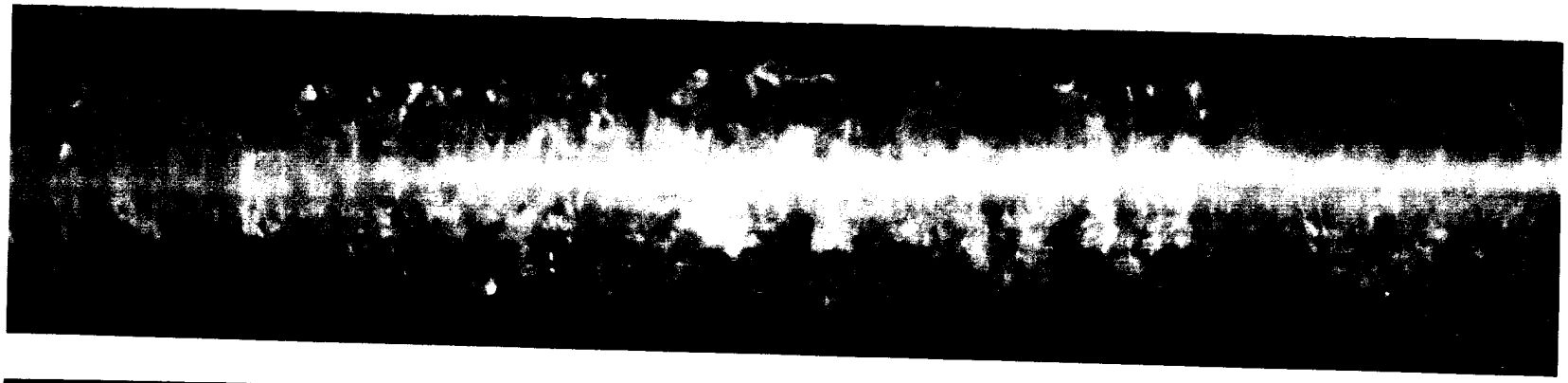

c) x/c: 6.9-12.1

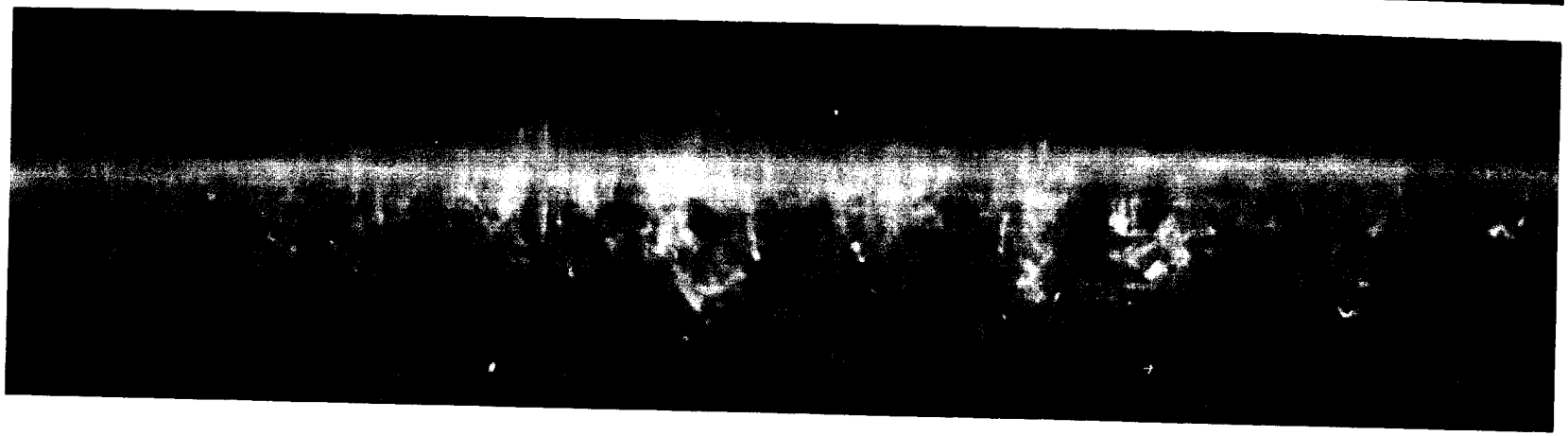

Figure 5.11 - Side view flow visualizations, Re=49,200, C_L=0.3

d) x/c: 18.5-23.7

e) x/c: 27.4-32.6

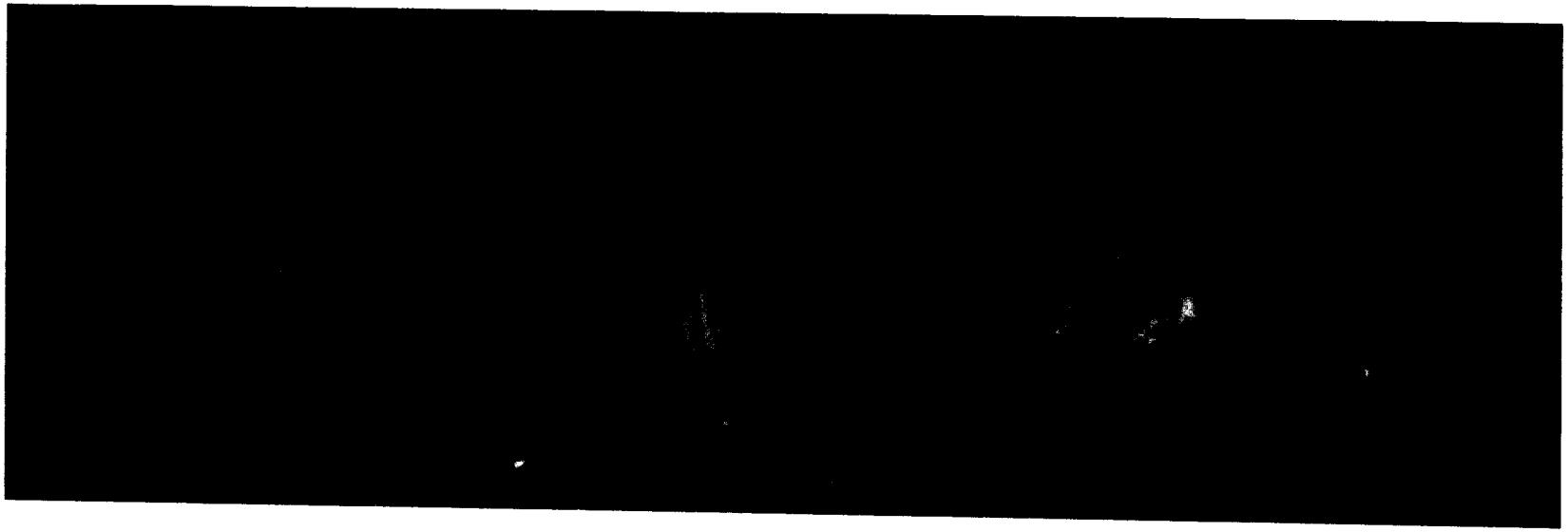

Figure 5.11 - Side view flow visualizations, Re=49,200, C_L=0.3

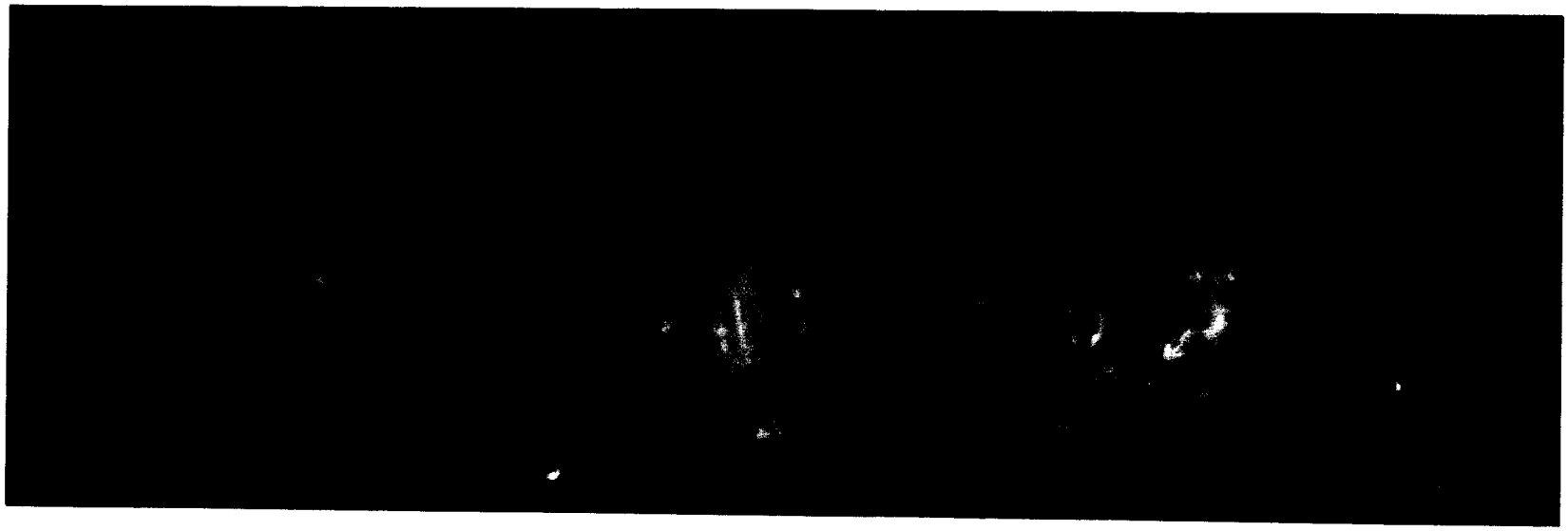

f) x/c: 32.6-38.1

Figure 5.11 - Side view flow visualizations, Re=49,200, C_L=0.3

a) x/c: 0-4.59

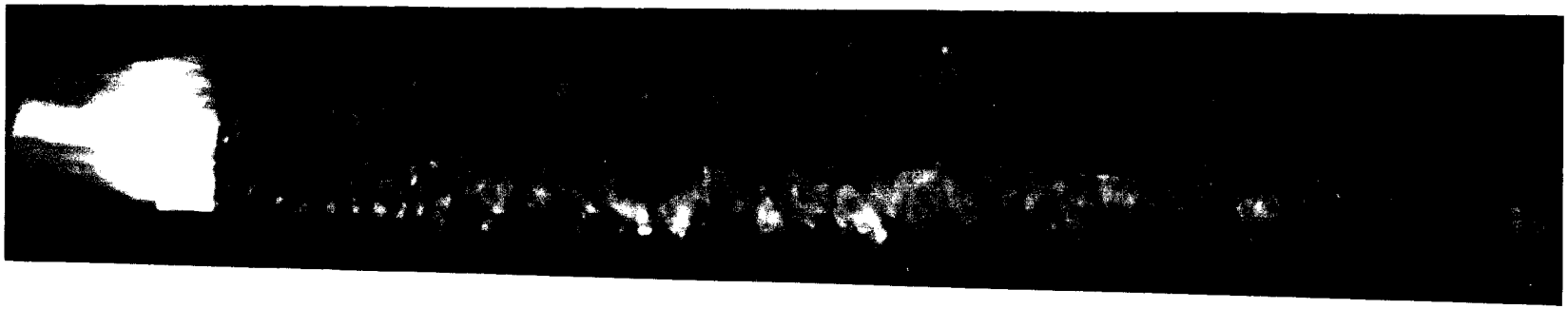

b) x/c: 7.4-12.6

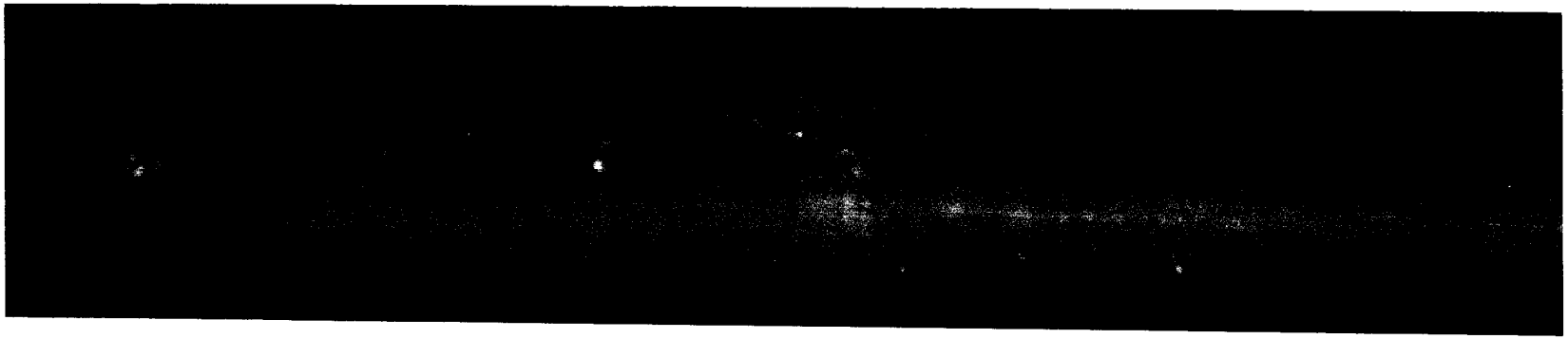

c) x/c: 15.1-20.3

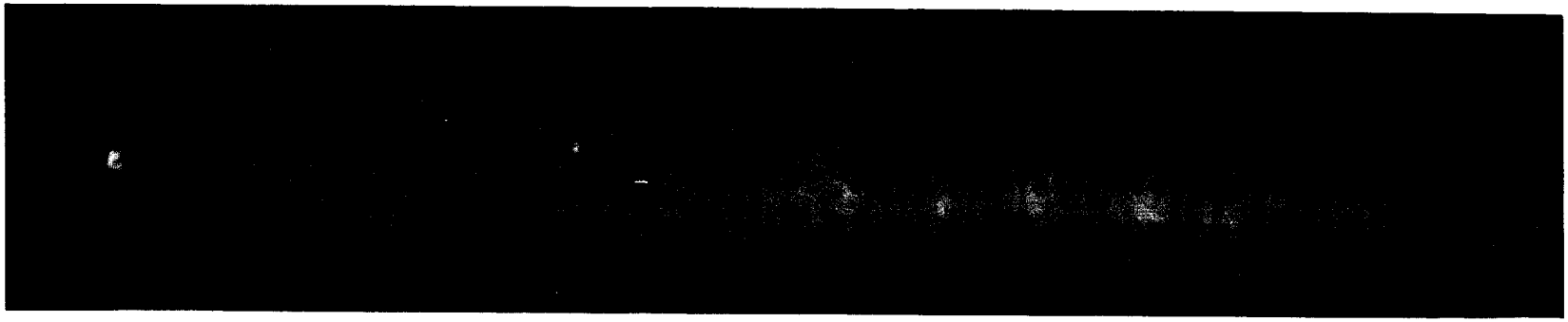

Figure 5.12 - Bottom view flow visualizations, Re=60,150, C_L=0.3

$C_L = 0.30$

$Re = 60,150$

1/

d) x/c: 23.4-28.6

e) x/c: 28.1-33.3

Figure 5.12 - Bottom view flow visualizations, Re=60,150, C_L=0.3

a) x/c: 0-4.59

b) x/c: 7.4-12.6

c) x/c: 15.1-20.3

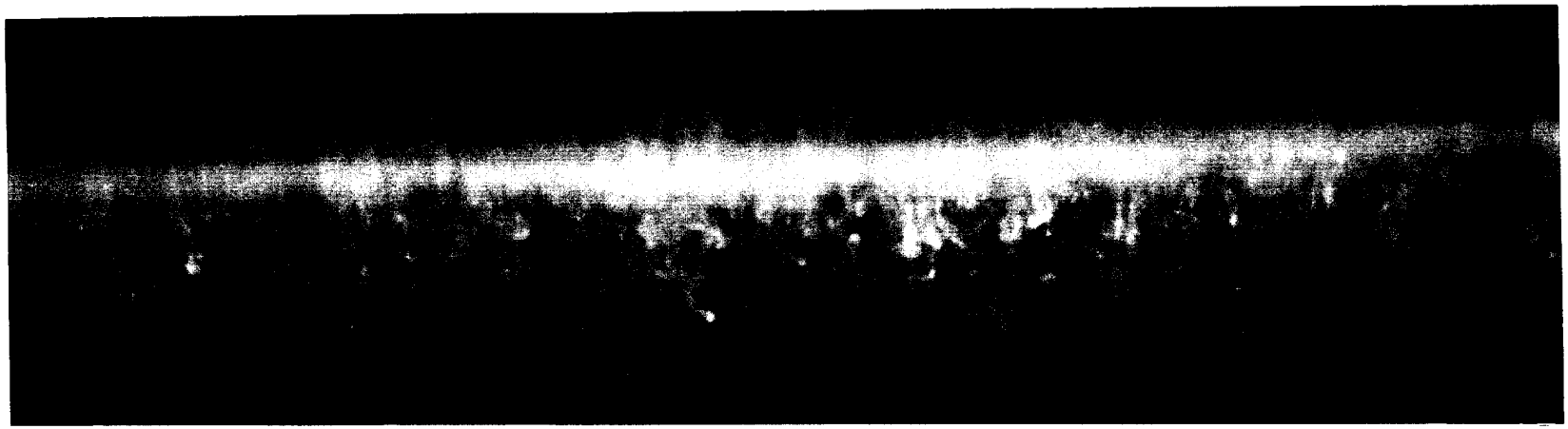

Figure 5.13 - Side view flow visualizations, Re=60,150, C_L=0.3

d) x/c: 23.4-28.6

e) x/c: 28.1-33.3

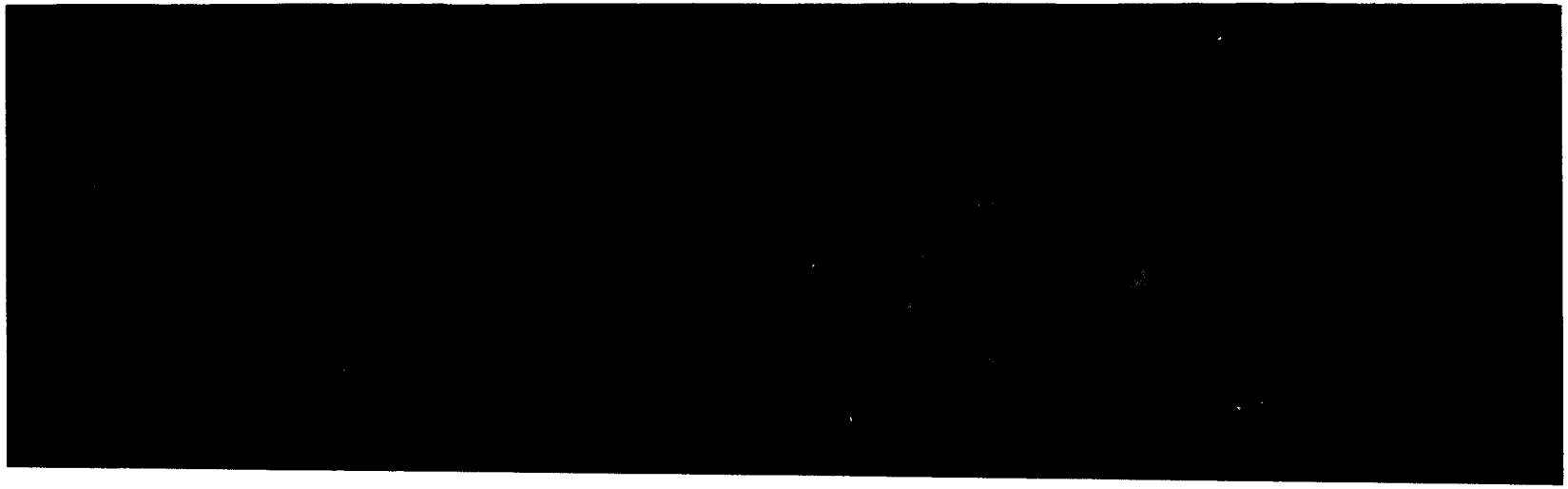

Figure 5.13 - Side view flow visualizations, Re=60,150, C_L=0.3

a) x/c: 0-4.7

b) x/c: 2.6-7.9

c) x/c: 6.7-12.0

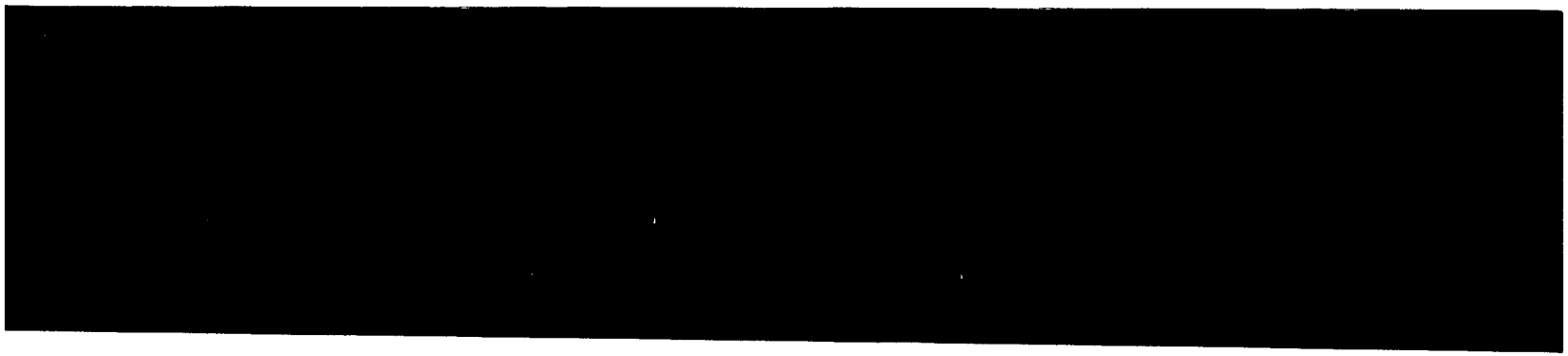

Figure 5.14 - Bottom view flow visualizations, Re=88,100, C_L=0.3

d) x/c: 11.8-17.1

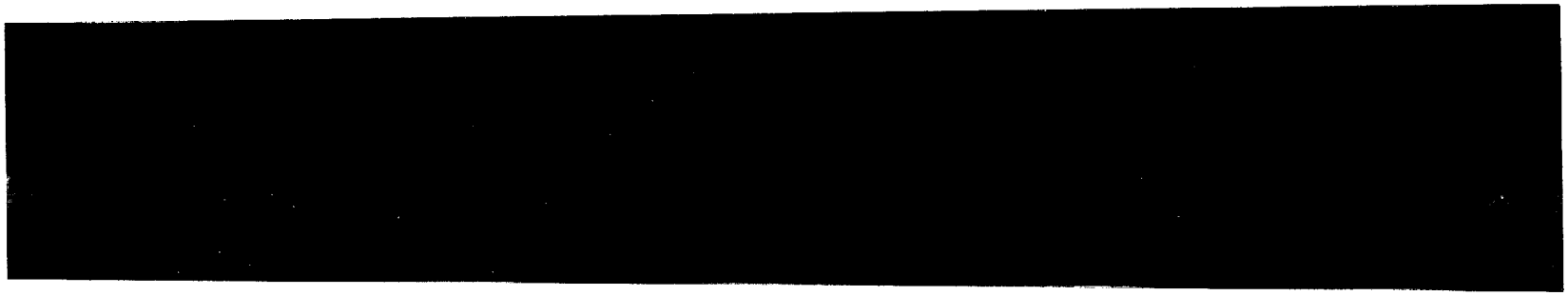

e) x/c: 26.7-32.0

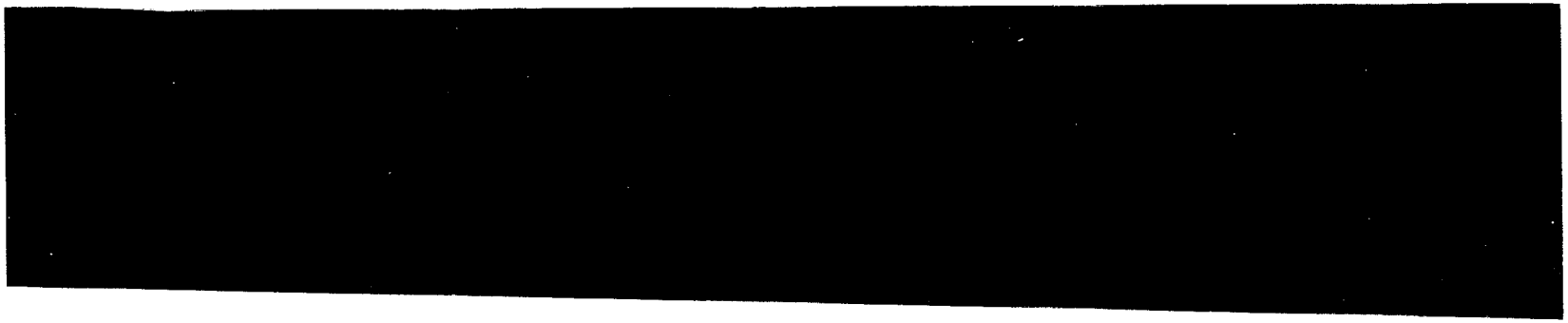

Figure 5.14 - Bottom view flow visualizations. Re=88,100, C_L=0.3

a) x/c: 0-4.7

b) x/c: 2.6-7.9

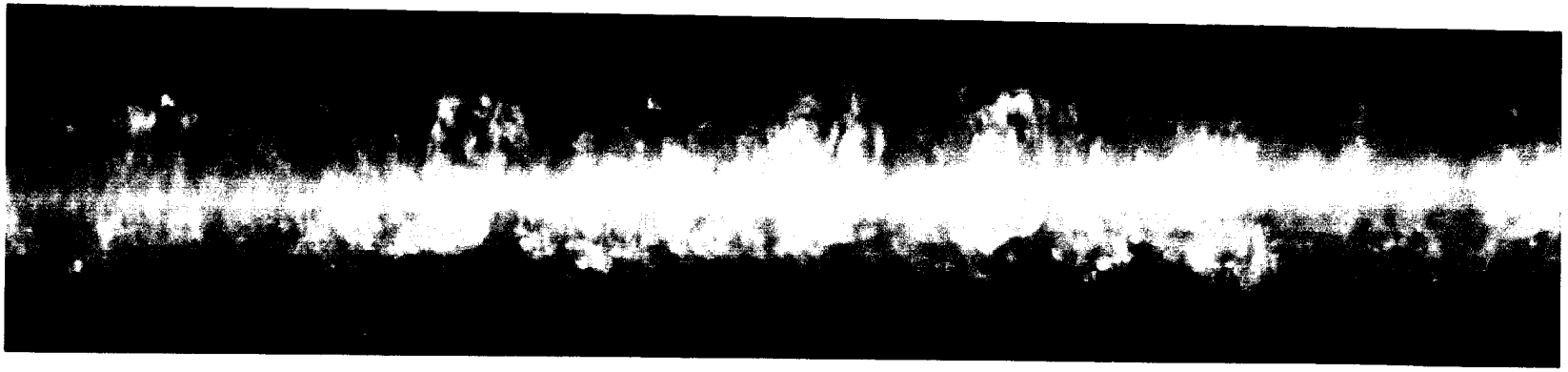

c) x/c: 6.7-12.0

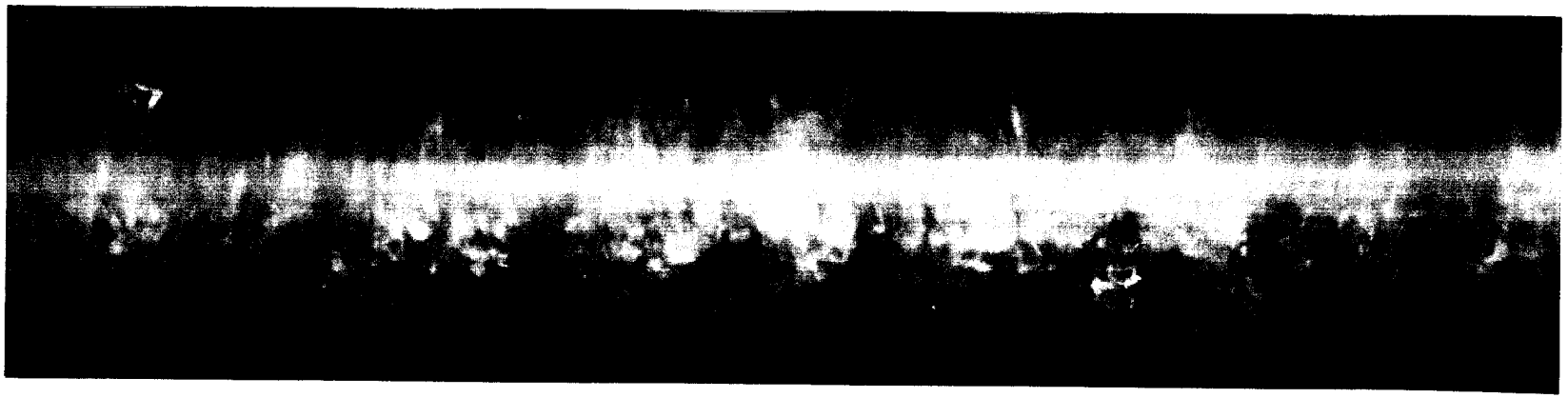

Figure 5.15 - Side view flow visualizations, Re=88,100, C_L=0.3

d) x/c: 11.8-17.1

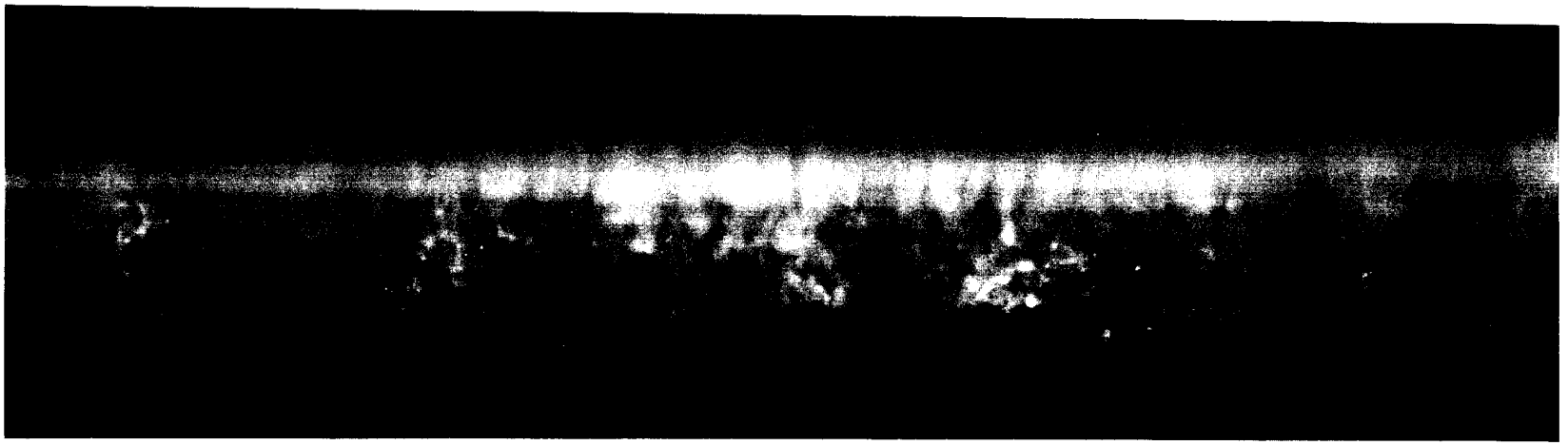

e) x/c: 26.7-32.0

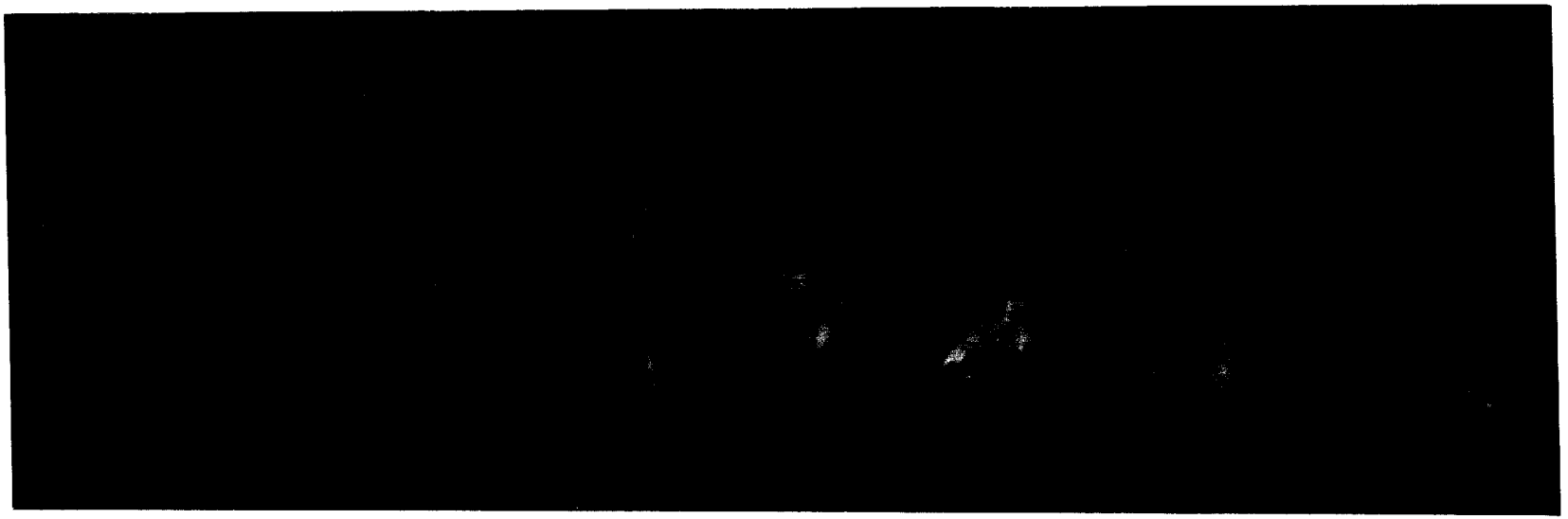

Figure 5.15 - Side view flow visualizations, Re=88,100, C_L=0.3

a) x/c: 0-1.8

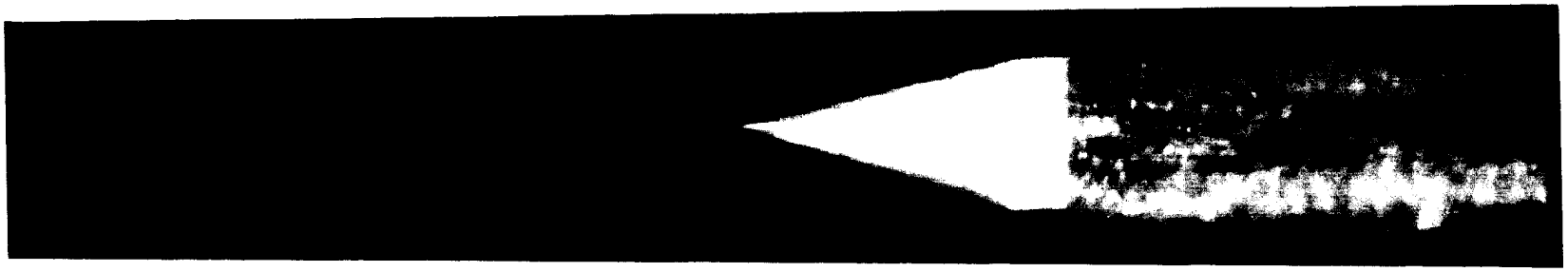

b) x/c: 3.4-8.7

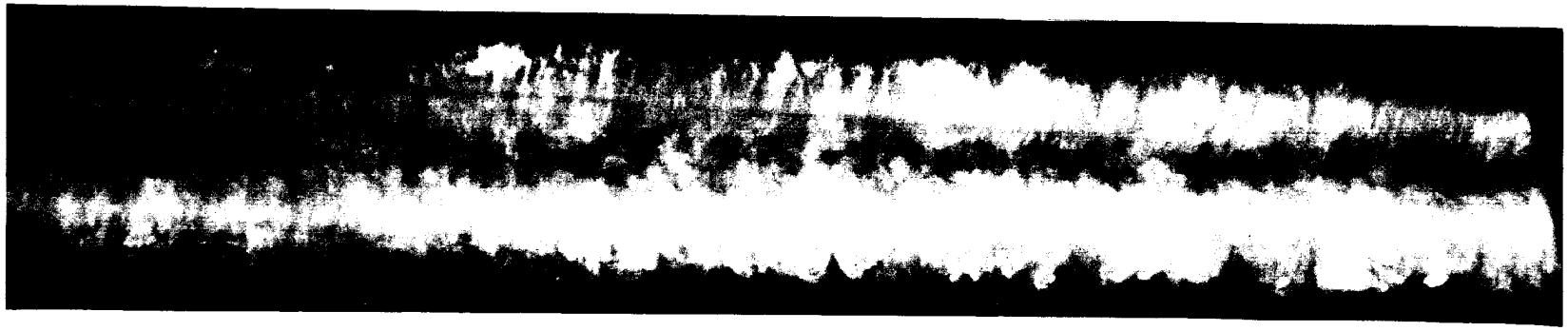

c) x/c: 10.6-16.0

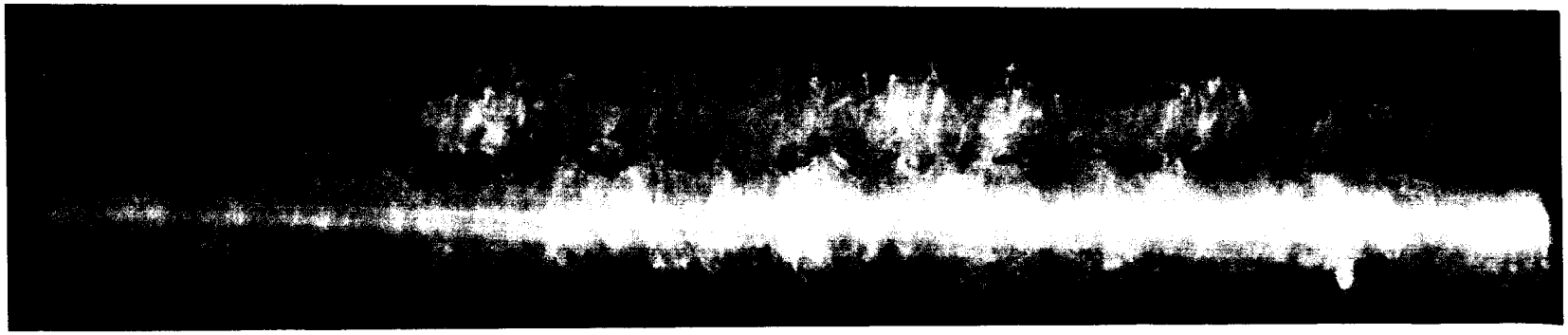

Figure 5.16 - Bottom view flow visualizations, Re=125,800, C_L=0.3

d) x/c: 18.5-23.8

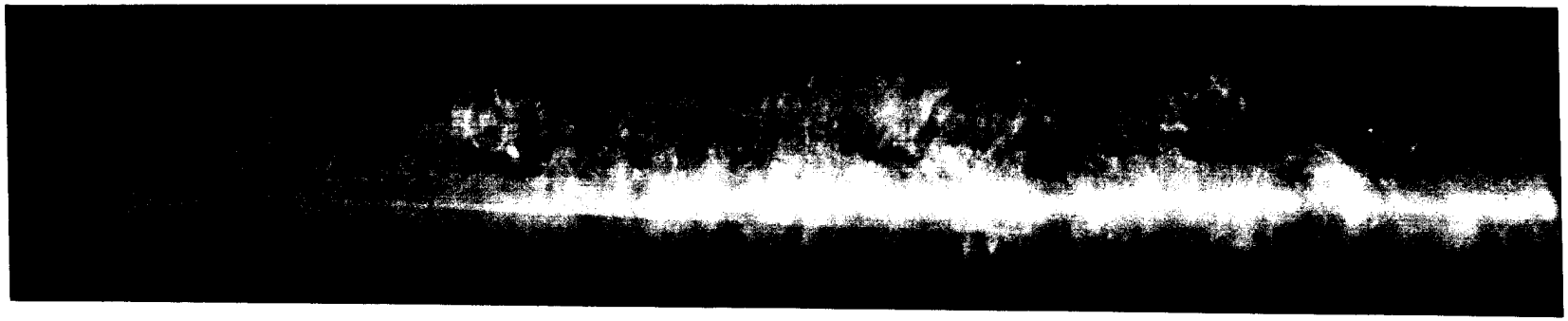

e) x/c: 25.3-30.6

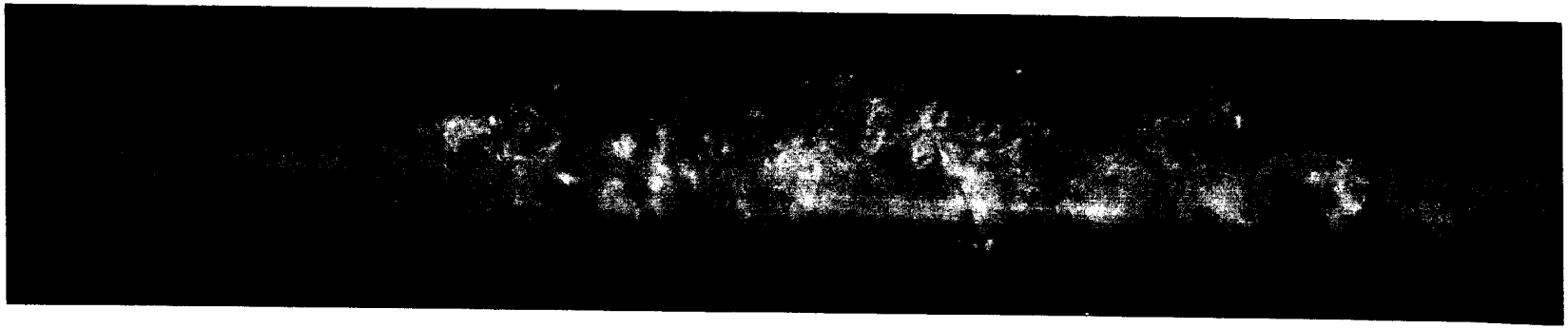

f) x/c: 31.5-36.8

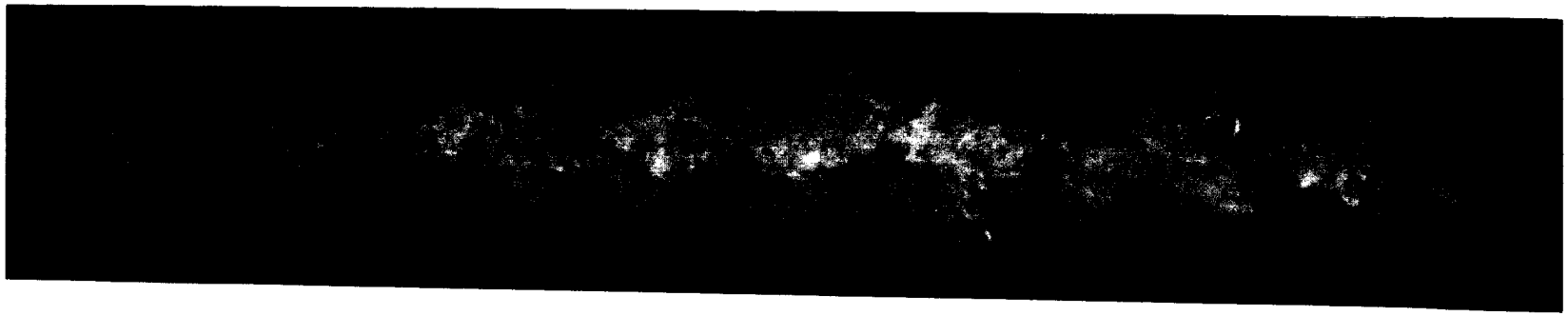

Figure 5.16 - Bottom view flow visualizations, Re=125,800, C_L=0.3

a) x/c: 0-1.8

b) x/c: 3.4-8.7

c) x/c: 10.6-16.0

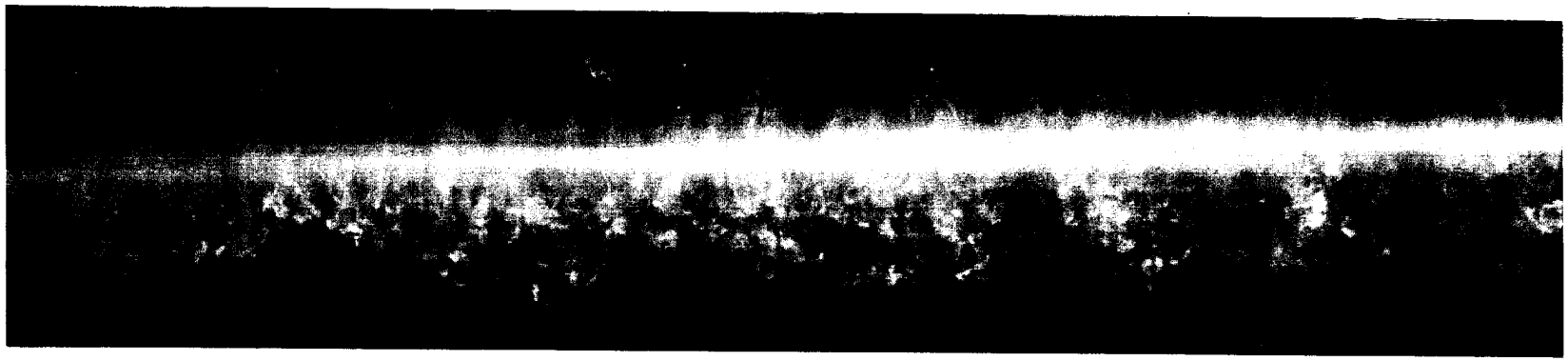

Figure 5.17 - Side view flow visualizations, Re=125,800, C_L=0.3

d) x/c: 18.5-23.8

e) x/c: 25.3-30.6

Figure 5.17 - Side view flow visualizations, Re=125,800, C_L=0.3

$C_L = 0.30$
$Re = 125,800$

+/

f) x/c: 31.5-36.8

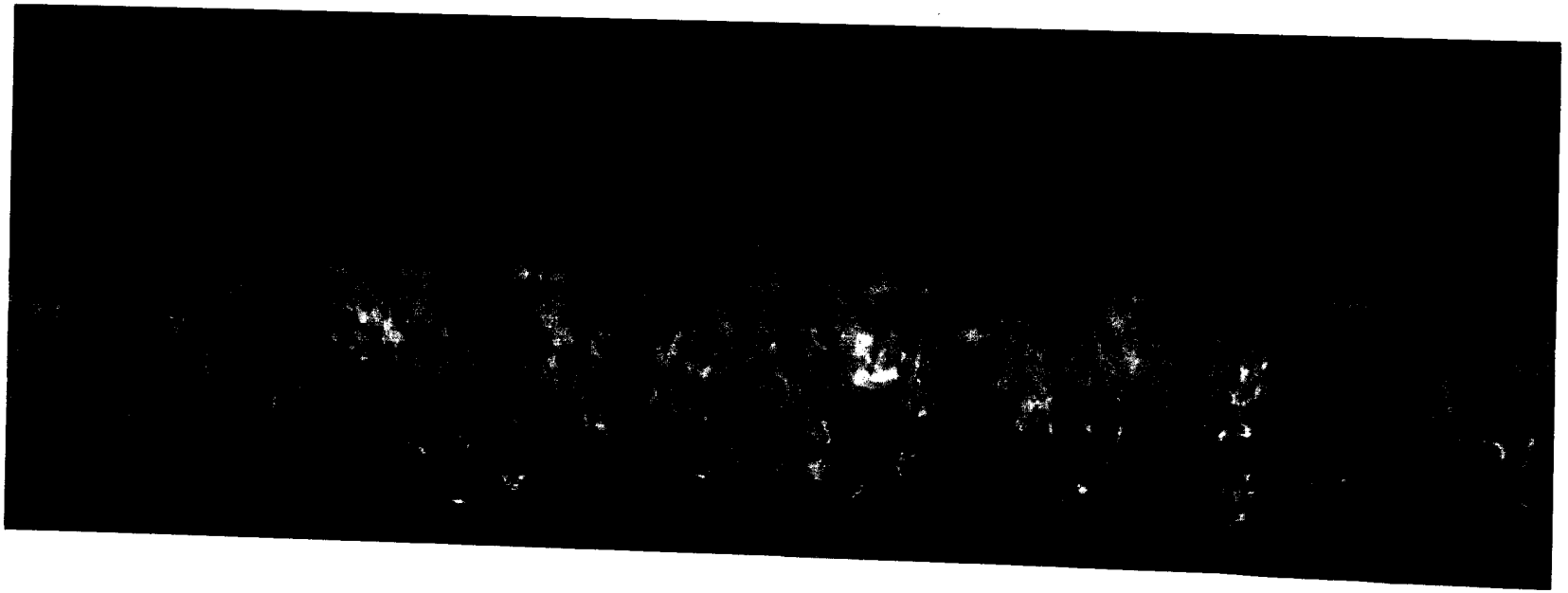

Figure 5.17 - Side view flow visualizations, Re=125,800, C_L=0.3

a) x/c: 0-2.1

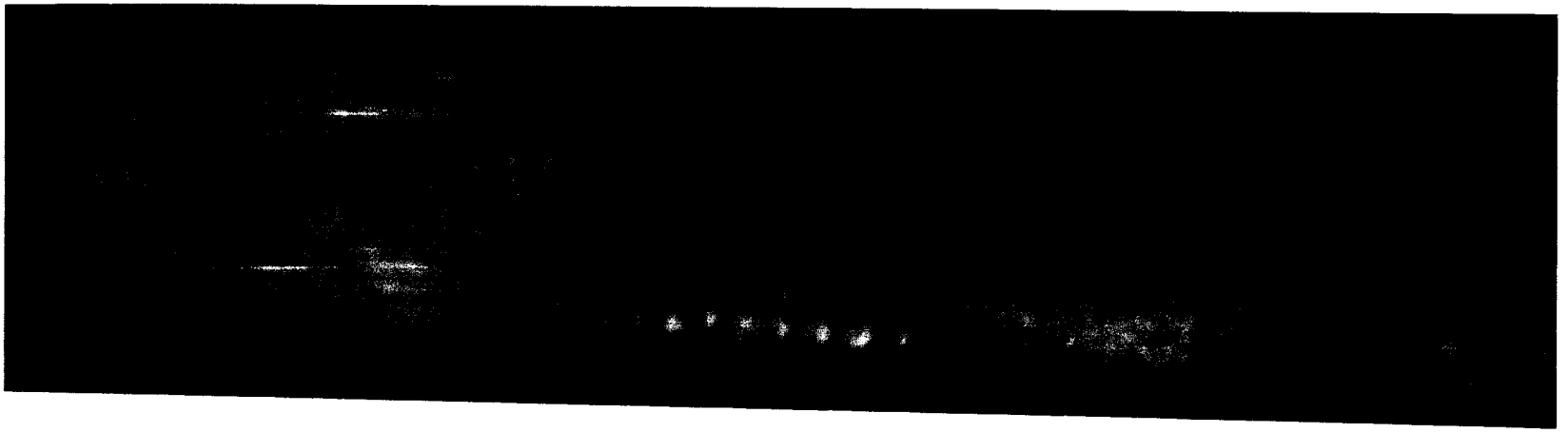

b) x/c: 1.3-3.9

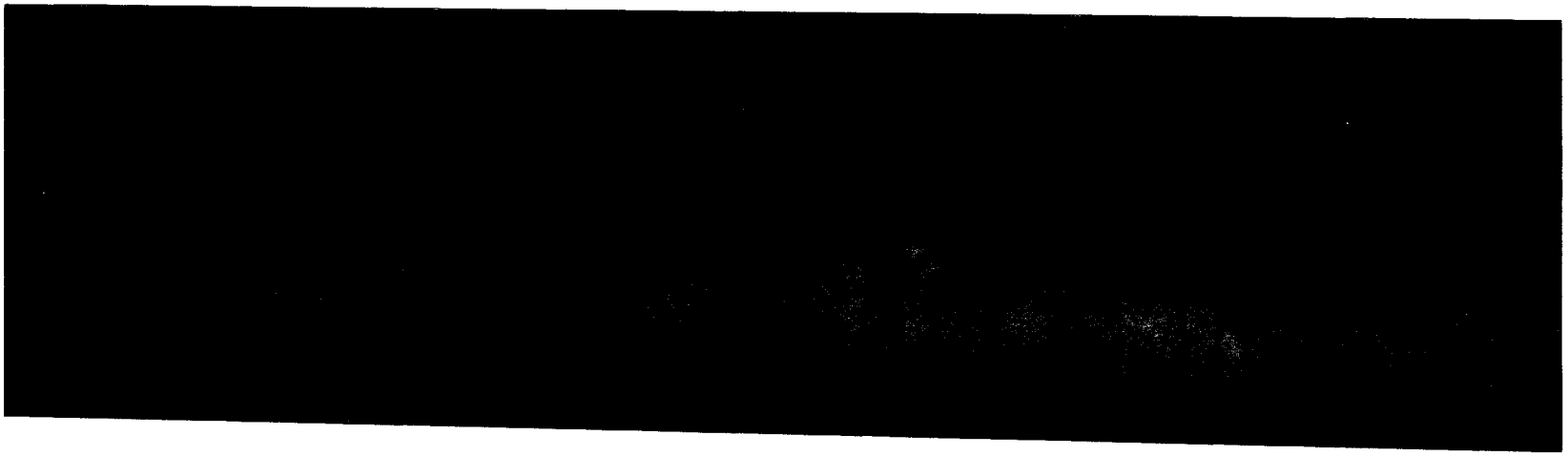

Figure 5.18 - Bottom view flow visualizations, Re=200,400, C_L=0.3

c) x/c: 5.2-7.8

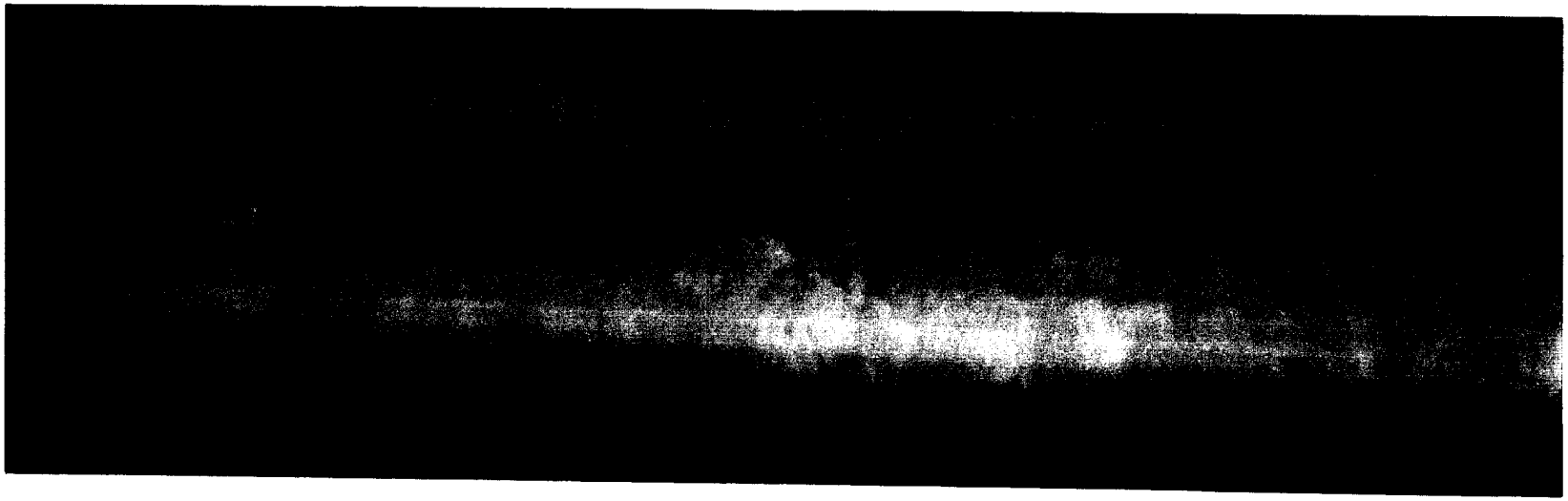

d) x/c: 12.2-14.8

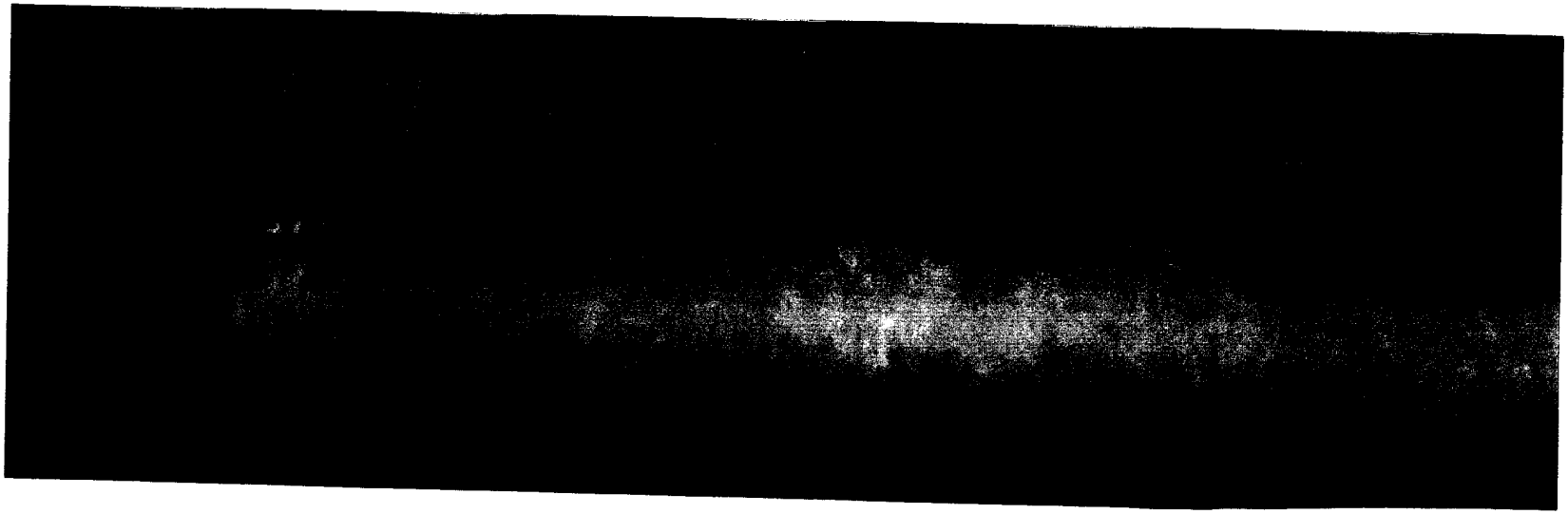

Figure 5.18 - Bottom view flow visualizations, Re=200,400, C_L=0.3

$C_L = 0.30$
$Re = 200,400$

e) x/c: 14.5-17.1

f) x/c: 18.4-21.0

Figure 5.18 - Bottom view flow visualizations, Re=200,400, C_L=0.3

g) x/c: 25.1-27.7

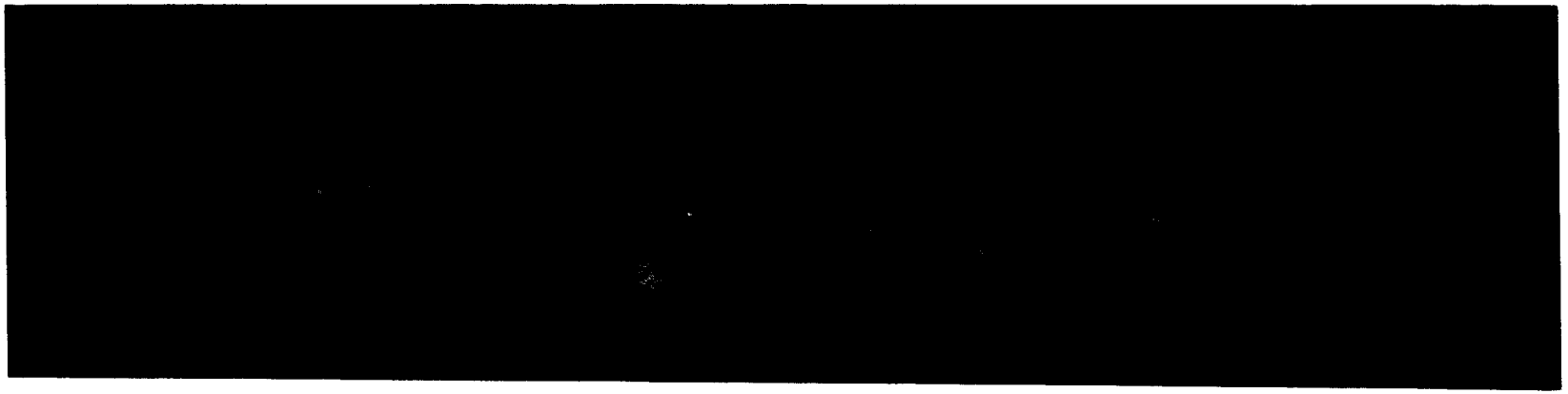

Figure 5.18 - Bottom view flow visualizations, Re=200,400, C_L=0.3

$C_L = 0.30$

$Re = 200,400$

a) x/c: 0-2.1

b) x/c: 1.3-3.9

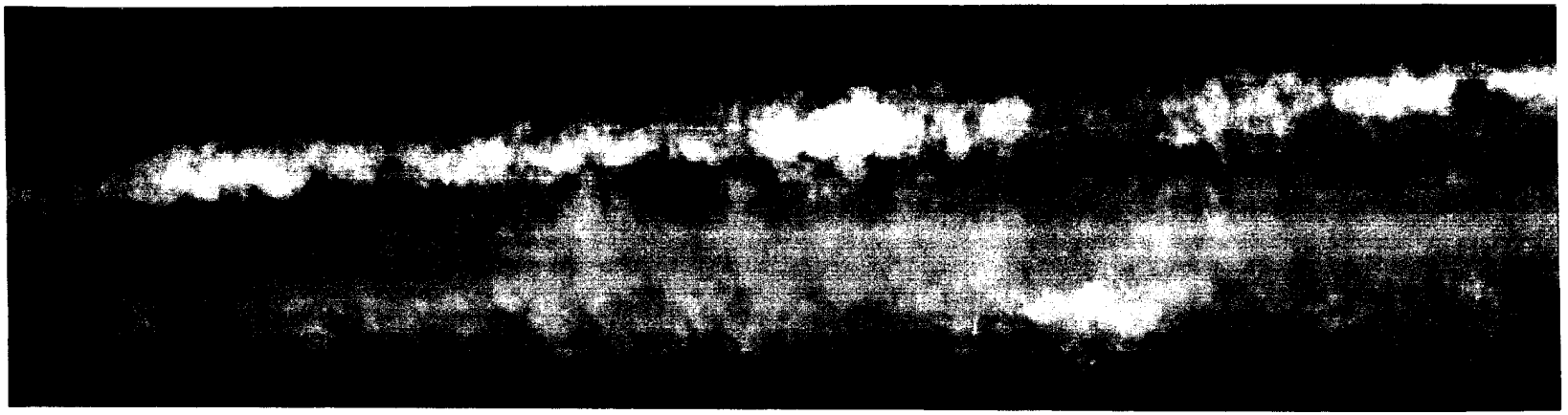

Figure 5.19 - Side view flow visualizations, Re=200,400, C_L=0.3

c) x/c: 5.2-7.8

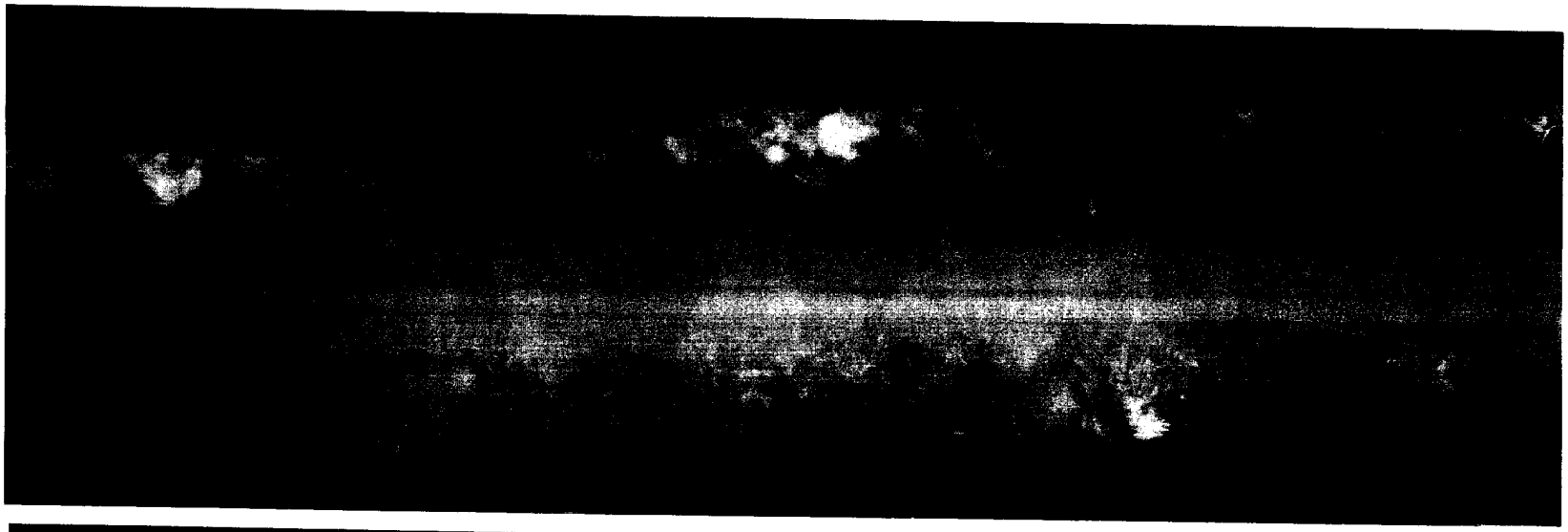

d) x/c: 12.2-14.8

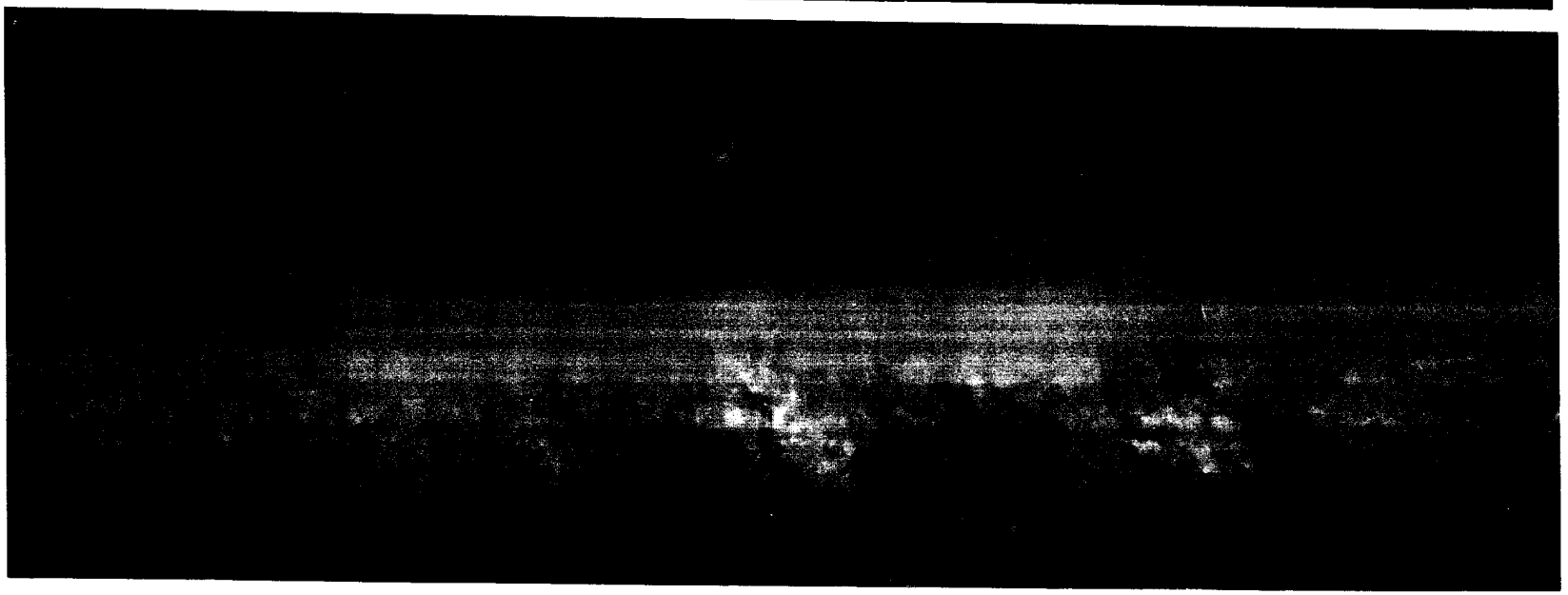

Figure 5.19 - Side view flow visualizations, Re=200,400, C_L=0.3

e) x/c: 14.5-17.1

f) x/c: 18.4-21.0

Figure 5.19 - Side view flow visualizations, Re=200,400, C_L=0.3

g) x/c: 25.1-27.7

a) x/c: 0-2.0

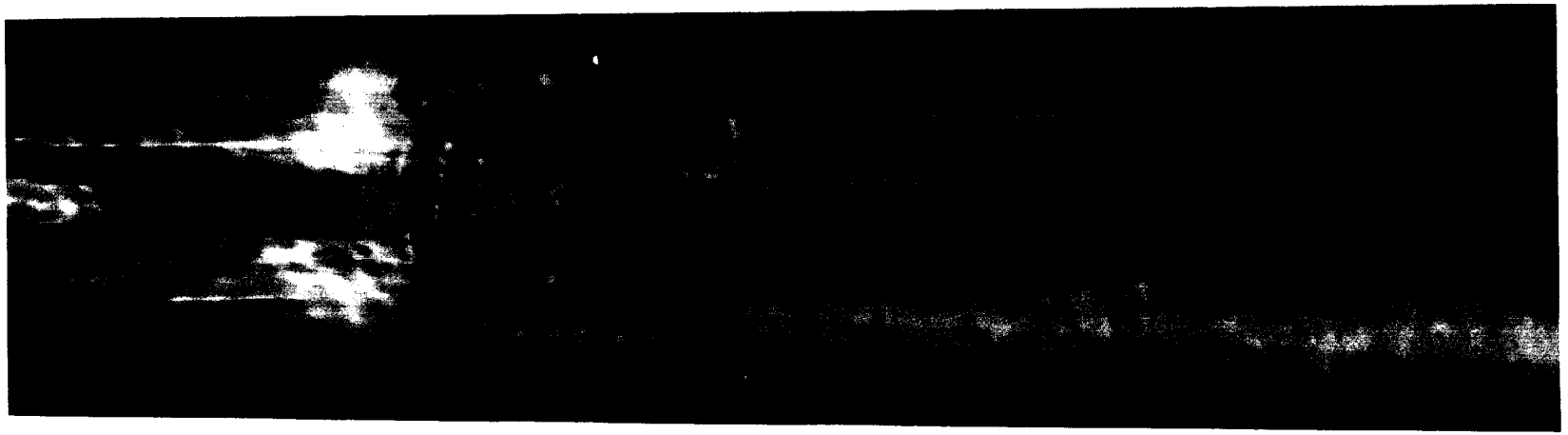

b) x/c: 2.9-5.6

Figure 5.20 - Bottom view flow visualizations, Re=285,400, C_L=0.3

c) x/c: 5.5-8.2

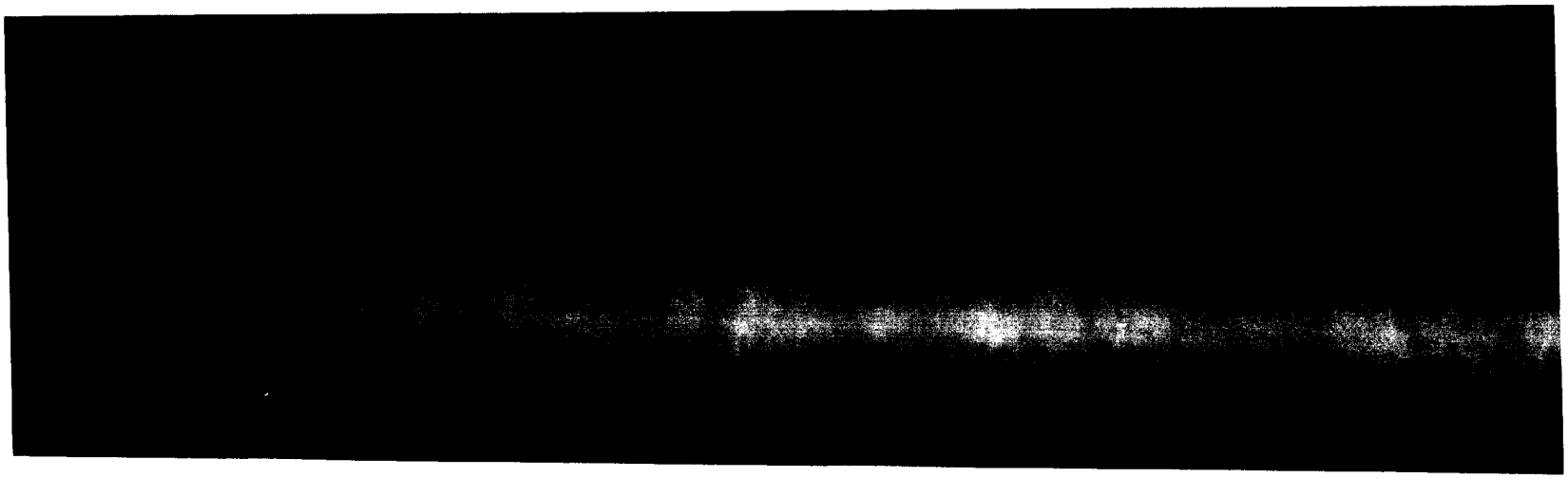

d) x/c: 8.3-11.1

Figure 5.20 - Bottom view flow visualizations, Re=285,400, C_L=0.3

e) x/c: 12.2-14.4

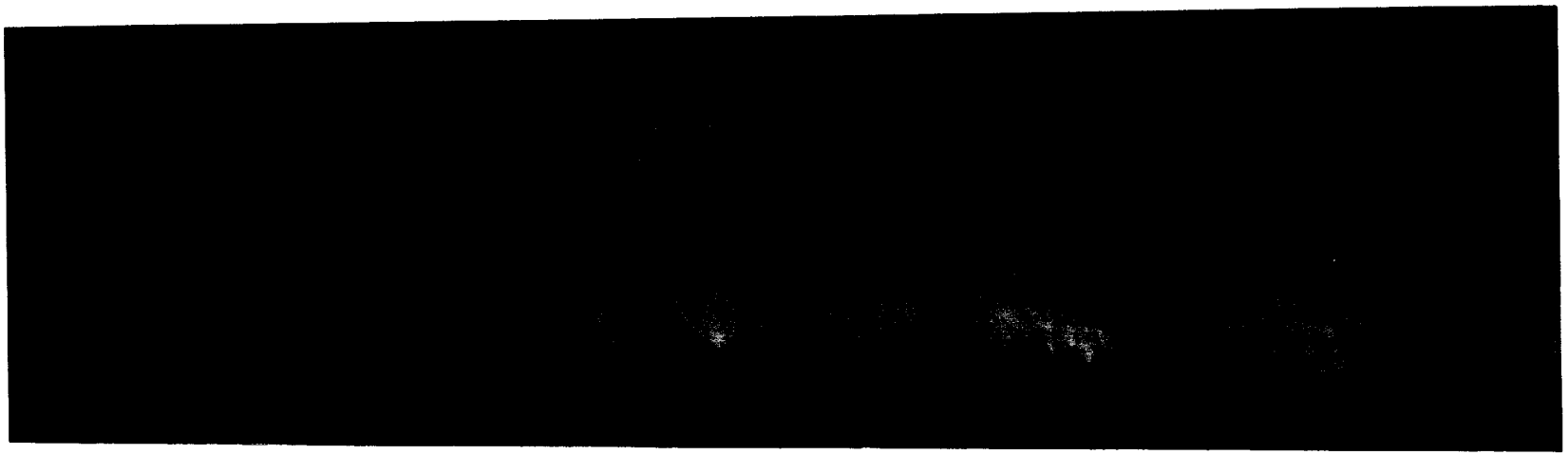

f) x/c: 15.8-18.5

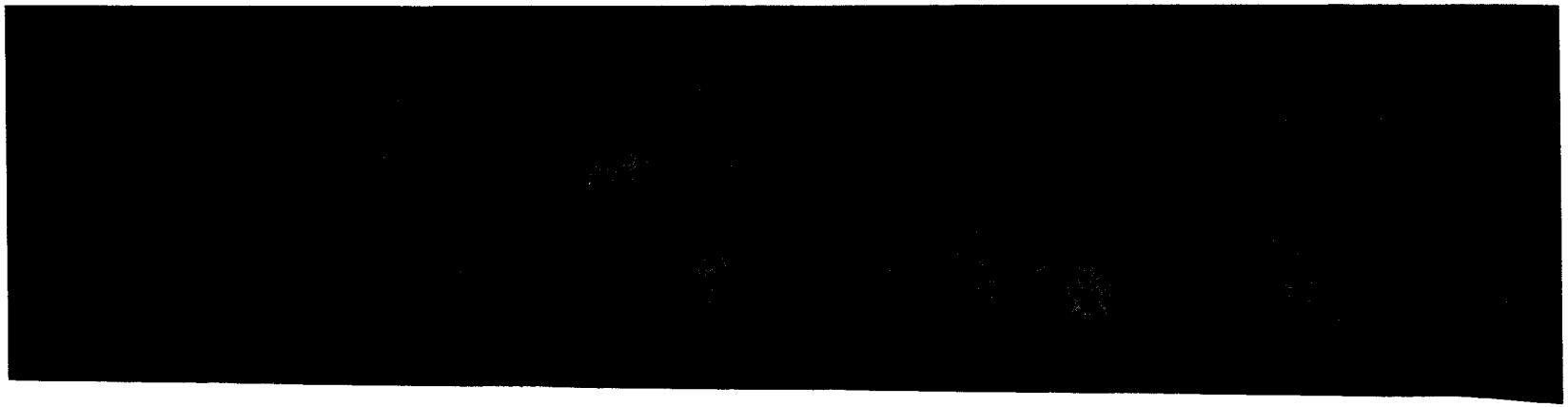

Figure 5.20 - Bottom view flow visualizations, Re=285,400, C_L=0.3

a) x/c: 0-2.0

b) x/c: 2.9-5.6

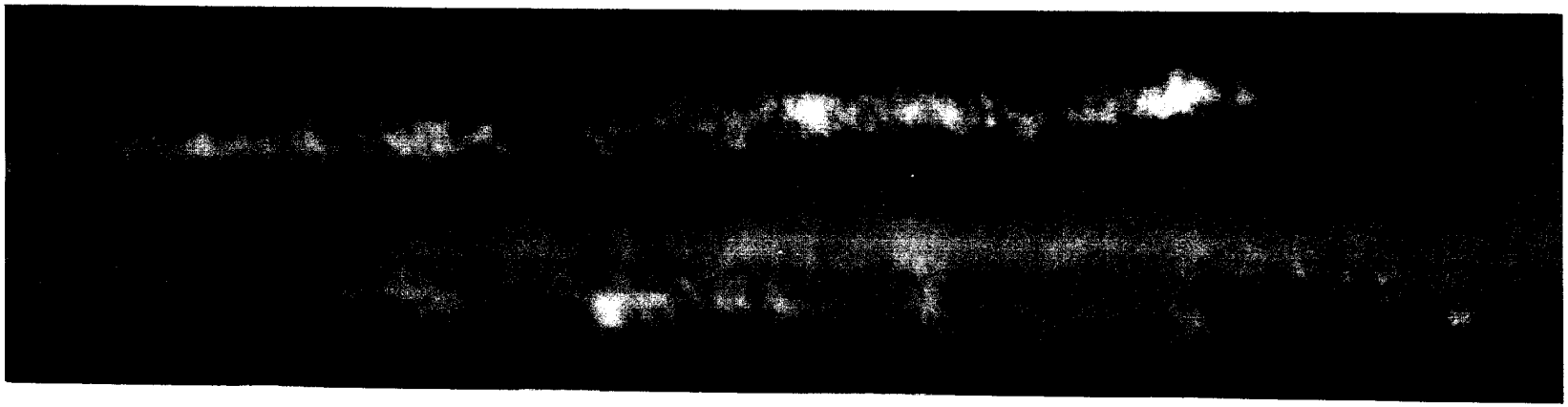

Figure 5.21 - Side view flow visualizations, Re=285,400, C_L=0.3

c) x/c: 5.5-8.2

d) x/c: 8.3-11.1

Figure 5.21 - Side view flow visualizations, Re=285,400, C_L=0.3

e) x/c: 12.2-14.4

f) x/c: 15.8-18.5

Figure 5.21 - Side view flow visualizations, Re=285,400, C_L=0.3

a) x/c: 0-2.6

b) x/c: 5.4-8.3

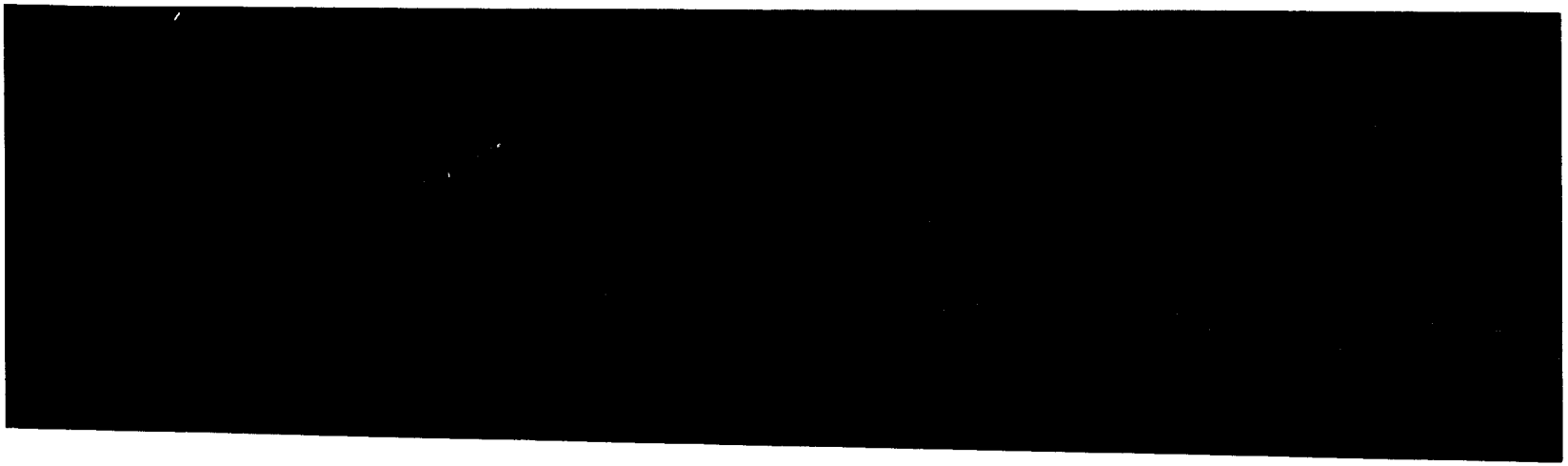

Figure 5.22 - Bottom view flow visualizations, Re=370,500, C_L=0.3

c) x/c: 12.7-15.6

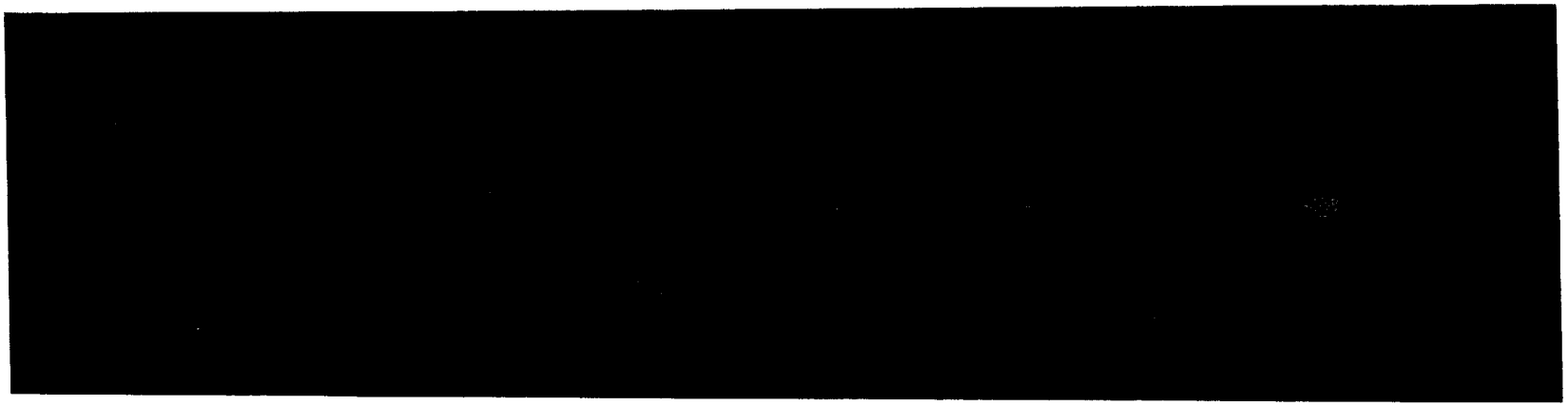

d) x/c: 19.2-22.0

Figure 5.22 - Bottom view flow visualizations, Re=370,500, C_L=0.3

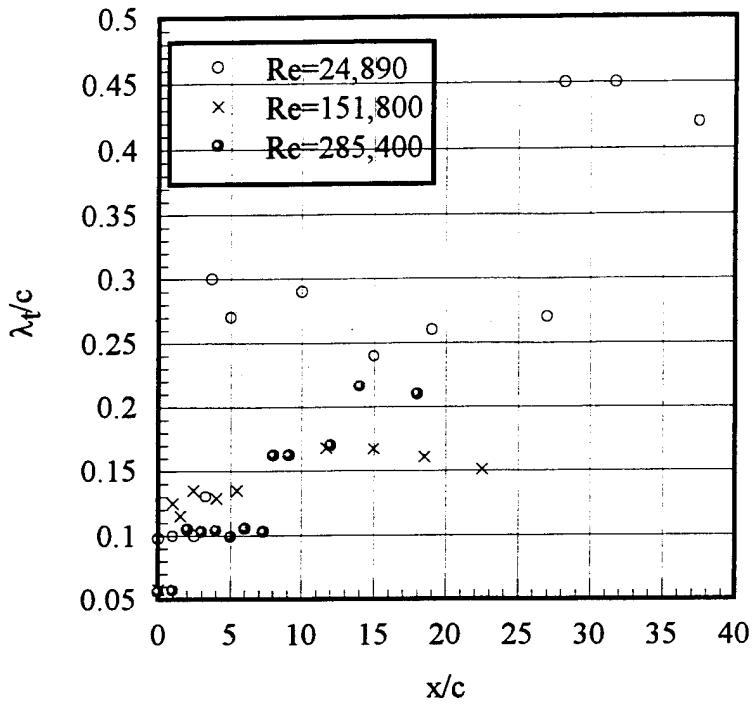

Figure 5.23 - Dominant turbulence scale as a function of downstream distance for a range of Reynolds numbers.

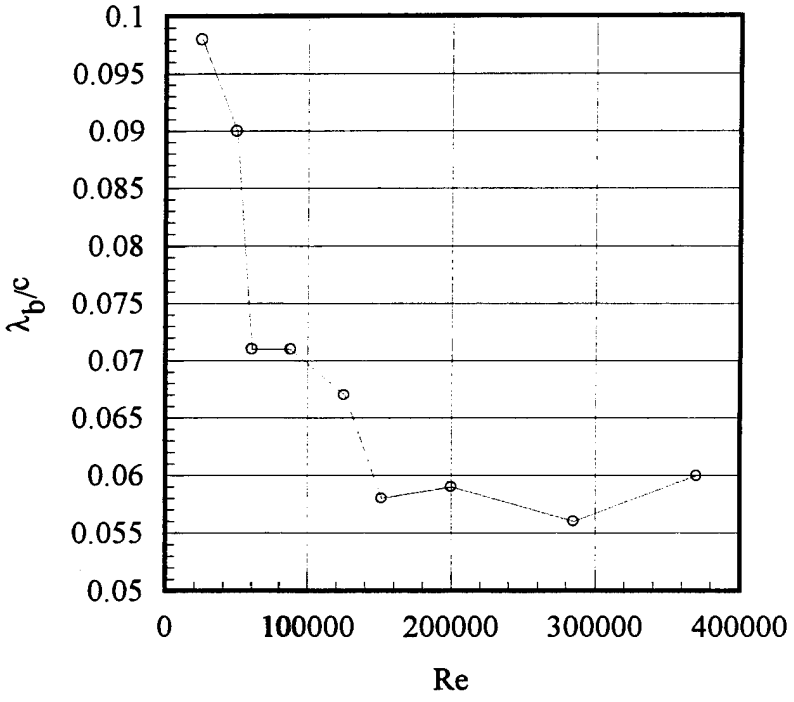

Figure 5.24 - Braid wake spacing as a function of Reynolds number

a) x/c: 0-1.9

b) x/c: 2.3-4.9

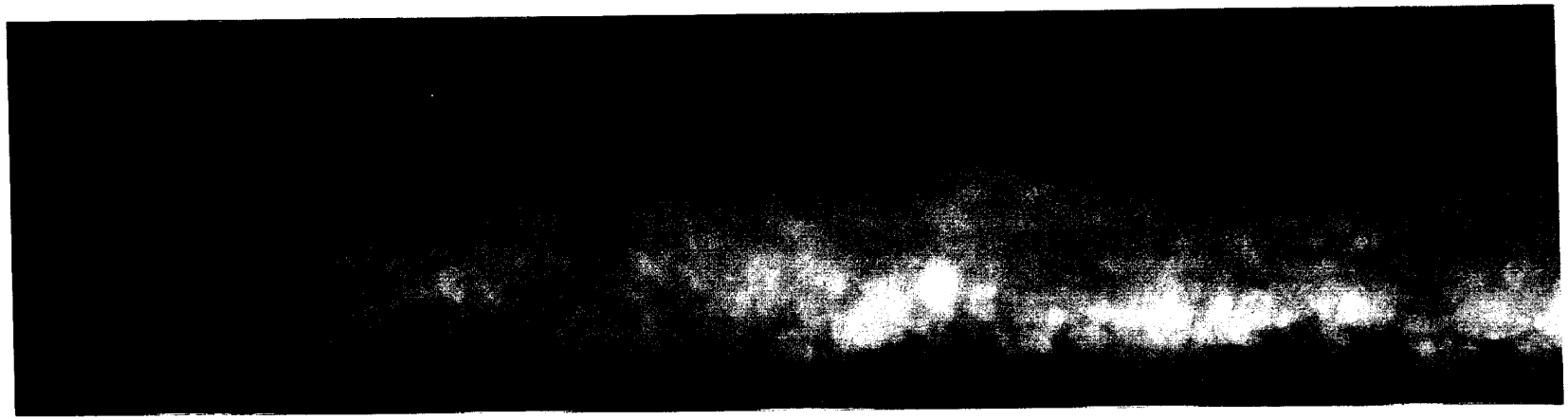

Figure 5.25 - Bottom view flow visualizations, Re=151,800, C_L=0.01

c) x/c: 4.5-7.2

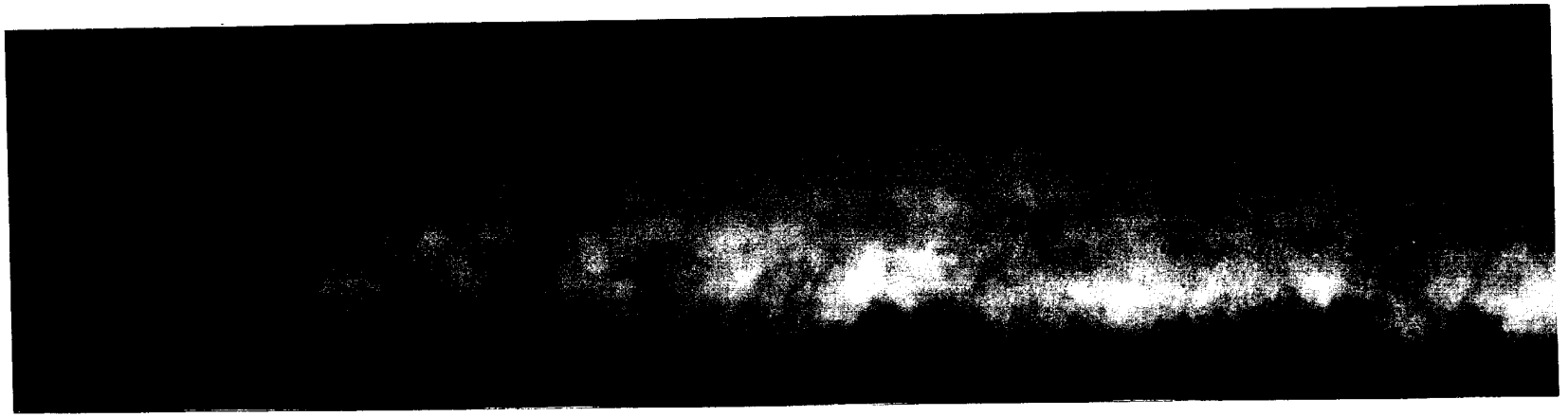

d) x/c: 9.8-12.4

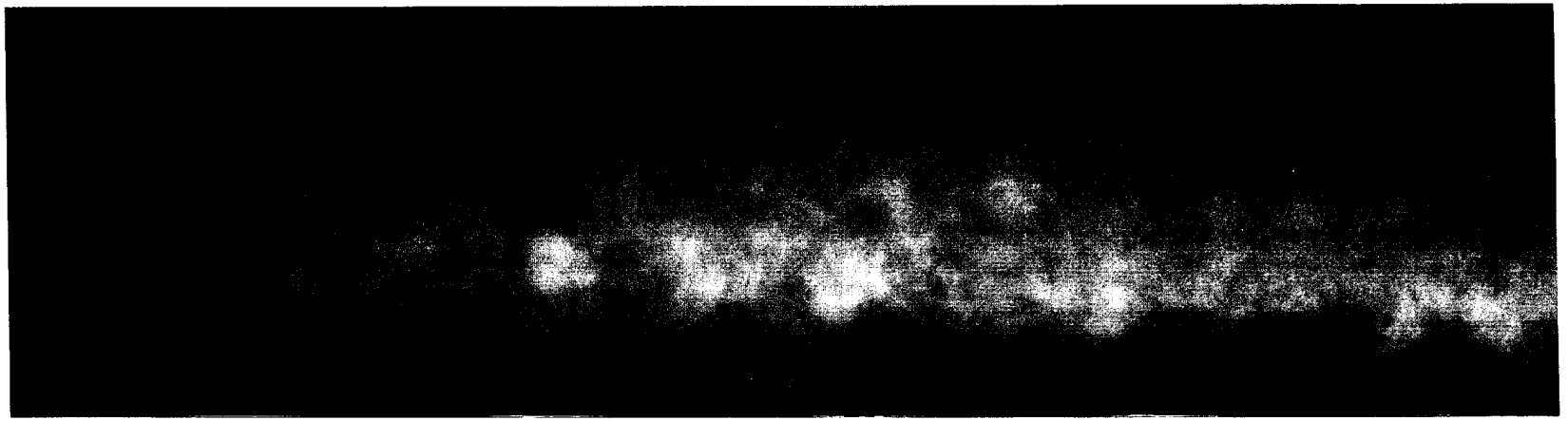

Figure 5.25 - Bottom view flow visualizations, Re=151,800, C_L=0.01

e) x/c: 19.4-22.0

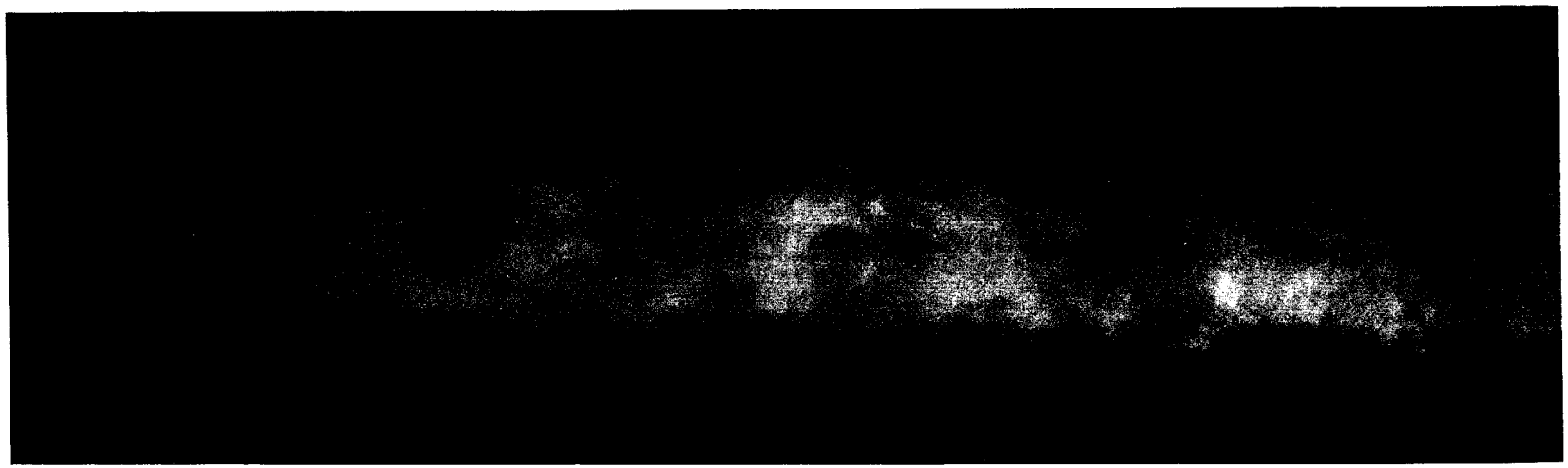

Figure 5.25 - Bottom view flow visualizations, Re=151,800, C_L=0.01

a) x/c: 0-1.9

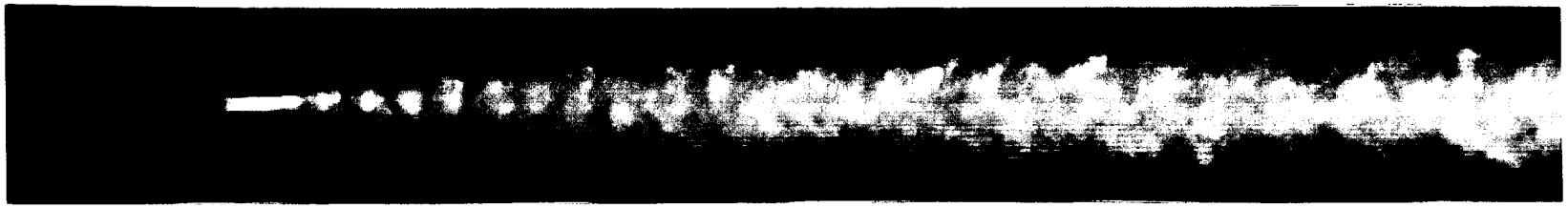

b) x/c: 2.3-4.9

c) x/c: 4.5-7.2

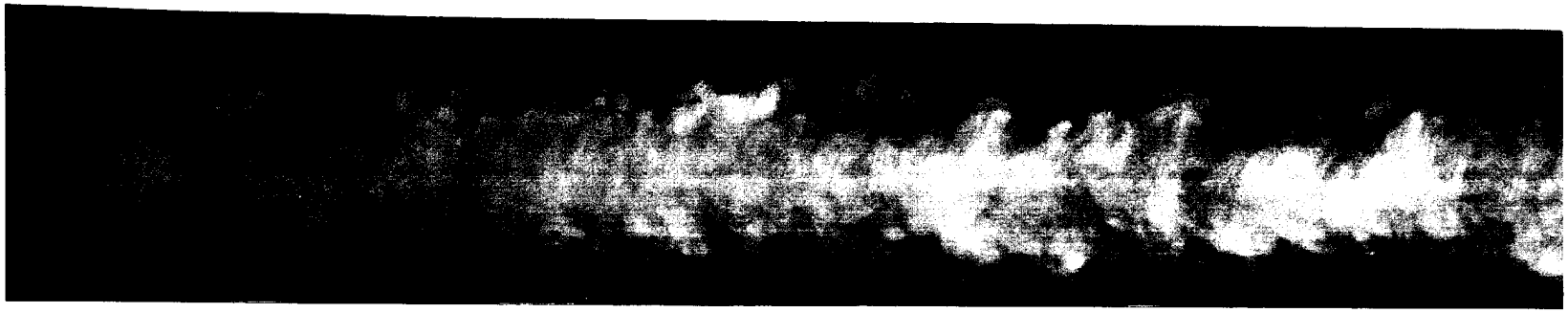

Figure 5.26 - Side view flow visualizations, Re=151,800, C_L=0.01

d) x/c: 9.8-12.4

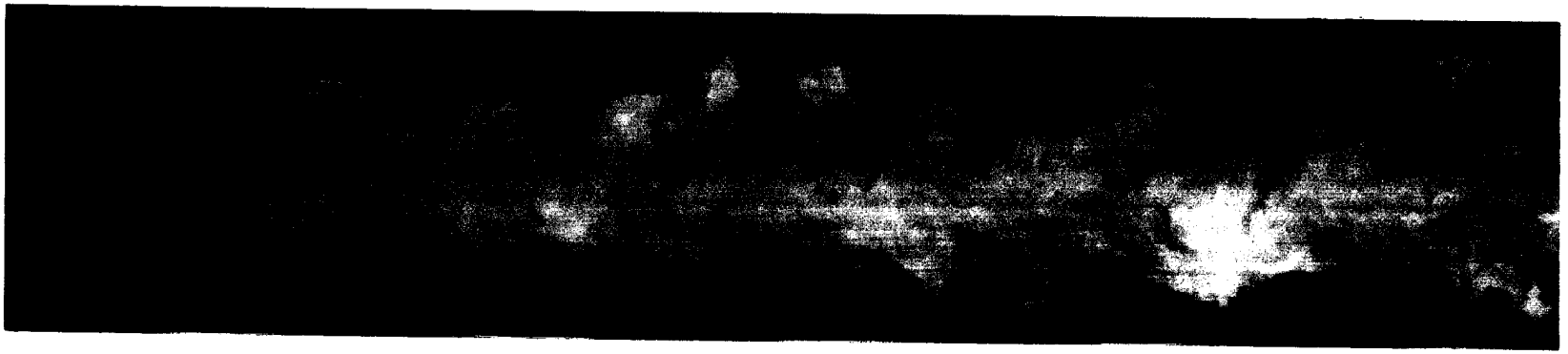

e) x/c: 19.4-22.0

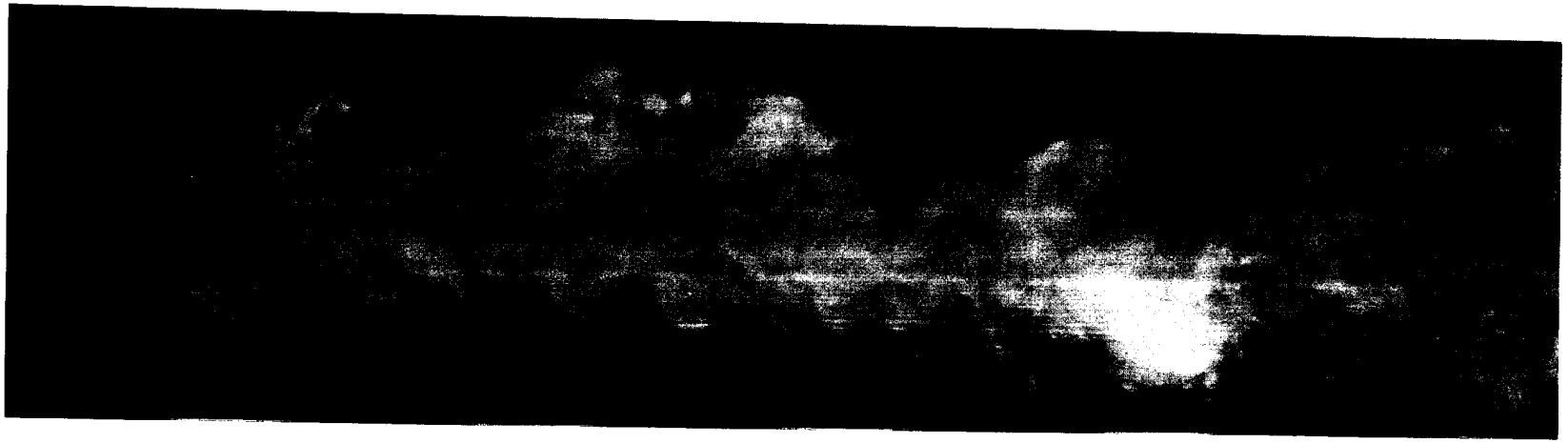

Figure 5.26 - Side view flow visualizations, Re=151,800, C_L=0.01

a) x/c: 0-1.7

b) x/c: 1.1-3.6

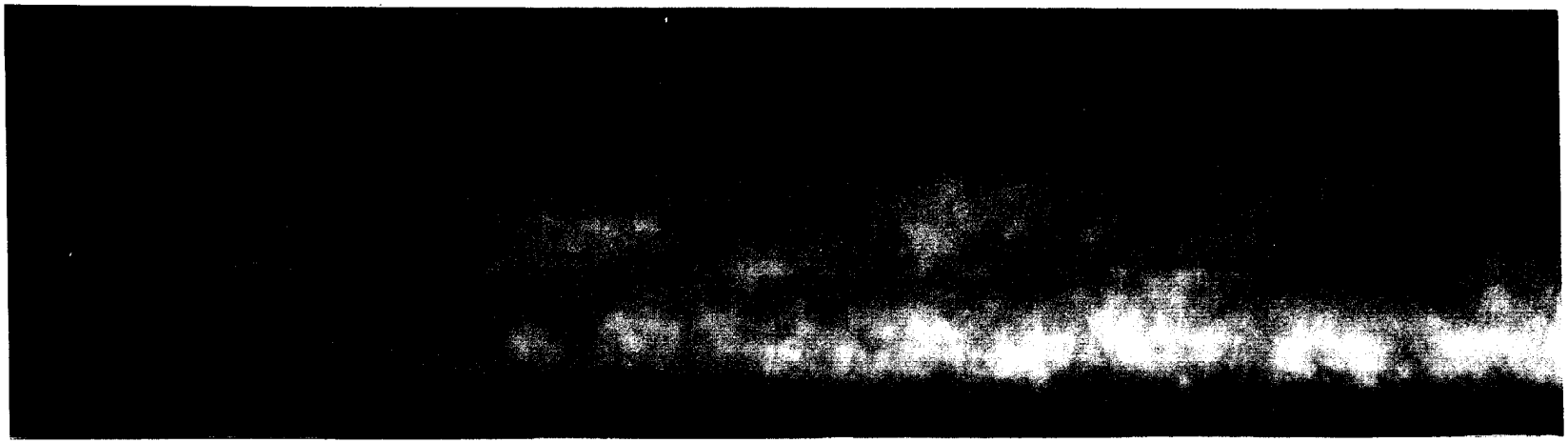

Figure 5.27 - Bottom view flow visualizations, Re=151,800, C_L=0.08

c) x/c: 3.1-5.6

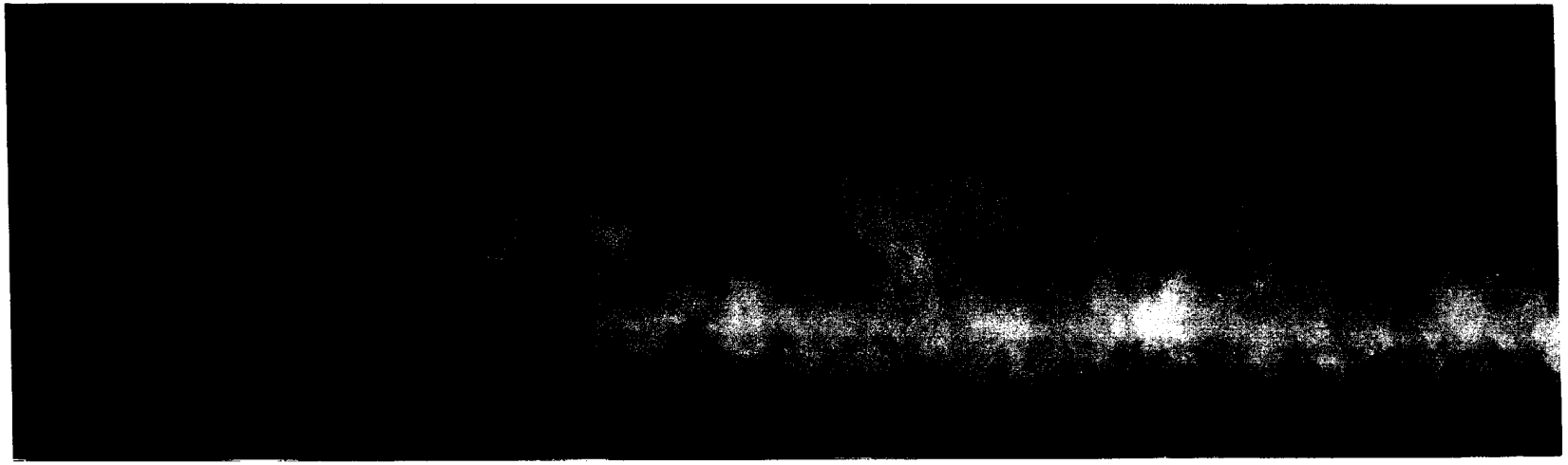

d) x/c: 9.8-12.4

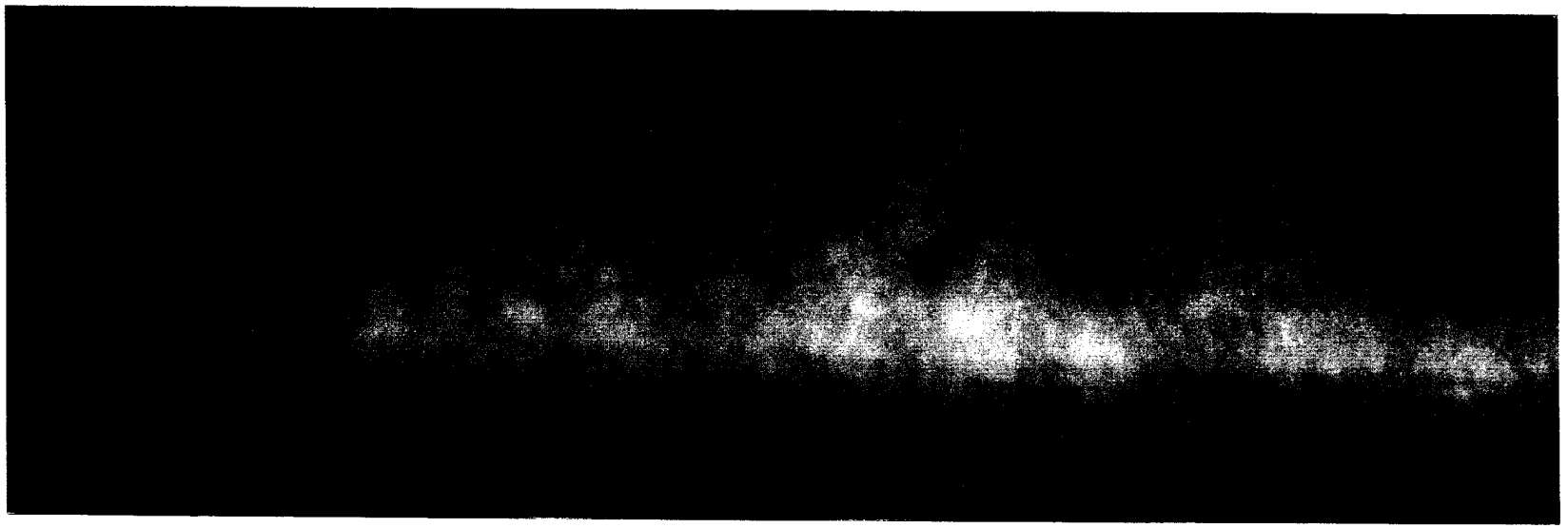

Figure 5.27 - Bottom view flow visualizations, Re=151,800, C_L=0.08

a) x/c: 0-1.7

b) x/c: 1.1-3.6

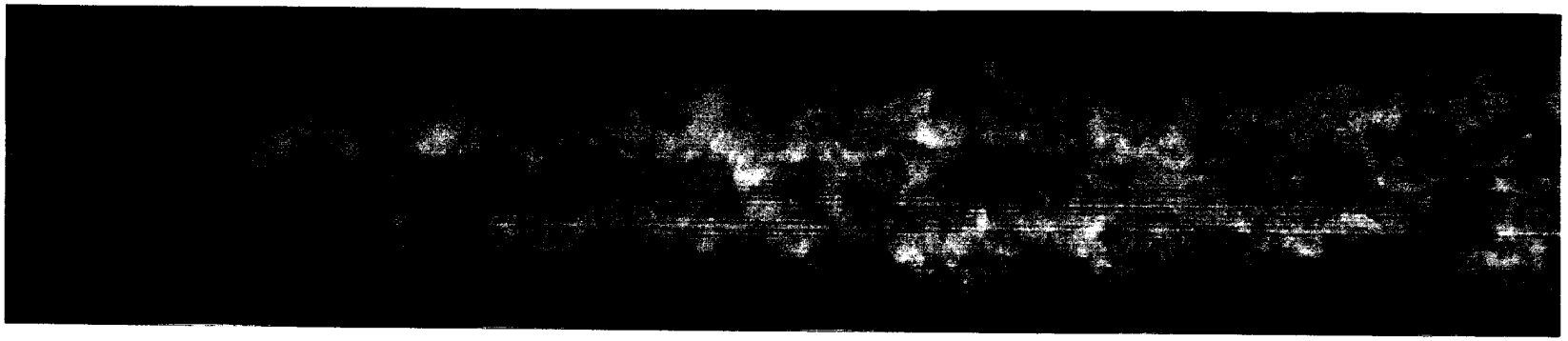

Figure 5.28 - Side view flow visualizations, Re=151,800, C_L=0.08

c) x/c: 3.1-5.6

d) x/c: 9.8-12.4

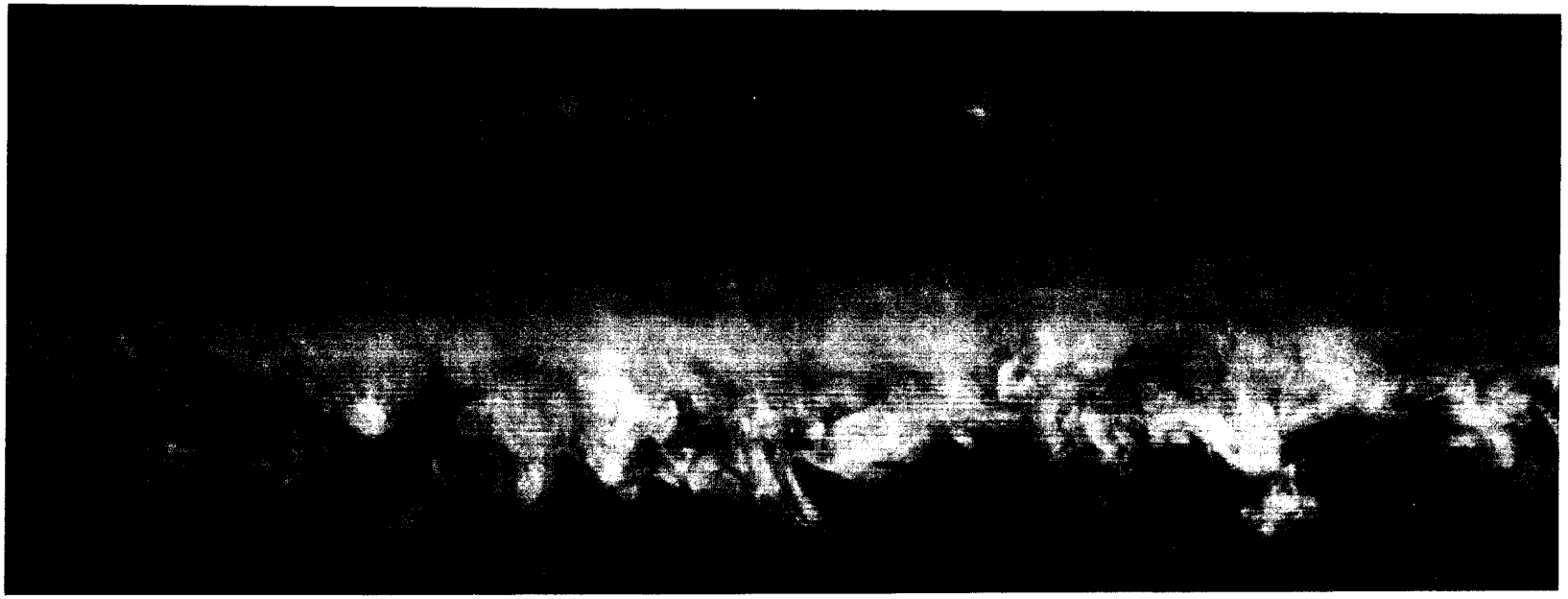

Figure 5.28 - Side view flow visualizations, Re=151,800, C_L=0.08

a) x/c: 0-2.3

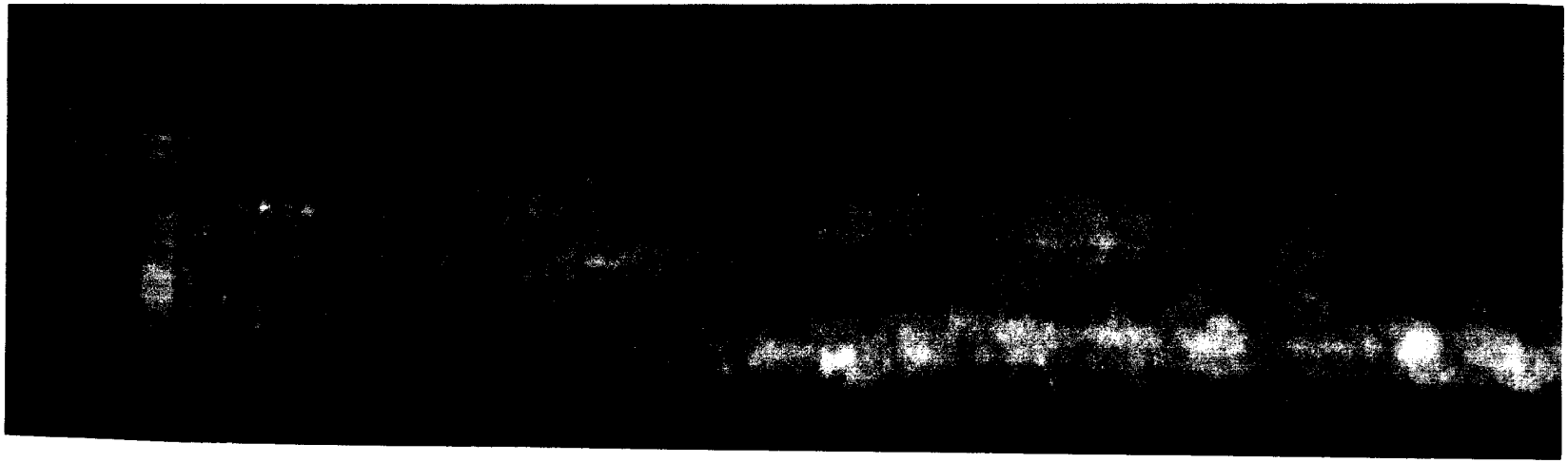

b) x/c: 4.0-6.6

Figure 5.29 - Bottom view flow visualizations, Re=151,800, C_L=0.15

c) x/c: 8.5-11.0

d) x/c: 18.8-21.3

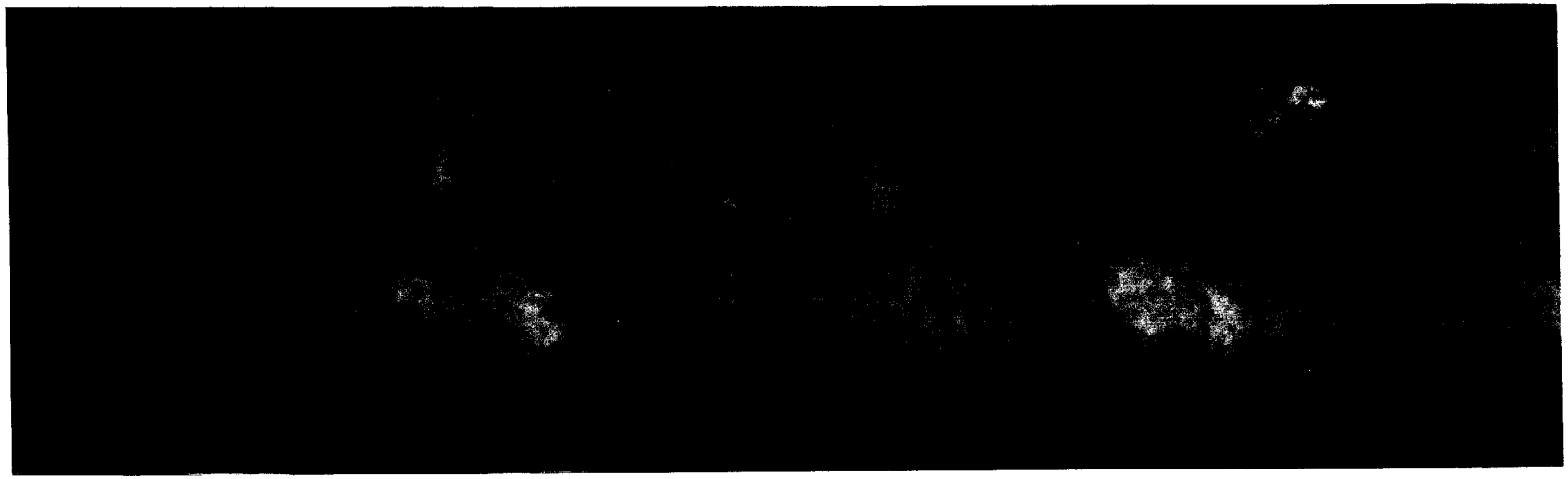

Figure 5.29 - Bottom view flow visualizations, Re=151,800, C_L=0.15

a) x/c: 0-2.3

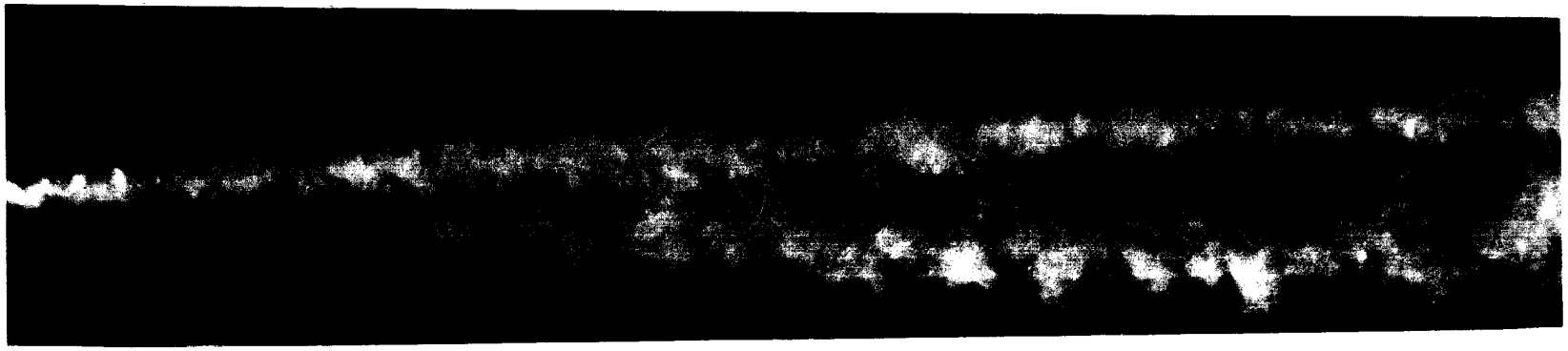

b) x/c: 4.0-6.6

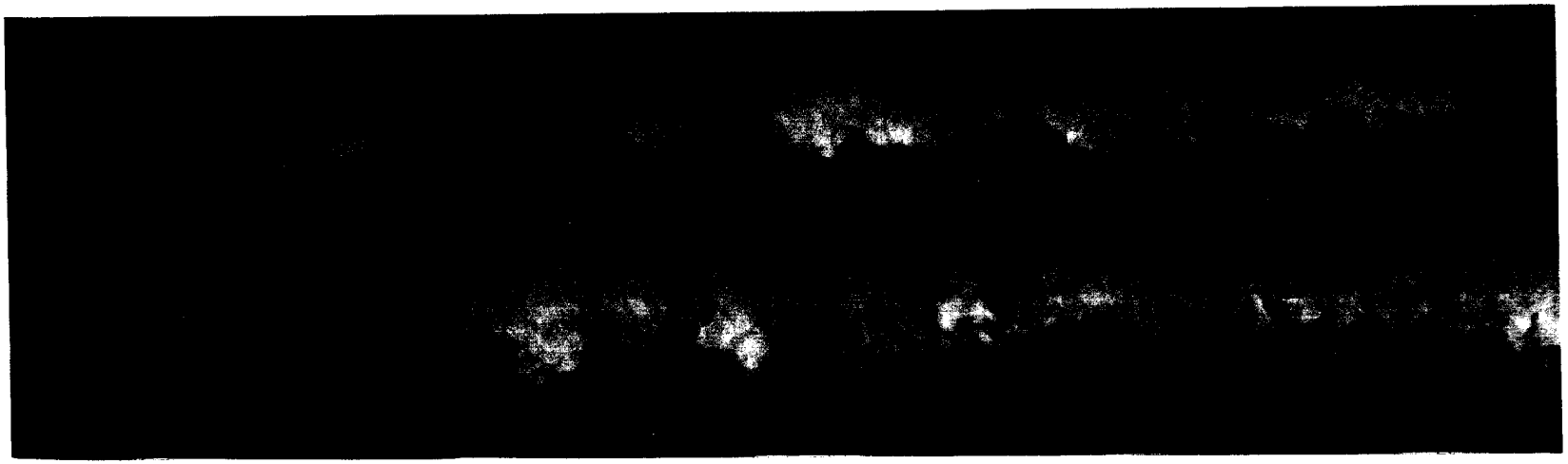

Figure 5.30 - Side view flow visualizations, Re=151,800, C_L=0.15

c) x/c: 8.5-11.0

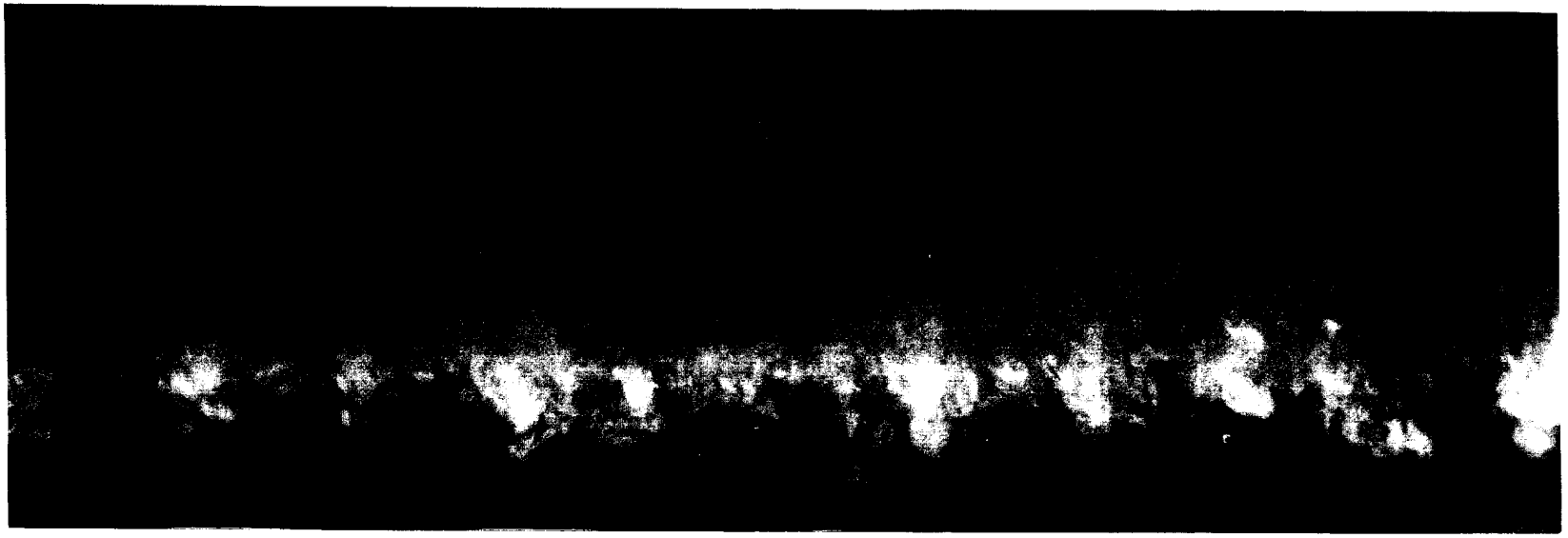

d) x/c: 18.8-21.3

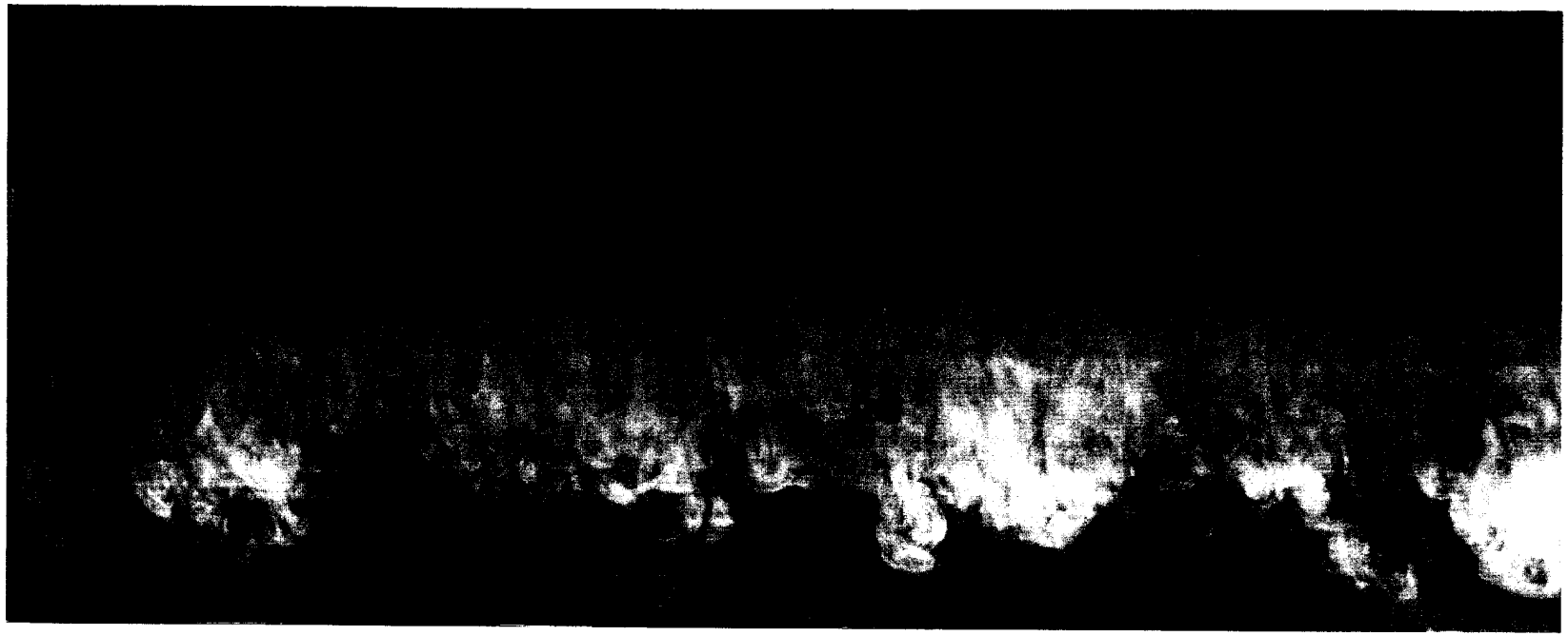

Figure 5.30 - Side view flow visualizations, Re=151,800, C_L=0.15

a) x/c: 0-1.8

b) x/c: 0.91-3.7

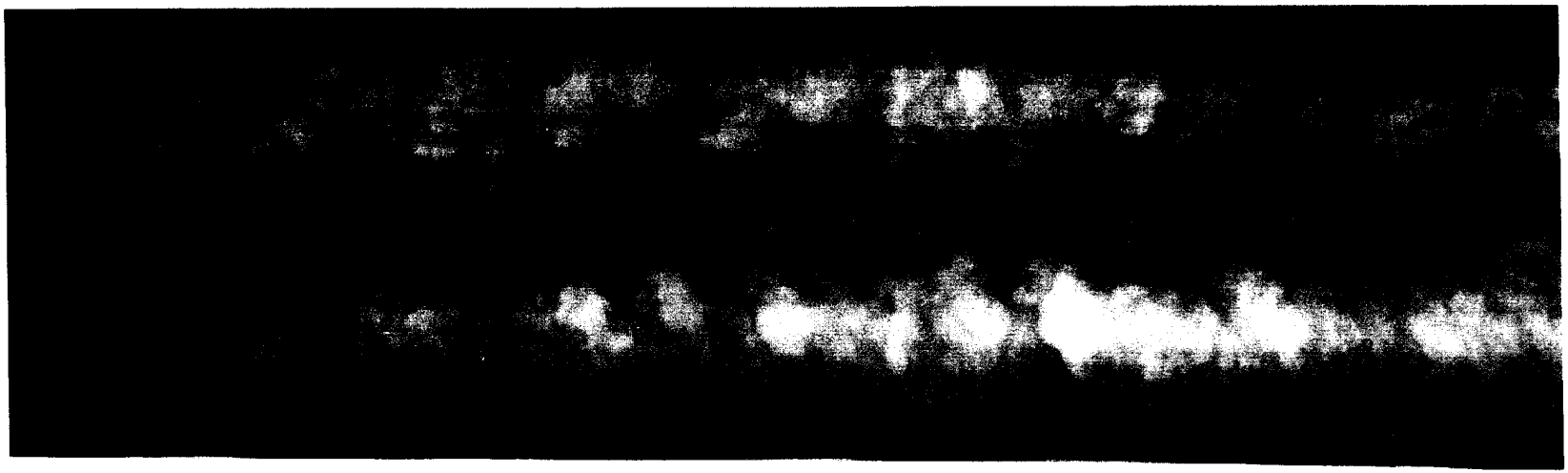

Figure 5.31 - Bottom view flow visualizations, Re=151,800, C_L=0.22

c) x/c: 2.6-5.4

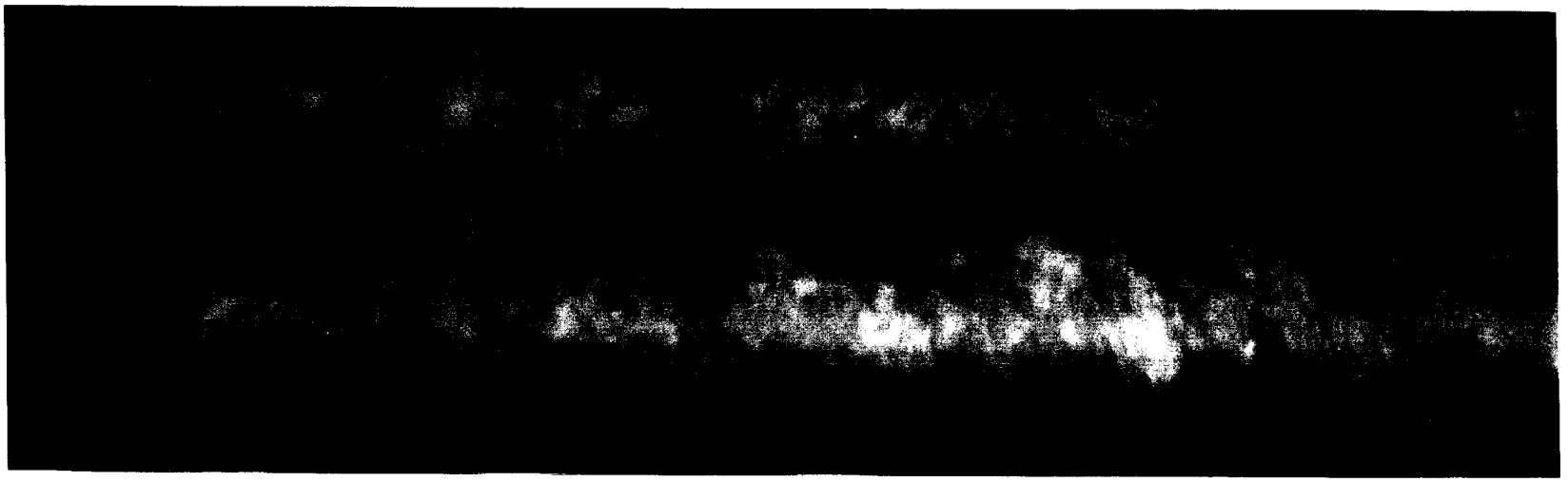

d) x/c: 3.8-6.6

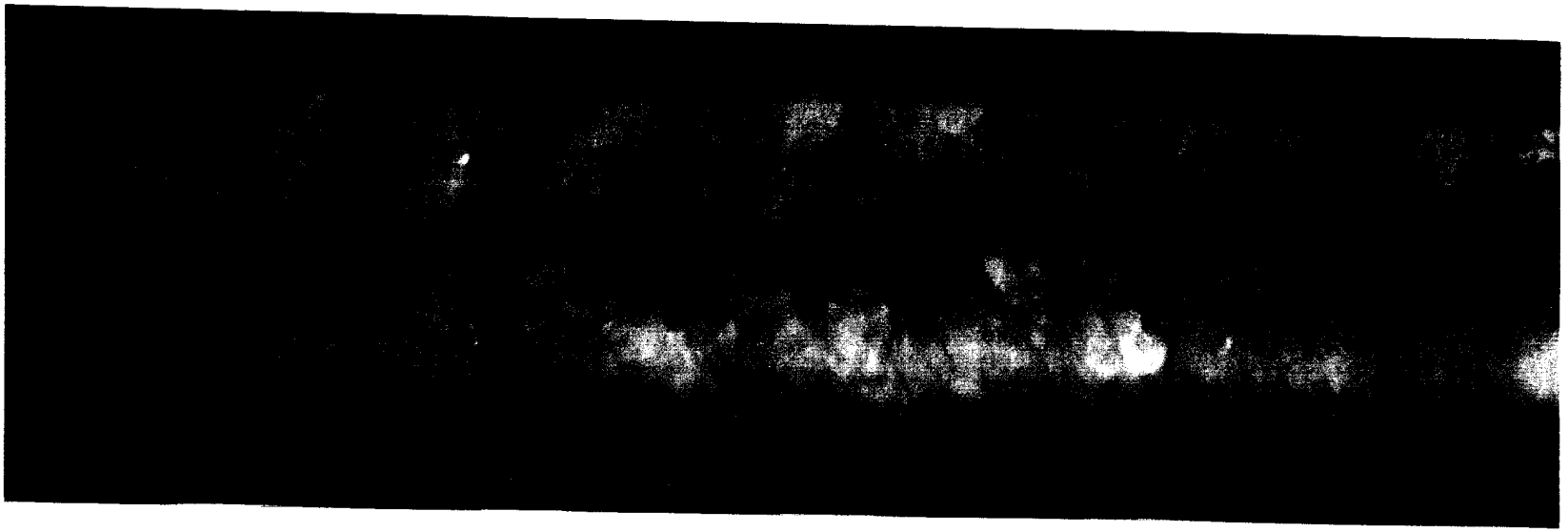

Figure 5.31 - Bottom view flow visualizations, Re=151,800, C_L=0.22

e) x/c: 6.3-9.1

f) x/c: 10-12.8

Figure 5.31 - Bottom view flow visualizations, Re=151,800, C_L=0.22

g) x/c: 56.2-58.9

Figure 5.31 - Bottom view flow visualizations, Re=151,800, C_L=0.22

a) x/c: 0-1.8

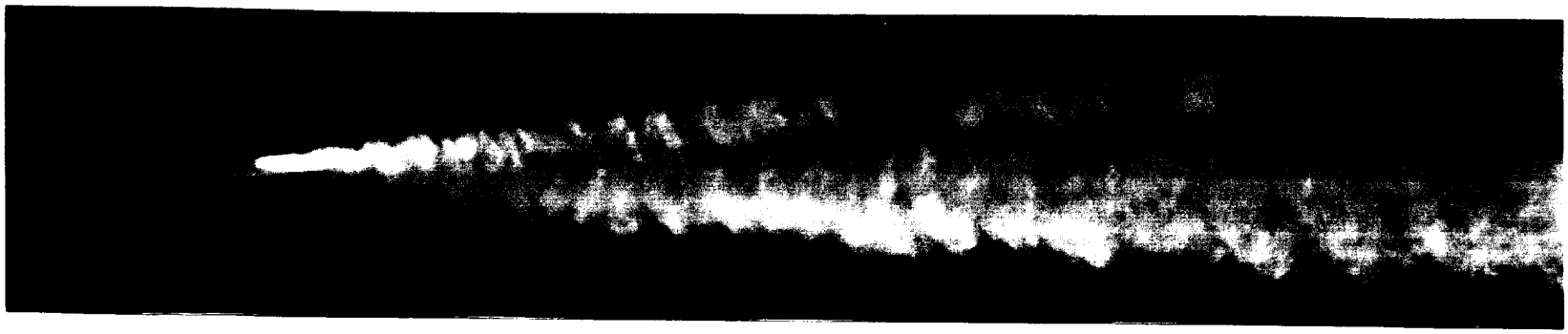

b) x/c: 0.91-3.7

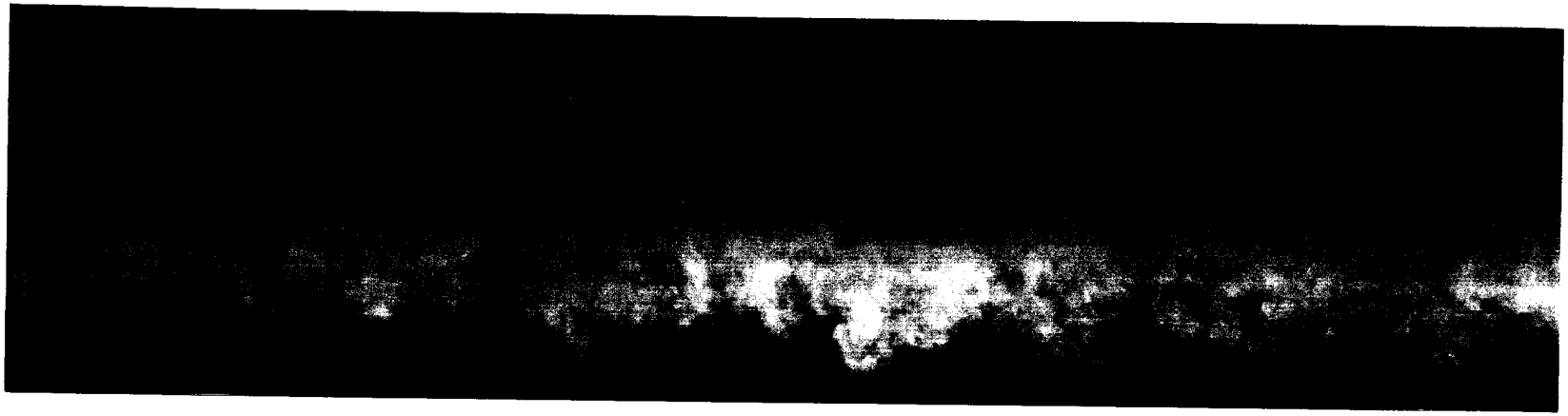

Figure 5.32 - Side view flow visualizations, Re=151,800, C_L=0.22

c) x/c: 2.6-5.4

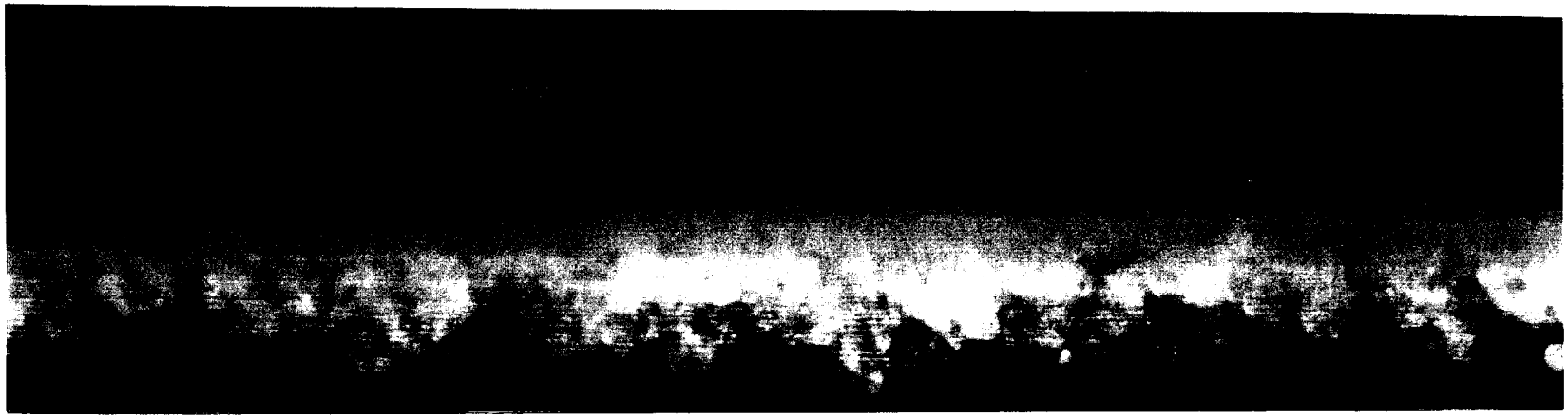

d) x/c: 3.8-6.6

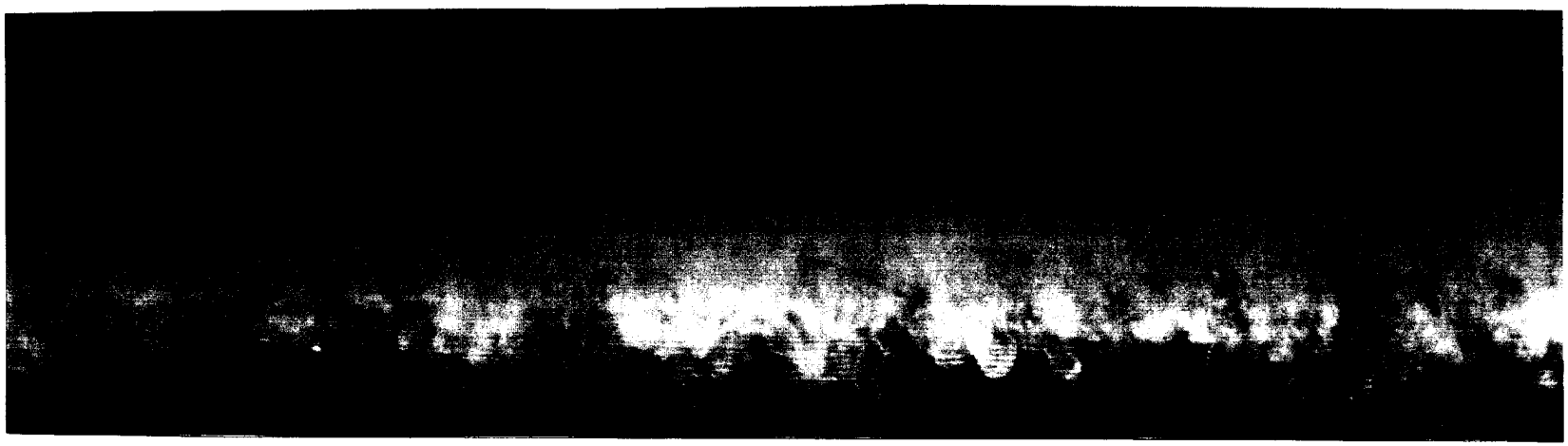

Figure 5.32 - Side view flow visualizations, Re=151,800, C_L=0.22

e) x/c: 6.3-9.1

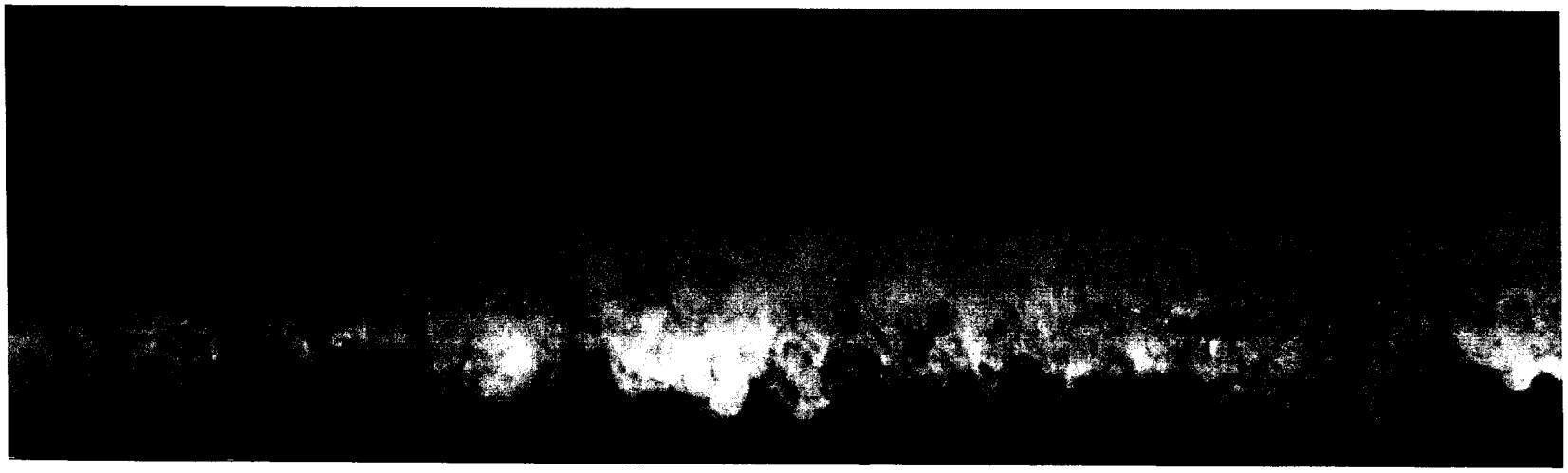

f) x/c: 10-12.8

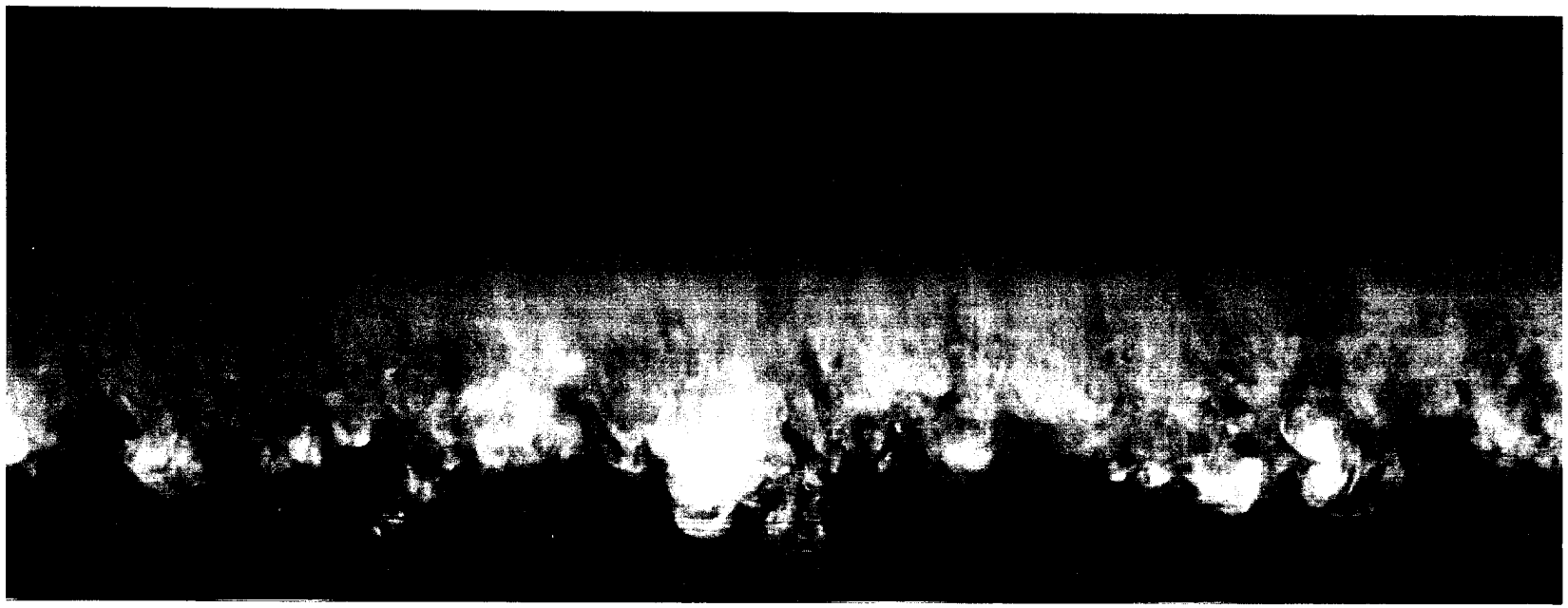

Figure 5.32 - Side view flow visualizations, Re=151,800, C_L=0.22

g) x/c: 56.2-58.

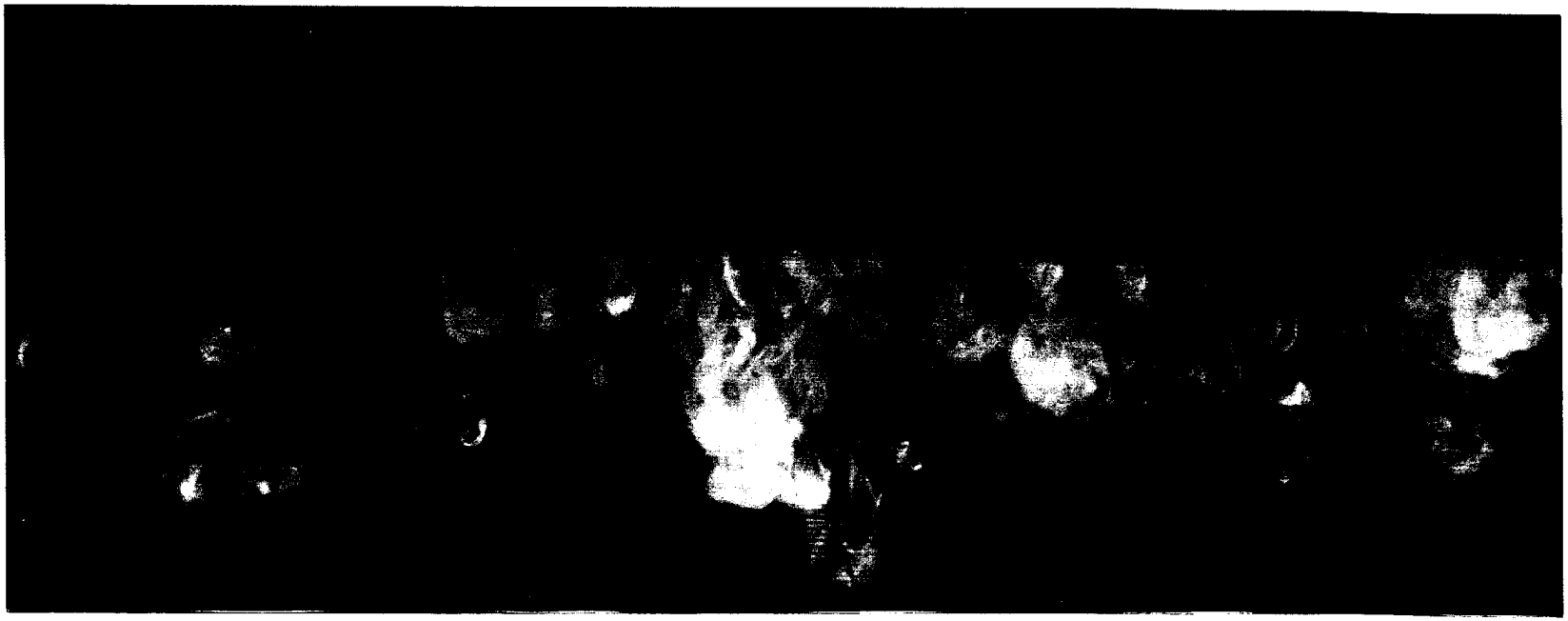

a) x/c: 0-2.3

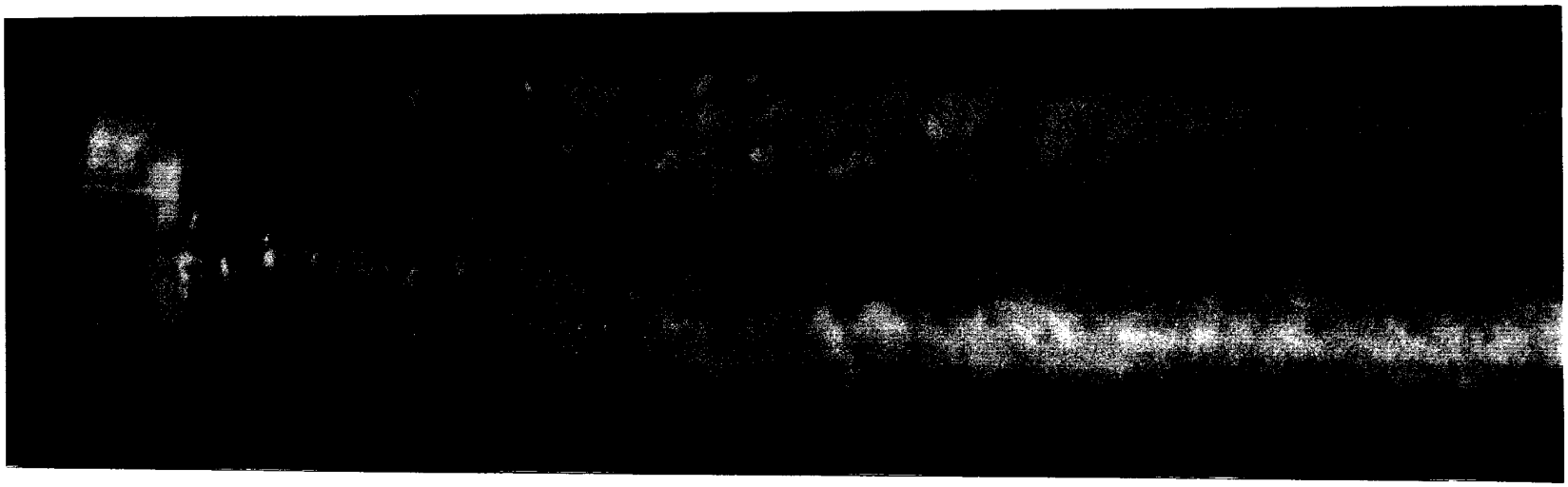

b) x/c: 1.8-4.3

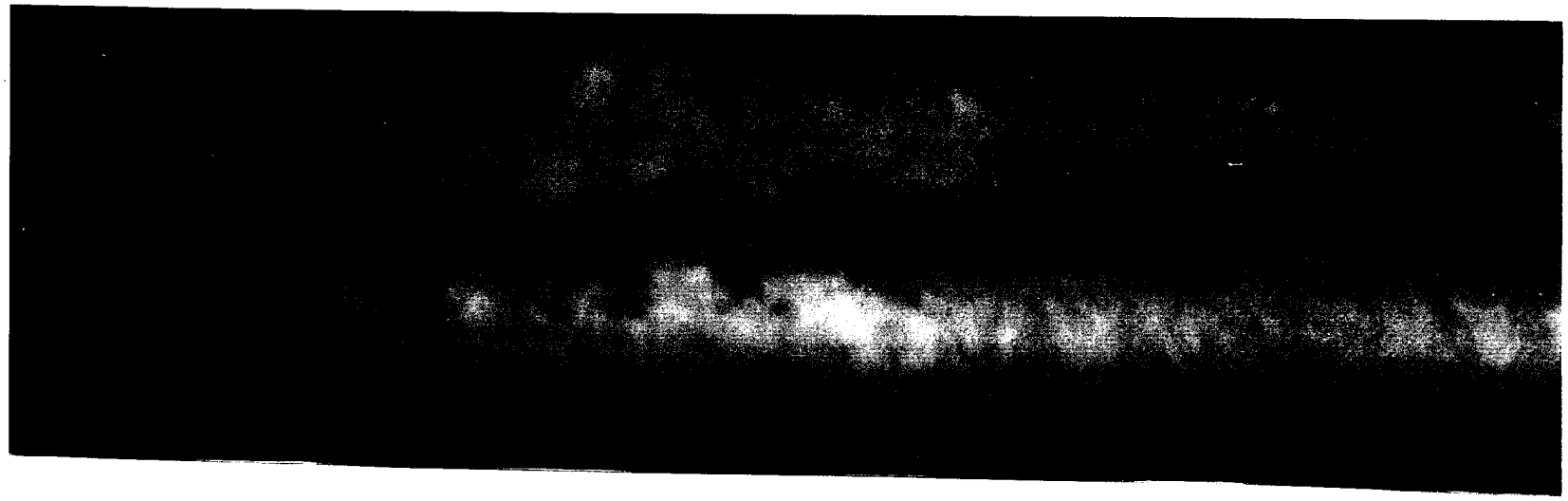

Figure 5.33 - Bottom view flow visualizations, Re=151,800, C_L=0.34

c) x/c: 4.1-6.6

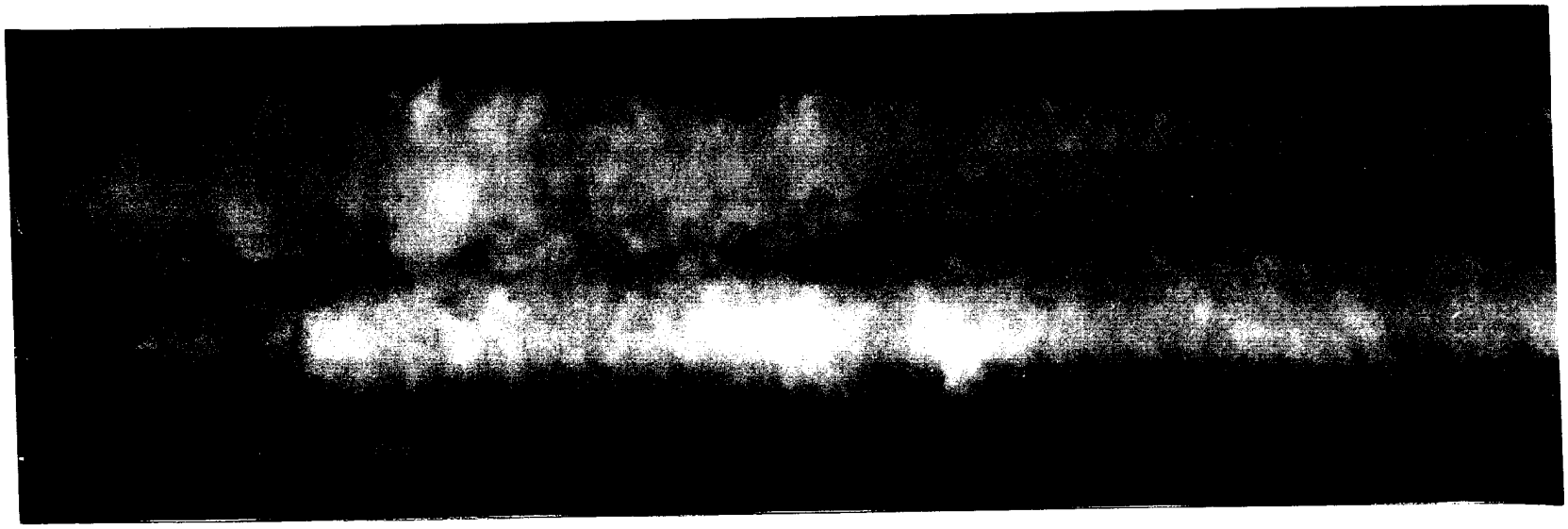

d) x/c: 6.2-8.7

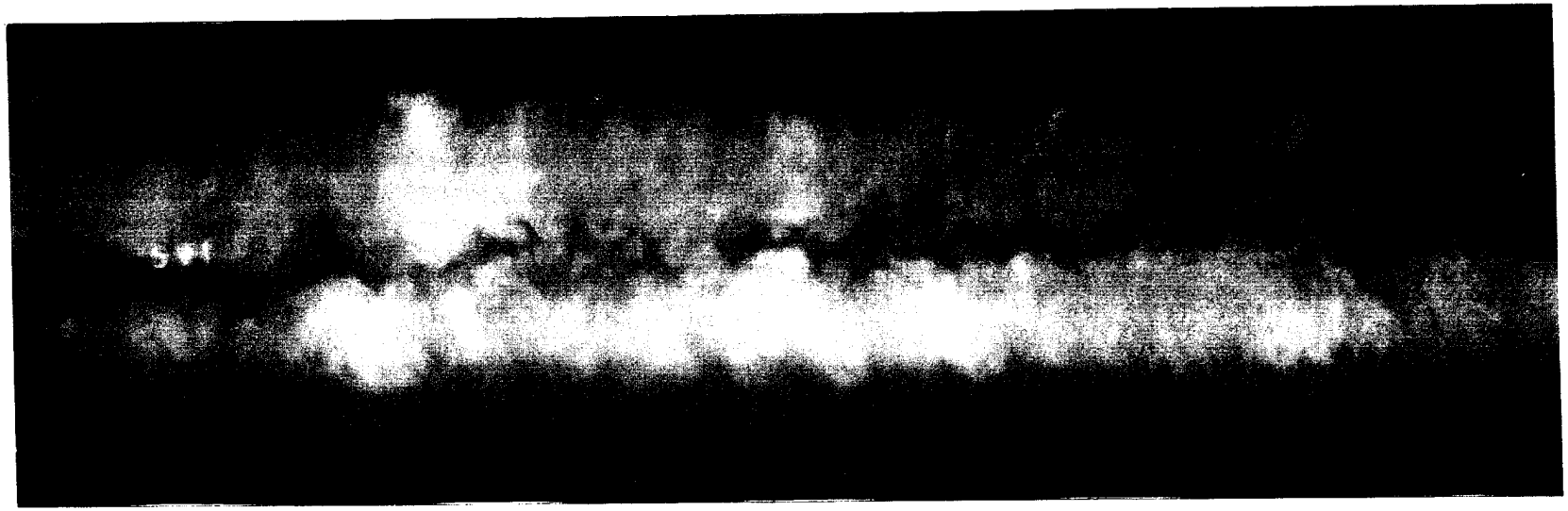

Figure 5.33 - Bottom view flow visualizations, Re=151,800, C_L=0.34

a) x/c: 0-2.3

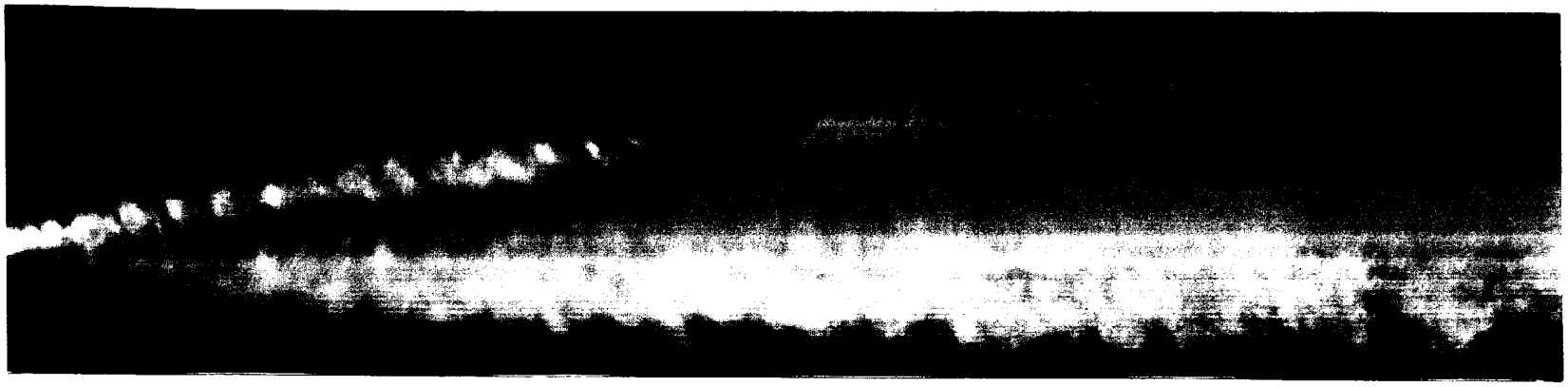

b) x/c: 1.8-4.3

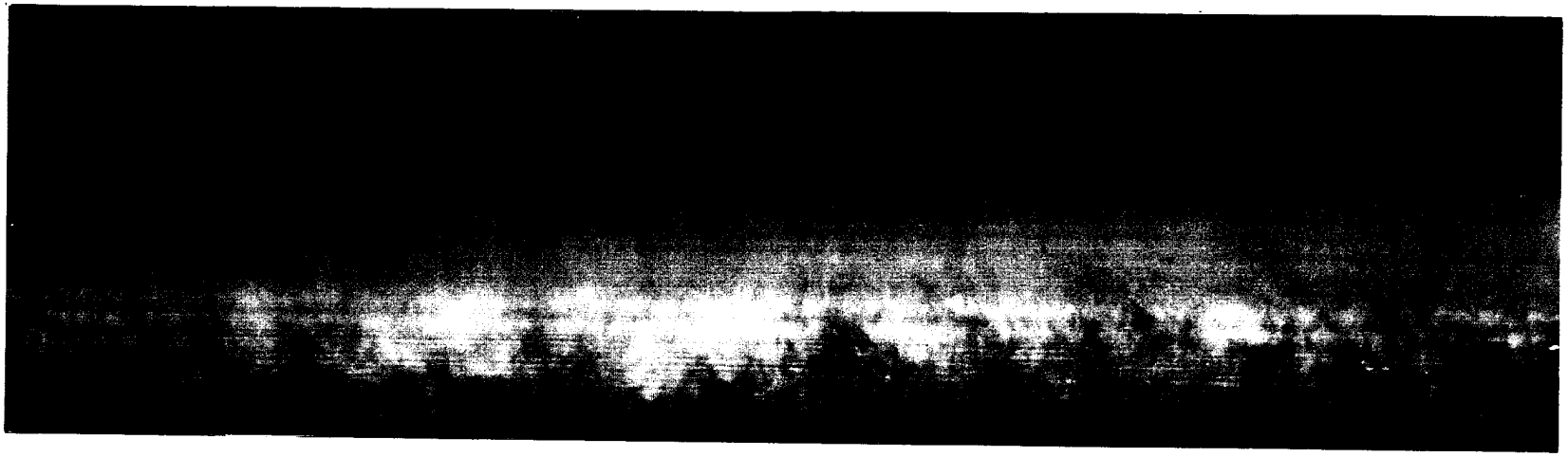

Figure 5.34 - Side view flow visualizations, Re=151,800, C_L=0.34

c) x/c: 4.1-6.6

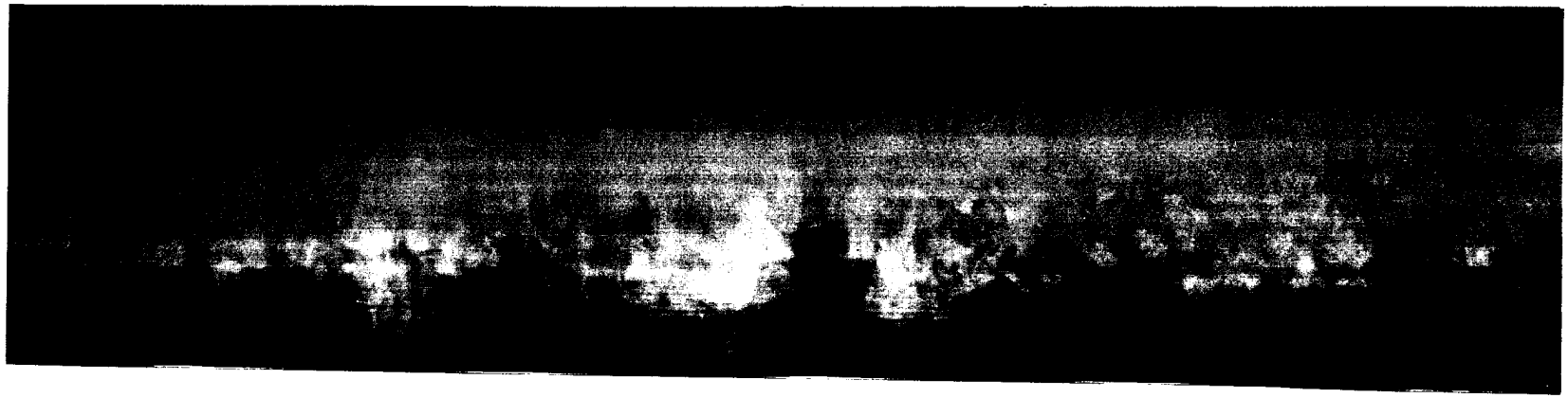

d) x/c: 6.2-8.7

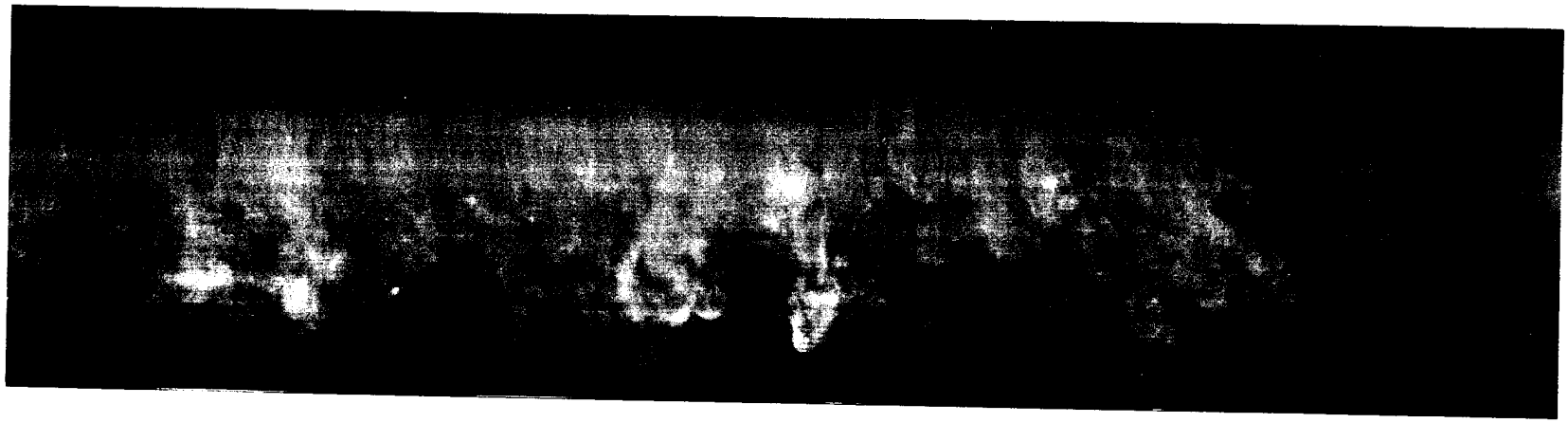

Figure 5.34 - Side view flow visualizations, Re=151,800, C_L=0.34

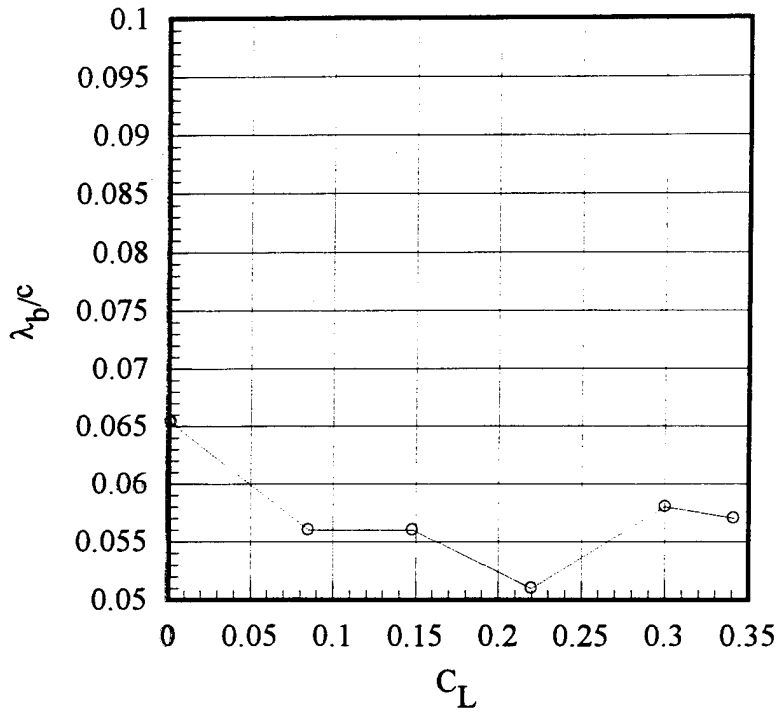

Figure 5.35 - Braid wake spacing as a function of lift coefficinet